Modelling of the hydrodynamics of bubble columns using a two-fluid model coupled with a population balance approach

Modelling of the hydrodynamics of bubble columns using a two-fluid model coupled with a population balance approach

Luca Gemello

N°d'ordre NNT : 2018LYSE1245

THESE de DOCTORAT DE L'UNIVERSITE DE LYON
opérée au sein de
l'Université Claude Bernard Lyon 1

Ecole Doctorale N° 162
(Mécanique, Energétique, Génie Civil et Acoustique - MEGA)

Spécialité de doctorat : Génie chimique et mécanique des fluides

Soutenue publiquement le 15/11/2018, par :
Luca Gemello

Modélisation de l'hydrodynamique des colonnes à bulles selon une approche couplant modèle à deux fluides et bilan de population

---

Devant le jury composé de :

Fletcher, David	Professeur	The University of Sydney	Rapporteur
Roig, Veronique	Professeure	Toulouse INP	Rapporteure
Abbas, Micheline	Maître de Conférences	Université Toulouse III	Examinatrice
Fongarland, Pascal	Professeur des Universités	Université Lyon 1	Examinateur
Montante, Giuseppina	Professeure	Università di Bologna	Examinatrice
Augier, Frédéric	Ingénieur de Recherche	IFP Energies nouvelles	Directeur de thèse
Marchisio, Daniele	Professeur	Politecnico di Torino	Directeur de thèse
Plais, Cécile	Ingénieur de Recherche	IFP Energies nouvelles	Encadrante de thèse
Vanni, Marco	Professeur	Politecnico di Torino	Invité

Doctoral Dissertation

Université Claude Bernard Lyon 1 - ED 162 MEGA
Politecnico di Torino - Chemical Engineering

Prepared in the laboratory of IFP Energies nouvelles

Speciality: Chemical Engineering and Fluid Mechanics

Modelling of the hydrodynamics of bubble columns using a two-fluid model coupled with a population balance approach

Luca Gemello

Supervisors
Frédéric Augier, Supervisor UCB Lyon 1 - IFP Energies nouvelles
Daniele Marchisio, Supervisor Politecnico di Torino
Cécile Plais, Co-supervisor IFP Energies nouvelles

Doctoral Examination Committee
David FLETCHER, The University of Sidney, Reviewer
Veronique ROIG, INP Toulouse, Reviewer
Frédéric AUGIER, UCB Lyon 1 - IFP Energies nouvelles, Supervisor
Daniele MARCHISIO, Supervisor Politecnico di Torino, Supervisor
Cécile PLAIS, IFP Energies nouvelles, Co-supervisor
Pascal FONGARLAND, UCB Lyon 1
Micheline ABBAS, Université Toulouse III
Giuseppina MONTANTE, Università di Bologna

Abstract

Modelling of the hydrodynamics of bubble columns using a two-fluid model coupled with a population balance approach

The simulation of bubble column reactors under industrial operating conditions is an exciting challenge. The main objective of this work is to predict the bubble size, in turn interconnected with the reactor hydrodynamic conditions, with computational models, by modelling bubble breakage and coalescence. Experimental data are collected for model validation, including bubble size measurements with an innovative cross-correlation technique. Experiments are carried out with tap water and demineralised water, with or without the addition of ethanol, and gathered results show that additives reduce coalescence and lower the mean bubble size. Two different spargers are used, in order to decouple the investigation of breakage and coalescence. The experimental data set is used to validate our unsteady three-dimensional Eulerian-Eulerian CFD simulations. A drag law for oblate bubbles is considered, together with a factor that accounts for the swarm effect. Several turbulence models are tested. The contribution of the bubbles to scalar mixing is assessed. To predict bubble size, a population balance model is coupled to the hydrodynamic model and is solved with the quadrature method of moments. A set of breakage and coalescence kernels is proposed, capable of predicting the bubble size for different operating conditions. Scale-up effects are also investigated.

Keywords Bubble columns, Bubble size, Computational fluid dynamics, Population balance modelling, QMOM.

Résumé

Modélisation de l'hydrodynamique des colonnes à bulles selon une approche couplant modèle à deux fluides et bilan de population

La simulation de réacteurs à bulles en régime industriel est un grand défi. L'objectif principal de ce travail est la prédiction de la taille des bulles à l'aide d'un modèle numérique de bilan de population, basé sur la modélisation des phénomènes de brisure et de coalescence, et pouvant être couplé aux conditions hydrodynamiques présentes dans les réacteurs. Différentes données expérimentales sont obtenues pour valider le modèle. La taille des bulles est mesurée à l'aide d'une technique innovante de corrélation croisée. Les essais, réalisés en eau du réseau (partiellement contaminée) et en eau déminéralisée avec ajout éventuel d'éthanol, montrent que les additifs réduisent la coalescence et diminuent la taille moyenne des bulles. Deux distributeurs du gaz différents sont utilisés pour découpler l'étude de la bri-sure et de la coalescence. Les données expérimentales sont utilisées initialement pour valider des simulations CFD 3D transitoires Eulériennes-Eulériennes. La loi de traînée est corrigée par un facteur de *swarm* pour intégrer l'effet d'une fraction de gaz élevée. Différents modèles de turbulence sont testés. La contribution des bulles au mélange de scalaires est évaluée. Enfin, pour prédire la taille des bulles, un bilan de population est couplé au modèle hydrodynamique préalablement validé et est résolu par la méthode de quadrature des moments (QMOM). Un set original de *kernels* de brisure et coalescence est proposé, capable de prédire la taille des bulles pour différentes conditions opératoires. Le comportement du modèle lors de l'extrapolation des réacteurs est également examiné.

Mots clés Colonnes à bulles, Taille des bulles, CFD, Bilan de population, QMOM.

Riassunto

Modellazione dell'idrodinamica delle colonne a bolle con un approccio che combina modello a due fluidi e bilancio di popolazione

La simulazione di colonne a bolle in condizioni industriali è un problema di grande rilevanza. L'obiettivo principale di questo lavoro è prevedere con modelli computazionali la dimensione delle bolle, legata alla fluidodinamica dei reattori, considerando i fenomeni di rottura e di coalescenza. La validazione del modello è effettuata tramite il confronto con dati sperimentali appositamente raccolti, tra cui la dimensione delle bolle, ottenuta con un'innovativa tecnica di cross-correlazione. Gli esperimenti effettuati con acqua parzialmente contaminata e con acqua demineralizzata con l'eventuale aggiunta di etanolo, mostrano che gli additivi riducono la coalescenza e diminuiscono la dimensione media delle bolle. Sono stati inoltre utilizzati negli esperimenti con due sparger diversi, per disaccoppiare lo studio di rottura e coalescenza. I dati sperimentali sono stati utilizzati per convalidare simulazioni CFD 3D transitorie Euleriane-Euleriane. Il modello per la forza di trascinamento è corretto da un fattore di *swarm* per considerare l'effetto delle interazioni tra le bolle. Sono stati testati diversi modelli di turbolenza, nonché il contributo delle bolle sulla miscelazione degli scalari. Per prevedere la dimensione delle bolle, è stato utilizzato un bilancio di popolazione risolto con il metodo di quadratura dei momenti. Nella presente tesi viene proposto un set di kernel di rottura e coalescenza per prevedere le dimensioni delle bolle in diverse condizioni operative, considerando anche gli effetti dello scale-up.

Parole chiave Colonne a bolle, Dimensione delle bolle, CFD, Bilancio di popolazione, QMOM.

Résumé substantiel

Cette thèse de doctorat porte sur la modélisation des réacteurs à bulles en régime industriel. L'objectif principal est la prédiction et la modélisation de la taille des bulles dans ces systèmes. Parmi les différents types de réacteurs gaz-liquide, les colonnes à bulles sont largement utilisées dans différents domaines du génie chimique. La géométrie de ces réacteurs est simple, sans parties mobiles. Les colonnes à bulles ont de faibles coûts d'exploitation et d'entretien et de bons taux de transfert de masse et de chaleur. Leur hydrodynamique peut toutefois être complexe et fortement dépendante de la géométrie et des débits de fluide. Le taux de vide, les vitesses du gaz et du liquide, la turbulence et la taille des bulles sont liés de manière complexe aux conditions opératoires. Les colonnes à bulles sont généralement utilisées en régime d'écoulement dit « hétérogène ». Dans ce régime, caractérisé par une forte fraction volumique en gaz et une recirculation liquide, différentes corrélations empiriques ont été développées pour aider les ingénieurs à réaliser les dimensionnements. Ces corrélations ont généralement des domaines de validation assez étroits en termes de conditions opératoires, géométries ou propriétés physiques. Des modèles avec une plus grande validité (c'est-à-dire pour le régime homogène et hétérogène) ont un fort intérêt dans le domaine industriel.

Dans le passé, la mise à l'échelle des colonnes à bulles a été basée sur l'utilisation de corrélations macroscopiques pour décrire l'hydrodynamique et le transport. De nos jours, la mécanique des fluides numérique (MFN ou CFD selon la terminologie anglo-saxonne), apparaît comme un outil clé pour prédire les propriétés globales et locales de ces systèmes. Plusieurs approches numériques sont envisageables pour simuler les écoulements à bulles. D'une part la phase dispersée peut être modélisée sous forme discrète, et les trajectoires individuelles des bulles sont calculées, on parle alors de modèles Lagrangiens. Ces modèles fournissent des informations à l'échelles des bulles mais ne peuvent guère être appliqués à un nombre de bulles dépassant quelques millions. D'autre part la phase dispersée peut être modélisée comme une phase « pseudo » continue en interaction avec la phase porteuse continue. Ce type de modèle, dit Euler-Euler ou modèles à 2 fluides, n'est pas limité par le nombre de bulles mais seule une description moyennée de l'écoulement des bulles est accessible. Ces deux familles de modèles nécessitent le choix de modèles physiques représentant les forces échangées entre les phases. Une troisième famille de modèles, basée sur la reconstruction des interfaces, n'est pas détaillée ici car elle ne peut pas être, à l'heure actuelle, utilisée pour simuler les écoulements industriels.

Quelle que soit l'approche choisie pour modéliser la phase dispersée, différentes modélisations de la turbulence sont possibles : simulation directe, simulation aux grandes échelles, ou simulation basée sur la moyenne temporelle des équations de Navier Stokes (ou Reynolds Average Navier Stokes Equations - RANS). Etant donné l'objectif de la thèse et sa finalité en termes de simulation de réacteurs

industriels, pouvant contenir plusieurs milliards de bulles, seule l'approche Euler-Euler basée sur une approche RANS est envisageable.

Les simulations CFD Eulériennes-Eulériennes classiques supposent que chaque élément de la phase dispersée a la même taille. Cette contrainte peut être levée en couplant la simulation numérique à un modèle de bilan de population (population balance modelling - PBM). Des équations sont alors ajoutées afin de calculer les distributions des bulles en termes de taille, de vitesse ou de composition chimique. Dans le présent travail, l'amélioration de la prédiction se concentre sur un couplage avec la taille et la distribution de taille des bulles (bubble size distribution - BSD), car il n'existe pas un bilan de population validé en régime hétérogène.

Trois types de méthodes sont disponibles a priori dans la littérature pour le calcul des bilans de population. Elles peuvent être divisées en : méthodes des classes (CM), méthodes Monte Carlo (MCM) et méthodes des moments. Dans la méthode des classes, l'espace des coordonnées internes est discrétisé. La méthode Monte Carlo résout des équations différentielles stochastiques pour reproduire un nombre fini de réalisations artificielles du système à l'étude. Ces deux groupes nécessitent d'énormes ressources de calcul et ne peuvent pas être utilisés à l'heure actuelle pour les systèmes gaz-liquide à l'échelle industrielle. Les méthodes basées sur le moment résolvent des équations de transport pour un petit ensemble de moments d'ordre inférieur de la BSD. Cette méthode nécessite des équations de fermeture qui peuvent être obtenues par plusieurs méthodes. Les méthodes basées sur la quadrature des moments (Quadrature-Based Moments Methods - QBMM) représentent un groupe important. En particulier, la méthode QMOM peut être utilisée si une seule coordonnée interne (c'est-à-dire la taille des bulles) est étudiée (Marchisio & Fox 2013).

La méthode QMOM est couplée à un modèle CFD Eulérien-Eulérien dans ce travail pour étudier la coalescence (Liao & Lucas 2010) et la brisure des bulles (Liao & Lucas 2009) et obtenir un bilan de population validé en régime hétérogène. Ces modèles ont également besoin de données expérimentales précises pour différents régimes, conditions opératoires et fluides. Ces données sont cependant difficiles à obtenir et à extrapoler. La prédiction de la distribution de la taille des bulles par les modèles CFD est donc un grand défi, car cela contribuerait à rendre la CFD complètement prédictive.

Jusqu'à récemment, il était encore difficile de mesurer correctement la taille des bulles pour un fort taux de gaz. La plupart des travaux expérimentaux publiés se concentrent sur le régime d'écoulement homogène (Krishna 2000), avec de faibles vitesses superficielles de gaz. Très peu d'articles traitent des mesures de BSD en régime hétérogène (Xue 2004, Chaumat et al. 2007, McClure et al. 2015, 2016, 2017). Ils sont basés sur une mesure utilisant des sondes multipoints. Cette technique est valide dans le cas de bulles ayant des trajectoires presque verticales. Dans le régime hétérogène, les bulles n'ont pas de trajectoires verticales, surtout dans le cas de larges colonnes. Cette technique a par ailleurs une faible précision en régime hétérogène (McClure et al. 2013, Xue 2004). Malgré cette limitation, les sondes multipoints ont l'avantage d'accéder à la distribution de cordes et à la vitesse des bulles.

Pour pallier à cette carence, une technique de corrélation croisée (CC) a été mise au point pour surmonter les limites des techniques précédentes. Cette technique peut mesurer la taille des bulles indépendamment de la trajectoire des bulles

(Raimundo 2015). Elle est donc bien adaptée au régime hétérogène (Raimundo et al. 2016). La technique CC ne fournit pas la BSD, mais un diamètre moyen, qui est mesuré de manière fiable à toutes les positions radiales. Cette technique est donc complémentaire des techniques existantes. Raimundo (2015) a utilisé l'eau du réseau pour ses mesures. Des mesures complémentaires sont nécessaires, afin de disposer d'une base de données expérimentales élargie, pouvant être utilisée pour valider indépendamment des modèles de brisure et de coalescence. La BSD est fortement influencée par le niveau de contamination de l'eau. Les phénomènes de brisure et coalescence doivent être étudiés en considérant l'effet des additifs. McClure et al. (2015) ont présenté un travail documenté sur les propriétés des bulles en présence d'additifs. L'addition d'alcool retarde la transition des régimes vers des vitesses superficielles de gaz plus élevées, en raison de la diminution de la coalescence (Keitel & Onken 1982) et de l'augmentation de la rigidité des bulles (Dargar & Macchi 2006). Un point d'intérêt industriel concerne l'effet du distributeur de gaz sur la taille des bulles (McClure et al. 2016). La modification du type de distributeur de gaz est un moyen simple pour modifier la BSD à l'entrée de la colonne.

En considérant simultanément les effets des additifs et du distributeur du gaz, les phénomènes de brisure et de coalescence peuvent être découplés. Différents essais ont été réalisés, en eau déminéralisée, eau du réseau et eau déminéralisée avec ajout d'éthanol. Les profils de diamètre moyen, de fraction de gaz et de vitesse du liquide sont mesurés. L'ajout d'éthanol est utilisé pour réduire la coalescence des bulles. Les mesures sont réalisées sur une colonne cylindrique avec un diamètre de 0,4 m dans une large gamme de vitesses de gaz superficielles, entre 0,03 m/s et 0,35 m/s. Deux distributeurs du gaz différents sont utilisés, générant ainsi des bulles de tailles initiales très différentes et simulant dans certains cas une forte brisure des bulles. Ce travail fournit une base de données expérimentales pour dissocier les phénomènes de brisure et de coalescence, en jouant sur la présence d'additifs e le type de distributeur de gaz.

À partir des résultats expérimentaux, des simulations CFD 3D transitoires Eulériennes-Eulériennes avec ANSYS Fluent sont réalisées pour atteindre l'objectif de ce travail. Les interactions entre le gaz et le liquide dominent ces systèmes et différentes forces interfaciales caractérisent l'environnement. Il n'y a pas de consensus sur la façon de simuler les colonnes de bulles en termes de forces d'interface et donc il faut focaliser l'attention sur ces forces. Parmi elles, la force de traînée est la plus importante (Hlawitschka et al. 2017). Pour simuler ces systèmes, il est nécessaire de trouver une loi de traînée appropriée sous le régime hétérogène. Pour fractions de gaz élevées, les lois de traînée pour les bulles de forme oblate devraient être utilisées, comme la loi de traînée de Tomiyama (1998). La force de traînée doit tenir compte de l'effet de la présence de nombreuses bulles (swarm effect en anglais), car la distance entre les bulles est faible et elles interagissent les unes avec les autres. Dans la littérature, plusieurs facteurs correctifs ont été proposés, mais ils ont été obtenus en régime homogène. Le facteur de swarm doit réduire l'effet de la loi de trainée pour fractions volumiques élevées. Plusieurs formulations de la loi de trainée ont été testées dans un modèle CFD de type RANS instationnaire 3D, et il a été identifié que la loi de trainée de Tomiyama couplée à un nouveau facteur de swarm basé sur les travaux de Simonnet et al. (2008) permettait de reproduire assez fidèlement l'hydrodynamique dans une très large gamme de colonnes et conditions

opératoires.

Le choix du modèle de turbulence est un autre point important, étudié durant la thèse. Le modèle de turbulence influence le mélange, qui est une propriété clé pour les réacteurs en colonne de bulles, et l'hydrodynamique. La contribution des bulles au mélange de scalaires doit être considérée en régime hétérogène, car elle a un fort effet sur le mélange en régime homogène (Alméras et al. 2016).

Une fois acquises les données expérimentales nécessaires, et la modélisation CFD permettant de reproduire les écoulements en régimes hétérogènes, le développement et la validation d'un modèle de Bilan de Population a pu être réalisée. Pour cela, les modèles courants de la littérature ont été testés selon une approche QMOM en 0D avec Matlab puis en CFD 3D URANS. Les modèles existants de brisure (Liao & Lucas 2009) et de coalescence (Liao & Lucas 2010), développés pour le régime homogène, sont testés en régime hétérogène. Concernant la brisure, il a été montré que le modèle de Laakkonen et al. (2006) permettait de fournir des simulations réalistes d'écoulements gouvernés par la brisure. Concernant la coalescence, des résultats satisfaisants sont obtenus en utilisant les modèles de fréquence de collision de Wang et al. (2005) et de probabilité de coalescence de Lehr et al. (2002), ces deux modèles ayant toutefois fait l'objet de modifications pour prédire quantitativement les diamètres de Sauter mesurés dans une large gamme de conditions opératoires.

Les perspectives de ce travail sont nombreuses. Le lien entre les propriétés physiques des liquides et la coalescence doit être clarifié. Il faudra faire plus un plus grand nombre d'expériences avec des additifs et de recueillir des données expérimentales sur les propriétés des liquides pertinentes pour obtenir un outil entièrement prédictif. Mais encore faut-il identifier les propriétés physiques pertinentes. La tension de surface en fait partie mais elle ne justifie les écarts de comportements observés. Le modèle de coalescence de Lehr et al. (2002) utilisé dans cette étude, basé sur une vitesse critique entre bulles, nécessiterait également d'être relié à des fondements théoriques plus solides. Concernant la modélisation hydrodynamique, le facteur de swarm proposé dans ce travail est complètement empirique, et il serait intéressant d'obtenir un facteur de swarm basé sur un modèle théorique ou sur des simulations numériques résolues à une échelle plus fine. En outre, l'étude des forces interfaciales secondaires, négligées dans ce travail, reste un axe important de recherche.

Bibliographie

Alméras, E., Plais, C., Euzenat, F., Risso, F., Roig, V. & Augier, F. (2016), 'Scalar mixing in bubbly flows: Experimental investigation and diffusivity modelling', *Chemical Engineering Science* 140, 114–122.

Chaumat, H., Billet, A. & Delmas, H. (2007), 'Hydrodynamics and mass transfer in bubble column: Influence of liquid phase surface tension', *Chemical Engineering Science* 62, 7378–7390.

Dargar, P. & Macchi, A. (2006), 'Effect of surface-active agents on the phase holdups of three-phase fluidized beds.', *Chemical Engineering and Processing* 45, 764–772.

Hlawitschka, M. W., Kováts, P., Zahringer, K. & Bart, H. J. (2017), 'Simulation and experimental validation of reactive bubble column reactors', *Chemical Engineering Science* 170(Supplement C), 306–319.

Keitel, G. & Onken, U. (1982), 'Inhibition of bubble coalescence by solutes in air/water dispersions.', *Chemical Engineering Science* 37, 1635–1638.

Krishna, R. (2000), 'A scale-up strategy for a commercial scale bubble column slurry reactor for Fischer-Tropsch synthesis.', *Oil & Gas Science and Technology* 55(4), 359–393.

Laakkonen, M., Alopaeus, V. & Aittamaa, J. (2006), 'Validation of bubble breakage, coalescence and mass transfer models for gas-liquid dispersion in agitated vessel', *Chemical Engineering Science* 61, 218–228.

Lehr, F., Millies, M. & Mewes, D. (2002), 'Bubble-size distributions and flow fields in bubble columns', *American Institute of Chemical Engineering Journal* 48(11), 2426–2443.

Liao, Y. & Lucas, D. (2009), 'A literature review of theoretical models for drop and bubble breakup in turbulent dispersions.', *Chemical Engineering Science* 64, 3389–3406.

Liao, Y. & Lucas, D. (2010), 'A literature review on mechanisms and models for the coalescence process of fluid particles.', *Chemical Engineering Science* 65, 2851–2864.

Marchisio, D. L. & Fox, R. O. (2013), *Computational Models for Polydisperse Particulate and Multiphase Systems.*, Cambridge University Press, Cambridge, UK.

McClure, D. D., Kavanagh, J. M., Fletcher, D. F. & Barton, G. W. (2013), 'Development of a CFD model of bubble column bioreactors: Part one - a detailed experimental study', *Chemical Engineering & Technology* 36(12), 2065–2070.

McClure, D. D., Kavanagh, J. M., Fletcher, D. F. & Barton, G. W. (2017), 'Experimental investigation into the drag volume fraction correction term for gas-liquid bubbly flows', *Chemical Engineering Science* 170, 91–97.

McClure, D. D., Norris, H., Kavanagh, J. M., Fletcher, D. F. & Barton, G. W. (2015), 'Towards a CFD model of bubble columns containing significant surfactant levels', *Chemical Engineering Science* 127, 189–201.

McClure, D. D., Wang, C., Kavanagh, J. M., Fletcher, D. F. & Barton, G. W. (2016), 'Experimental investigation into the impact of sparger design on bubble columns at high superficial velocities', *Chemical Engineering Research and Design* 106, 205–213.

Raimundo, P. M. (2015), Analysis and modelization of local hydrodynamics in bubble columns, PhD thesis, Université Grenoble Alpes.

Raimundo, P. M., Cartellier, A., Beneventi, D., Forret, A. & Augier, F. (2016), 'A new technique for in-situ measurements of bubble characteristics in bubble columns operated in the heterogeneous regime', *Chemical Engineering Science* 155, 504 – 523.

Simonnet, M., Centric, C., Olmos, E. & Midoux, N. (2008), 'CFD simulation of the flow field in a bubble column reactor: Importance of the drag force formulation to describe regime transitions.', *Chemical Engineering and Processing* 47, 1726–1737.

Tomiyama, A. (1998), 'Struggle with computational bubble dynamics.', *Multiphase Science and Technology* 10(4), 369.

Wang, T. F., Wang, J. F. & Jin, Y. (2005), 'Theoretical prediction of flow regime transition in bubble columns by the population balance model', *Chemical Engineering Science* 60, 6199–6209.

Xue, J. (2004), Bubble velocity, size and interfacial area measurements in bubble columns, PhD thesis, Sever Institute of Washington University, St. Louis, Missouri.

Contents

List of Figures

List of Tables

Chapter 1

Introduction

Gas-liquid systems play a key role in different chemical engineering fields. The simplest and most representative systems are bubble columns reactors. Bubble columns are often used for reactions with slow kinetics such as oxidation, alkylation, hydrogenation, hydroformylation, chlorination, Fischer-Tropsch synthesis, fermentation, coal liquefaction and desulfurization (Chaumat et al. 2007, Ranade 2002). These reactors are also used nowadays for wastewater treatment, production of organic acids or yeasts and cell cultures (Tisnadjaja et al. 1996). The geometry of the bubble column reactors is really simple and without any moving parts. These reactors have low operation costs, low maintenance and good mass and heat transfer rates, but their hydrodynamics is complex and strongly depends on geometry, fluid flow rates and potential presence of internals. Local and global properties such as phase velocities, flow pattern, turbulence, gas hold-up and bubble size are linked to the operating conditions and the design variables in a complex way.

Industrially, bubble column reactors often operate in the heterogeneous churn-turbulent flow regime. It is therefore important to study these systems under these operating conditions. This regime is characterized by a high volume fraction of gas and by a strong liquid recirculation. Several empirical correlations were developed to design these systems. These correlations generally have narrow validity domains in terms of operating conditions, geometries or physical properties. Computational models for the simulation of bubble column reactors with a larger range of validity (i.e. for both homogeneous and heterogeneous regime) should be developed.

For decades, scale-up of bubble columns was based on the use of macroscopic correlations to describe hydrodynamics and transport (Deckwer 1992, Xiao et al. 2017). Nowadays, Computational Fluid Dynamics (CFD) appears as a promising tool to predict global and local properties of interest in bubbly flows (Jakobsen et al. 2005), overcoming the constraints of the traditional scale-up approach, such as the systematic use of expensive experimental setups of increasing sizes. Although numerical tools are very promising, they still need development to be fully useful and predictive in some complex flow configurations, as it is the case for industrial bubbly flows at high gas fraction. Under these conditions, also known as heterogeneous regime, the disperse phase is formed by bubbles that interact with each other due to their chaotic movement. The size of the bubbles depends on the operating conditions, global hydrodynamics and turbulence.

Various models are available for the simulation of disperse two-phase flows. In the Eulerian-Lagrangian point-particle approach, the continuous phase is calcu-

lated using the average Navier-Stokes equations and the pathway of each bubble is followed. This model is then limited to low gas velocity and gas hold-up. The Eulerian-Eulerian (two-fluid) model considers the two phases as inter-penetrating continua (Zhang 2007, Vaidheeswaran & Lopez de Bertodano 2017). A third family of models, based on the DNS interface tracking, e.g. Volume of fluid methods or Level-set methods, is not detailed here as it cannot currently be used to simulate industrial flows. The first two families of models require the choice of physical models representing the gas-liquid interactions. Gas-liquid interactions dominate these systems and interfacial forces ought to be studied, as detailed below.

Different turbulence models are available: Direct Numerical Simulations (DNS), Large eddy simulations (LES), or simulation based on Reynolds-averaged Navier-Stokes equations (RANS). Given the objective of the thesis and its purpose in terms of industrial reactor simulation, which can contain several billion bubbles, only the Euler-Euler approach based on a RANS approach is possible.

One important limitation of Eulerian-Eulerian classical CFD modelling is due to the assumption that all bubbles have the same size and velocity. A Population Balance Model (PBM) can then be used in order to overcome this limitation. The bubble size distribution (BSD) can be numerically predicted when CFD is coupled with a PBM. In the literature, three groups of methods can be found: Class methods (CM), Monte Carlo methods (MCM) and Moment Methods. The first group discretize the space of the internal coordinates. In Monte Carlo methods, stochastic differential equations are solved. These two groups have high computational costs and hence they cannot be used for the industrial purposes studied in this work. Moments Methods solve transport equations for the lowest-order moments of the BSD. This method requires closing equations. A Quadrature-based Moments Method (QBMM) approach (Marchisio & Fox 2013) limits the number of equations to solve. In particular, the Quadrature Method of Moments (QMOM) can be used if only one internal coordinate (i.e. bubble size) is studied. Bubble coalescence (Liao & Lucas 2010) and bubble breakage (Liao & Lucas 2009) phenomena ought to be studied and they should be decoupled in order to propose an accurate model. These models also need accurate experimental data for all regimes, different operating conditions and fluids. These data are however difficult to get and extrapolate. The prediction of BSD by CFD models is thus an exciting challenge as it would help to make CFD completely predictive.

These models need experimental data for different operating conditions. The bubble size distribution (BSD) is a key parameter for bubble column reactor performance, but until recently it was still difficult to measure properly BSD beyond a few percentage of gas hold-up (Xue 2004, Chaumat et al. 2007, Raimundo 2015, McClure et al. 2017). Most of the experimental published works focused on the homogeneous bubbly flow regime (Krishna 2000) at low superficial gas velocities. Only a very few papers deal with BSD measurements in the heterogeneous regime (Xue 2004, Chaumat et al. 2007, McClure et al. 2015, 2016, 2017). They are based on the calculation of chord distributions by multi-point needle probes. This technique has been validated in the case of bubbles having almost vertical trajectories. In the case of heterogeneous regime, bubbles do not have vertical trajectories, especially when the distance from the column centre increases, causing low accuracy (McClure et al. 2013, Xue 2004). Despite this limitation, multi-point probes have the advantage of accessing both the bubble chord distribution and the

bubble velocity.

To overcome the limitations of chord-based measurement techniques, a cross-correlation (CC) technique has been recently developed to measure the bubble size independently of the bubble trajectory. It is thus well suited to heterogeneous regimes (Raimundo 2015, Raimundo et al. 2016). However, CC techniques do not provide chord distributions, but a mean diameter, that is measured with confidence at any radial position. This technique is therefore complementary to the existing ones, providing a reliable average measurement for every position of the column. Raimundo (2015) used tap water and air in bubble columns of different diameters (0.15 m, 0.4 m, 1 m and 3 m). These experimental measurements allow validating CFD simulations at different scales and help to draw conclusions on the capability of CFD to scale up gas-liquid reactors.

Another important issue concerning bubbly flows is the impact of additives and impurities. Industrial applications rarely involve pure fluids, as generally liquids of complex compositions are employed. A few experimental well-documented works provide data on bubble properties in the presence of additives (McClure et al. 2015). Among the most common additives, alcohols are often investigated, with particular attention on their effects on breakage and coalescence. Alcohol addition delays the transition of bubbling regimes to higher gas velocity, due to the decreased coalescence rates (Keitel & Onken 1982, Guo et al. 2017) and the increased bubble rigidity (Dargar & Macchi 2006).

A point of industrial interest concerns the effect of the sparger on the bubble size, which has been reported in some articles (Chaumat et al. 2007, McClure et al. 2016). The sparger choice might influence the bubble size and the hydrodynamics inside the bubble column. The choice of the sparger appears as a way to modify the BSD at the entrance of the column. By considering simultaneously additives and spargers effects, breakage and coalescence phenomena can be decoupled.

Another point of interest is the role played by the interfacial forces, that must be accurately modelled, as stated by McClure et al. (2013). Gas-liquid interaction is the result of various forces: the drag force is the most important to consider (Hlawitschka et al. 2017). Literature reports several drag laws mostly based on semi-empirical correlations with a limited validity: for example, the drag law proposed by Schiller & Naumann (1935) should be preferably used for spherical bubbles. At high gas volume fractions, the regime is heterogeneous and drag laws for oblate bubbles should be used, as the drag law of Tomiyama (1998). In the heterogeneous regime, the distance between bubbles is small and the boundary layers of the bubbles interact with each other modifying the drag force. This phenomenon is known as the swarm effect. In literature, several swarm factors have been proposed. Some of them are suitable for low gas volume fractions, while for high gas volume fractions very few correlations have been developed (e.g. Simonnet et al. (2008), McClure et al. (2017)). The existing swarm factors are often empirical or obtained with DNS simulations. They usually have a narrow range of validity and they are based on experiments conducted under homogeneous regimes. Therefore, their validity in the heterogeneous regime is not established yet. Other interfacial forces could be considered, i.e. lift, wall lubrication and turbulent dispersion forces.

Besides interfacial forces, another important point, for obtaining reasonable results in the simulation of bubble columns operating under the heterogeneous regime, is the choice of the turbulence model. The turbulence model influences

the turbulent mixing, that is a key property for bubble column reactors. The turbulence model is important not only to predict the hydrodynamics but also to properly predict the turbulent mixing of the involved scalars, namely enthalpy and reactant concentrations (Shaikh & Al-Dahhan 2013). The contribution of the bubbles to mixing needs to be considered, as Alméras et al. (2016) stated that it impacts strongly on the mixing in bubble flows under the homogeneous regime. Its effect under the heterogeneous regime should be studied. However, the objective of this work is not to develop new turbulence models but rather use existing ones in a commercial CFD software such as ANSYS Fluent.

The main goal of this work is to study breakage and coalescence phenomena in bubble columns under the heterogeneous flow regime, providing suitable and innovative models that can predict correctly the bubble size for a wide range of operating conditions. This will pave the way for fully-predictive CFD-PBM simulations.

To reach this goal, it is necessary to carry out experiments in which coalescence and breakage change depending on the operating conditions. These experimental data will allow the validation of bubble coalescence and breakage models. Demineralised water, tap water and demineralised water with different ethanol concentrations are employed to suppress bubble coalescence. Experiments are performed on a cylindrical column with a diameter of 0.4 m in a wide range of superficial gas velocities, going from 0.03 m/s to 0.35 m/s. Two different spargers are used, generating very different initial bubble sizes and simulating in some cases strong bubble breakage. Besides the mean diameter profiles, gas fraction and liquid velocity distributions are measured, providing a very useful and accurate set of experimental data. These experiments provide an experimental database, useful to decouple breakage and coalescence phenomena.

To achieve the objective of this work, 0D simulations with Matlab and 3D transient Eulerian-Eulerian CFD simulations with ANSYS Fluent are carried out. The existing breakage (Liao & Lucas 2009) and coalescence (Liao & Lucas 2010) kernels, suitable for the homogeneous regime, are tested for the heterogeneous regime. Under the heterogeneous regime, most of the existing models are not valid and it is necessary to find coalescence and breakage kernels that can be used under both homogeneous and heterogeneous regimes. Concerning breakage, the model of Laakkonen et al. (2006) provides CFD results in good agreement with the experiments. Concerning coalescence, the Wang et al. (2005) collision frequency can be used but it cannot be associated at a film drainage model for the coalescence frequency. A critical approach velocity model needs to be considered. A new set of breakage and coalescence kernels is then proposed, that provides an accurate bubble size prediction in a wide range of tested operating conditions. Effects of turbulence model, water contamination, inlet conditions and scale-up are detailed in order to validate the proposed kernels for industrial applications.

This dissertation is organized as follows:

- In Chapter 1 a general introduction of the context and the objectives of the thesis have been presented. The goal of this chapter is to clarify the aim of the thesis and to show a short preview of the work that has been done during the thesis. The structure of the thesis is detailed.

- In Chapter 2 the bubble column hydrodynamics is described, with particular attention to flow regimes and main properties of these systems. This

chapter is useful to introduce the general background that is necessary to fully understand the following chapters.

- In Chapter 3 the experimental results are shown. Experimental tools, setup and data are detailed, describing the measurement methods. This part reports experimental data obtained by measuring bubble sizes with cross-correlation technique. Experiments with demineralised water, tap water and adding small quantities of ethanol are compared. Gas distribution effects are detailed and commented. These experimental results were published in the article of Gemello et al. (2018a) during the PhD and they are presented with further details in this part.

- In Chapter 4 the CFD results concerning drag laws, swarm corrections and turbulence are presented. In this part, a correlation for the drag force coefficient is tested and improved to consider the so-called swarm effect at high gas volume fractions. The swarm factor proposed in this work is the adjustment of the swarm factor proposed by Simonnet et al. (2008). It provides a precise prediction of gas volume fraction and liquid velocity in a wide range of tested operating conditions. Several turbulence models are tested. Finally, the contribution of the bubbles on mixing, as proposed by (Alméras et al. 2015), is evaluated via an analysis of the mixing time. Results are validated by comparison with experimental data of Chapter 3. These CFD simulations require the knowledge of the average bubble diameter. Once CFD hydrodynamics is validated for a known bubble size, it is possible to study the population balance. If this order is not respected, it will not be possible to carry out CFD-PBM simulations and validate the population balance. The work described in this chapter has been previously published in Gemello et al. (2018b) during the PhD. Further details are shown in this part of the dissertation.

- In Chapter 5 the population balance is introduced and the CFD-PBM results are detailed. The Quadrature Method of Moments proposed by Marchisio et al. (2003) is presented in detail and used as PBM. Coalescence and breakage models are validated using experimental results of Chapter 3. The breakage and coalescence kernels suggested in this part allow prediction of the bubble size for several operating conditions. Effects of turbulence model, water contamination, inlet conditions, sparger and scale-up are detailed in order to validate the proposed kernels for industrial applications. This work has been published in Gemello et al. (2018c) and it is presented with further details in this chapter.

- In Chapter 6 the general conclusions of this thesis are presented. The main results and conclusions obtained in the three previous chapters are reported. The limits of this work are presented in order to suggest some interesting perspectives that could follow this work.

Bibliography

Alméras, E., Plais, C., Euzenat, F., Risso, F., Roig, V. & Augier, F. (2016), 'Scalar mixing in bubbly flows: Experimental investigation and diffusivity modelling', *Chemical Engineering Science* 140, 114–122.

Alméras, E., Risso, F., Roig, V., Cazin, S., Plais, C. & Augier, F. (2015), 'Mixing by bubble-induced turbulence', *Journal of Fluid Mechanics* 776, 458–474.

Chaumat, H., Billet, A. & Delmas, H. (2007), 'Hydrodynamics and mass transfer in bubble column: Influence of liquid phase surface tension', *Chemical Engineering Science* 62, 7378–7390.

Dargar, P. & Macchi, A. (2006), 'Effect of surface-active agents on the phase holdups of three-phase fluidized beds.', *Chemical Engineering and Processing* 45, 764–772.

Deckwer, W. D. (1992), *Bubble Column Reactors.*, Wiley, Chichester, New York.

Gemello, L., Cappello, V., Augier, F., Marchisio, D. L. & Plais, C. (2018b), 'CFD-based scale-up of hydrodynamics and mixing in bubble columns', *Chemical Engineering Research and Design* Forthcoming.

Gemello, L., Plais, C., Augier, F., Cloupet, A. & Marchisio, D. L. (2018a), 'Hydrodynamics and bubble size in bubble columns: Effects of contaminants and spargers', *Chemical Engineering Science* 184, 93–102.

Gemello, L., Plais, C., Augier, F. & Marchisio, D. L. (2018c), 'Population balance modelling of bubble columns under industrial operating conditions', ... Forthcoming.

Guo, K., Wang, T., Liu, Y. & Wang, J. (2017), 'CFD-PBM simulations of a bubble column with different liquid properties', *Chemical Engineering Journal* 329(Supplement C), 116–127. XXII International conference on Chemical Reactors CHEMREACTOR-22.

Hlawitschka, M. W., Kováts, P., Zahringer, K. & Bart, H. J. (2017), 'Simulation and experimental validation of reactive bubble column reactors', *Chemical Engineering Science* 170(Supplement C), 306–319.

Jakobsen, H. A., Lindborg, H. & Dorao, C. A. (2005), 'Modeling of bubble column reactors: Progress and limitations', *Industrial & Engineering Chemistry Research* 44(14), 5107–5151.

Keitel, G. & Onken, U. (1982), 'Inhibition of bubble coalescence by solutes in air/water dispersions.', *Chemical Engineering Science* 37, 1635–1638.

Krishna, R. (2000), 'A scale-up strategy for a commercial scale bubble column slurry reactor for Fischer-Tropsch synthesis.', *Oil & Gas Science and Technology* 55(4), 359–393.

Laakkonen, M., Alopaeus, V. & Aittamaa, J. (2006), 'Validation of bubble breakage, coalescence and mass transfer models for gas-liquid dispersion in agitated vessel', *Chemical Engineering Science* 61, 218–228.

Liao, Y. & Lucas, D. (2009), 'A literature review of theoretical models for drop and bubble breakup in turbulent dispersions.', *Chemical Engineering Science* 64, 3389–3406.

Liao, Y. & Lucas, D. (2010), 'A literature review on mechanisms and models for the coalescence process of fluid particles.', *Chemical Engineering Science* 65, 2851–2864.

Marchisio, D. L. & Fox, R. O. (2013), *Computational Models for Polydisperse Particulate and Multiphase Systems.*, Cambridge University Press, Cambridge, UK.

Marchisio, D. L., Vigil, R. D. & Fox, R. O. (2003), 'Quadrature method of moments for aggregation-breakage processes', *Journal of Colloid and Interface Science* 258, 322–334.

McClure, D. D., Kavanagh, J. M., Fletcher, D. F. & Barton, G. W. (2013), 'Development of a CFD model of bubble column bioreactors: Part one - a detailed experimental study', *Chemical Engineering & Technology* 36(12), 2065–2070.

McClure, D. D., Kavanagh, J. M., Fletcher, D. F. & Barton, G. W. (2017), 'Experimental investigation into the drag volume fraction correction term for gas-liquid bubbly flows', *Chemical Engineering Science* 170, 91–97.

McClure, D. D., Norris, H., Kavanagh, J. M., Fletcher, D. F. & Barton, G. W. (2015), 'Towards a CFD model of bubble columns containing significant surfactant levels', *Chemical Engineering Science* 127, 189–201.

McClure, D. D., Wang, C., Kavanagh, J. M., Fletcher, D. F. & Barton, G. W. (2016), 'Experimental investigation into the impact of sparger design on bubble columns at high superficial velocities', *Chemical Engineering Research and Design* 106, 205–213.

Raimundo, P. M. (2015), Analysis and modelization of local hydrodynamics in bubble columns, PhD thesis, Université Grenoble Alpes.

Raimundo, P. M., Cartellier, A., Beneventi, D., Forret, A. & Augier, F. (2016), 'A new technique for in-situ measurements of bubble characteristics in bubble columns operated in the heterogeneous regime', *Chemical Engineering Science* 155, 504 – 523.

Ranade, V. V. (2002), *Computational Flow Modeling for Chemical Reactor Engineering.*, Academic Press, San Diego, California, USA.

Schiller, L. & Naumann, N. (1935), 'A drag coefficient correlation.', *Vdi Zeitung* 77, 318.

Shaikh, A. & Al-Dahhan, M. (2013), 'Scale-up of bubble column reactors: A review of current state-of-the-art', *Industrial & Engineering Chemistry Research* 52(24), 8091–8108.

Simonnet, M., Gentric, C., Olmos, E. & Midoux, N. (2008), 'CFD simulation of the flow field in a bubble column reactor: Importance of the drag force formulation to describe regime transitions', *Chemical Engineering and Processing: Process Intensification* 47(9), 1726–1737.

Tisnadjaja, D., Gutierrez, N. A. & Maddox, I. S. (1996), 'Citric acid production in a bubble-column reactor using cells of the yeast Candida guilliermondii immobilized by adsorption onto sawdust', *Enzyme and Microbial Technology* 19(5), 343–347.

Tomiyama, A. (1998), 'Struggle with computational bubble dynamics.', *Multiphase Science and Technology* 10(4), 369.

Vaidheeswaran, A. & Lopez de Bertodano, M. (2017), 'Stability and convergence of computational eulerian two-fluid model for a bubble plume', *Chemical Engineering Science* 160, 210–226.

Wang, T. F., Wang, J. F. & Jin, Y. (2005), 'Theoretical prediction of flow regime transition in bubble columns by the population balance model', *Chemical Engineering Science* 60, 6199–6209.

Xiao, Q., Wang, J., Yang, N. & Li, J. (2017), 'Simulation of the multiphase flow in bubble columns with stability-constrained multi-fluid CFD models', *Chemical Engineering Journal* 329(Supplement C), 88–99. XXII International conference on Chemical Reactors CHEMREACTOR-22.

Xue, J. (2004), Bubble velocity, size and interfacial area measurements in bubble columns, PhD thesis, Sever Institute of Washington University, St. Louis, Missouri.

Zhang, D. (2007), Eulerian modeling of reactive gas-liquid flow in a bubble column, PhD thesis, Enschede, The Netherlands.

Chapter 2

Bubble column hydrodynamics

Bubble column hydrodynamics is very complex and linked to the column geometry and the operating conditions.

In simple bubble columns, liquid is the continuous phase whereas gas is the disperse phase and is injected at the bottom of the column. Global properties and local ones are equally important in the study of these systems.

The main global property is the global gas hold-up, defined as the average gas fraction in the column. It is calculated as the global ratio between the volume of the gas and the total volume. Important local parameters are gas volume fraction, velocities of liquid and gas and bubbles size. The gas volume fraction α_g is defined as the local ratio between the volume of the gas and the total one and it depends strongly on the superficial gas velocity v_{sg}.

$$\alpha_g = \frac{V_g}{V_g + V_l}; \tag{2.1}$$

$$v_{sg} = \frac{\dot{V}_g}{A} = \frac{\int_0^R 2\pi r \alpha_g(r) v_g(r) dr}{\int_0^R 2\pi r dr}. \tag{2.2}$$

The liquid phase often operates in a batch manner; it could also operate in a semi-batch manner, with a circulation in the same or in opposite direction of the gas.

2.1 Flow regimes

Different flow regimes are present in bubble columns, depending on the superficial gas velocity and on the dimension of the column (Fig. 2.1):

- Homogeneous regime (bubbly flow);
- Transition regime;
- Heterogeneous regime (churn-turbulent flow);
- Slug flow regime.

As shown in Fig. 2.2, three main regimes are available (Krishna 2000): homogeneous, transition and heterogeneous (or churn-turbulent). This representation

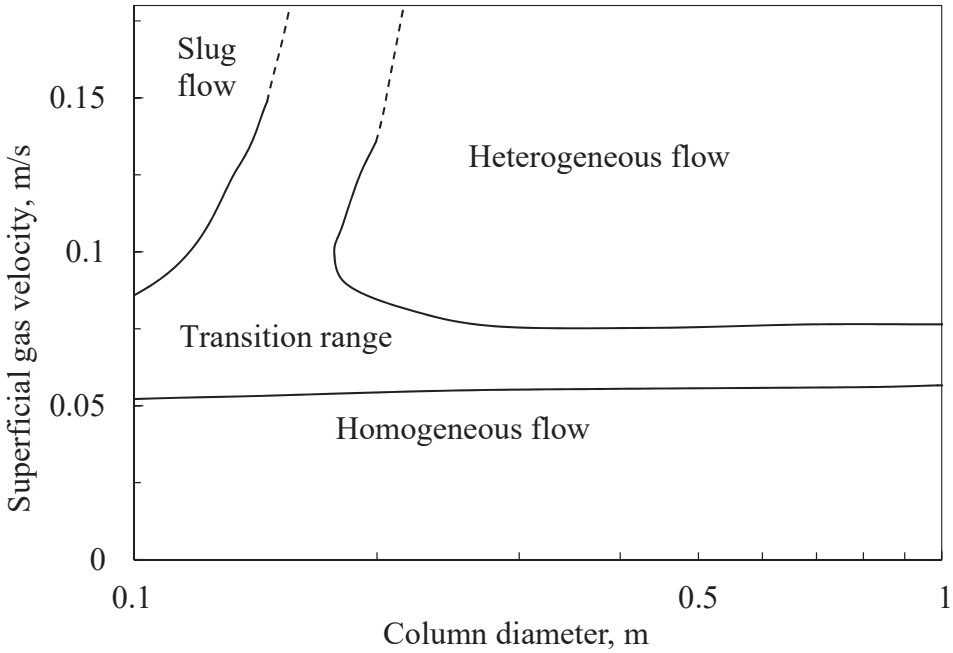

Figure 2.1: Gas-liquid flow configurations in a vertical tube (Wiswanathan 1969, Shah et al. 1982).

is not universal: it depends on the design of the sparger. The transition regime can be absent if the gas is not distributed uniformly and can be influenced by the contamination of the liquid phase. The homogeneous regime (or bubbly regime or dispersed regime) occurs at low superficial gas velocity and the gas volume fraction has a strong dependency on the superficial gas velocity. The bubbles have a narrow size distribution which almost does not depend on the spatial position. The time-averaged profile of the gas hold-up is approximately flat (Fig. 2.2). The path of the bubble is quite linear: the phenomena of bubble coalescence and break-up are negligible. Non-coalescing, small and almost spherical bubbles are continuously generated in the distributor at the bottom. The bubbles drag a considerable amount of liquid to the top of the column. The liquid must return down, in order to have net liquid flow in the column equal to zero. The liquid flowing in the opposite direction delays the bubbles rise, increasing the gas hold-up.

In the transition regime, the gas volume fraction reaches a maximum. After reaching the maximum, if the superficial gas velocity increases, the gas volume fraction decreases or it remains quite constant (Fig. 2.2). In this case, some big bubbles start to appear in the centre of the column and the path is not linear. The bubbles interact with each other.

The heterogeneous regime is present for high superficial gas velocities. The gas volume fraction increases with the superficial gas velocity more slowly than in the homogeneous regime (Fig. 2.2). The movement of the bubbles is chaotic, the path is irregular and the regime is characterized by a highly turbulent flow. The distribution of bubble diameters is wide, with some big bubbles, especially in the centre of the column. The bubbles are smaller near the wall: some bubbles go down with the high recirculation of the liquid. The profile of the gas volume fraction is not flat along the radial position: the profile is parabolic, with a maximum in the

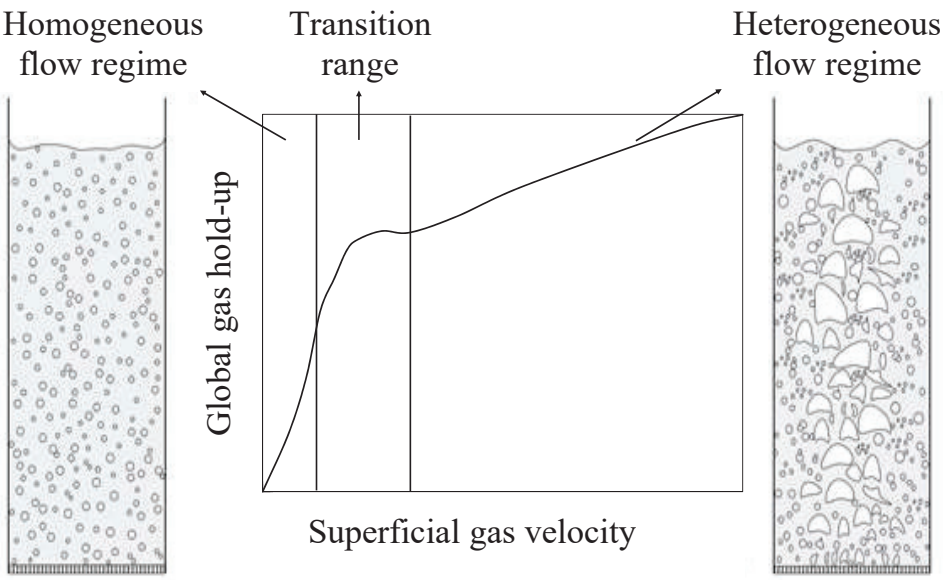

Figure 2.2: Representation of the flow regimes in bubble column (Krishna 2000).

centre of the column. The bubble velocity radial profile is also parabolic.

Slug regime is strongly unstable: some huge gas bubbles are distributed over the entire column diameter and pass through the liquid intermittently. The bubbles cause large pressure and liquid flow rate fluctuations, like a large wave. This regime is limited to columns with small diameters for very high superficial gas velocities.

2.2 Gas volume fraction

The global gas hold-up is the mean gas volume fraction into the column. The gas hold-up does not only depend on the superficial gas velocity but also on the gas injector, on the properties of the liquid in the column and on the pressure.

A homogeneous regime is normally present in case of very low superficial gas velocity. In the case of large orifices in the gas distributor, a wide bubble size distribution appears: the heterogeneous regime appears also at low the superficial gas velocities.

The properties of the liquid have a big influence on the hold-up. Cases in literature report that the gas volume fraction is lower in the case of higher viscosity (Zahradník et al. 1997, Kantarci et al. 2005); bubble coalescence is increased creating big bubbles that rise more rapidly than the smaller ones. The surface tension is equally important: if this property decreases, for example by adding surfactants, the coalescence of the bubble decreases with smaller bubbles and higher gas volume fraction. Increasing the pressure, the global gas volume fraction increases, depending on the liquid and the gas present into the column.

Under the heterogeneous regime, the gas volume fraction profile can be estimated with a symmetric polynomial expression (Schweitzer 2001):

$$\alpha_g = \bar{\alpha}_g \left[a \left(r^6 - 1 \right) + b \left(r^4 - 1 \right) + c \left(r^2 - 1 \right) \right] \tag{2.3}$$

where r is the dimensionless radial position, $\bar{\alpha}_g$ is the mean gas fraction and $a = -1.7889$, $b = 1.228$ and $c = -0.939$ are fitting parameters.

Using this correlation, the local gas volume fraction can be estimated in each radial position of the column, knowing the total gas hold-up for a giving height (Fig. 2.3): the profile is closely linked to the liquid circulation pattern in the column (Forret 2003).

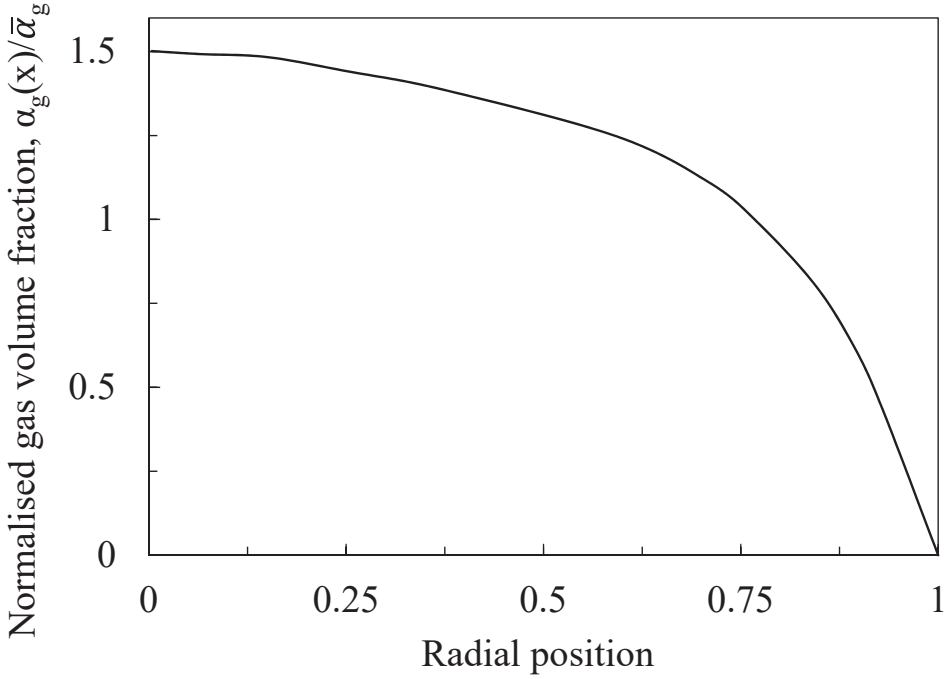

Figure 2.3: Radial profile of the normalized gas hold-up (Forret 2003).

2.3 Bubble shape and size

The bubble shape depends on the superficial gas velocity and on the flow conditions. Dimensionless numbers can be used to predict the shape of the bubbles: Reynolds number, Eötvös number and Morton number (Fig. 2.4) (Clift et al. 1978).

The bubble Reynolds is defined as the ratio between inertial and viscous forces:

$$Re_b = \frac{\rho_l \, u_b \, d_{eq}}{\mu_l} \tag{2.4}$$

where ρ_l is the density of the liquid, μ_l the viscosity of this phase, u_b is the mean velocity of the bubbles and d_{eq} is the equivalent diameter of a spherical bubble with the same volume (V), (Smolianski et al. 2008):

$$d_{eq} = \sqrt[3]{\frac{6\,V}{\pi}}. \tag{2.5}$$

The Eötvös number, also called Bond number, determines the impact of surface tension forces compared with body force. It is calculated as the ratio of gravitational forces to surface tension forces:

$$Eo = \frac{\Delta\rho \, g \, {d_{eq}}^2}{\sigma} \tag{2.6}$$

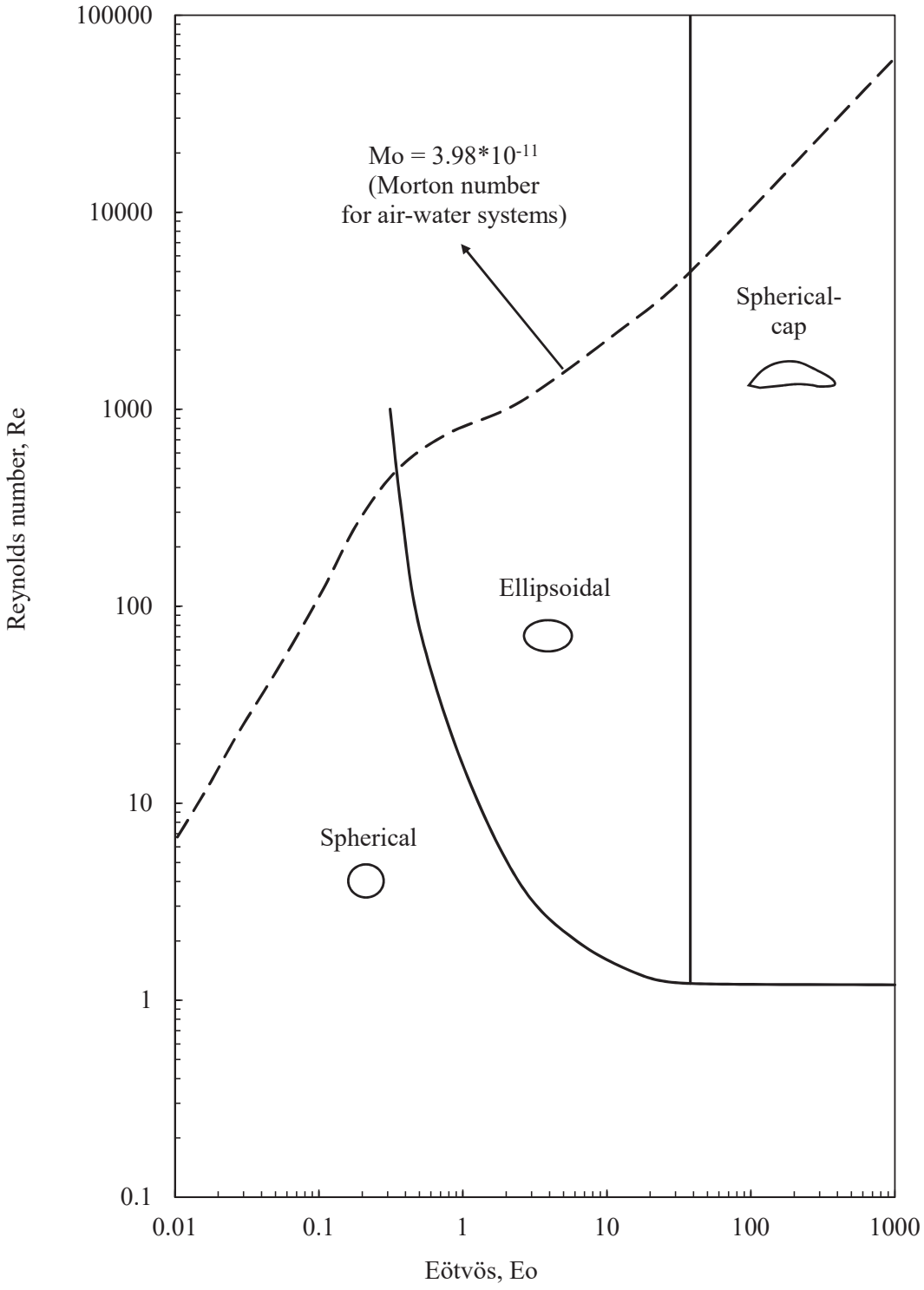

Figure 2.4: Shape regimes for bubbles and drops in unhindered gravitational motion through liquids (Clift et al. 1978).

where $\Delta\rho$ is the difference between the density of the liquid and gas phase, g is the gravity acceleration and σ is the surface tension.

The Morton number is defined as:

$$Mo = \frac{\Delta\rho\, g\, {\mu_l}^4}{{\rho_l}^2\, \sigma^3}. \tag{2.7}$$

For water-liquid systems, the Morton number is 3.98×10^{-11}.

The size of the bubble is not identical for all the bubbles in the column, but it is characterized by a distribution. For all the calculations, it is then necessary to define a mean bubble diameter. The most common diameter for several applications is the Sauter mean diameter, defined as the ratio between the total volume of the bubbles and the total surface:

$$d_{Sauter} = d_{32} = \frac{\sum {d_V}^3}{\sum {d_S}^2} = \frac{V_{tot}}{6\, S_{tot}} \tag{2.8}$$

where d_V is the diameter of an isovolumic spherical bubble and d_S the diameter of a spherical bubble with the same surface.

The arithmetic diameter is instead defined as:

$$d_{10} = \frac{\int d_b\, f_N(d_b) \mathrm{d}d_b}{\int f_N(d_b) \mathrm{d}d_b} = \frac{\sum d_b}{N_b} \tag{2.9}$$

where N_b is the number of the bubbles.

Different parameters influence the bubble size: superficial gas velocity, gas volume fraction, liquid properties, radial and axial position. The mean diameter increases slowly with superficial gas velocity. Especially for high superficial gas velocities, the dimensions of the bubbles change along the radial position of the column; in this situation bigger bubbles are present in the centre of the column.

The surface tension has a great impact on the size of the bubbles: a reduction of the surface tension decreases bubble size (Chaumat et al. 2007) and this induces higher gas hold-up and higher mass transfer coefficient. The surface tension has a higher effect in the homogeneous regime than in the heterogeneous one, where the effect of macro-scale turbulence eclipses the other ones, as stated by Zahradník et al. (1995) and Camarasa et al. (1999). The surfactants in water delay the transition of bubbling regimes to higher gas velocity, given the decrease of coalescence and the increase in bubble rigidity (Dargar & Macchi 2006). The impact of the viscosity of the liquid phase hardly influences the bubble (Akita & Yoshida 1974).

The gas distributor, however, influences all the properties, particularly on the size distribution in the lowest part of the column. Das & Das (2015) studied the bubble formation from submerged orifices. The initial bubble size depends on the sparger design, on the orifice orientation and on the operating conditions, as the rate of periodic attachment and detachment increases with the gas flow rate. Different models have been developed to estimate the initial bubble size. Most of them are calculated by considering a force equilibrium, as detailed by Liu et al. (2013). They are mostly studied for the homogeneous regime. In the case of heterogeneous regime, some experimental data close to the bottom are desirable, as the existing models are not already validated under these operating conditions.

2.4 Bubble velocity

As the bubble size, the bubble velocity is influenced by different parameters. The bubble velocity depends on the superficial gas velocity, the pressure and the properties of the liquid phase, as for the gas volume fraction. In a homogeneous flow, the rising of the bubble is regular and the bubble velocity radial profile is flat. In the transition and heterogeneous flows, the bubbles rise non-linearly and the velocity depends strongly on the radial position. The movement is chaotic: given liquid recirculation, the bubble velocity radial profile results parabolic. The velocity increases always with the superficial gas velocity in the centre; there is the opposite effect close to the wall, given that the recirculation of the liquid pushes down the bubbles (Xue 2004).

The pressure influences the bubble velocity, as shown by Xue (2004), increasing the bubble velocity in the central zone of the column and decreasing it near the wall. In fact, the gas volume fraction increases, enhancing the liquid recirculation that has a positive effect in the centre of the column and a negative one near the wall. The present work considers only atmospheric pressure.

The presence of surfactants influences the terminal rising velocity of a single bubble significantly. In the case of pure water, the profile of terminal velocity shows maximum, as shown in Fig. 2.5 (Clift et al. 1978).

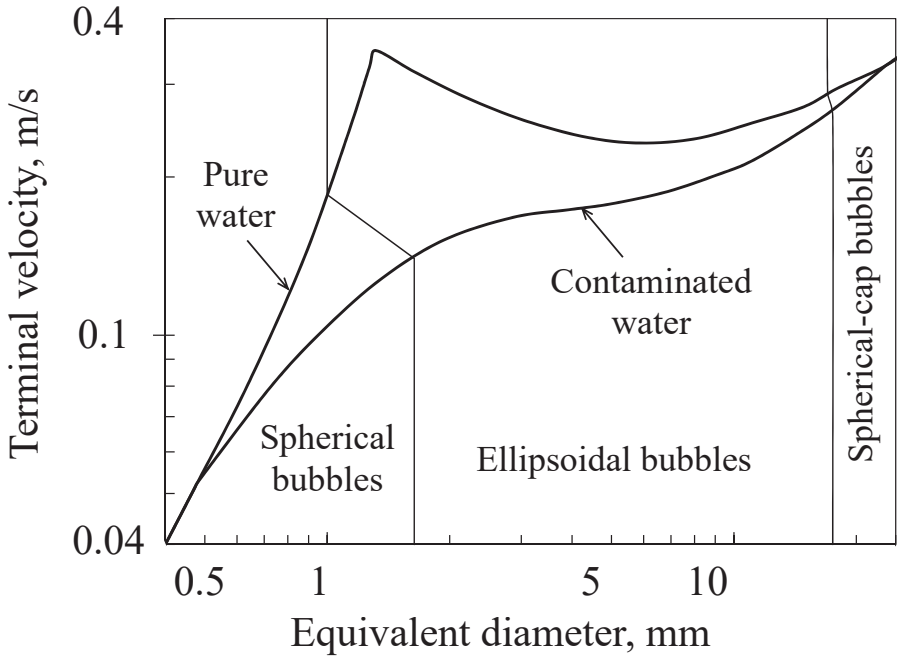

Figure 2.5: Terminal velocity of air bubbles in water at 20°C (Clift et al. 1978)

The surfactant modifies the velocity field near a fluid-fluid interface. This phenomenon has been explained for the first time by Frumkin & Levich (1947) and Levich (1962): they suggested that surfactants tend to stay along the bubble surface and accumulate near it (Kulkarni & Joshi 2005).

2.5 Liquid velocity induced by bubbles

The liquid velocity in the centre of the column increases, increasing the velocity of the gas. The recirculation increases near the wall, where the liquid comes down. Forret (2003) studied this phenomenon with a bubble column of 1 m in diameter: the result is a parabolic profile for the liquid with a maximum in the centre (Fig. 2.6). Some issues appear close to the wall: the liquid velocity should be zero at the boundary, therefore the Forret (2003) model is only valid outside the boundary layer.

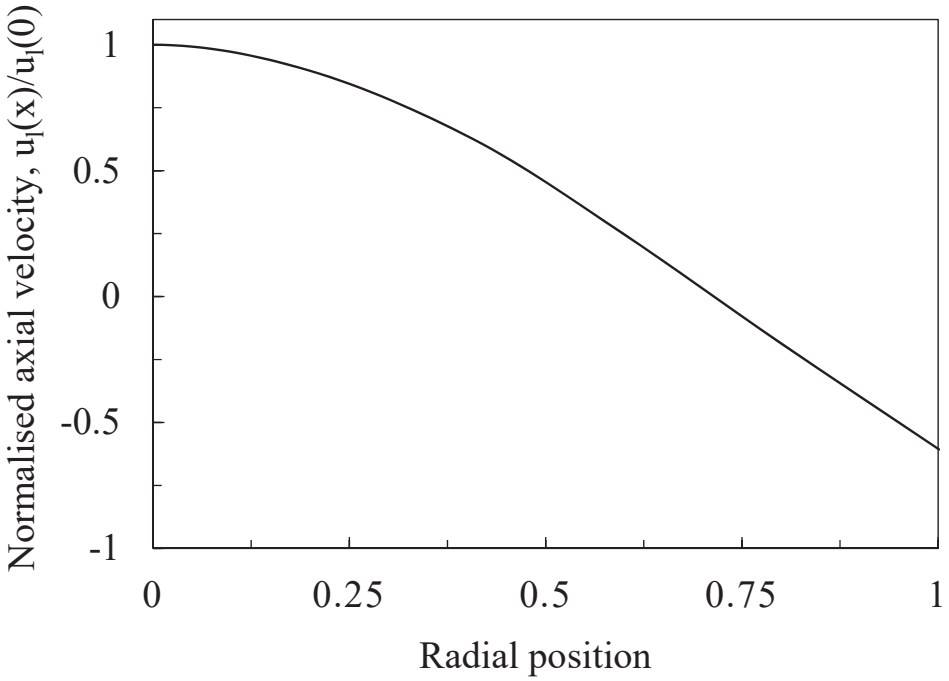

Figure 2.6: Radial profile of the normalized liquid velocity proposed by Forret (2003)

For a stabilized region of the column, the profile is obtained using the correlation proposed by Forret (2003):

$$u_l(x) = \frac{u_l(0)}{a - c}\left[a \exp(-b\, x^2) - c\right] \tag{2.10}$$

with a=2.976, b=0.943 and c=1.848, empirical parameters determined at ambient conditions in a wide range of validity under the heterogeneous regime. They were established by Forret (2003) thanks to several measurements of the axial liquid velocity with a Pavlov tube in bubble columns with a diameter between 0.15 mm and 1 m. The liquid velocity depends on the dimensionless radial position r and on the liquid velocity in the column centre.

This equation is empirical, but it allows to define the shape of the radial velocity profile if the liquid velocity in the column centre is known. The upward flow rate is equal to the downward one, in accordance with experimental data. This correlation is also suitable for contaminated systems and in presence of additives.

Under the heterogeneous regime, the liquid velocity in the centre of the column is obtained with the correlation proposed by Miyauchi & Shyu (1970):

$$u_l(0) = 2.47 {v_{sg}}^{0.5} D^{0.28}, \tag{2.11}$$

This correlation is empirical, but it has a wide range of validity in the so-called "stabilized region" (H/D>1). This equation can be used for obtaining a first approximation of the axial liquid velocity in the centre for many operating conditions under the heterogeneous regime. This correlation can be also used for scale-up purposes. Unfortunately, this correlation cannot be used for contaminated systems and in presence of additives.

Bibliography

Akita, K. & Yoshida, F. (1974), 'Bubble size, interfacial area, and liquid-phase mass transfer coefficient in bubble columns.', *Industrial & Engineering Chemistry Process Design and Development* 13(1), 84–91.

Camarasa, E., Vial, C., Poncin, S., Wild, G., Midoux, N. & Bouillard, J. (1999), 'Influence of coalescence behaviour of the liquid and of gas sparging on hydrodynamics and bubble characteristics in a bubble column.', *Chemical Engineering and Processing* 38, 329–344.

Chaumat, H., Billet, A. & Delmas, H. (2007), 'Hydrodynamics and mass transfer in bubble column: Influence of liquid phase surface tension', *Chemical Engineering Science* 62, 7378–7390.

Clift, R., Grace, J. R. & Weber, M. E. (1978), *Bubbles, Drops, and Particles.*, Academic Press, New York, New York.

Dargar, P. & Macchi, A. (2006), 'Effect of surface-active agents on the phase holdups of three-phase fluidized beds.', *Chemical Engineering and Processing* 45, 764–772.

Das, A. & Das, P. K. (2015), 'Numerical study of bubble formation from submerged orifice under reduced gravity condition', *Procedia IUTAM* 18, 8–17.

Forret, A. (2003), Hydrodynamics scale-up of slurry bubble columns., PhD thesis, Université Claude Bernard Lyon 1 - IFPEN, Lyon.

Frumkin, A. & Levich, V. G. (1947), 'On the surfactants and interfacial motion.', *Z. Fizicheskoi Khimii* 21, 1183–1204.

Kantarci, N., Borak, F. & Ulgen, K. O. (2005), 'Bubble column reactors.', *Process Biochemistry* 40, 2263–2283.

Krishna, R. (2000), 'A scale-up strategy for a commercial scale bubble column slurry reactor for Fischer-Tropsch synthesis.', *Oil & Gas Science and Technology* 55(4), 359–393.

Kulkarni, A. A. & Joshi, J. B. (2005), 'Bubble formation and bubble rise velocity in gas-liquid systems: A review.', *Industrial & Engineering Chemistry Research* 44, 5873–5931.

Levich, V. G. (1962), *Physicochemical Hydrodynamics*, Prentice Hall, Englewood Cliffs, NJ.

Liu, C., Liang, B., Tang, S. & Min, E. (2013), 'Effects of orifice orientation and gas-liquid flow pattern on initial bubble size', *Chinese Journal of Chemical Engineering* 21(11), 1206–1215.

Miyauchi, T. & Shyu, C.-N. (1970), 'Flow of fluid in gas-bubble columns', *Chemical engineering* 34(9), 958–964.

Schweitzer, J. M. (2001), 'Local gas hold-up measurements in fluidized bed and slurry bubble column.', *Chemical Engineering Science* 56(3), 1103–1110.

Shah, Y. T., Kelkar, B. G., Godbole, S. P. & Deckwer, W. D. (1982), 'Design parameters estimations for bubble column reactors', *American Institute of Chemical Engineering Journal* 28(3), 353–379.

Smolianski, A., Haario, H. & Luukka, P. (2008), 'Numerical study of dynamics of single bubbles and bubble swarms.', *Applied Mathematical Modelling* 32(5), 641–659.

Wiswanathan, K. (1969), *Flow Patterns in Bubble Columns.*, Gulf, Houston, Tex.

Xue, J. (2004), Bubble velocity, size and interfacial area measurements in bubble columns, PhD thesis, Sever Institute of Washington University, St. Louis, Missouri.

Zahradník, J., Fialová, M., Kaštánek, F., Green, K. D. & Thomas, N. H. (1995), 'The effect of electrolytes on bubble coalescence and gas hold-up in bubble column reactors.', *Chemical Engineering Research and Design* 73, 341–346.

Zahradník, J., Fialová, M., Røužička, M., Drahoš, J., Kaštánek, F. & Thomas, N. H. (1997), 'Duality of the gas-liquid flow regimes in bubble column reactors', *Chemical Engineering Science* 52(21), 3811–3826.

Chapter 3

Experimental study of hydrodynamics and bubble size

3.1 Introduction

Bubble dispersion and bubble size are important parameters that influence the performance of bubble column reactors. The bubble size depends on operating conditions, global hydrodynamics and turbulence. Bubbles have a high polydispersity, i.e. they are characterized by different sizes and velocities (Rusche & Issa 2015). Only a very few papers are focused on bubble size measurements in the heterogeneous regime, i.e. Xue (2004), Chaumat et al. (2007), McClure et al. (2015, 2016, 2017). They are based on the calculation of chord distributions by multi-point needle probes. This technique has been validated in the case of bubbles having almost vertical trajectories. In the case of heterogeneous regime, bubbles do not have vertical trajectories and their path becomes more chaotic as the distance from the column centre increases. The measurement has then low accuracy, as stated by McClure et al. (2013) and Xue (2004). Multi-point probes access both the bubble chord distribution and the bubble velocity. To overcome the limits of classical techniques, a cross-correlation (CC) technique has been recently developed to measure the bubble size. The cross-correlation technique does not depend on the trajectory of the bubbles, so it is well adapted to the heterogeneous regime (Raimundo 2015, Raimundo et al. 2016). In return, cross-correlation technique does not provide chord distributions, but a Sauter mean diameter, that is measured with confidence at any radial position. Chord-based measurement techniques and CC technique are therefore complementary.

The impact of contaminants and additives is a key point concerning bubbly flows for industrial applications, that never involve only pure fluids: complex compositions are used. In literature, the effects of additives are not well-studied: few experimental well-documented works provide data on phases velocity and on bubble size distribution (McClure et al. 2015). In aqueous solutions with alcohol, the bubbles are smaller and the transition of bubbling regimes is delayed to higher gas velocity, due to the coalescence decrease (Keitel & Onken 1982, Guo et al. 2017) and the bubble rigidity increase (Dargar & Macchi 2006). This effect increases with alcohol molecular weight, as stated by Jamialahmadi & Miiller-Steinhagen (1992). The decrease of surface tension due to the alcohol presence is not enough to explain this behaviour. Several authors (Clift et al. 1978, Kelkar et al. 1983, Lindland

& Terjesen 1965, Raymond & Zieminski 1971) suggest that these differences are linked to the reduction of the bubble-rise velocity.

The sparger effect on the bubble size is another point of industrial interest, as stated by Chaumat et al. (2007) and McClure et al. (2016). The choice of the sparger gives the possibility to modify the bubble size at the column inlet. The sparger effect is important for a height of approximately one column diameter (Polli et al. 2002).

The objective of this part of the work is to produce data that could validate bubble coalescence and breakage models. Experiments in which coalescence and breakage change depending on the operating conditions are carried out. Demineralised water, tap water and demineralised water with different ethanol concentrations are used in order to decrease bubble coalescence. Experiments are also carried out using two different spargers, generating very different initial bubble sizes and simulating in some cases strong bubble breakage. By considering simultaneously additives and spargers effects, breakage and coalescence phenomena can be decoupled. Besides the mean diameter profiles, gas fraction and liquid velocity distributions are measured, providing a very useful and accurate set of experimental data. The cross-correlation technique was first presented by Raimundo (2015) and it was tested with tap water only. In this work, this technique is employed under the presence of impurities and additives. Different radial and axial positions are considered.

3.2 Experimental tools

3.2.1 Gas volume fraction

The global gas volume fraction, also called gas hold-up, can be calculated by using the difference of liquid height before and after gas injection:

$$\bar{\alpha}_g = 1 - \frac{H_0}{H_f} \tag{3.1}$$

where H_0 is the non-aerated liquid height and H_f is the aerated liquid height.

This method is not very precise due to the interface deformation at the top of the column: a characteristic error of about 10% is associated with this technique.

The local gas fraction can be obtained thanks to an optical probe. The local gas volume fraction is calculated as the fraction of time in which the gas is detected at the probe tip, as detailed by Raimundo (2015). A 1C conical mono-fibre optical probe is used in this work (Fig. 3.1).

3.2.2 Bubble size

Different methods could be considered to obtain the bubble size: optical probe, cross-correlation and endoscope.

Using an optical probe, the bubble chord can be computed by multiplying the time of detection of a bubble and the bubble velocity. Liu et al. (1996) explained how chord length can be transformed into bubble size by modelling the bubbles as ellipsoidal. This model is defined starting with the horizontal radius and the shape of the bubble. Using this model, it is possible to obtain the vertical Sauter

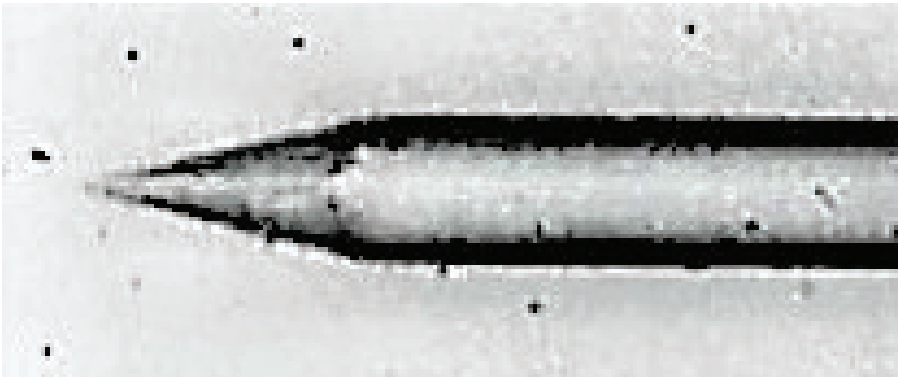

Figure 3.1: Tip of a 1C mono-fibre optical probe (Cartellier & Barrau 1998).

mean diameter from the mean bubble chord, as detailed by Raimundo (2015). This technique is valid in the case of bubbles having almost vertical trajectories. In the case of heterogeneous flow regime, bubbles trajectories are not vertical, causing low accuracy, as stated by McClure et al. (2013). This work is focused on the heterogeneous flow regime and then the optical probe technique cannot be used.

An endoscope could be adapted to high gas volume fraction flows. A camera captures a high-speed video. A Light Emitting Diode (LED) on the opposite side provides the necessary light. In each video at least 150 bubbles should be considered. Each vertical and horizontal diameter is measured manually. This approach is tedious and requires too much time to get the results. Consequently, it is not suitable to obtain bubble size at several operating conditions. Small bubbles are not detected due to the tool resolution. Huge bubbles are not measured as they are bigger than the maximum size of the photos.

The mean bubble size can be obtained from the spatial cross-correlation (CC) of the signals of two optical probes (Fig. 3.2). The cross-correlation quantifies the similarity of two signals, analysing them simultaneously. The cross-correlation function is then calculated as follows (Raimundo 2015):

$$CC = \frac{\int_0^{t_{\text{exp}}} signal_A(t) signal_B(t) dt}{t_{\text{exp}}}. \tag{3.2}$$

Its value is equal to unity (maximum) if the two probes are in the same position, considering that the signals are identical. The cross-correlation decreases with the distance between the probes. Its signal reaches an asymptotic value, that depends on the local gas volume fraction. The time-averaged horizontal diameter of the bubbles is obtained by using the CC signal, the distance between the probes and the eccentricity of the bubbles. The two probes are placed at the same height, with a distance equal to 1 mm (Fig. 3.2). This technique can be used in the case of heterogeneous regime and high gas volume fractions, as stated by Raimundo (2015) and Raimundo et al. (2016). It has been validated by comparing its results with endoscopic measurements. The error is lower than 10% for every operating condition.

In the case of heterogeneous regime, the bubbles are often oblate. The CC technique measures the horizontal diameters, by using the Sauter mean diameter of the bubbles. In the case of oblate form of the bubbles, the slope of the linear part of the curve (θ) of the cross-correlation in function of the distance between

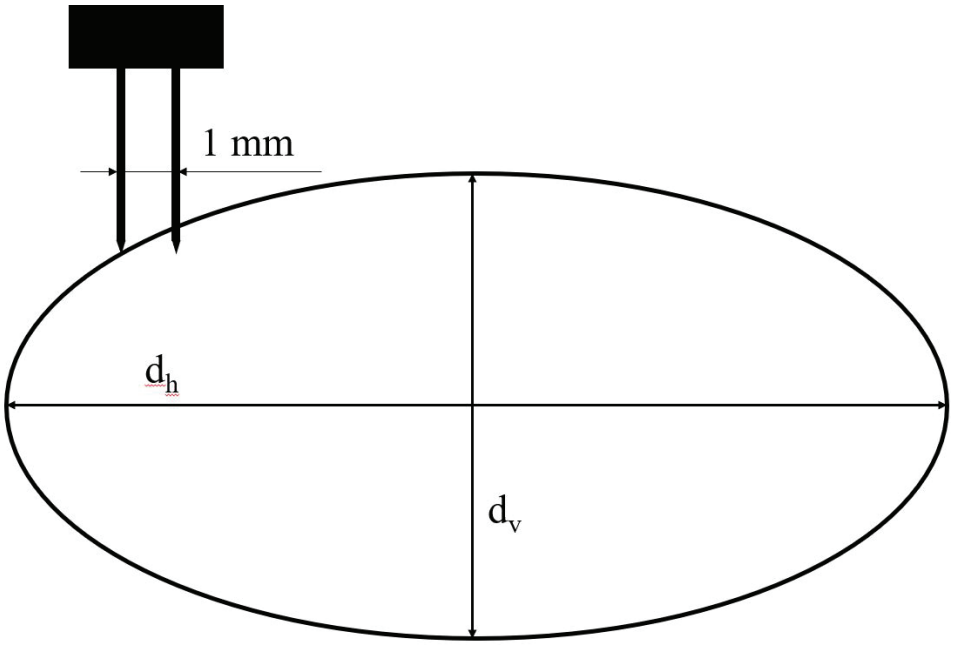

Figure 3.2: Schematic representation of the CC technique.

the probes depends only on the bubble sizes. The horizontal Sauter mean diameter ($d_{h,32}$) can therefore be calculated as (Raimundo 2015):

$$d_{h,32} = -\frac{1.46}{\theta\, 0.505 \exp(0.7 Ecc)}, \tag{3.3}$$

where Ecc is the eccentricity. A constant eccentricity equal to 0.70 is considered, as this value has been obtained by Raimundo (2015) with experiments in the same range of measurements. If the bubble shape is known, the time-averaged Sauter mean diameter, also called Sauter mean diameter, can be computed, by using the time-averaged horizontal diameter of the bubbles. The eccentricity considered in this work is in accordance with the value calculated by using the Wellek et al. (1966) correlation for liquid drops, that depends on the surface tension and on the Eötvös number.

3.2.3 Liquid velocity

The liquid velocity in bubble columns of different diameters in the heterogeneous regime can be obtained by using a modified Pitot tube, called a Pavlov tube (Fig. 3.3) (Forret 2003). The differential pressure between two opposite holes is measured in order to obtain the liquid velocity. As the presence of two phases is important, Vial et al. (2003) propose to add a calibration parameter and a correction parameter that considers the gas fraction. These measurements have an associated error of about 10-20%, that depends on the gas fraction.

The measured differential pressure ΔP allows the liquid velocity to be obtained:

$$u_{L,i}(r,t) = \begin{cases} \sqrt{\frac{2\Delta P_i}{\rho_L}} & for\ \Delta P_i \geq 0 \\ -\sqrt{\frac{-2\Delta P_i}{\rho_L}} & for\ \Delta P_i \leq 0 \end{cases} \tag{3.4}$$

where $u_{L,i}$ is the instantaneous liquid velocity and ΔP_i is the instantaneous differential pressure.

The average liquid velocity u_L is obtained by sampling the instantaneous liquid velocity:

$$u_L(r) = \frac{\sum_{i=1}^{N} u_{L,i}(r,t)}{N}. \tag{3.5}$$

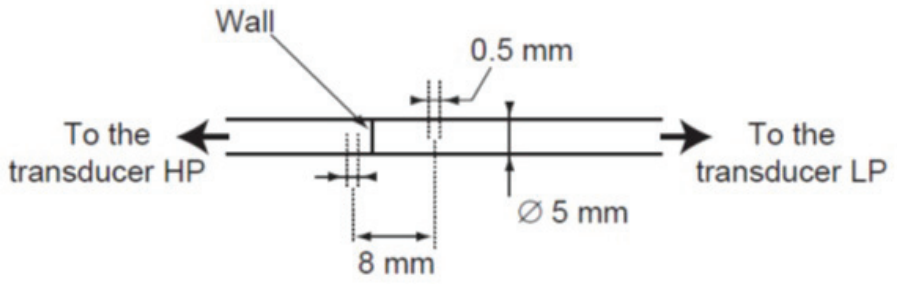

Figure 3.3: Pavlov tube (Forret 2003).

3.3 Experimental setup

Experiments are carried out in a 0.4 m diameter cylindrical bubble column (Fig. 3.4a) at atmospheric pressure for a wide range of superficial gas velocity, that varies from 0.03 m/s to 0.35 m/s. The net liquid flow rate is zero. The initial liquid height (without gas) is equal to 4 diameters (H/D=4). This ratio is higher than the critical value above which the gas volume fraction does not depend on the initial height, as stated by Sasaki et al. (2017). The total column height is about 8 diameters, in order to work with very high gas volume fractions.

The techniques detailed above are used to obtain the experimental data: the global gas volume fraction by using the difference of liquid height, the local gas volume fraction by using a 1C conical mono-fibre optical probe, the Sauter mean diameter by using the CC technique and the liquid velocity by using a Pavlov tube with a sampling frequency of 400 Hz.

Different water qualities are tested in this work: demineralised water (pure water or slightly contaminated water), tap water (fully contaminated water) and small percentages of ethanol (0.01% and 0.05% by volume) in demineralised water.

The gas enters the column through a perforated sparger placed at the bottom of the column. Two different spargers are tested. The first sparger has 92 holes of 2 mm of diameter (Fig. 3.4b), that assures a homogeneous gas distribution. The second sparger has 7 holes of 9 mm (Fig. 3.4c), that allows analysis of the effects of the sparger on hydrodynamics and bubble dimensions. In the second sparger, one hole is in the sparger centre, while the other 6 holes create a hexagon at a dimensionless radial position of 0.65 (Fig. 3.4c). In the following sections, the results are mainly collected using the first sparger (92 holes of 2 mm), while the results collected with the second sparger (7 holes of 9 mm) are reported in Section 3.4.5.

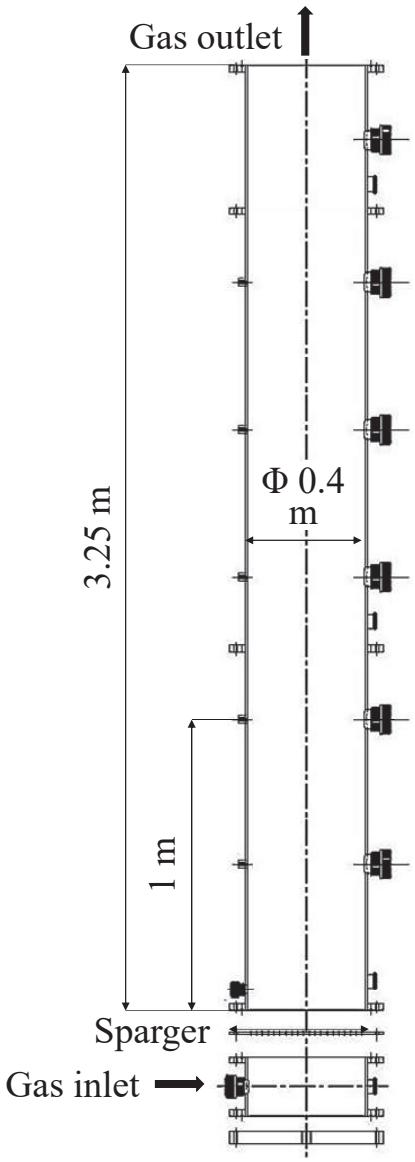

(a) *Axial section of the bubble column*

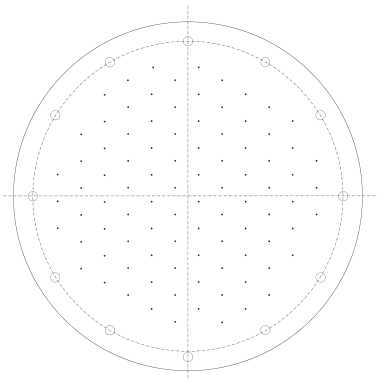

(b) *Perforated sparger with 92 holes of 2 mm*

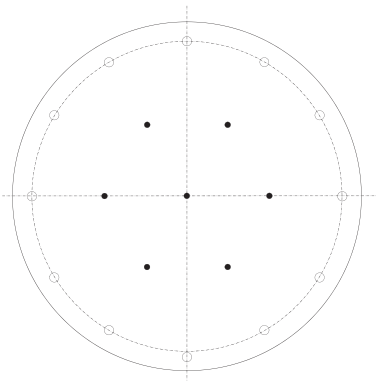

(c) *Perforated sparger with 7 holes of 9 mm*

Figure 3.4: Bubble column and spargers.

3.4 Experimental results

3.4.1 Gas hold-up

The global gas volume fraction is the first macroscopic property that is studied. The global gas volume fraction increases with the superficial gas velocity with different slopes, depending on the operating conditions. This change of slope allows the homogeneous and the heterogeneous regimes to be distinguished. In Fig. 3.5 and Table A.1 the measured gas hold-up is reported versus the superficial gas velocities for demineralised water, tap water and demineralised water with different concentrations of ethanol. With demineralised water, the regime is homogeneous up to a superficial gas velocity of 0.05 m/s (Fig. 3.5). The global gas volume fraction increases quickly with a linear dependence on the superficial gas velocity. After a superficial gas velocity of 0.05 m/s, the transition regime occurs, in which the gas hold-up has a low dependence on the superficial gas velocity. The hold-up curve has a monotonic increasing trend, without any local maximum in the transitional regime in these experiments. The heterogeneous regime begins at a superficial gas velocity of about 0.09 m/s: at this superficial gas velocity, the gas hold-up starts to increase with a dependence that is quite linear.

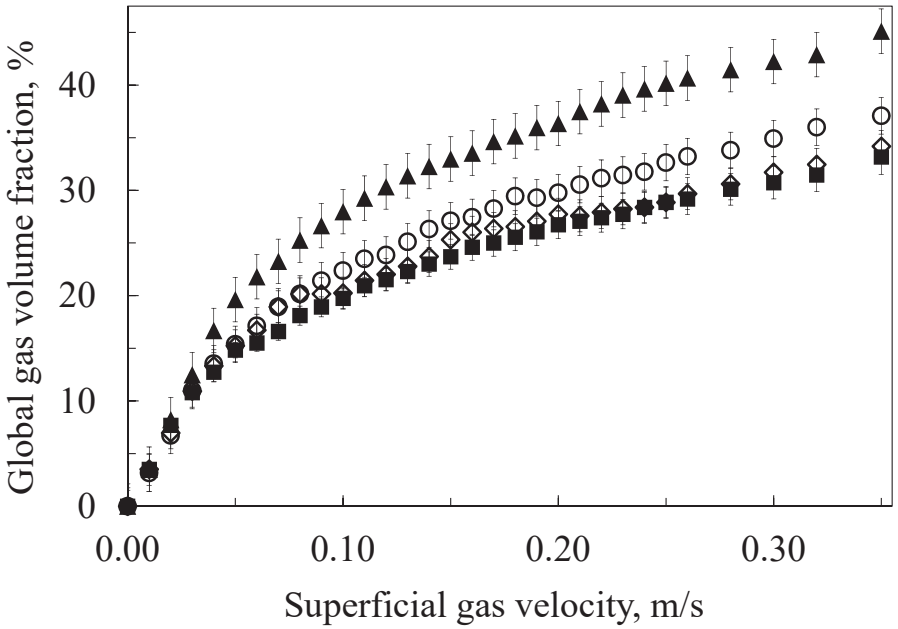

Figure 3.5: Gas hold-up versus superficial gas velocity for demineralised water (■), tap water (◇), ethanol 0.01% (○) and ethanol 0.05% (▲).

In the case of tap water, the gas hold-up curve shows some differences corresponding to the transition regime, as reported in Fig. 3.5. The behaviour at the transition regime is influenced by the water quality used to fill the column. Tap water results are not fully reproducible, as the water quality changes daily. It is possible to observe that far away from the transitional regime, the trends for demineralised water and tap water are similar.

The addition of small quantities of ethanol in water changes radically the hydrodynamics, in particular in the case of heterogeneous regime. These differences

are bigger when the ethanol concentration is higher. The trends are similar under the homogeneous regime, but the transition is delayed, as shown in Fig. 3.5. In the case of heterogeneous regime, the differences of gas hold-up between ethanol solutions and demineralised water are almost constant as the superficial gas velocity increases.

3.4.2 Local gas volume fraction

The local gas volume fraction is affected by the superficial gas velocity and the radial and axial positions. The optical probe measures correctly the local gas volume fraction for every operating condition. The local gas volume fraction is maximum in the column centre and minimum close to the wall, as suggested by the correlation of Schweitzer (2001). The gas volume fraction profile is symmetric and it can be assumed, in first approximation, as parabolic. Increasing the superficial gas velocity, the local gas fraction value becomes higher for every bubble column position. The effect is more important in the column centre, where the largest bubbles rise to the top. Close to the wall, the smallest bubbles are dragged down by the liquid that recirculates.

In the case of homogeneous regime, the radial profile is less pronounced. Big bubbles appear in the centre of the column and the gas fraction radial profile has a stronger concavity in the case of heterogeneous and transition regimes, as reported in Fig. 3.6 and Table A.2.

The axial gas fraction profile in the column centre increases along the axial position (Fig. 3.7, Table A.6 and Table A.7). More gas is trapped in the highest part of the column. This axial effect is present under both the homogeneous and the heterogeneous regimes. This effect may be important for industrial applications: increasing the axial position, the radial gas volume fraction profile is more pronounced and can lead to strong heterogeneities in products concentrations, for instance.

As observed with the global gas hold-up (Fig. 3.5), the effect of the tap water on the gas volume fraction is low for both homogeneous and heterogeneous regimes (Fig. 3.6 and Table A.3). Adding few percent of ethanol, the transition is delayed: with a superficial gas velocity of 0.06 m/s, the radial gas volume fraction profile is almost flat. In the case of homogeneous regime, the local gas fraction is almost not influenced by the presence of ethanol. In the case of heterogeneous regime, the local gas fraction is higher if small quantities of ethanol are present (Fig. 3.6).

In the case of heterogeneous regime, the local gas fraction increases adding a small quantity of alcohol for every position: this discrepancy is important both for the radial (Fig. 3.6, Table A.4 and Table A.5) and the axial position (Fig. 3.7 and Table A.7). The ethanol effect on the gas fraction is almost absent in the case of homogeneous regime (Table A.6).

To further study and validate the local gas fraction measurements, they are compared with the correlation of Schweitzer (2001) (Eq. (2.3)). It is suitable for the prediction of gas fraction profiles under the heterogeneous regime. It does not consider an axial evolution. In accordance with the experiments of Forret (2003), this correlation considers the local gas fraction near the wall close to zero.

Considering a superficial gas velocity of 0.16 m/s, the global gas volume fraction (measured with the difference of height of the liquid into the column) is equal to

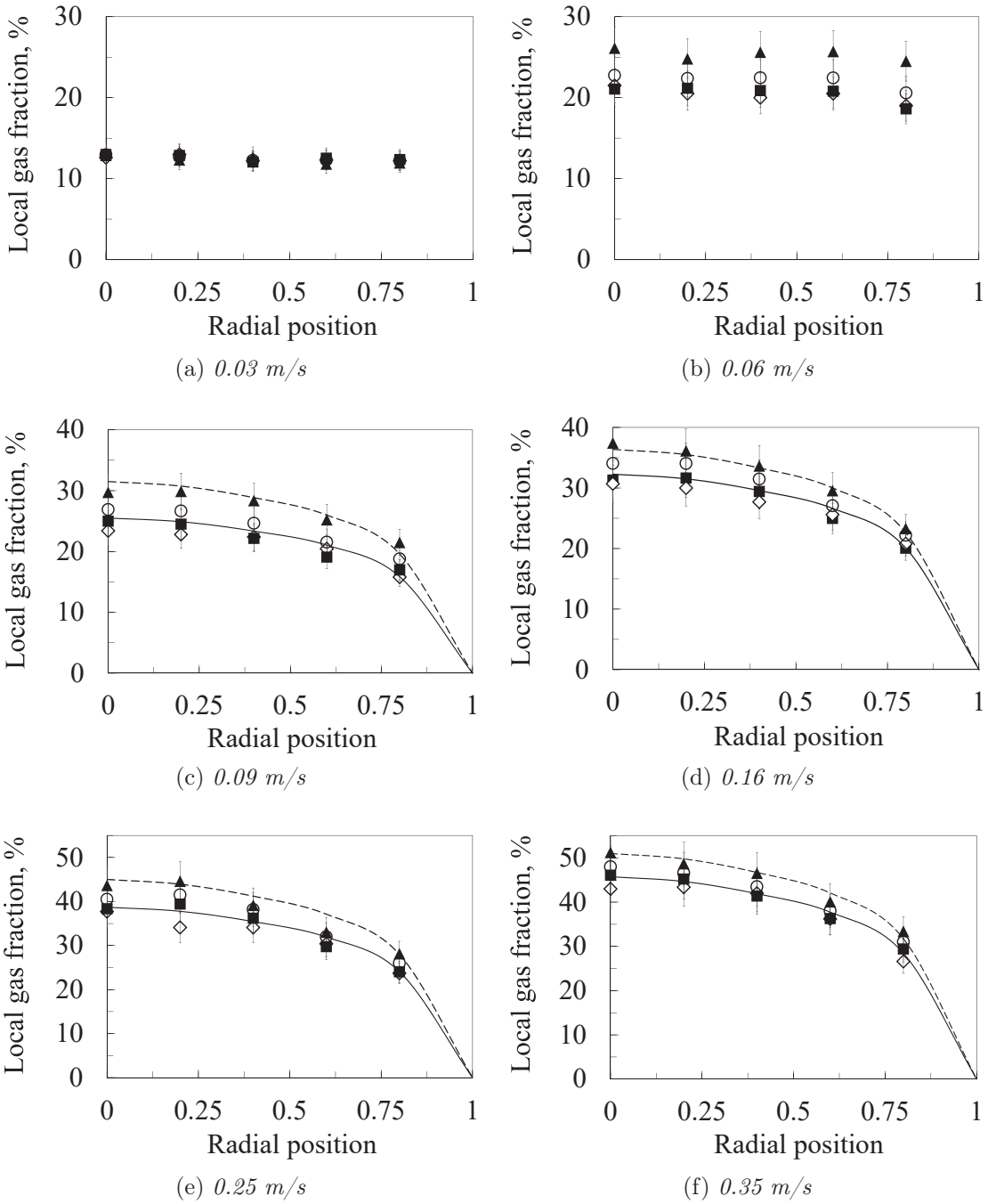

(a) *0.03 m/s* (b) *0.06 m/s*

(c) *0.09 m/s* (d) *0.16 m/s*

(e) *0.25 m/s* (f) *0.35 m/s*

Figure 3.6: Radial gas fraction profiles at H/D=2.5 with demineralised water (■), tap water (◇), ethanol 0.01% (○) and ethanol 0.05% (▲) at different superficial gas velocities. Comparison with Schweitzer (2001) correlation profiles for water (solid lines) and ethanol 0.05% (dashed lines).

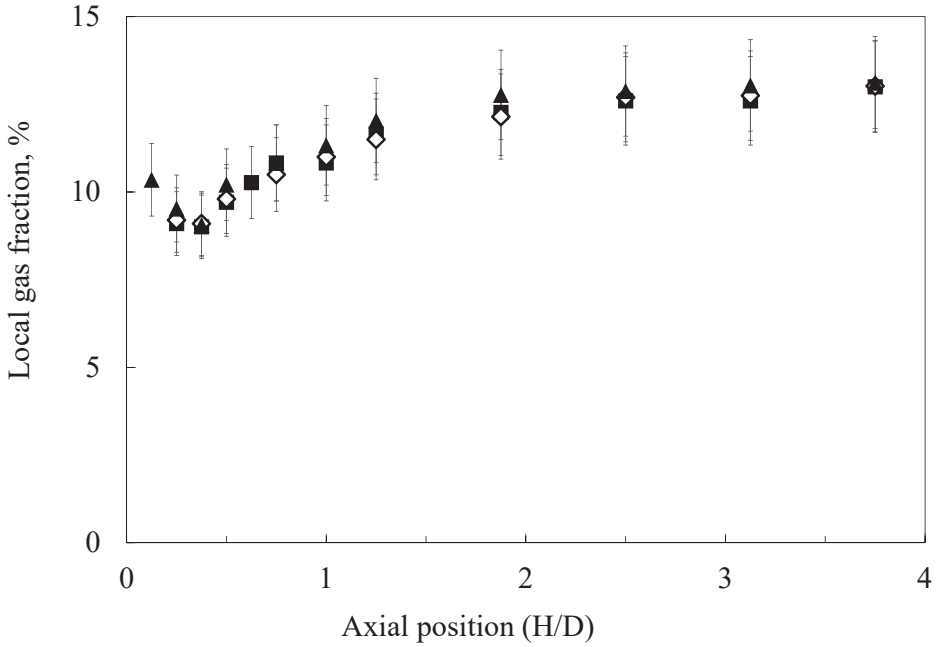

(a) *0.03 m/s*

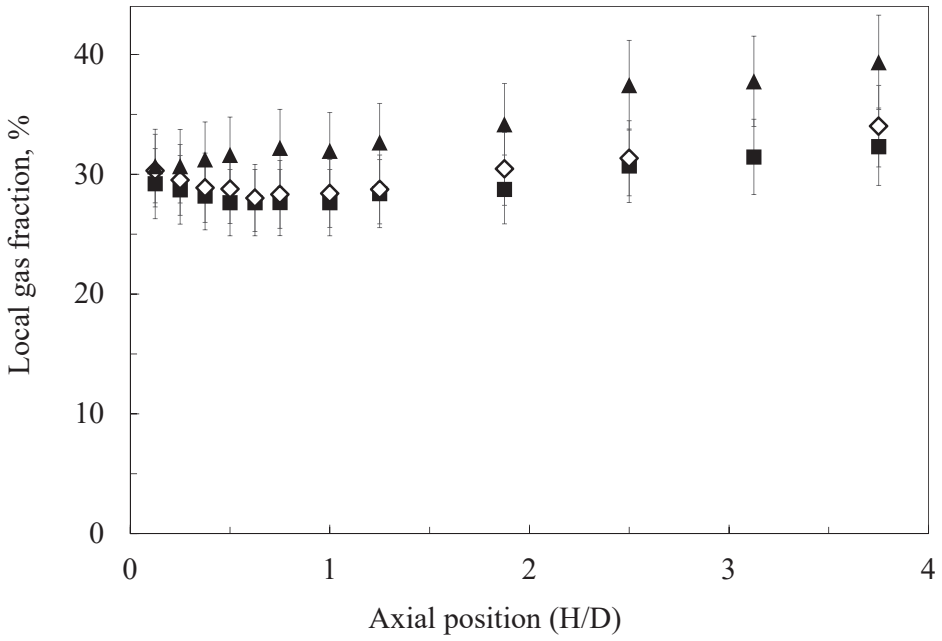

(b) *0.16 m/s*

Figure 3.7: Axial gas fraction profile in the centre of the column with demineralised water (■), tap water (◇), ethanol 0.01% (○) and ethanol 0.05% (▲) at different superficial gas velocities.

0.26. Another method to compute the mean gas fraction is to average the radial local gas fraction profile in a certain axial position. In order to compute this average, it is necessary to assume that the fraction of gas near the wall is equal to zero, as suggested by Schweitzer (2001) and Forret (2003). In the same operating conditions, with a H/D = 2.5, the average of the radial local gas fraction profile is equal to 0.22. This discrepancy is due to different factors: the importance of the axial effect (Fig. 3.7), the assumption of absence of gas near the wall and the low precision of the gas hold-up measured with the difference of liquid height.

The correlation of Schweitzer (2001), calculating the mean gas fraction as the average in the axial position of interest, fits well the experimental profile in the case of heterogeneous regime and demineralised water (Fig. 3.6). The correlation of Schweitzer (2001) cannot be used in the case of homogeneous regime: the experimental radial profile is flat, while the profile obtained from this correlation is parabolic.

Under the heterogeneous regime, the correlation of Schweitzer (2001) is suitable also in the case of tap water and alcohol addition: the mean gas fraction changes, but a correct radial profile is obtained, as reported in Fig. 3.6.

The results of this work are qualitatively compared with the experimental results of McClure et al. (2016). McClure et al. (2016) use 'tree' type spargers, located at a height of 0.135 m. The radial profiles with this sparger have an M-shape if a symmetric sparger is used, as shown in Fig. 3.8. A perforated plate injects gas homogeneously, while a 'tree' type sparger cannot. The different type of sparger cause the experimental data differences between this work and McClure et al. (2016). For different operating conditions, the sparger choice can significantly influence the global hydrodynamics.

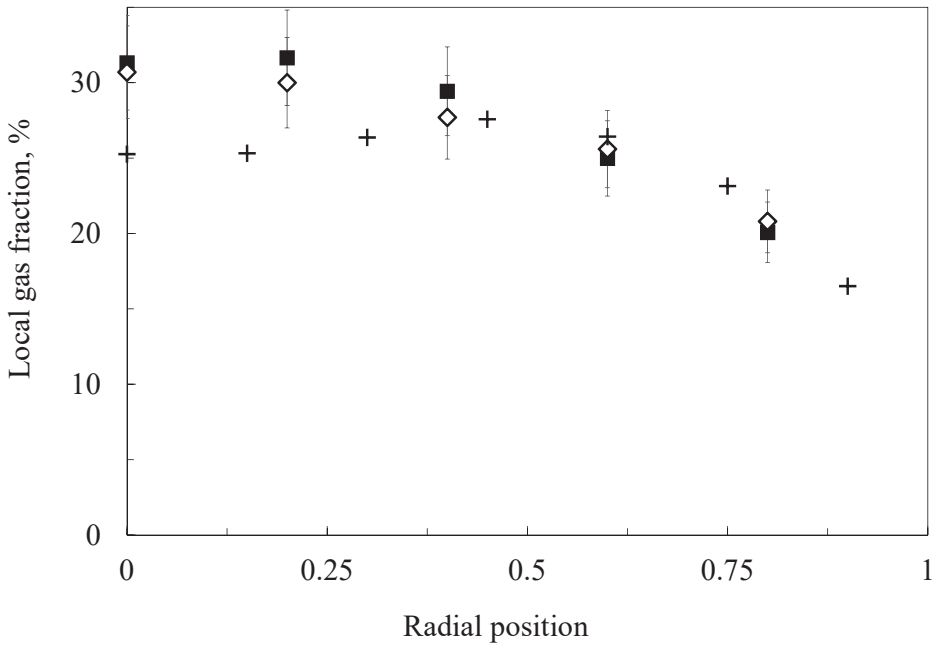

Figure 3.8: Radial gas fraction profiles at H/D=2.5 with demineralised (■) and tap water (◇) versus the experimental data of McClure et al. (2016) (+).

3.4.3 Axial liquid velocity

The mean radial profile of axial liquid velocity depends on global hydrodynamics and on bubbles recirculation, as observed by Krishna et al. (2000b). Its radial profile has a quadratic shape in the case of heterogeneous regime, with a strong liquid recirculation, that goes up in the column centre and goes down next to the wall, as reported in Fig. 3.9 and Table A.8. The radial profile is more pronounced in the case of heterogeneous regime and it is almost flat under the homogeneous regime. For a superficial gas velocity of 0.06 m/s, using demineralised water, the transition regime appears: the radial profile is quadratic with a weak concavity, i.e. the profile is halfway between the homogeneous and the heterogeneous regime. These results are in accordance with gas hold-up and local gas volume fraction profiles.

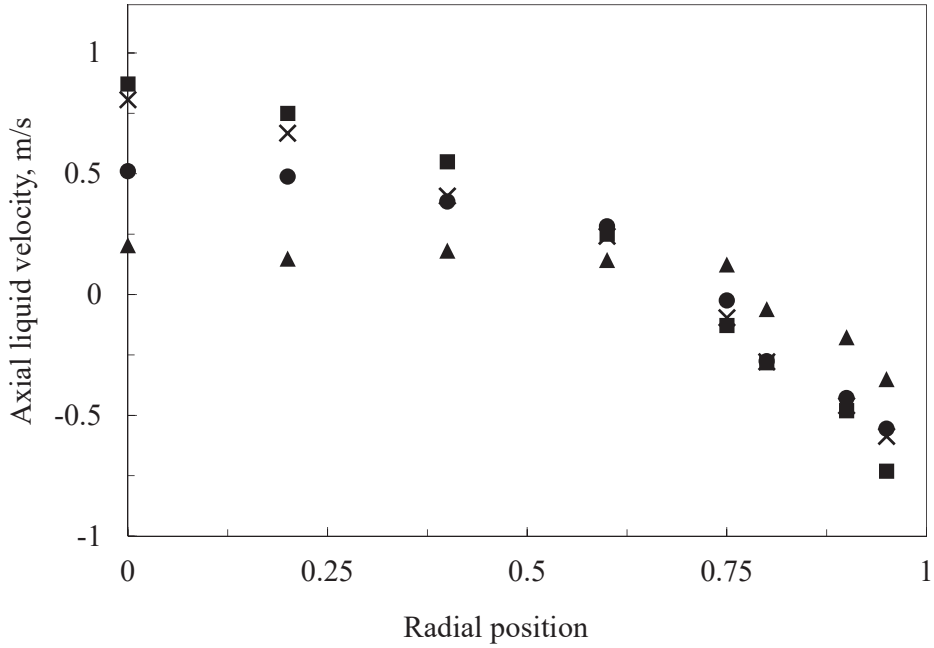

Figure 3.9: Radial profile of axial liquid velocity at H/D=2.5 with demineralised water for different superficial gas velocities: 0.03 m/s (▲), 0.06 m/s (●), 0.09 m/s (×) and 0.16 m/s (■).

In the case of heterogeneous regime, the mean axial liquid velocity profile and the recirculation does not seem to be influenced by the presence of contaminants in the water (Fig. 3.10 and Table A.9). The velocity profile depends on the vertical position close to the sparger, while the dependence is negligible in the case of H/D>1.

These experimental data are compared with the correlation of Forret (2003) (Eq. (2.10)) (Fig. 3.10). This correlation allows the radial profile of the liquid axial velocity to be defined if the liquid velocity at the column centre is known. This equation can be used in presence of contaminants and additives.

The experimental liquid velocity in the centre of the column is then compared with the correlation proposed by Miyauchi & Shyu (1970) (Eq. (2.11)), that can be used for many operating conditions under the heterogeneous regime. This correlation can also be used for scale-up purposes, but it cannot be used in presence

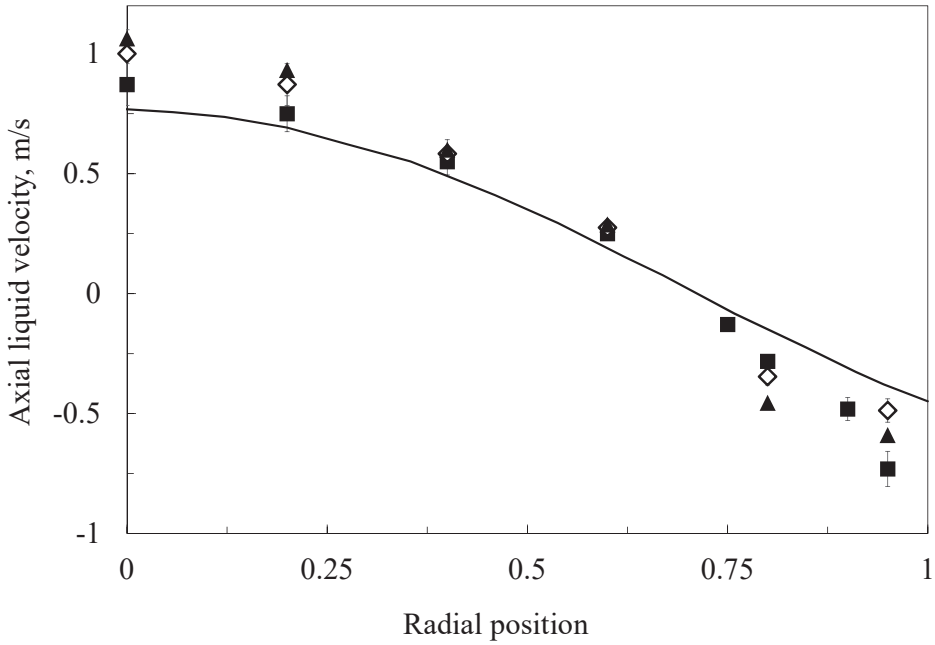

Figure 3.10: Radial profile of axial liquid velocity for a superficial gas velocity of 0.16 m/s at H/D=2.5 for demineralised water (■), tap water (◇) and ethanol 0.05% (▲); radial profiles are compared with the correlations proposed by Miyauchi & Shyu (1970) and Forret (2003) (solid line).

of contaminants and additives. It slightly underestimates the liquid velocity in the column centre also without additives.

3.4.4 Bubble size

The Sauter mean diameter is obtained from the CC measurements for different water qualities, for a wide range of superficial gas velocity, from 0.03 m/s to 0.35 m/s. These results are given on Fig. 3.11 and reported in Table A.10, Table A.11, Table A.12 and Table A.13.

The radial profile of the Sauter mean diameter is symmetrical with a maximum in the centre. In the case of homogeneous regime, the profile is flatter. When the superficial gas velocity increases, the concavity grows. In the case of heterogeneous regime, big bubbles are formed. These bubbles they rise in the column centre, while small bubbles are dragged down by the liquid recirculation near the wall. Radial profiles of gas volume fraction, liquid velocity and bubble size are interconnected and consistent.

The axial evolution of the Sauter mean diameter in the column centre is reported in Fig. 3.12, in Table A.14 and in in Table A.15. The Sauter mean diameter slightly decreases for both media close to the sparger. Close to the bottom, the bubble size profile is not developed and it needs about 0.5 m to reach a stable radial profile; above this height, the bubble size grows along the axial position. (Fig. 3.12). This increase can be partially due to the decrease of pressure along the column. The ideal gas law can be used to obtain a first approximation valuation: this effect is less than 5%, while experimentally the increase is more than 20%. It means that other factors are involved. This phenomenon is still difficult to explain. A partial

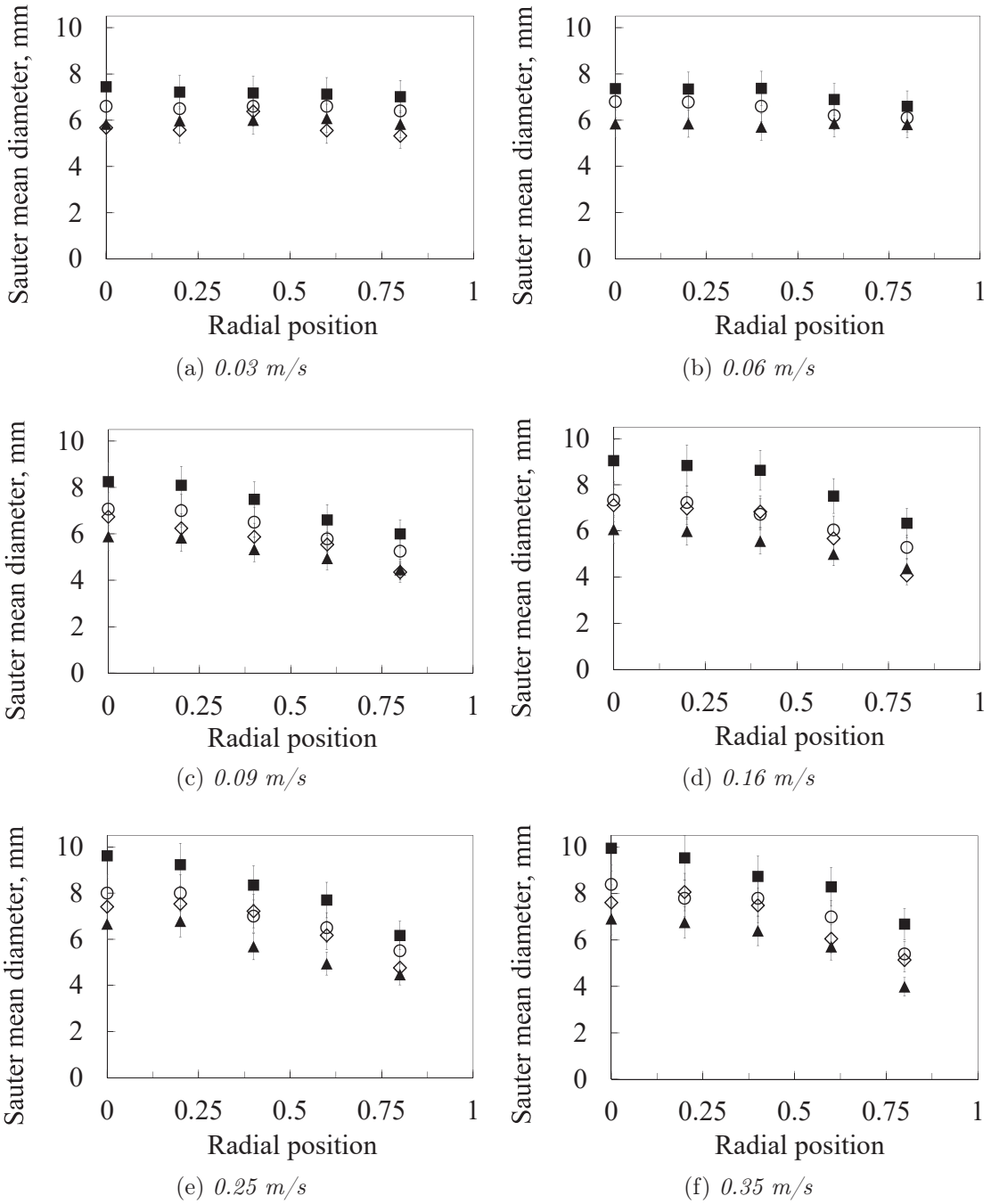

(a) *0.03 m/s* (b) *0.06 m/s*

(c) *0.09 m/s* (d) *0.16 m/s*

(e) *0.25 m/s* (f) *0.35 m/s*

Figure 3.11: Sauter mean diameter profiles at H/D=2.5 with demineralised water (■), tap water (◇), ethanol 0.01% (○) and ethanol 0.05% (▲) at different superficial gas velocities.

explanation could be the higher concavity of the radial profiles along the axial position, that causes an increase of the parabola maximum. The main phenomenon that should cause the axial increase should be the bubble coalescence.

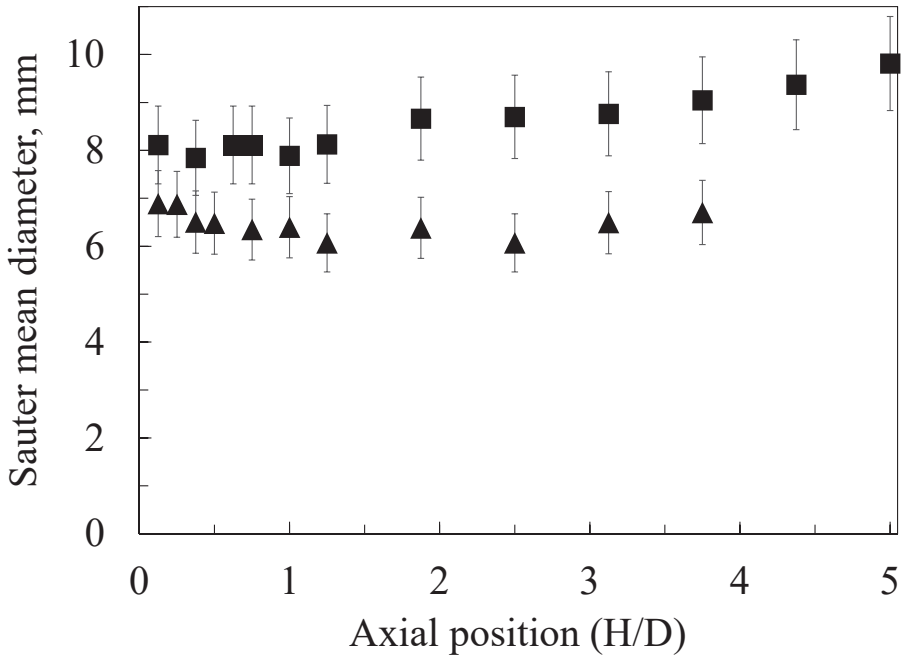

Figure 3.12: Axial Sauter mean diameter profile in the centre of the column for a superficial gas velocity of 0.16 m/s (heterogeneous regime) with demineralised water (■) and ethanol 0.05% (▲).

The Sauter mean diameter in demineralised water is higher than in tap water (Fig. 3.11) for every operating condition: water contamination has an important effect on the bubble size. Adding ethanol, the Sauter mean diameter becomes lower in comparison with the case of demineralised water, but increases with the superficial gas velocity. Adding ethanol, the radial profile is almost flat both for 0.03 m/s and for 0.06 m/s (Fig. 3.11), confirming the delay in entering the transition regime, as suggested by global and local gas volume fraction. The bubble size is lower if the concentration of ethanol is higher. The ethanol effect is consistent with the results of McClure et al. (2015), adding 2-propanol into water. Small quantity of ethanol and presence of impurities in tap water decrease coalescence; as a consequence, the Sauter mean diameter is lower.

The surface tension difference is too small to have an effect: at 17 °C, with an ethanol concentration of 0.05%, it goes from 0.07335 N/m to 0.07325 N/m. The surface tension decrease is not enough to explain the differences: a small variation of temperature would have a stronger effect than the presence of ethanol. It means that other phenomena are at stake. (Kelkar et al. 1983) suggest that the differences are caused by the bubble-rise velocity reduction. This explanation is reasonable for the homogeneous regime, where the bubbles go up vertically and the bubble velocity tends to the terminal velocity. As suggested by several authors (Camarasa et al. 1999, Zahradník et al. 1995, 1997), under the heterogeneous regime, the macro-scale turbulence effect eclipses the others. The effect on the gas fraction can be entirely explained by the delay in entering the transitional regime (Krishna et al. 2000a). The homogeneous regime is larger and the gas hold-up at transition

in presence of alcohol can be estimated by using the correlation proposed by Reilly et al. (1994).

As presented in Fig. 3.11 for a superficial gas velocity of 0.06 m/s, lower coalescence causes a transition delay: a lower coalescence rate causes smaller bubbles, resulting in a higher gas hold-up into the column. Bigger bubbles feel a higher buoyancy force (in comparison with the drag force) and they rise more quickly. As big bubbles rise quickly in the column centre, the transition from the homogeneous regime to the transition regime and to the heterogeneous regime is affected. By using an endoscope, Raimundo (2015) measured the bubble size distributions, observing that they are wide, but still unimodal or bimodal with a predominant peak. The biggest bubbles are in the column centre.

The principal effect of alcohol is to modify the surface mobility of the bubbles, as stated by Najafi et al. (2007). In the case of pure systems, the bubble interface is mobile. In this case, the liquid film between the approaching bubbles drains out quickly. Alcohol forms a monolayer at the interface; that causes an additional resistance to the liquid film motion (Jamialahmadi & Miiller-Steinhagen 1992). This additional resistance increases the liquid film drainage time. Consequently, the overall coalescence rate decreases. Takahashi (2005) stated that another important aspect is linked to the effect of alcohol on the zeta-potential of the bubbles.

3.4.5 Effect of the sparger on demineralized water systems

A sparger with 92 holes of 2 mm in diameter (Fig. 3.4b) ensures a homogeneous gas distribution and a generation of small bubbles. The bubble distribution is optimal. Dead zones in the bubble column are absent.

A sparger with 7 holes of 9 mm is used to form bigger bubbles and to enhance bubble breakage close to the bottom of the column. Gas injection with this sparger is completely different: the gas is injected heterogeneously in a small fraction of the column section and is then concentrated close to the holes. In correspondence of the column centre, where the data is collected, the new sparger has a hole (Fig. 3.4c).

The axial gas fraction profiles obtained with the two spargers are compared in Fig. 3.13 (Table A.16, Table A.17 and Table A.18). More gas accumulates near the sparger in the column centre if the 7-holes sparger is used, in the case of heterogeneous regime. The sparger effect is important for every column position in the case of homogeneous regime and it determines the gas volume fraction in the entire column: using the 7-holes sparger, the gas fraction is lower than when using the 92-holes sparger for every axial position. Under the heterogenous regime, the sparger effect is important in the lowest part on the column, while its effect is almost null above a certain height.

Close to the bottom of the column, by using the 92-holes sparger, the radial profile of the gas fraction is almost flat (Fig. 3.14) contrary to the results obtained with the 7-holes sparger: a strong bubble accumulation appears above the holes, while the gas concentration is low in the other radial positions. As shown in Fig. 3.14 (Table A.19 and Table A.20), the gas volume fraction with the two spargers is approximately identical under the heterogeneous regime above an axial position of 0.5 m.

The initial dimension of the bubbles is strongly influenced by the sparger choice, with the formation of very large bubbles (more than 20 mm) close to the bottom

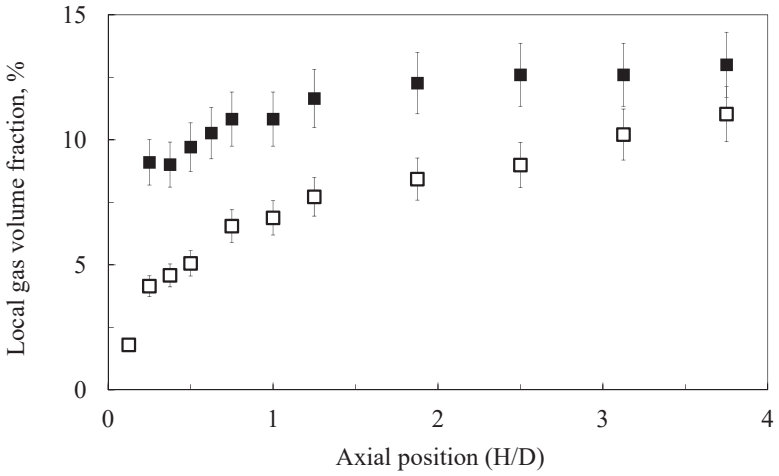

(a) *0.03 m/s*

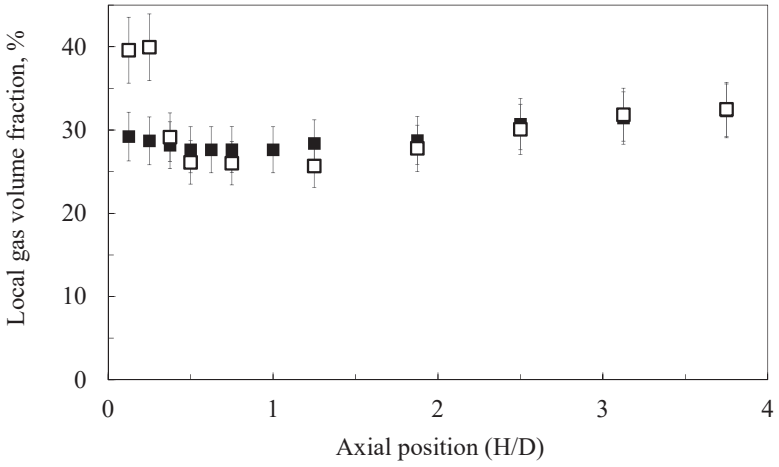

(b) *0.16 m/s*

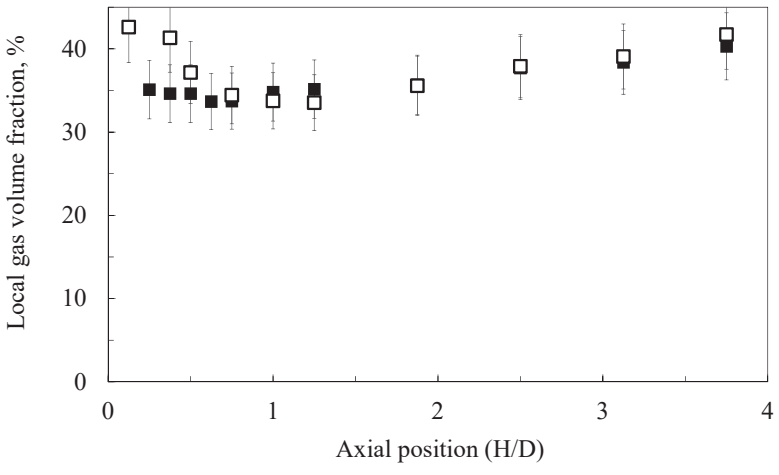

(c) *0.25 m/s*

Figure 3.13: Axial gas fraction profile at the centre of the column with demineralised water: sparger with 92 holes of 2 mm (■) vs sparger with 7 holes of 9 mm (□) with different superficial gas velocities.

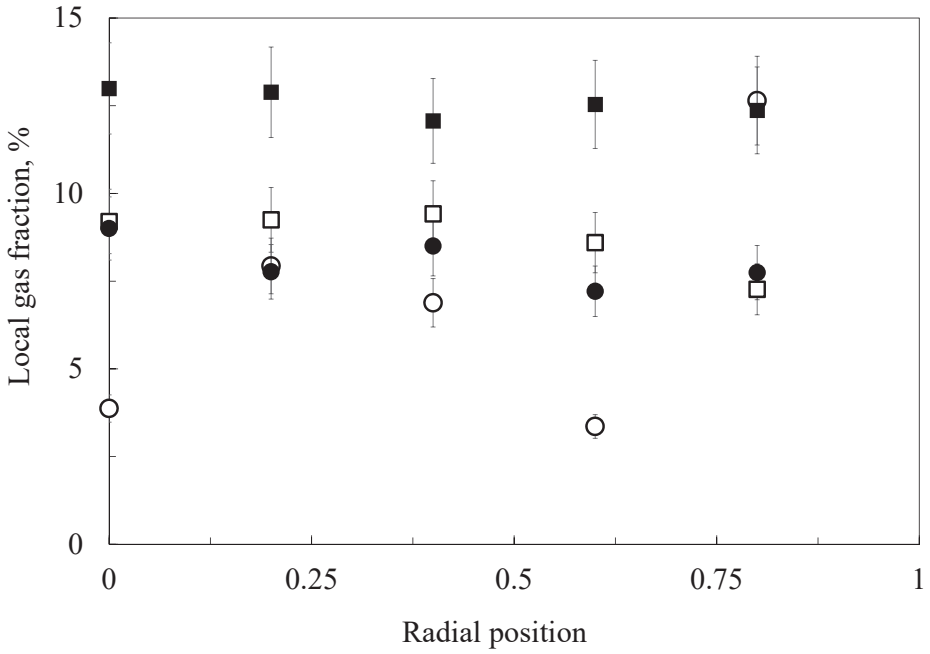

(a) *0.03 m/s*

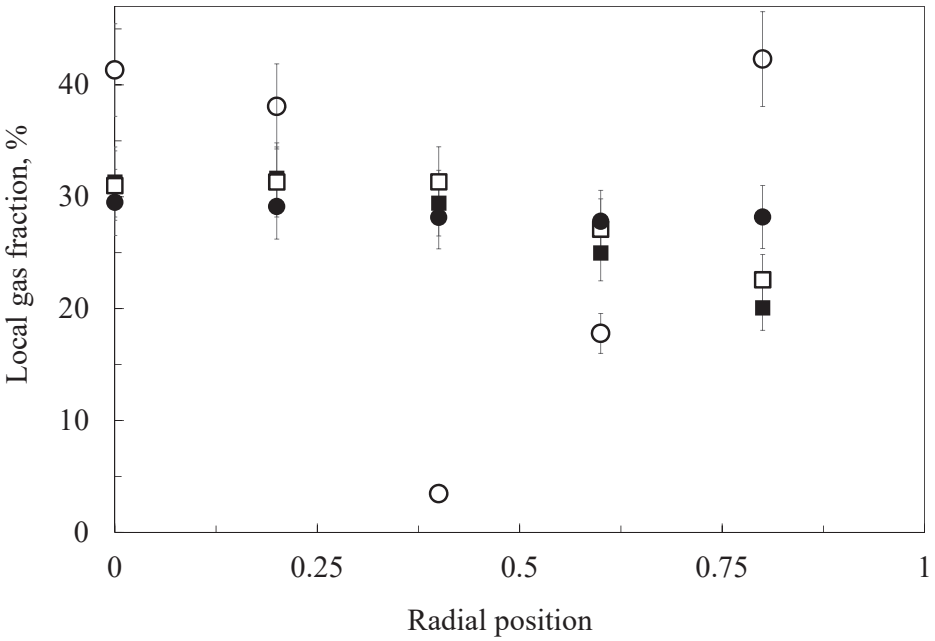

(b) *0.16 m/s*

Figure 3.14: Radial gas fraction profile at different axial positions with demineralised water: sparger with 92 holes of 2 mm (H/D=2.5 (■) and H/D=0.25 (●) vs sparger with 7 holes of 9 mm (H/D=2.5 (□) and H/D=0.25 (○)) with different superficial gas velocities.

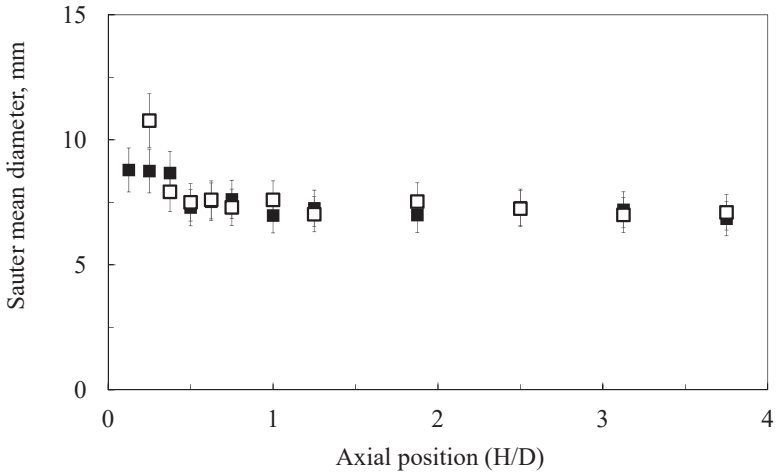

(a) *0.03 m/s*

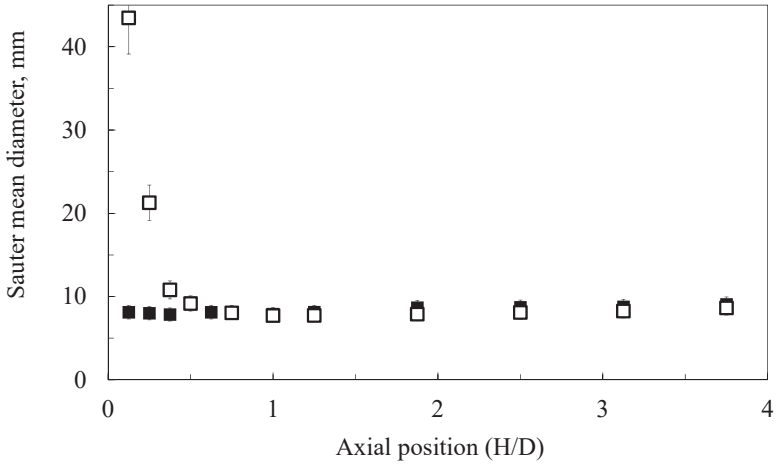

(b) *0.16 m/s*

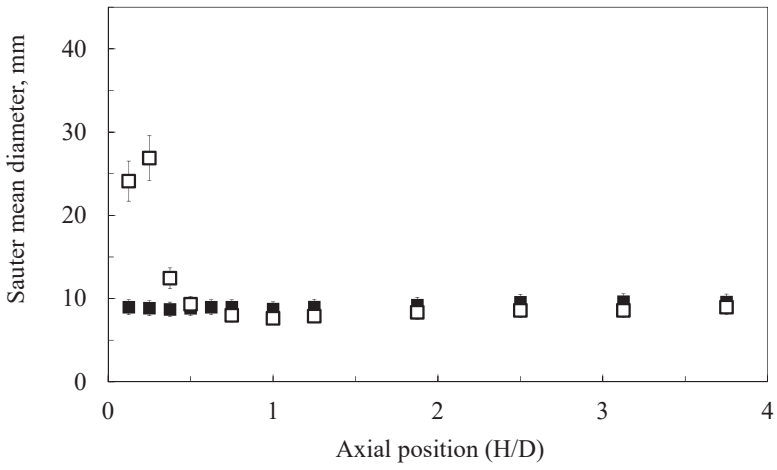

(c) *0.25 m/s*

Figure 3.15: Axial Sauter mean diameter profile at the centre of the column: sparger with 92 holes of 2 mm (■) vs sparger with 7 holes of 9 mm (□) with different superficial gas velocities.

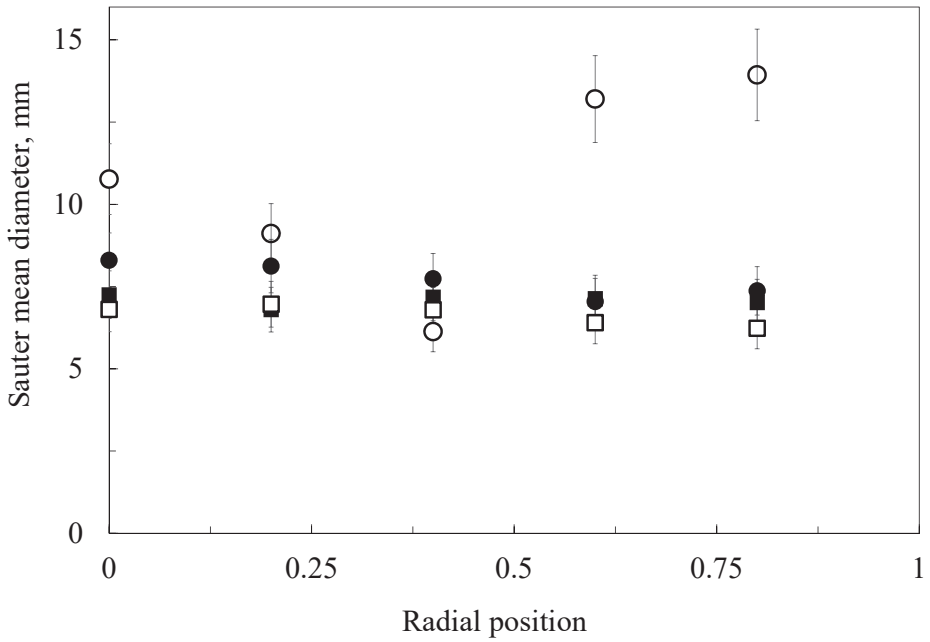

(a) *0.03 m/s*

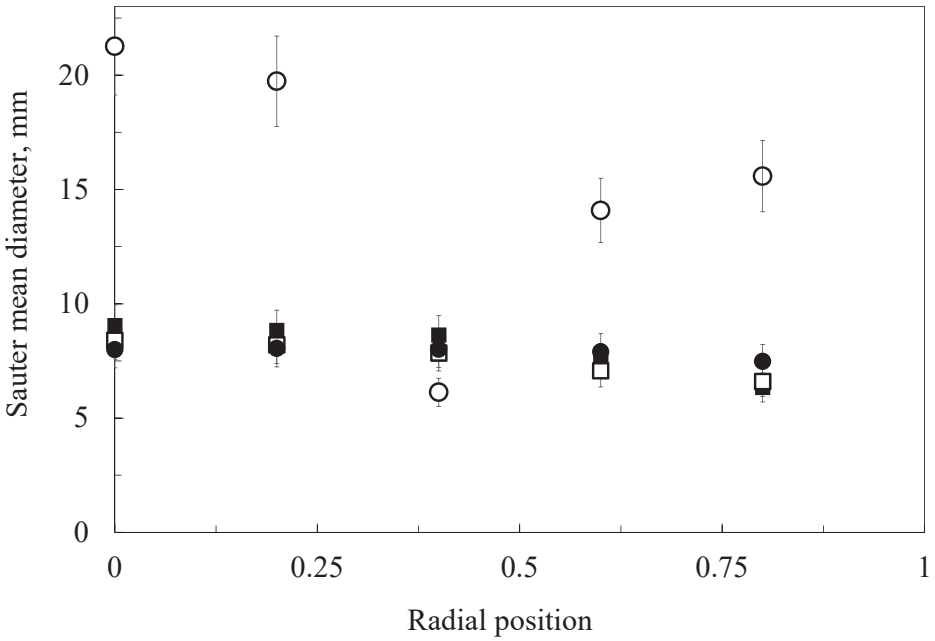

(b) *0.16 m/s*

Figure 3.16: Radial Sauter mean diameter profile at different axial positions with demineralised water: sparger with 92 holes of 2 mm (H/D=2.5 (■) and H/D=0.25 (●)) vs sparger with 7 holes of 9 mm (H/D=2.5 (□) and H/D=0.25 (○)) with different superficial gas velocities.

using the 7-holes sparger in correspondence of the holes, as shown in Fig. 3.15 (Table A.21, Table A.22 and Table A.23). The Sauter mean diameter decreases rapidly along the axial position and after some centimetres, the bubble size is almost identical to the case of 92-holes sparger (Fig. 3.16, Table A.24 and Table A.25). Under the heterogeneous regime, the sparger has a weak effect both on gas fraction and on Sauter mean diameter above an axial position of 1 m. In the case of heterogeneous regime, the initial bubble size does not influence the final bubble size. This effect cannot be neglected in the lowest part of the column. Close to the bottom, the radial profile of the Sauter mean diameter is flat with the 92-holes sparger, while it is irregular with the other sparger, as detailed in Fig. 3.16. The irregularity of this profile is partially due to the creation of random preferential paths of the bubbles. The sparger effect on the bubble size is only important in the region close to the bottom, where the Sauter mean diameter is very high. If the Sauter mean diameter is very high, bubble breakage is stronger than bubble coalescence. Bubble breakage is the main phenomenon and bubble coalescence can be neglected.

3.4.6 Effect of sparger for different media

The effects of additives and sparger design are coupled. The sparger effect is the same both with demineralised water and with ethanol addition under the heterogeneous regime: more gas accumulates near the sparger in the column centre. Under the heterogeneous regime, the sparger effect becomes null above 1 m: the gas fraction is not influenced by the sparger above this height, both with demineralised water and in presence of ethanol (Fig. 3.17 and Table A.17)). This aspect is reasonably consistent with the conclusion of Polli et al. (2002), stating that the sparger effect is important up to a distance of the order of magnitude of the diameter of the column. Under the heterogeneous regime, alcohol addition has a relatively low effect close to the sparger, but it affects the gas fraction in the entire bubble column. Under the homogeneous regime, the ethanol addition has a lower effect than under the heterogeneous regime (Fig. 3.17), while the sparger choice influences the gas fraction in the entire column (Table A.16).

As shown in Fig. 3.18, the final dimension of the bubbles is almost not influenced by the initial bubble size under the heterogeneous regime, while the alcohol presence is very important (Table A.21, Table A.22 and Table A.23). The alcohol presence almost does not influence the rate of bubble size decrease. The alcohol effect is important only when the bubble size reaches equilibrium. In the lower part of the column with the 7-holes sparger, when the bubbles are huge, bubble breakage can be considered as the main phenomenon and bubble coalescence is negligible. It allows decoupling bubble breakage and bubble coalescence. A priori, the alcohol presence can infer coalescence and break-up rates. Experimental data show that the presence of alcohol almost does not modify the rate with which bubbles coming out of the sparger reduce their size, but on the contrary it affects the final equilibrium size. From these observations, it is possible to state that the alcohol does not change significantly the break-up rate, but it reduces the coalescence rate. The main alcohol effect is on the bubble surface mobility and then it is reasonable that the coalescence rate, that depends on the bubble surface mobility, is influenced in turn by the presence of alcohol.

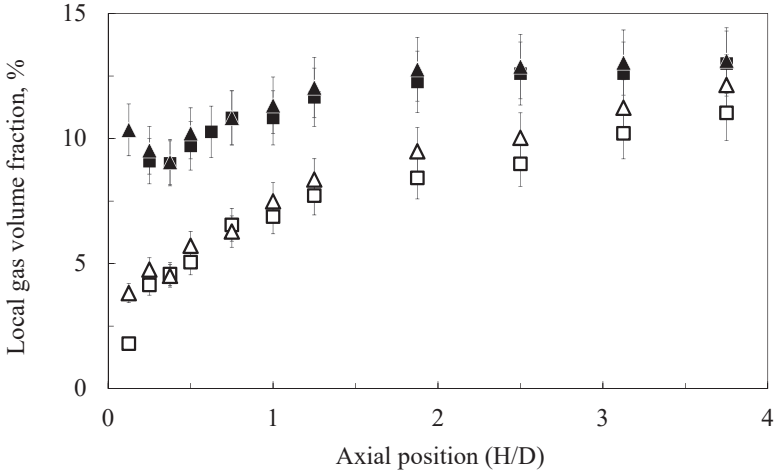

(a) *0.03 m/s*

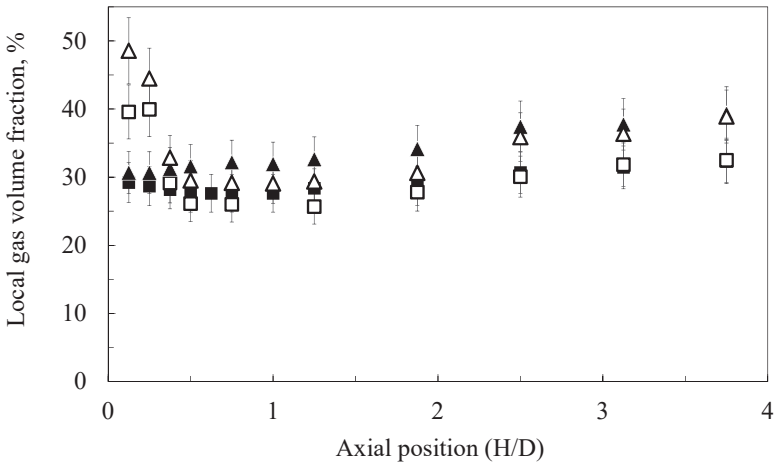

(b) *0.16 m/s*

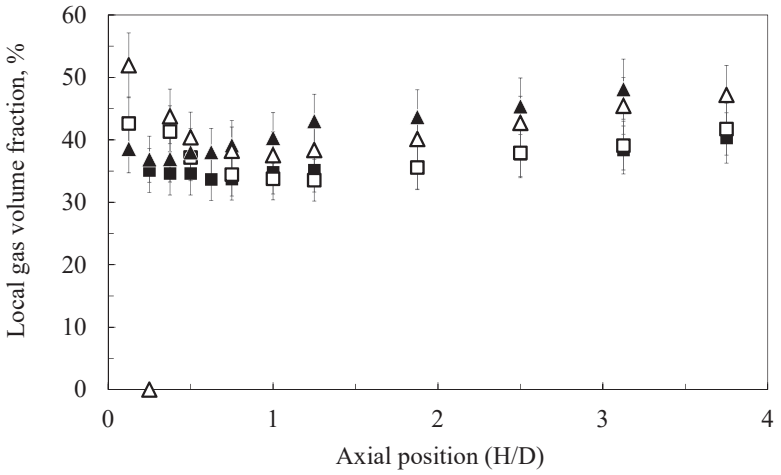

(c) *0.25 m/s*

Figure 3.17: Axial gas fraction profile at the centre of the column: sparger with 92 holes of 2 mm (with demineralised water (■) and ethanol 0.05% (▲)) vs sparger with 7 holes of 9 mm (with demineralised water (□) and ethanol 0.05% (△)) with different superficial gas velocities.

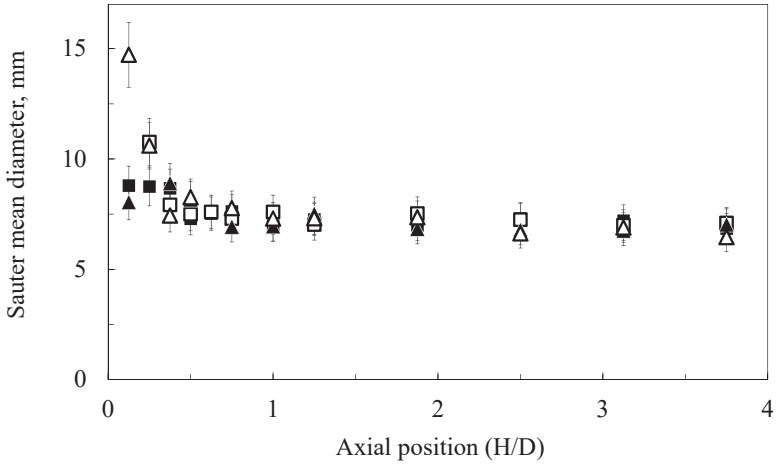

(a) *0.03 m/s*

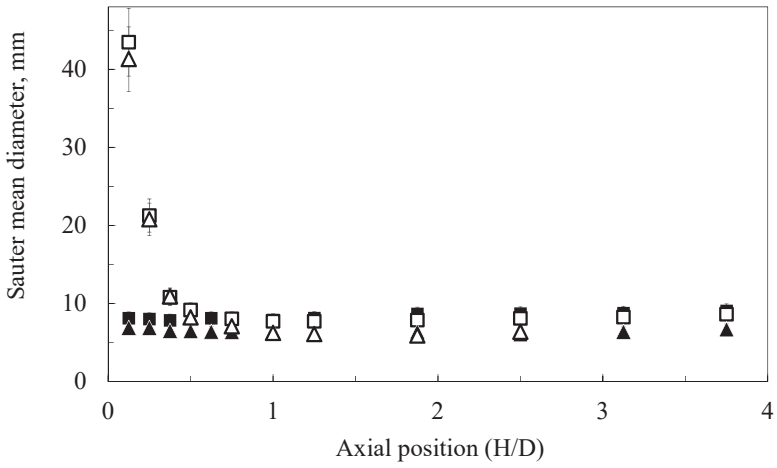

(b) *0.16 m/s*

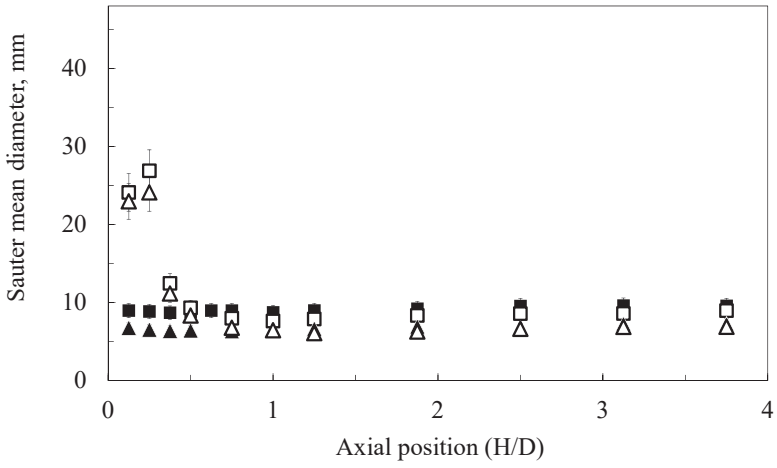

(c) *0.25 m/s*

Figure 3.18: Axial Sauter mean diameter profile at the centre of the column: sparger with 92 holes of 2 mm (with demineralised water (■) and ethanol 0.05% (▲)) vs sparger with 7 holes of 9 mm (with demineralised water (□) and ethanol 0.05% (△)) with different superficial gas velocities.

3.5 Conclusions and perspectives

The goal of this experimental part is to study hydrodynamics and bubble size in bubble columns under the heterogeneous regime, with the objective of highlighting and studying the breakage and coalescence phenomena.

The use of different quality of water and the addition of small quantities of ethanol is used to control coalescence. Bubble sizes in fully contaminated systems are significantly lower than in pure or slightly contaminated water. The presence of small percentages of ethanol into demineralised water delays the transition regime and heterogeneous regime occurs later. Water contamination increases the gas volume fraction and decreases the bubble dimension in the case of heterogeneous regime. Tap water causes similar consequences. Surface tension variations are not enough to explain these differences. The alcohol presence modifies the surface mobility of the bubbles. If the surface mobility is lower the coalescence rate decreases and then the bubbles are smaller. Further investigations concerning interface physical properties are necessary to understand how alcohol presence inhibits coalescence.

The sparger choice strongly influences gas volume fraction and bubble size in the lowest part of the column, close to the bottom. By using a perforated sparger with big holes, there is an accumulation of big bubbles close to the bottom, in correspondence of the holes. In this zone, bubble breakage is the main phenomenon. It allows identifying some configurations in which bubble generation and breakage are the only governing phenomena. The use of both different spargers and alcohol addition allows stating that bubble breakage is almost not influenced by the presence of alcohol: alcohol effect changes the surface mobility and then affects mainly the bubble coalescence. Coalescence models ought to consider the impact of additives, that drastically change the coalescence rate without modifying the physical properties involved.

Bubble size distributions (BSD) would be interesting to get, but unfortunately the CC technique is not able to calculate the BSD: A possible perspective could be to couple a classical optical probe for BSD measurements with a CC probe for the Sauter mean diameter. It could allow rescaling the BSD, that is not precisely measured with a classical optical probe in the case of heterogeneous regime.

Bibliography

Camarasa, E., Vial, C., Poncin, S., Wild, G., Midoux, N. & Bouillard, J. (1999), 'Influence of coalescence behaviour of the liquid and of gas sparging on hydrodynamics and bubble characteristics in a bubble column.', *Chemical Engineering and Processing* 38, 329–344.

Cartellier, A. & Barrau, E. (1998), 'Monofiber optical probes for gas detection and gas velocity measurements: conical probes.', *International Journal of Multiphase Flow* 24(8), 1265–1294.

Chaumat, H., Billet, A. & Delmas, H. (2007), 'Hydrodynamics and mass transfer in bubble column: Influence of liquid phase surface tension.', *Chemical Engineering Science* 62, 7378–7390.

Clift, R., Grace, J. R. & Weber, M. E. (1978), *Bubbles, Drops, and Particles.*, Academic Press, New York, New York.

Dargar, P. & Macchi, A. (2006), 'Effect of surface-active agents on the phase holdups of three-phase fluidized beds.', *Chemical Engineering and Processing* 45, 764–772.

Forret, A. (2003), Hydrodynamics scale-up of slurry bubble columns., PhD thesis, Université Claude Bernard Lyon 1 - IFPEN, Lyon.

Guo, K., Wang, T., Liu, Y. & Wang, J. (2017), 'CFD-PBM simulations of a bubble column with different liquid properties', *Chemical Engineering Journal* 329(Supplement C), 116–127.

Jamialahmadi, M. & Miiller-Steinhagen, H. (1992), 'Inhibition of bubble coalescence by solutes in air/water dispersions.', *Chemical Engineering Journal* 50, 47–56.

Keitel, G. & Onken, U. (1982), 'Inhibition of bubble coalescence by solutes in air/water dispersions.', *Chemical Engineering Science* 37, 1635–1638.

Kelkar, B. G., Godbole, S. P., Honath, M. F. & Shah, Y. T. (1983), 'Effect of addition of alcohols on gas holdup and backmixing in bubble columns.', *American Institute of Chemical Engineering Journal* 29, 361–369.

Krishna, R., Dreher, A. J. & Urseanu, M. I. (2000a), 'Influence of alcohol addition on gas hold-up in bubble columns: Development of a scale up model.', *International Communications in Heat and Mass Transfer* 27(4), 465–472.

Krishna, R., Urseanu, M. I., Van Baten, J. & Ellenberger, J. (2000b), 'Liquid phase dispersion in bubble columns operating in the churn-turbulent flow regime', *Chemical Engineering Journal* 78(1), 43 – 51.

Lindland, K. P. & Terjesen, S. G. (1965), 'The effect of a surface-active agent on mass transfer in falling drop extraction.', *Chemical Engineering Science* 5(1), 1–12.

Liu, W., Clark, N. N. & Karamavruc, A. I. (1996), 'General method for the transformation of chord-length data to a local bubble-size distribution.', *American Institute of Chemical Engineering Journal* 42(10), 2713–2720.

McClure, D. D., Kavanagh, J. M., Fletcher, D. F. & Barton, G. W. (2013), 'Development of a CFD model of bubble column bioreactors: Part one - a detailed experimental study', *Chemical Engineering & Technology* 36(12), 2065–2070.

McClure, D. D., Kavanagh, J. M., Fletcher, D. F. & Barton, G. W. (2017), 'Experimental investigation into the drag volume fraction correction term for gas-liquid bubbly flows', *Chemical Engineering Science* 170, 91–97.

McClure, D. D., Norris, H., Kavanagh, J. M., Fletcher, D. F. & Barton, G. W. (2015), 'Towards a CFD model of bubble columns containing significant surfactant levels.', *Chemical Engineering Science* 127, 189–201.

McClure, D. D., Wang, C., Kavanagh, J. M., Fletcher, D. F. & Barton, G. W. (2016), 'Experimental investigation into the impact of sparger design on bubble columns at high superficial velocities.', *Chemical Engineering Research and Design* 106, 205–213.

Miyauchi, T. & Shyu, C. N. (1970), 'Flow of fluid in gas-bubble columns', *Chemical engineering* 34(9), 958–964.

Najafi, A. S., Drelich, J., Yeung, A., Xu, Z. & Masliyah, J. (2007), 'A novel method of measuring electrophoretic mobility of gas bubbles.', *Journal of Colloid and Interface Science* 308(2), 344–350.

Polli, M., Di Stanislao, M., Bagatin, R., Abu Bakr, E. & Masi, M. (2002), 'Bubble size distribution in the sparger region of bubble columns', *Chemical Engineering Science* 57(1), 197–205.

Raimundo, P. M. (2015), Analysis and modelization of local hydrodynamics in bubble columns., PhD thesis, Université Grenoble Alpes.

Raimundo, P. M., Cartellier, A., Beneventi, D., Forret, A. & Augier, F. (2016), 'A new technique for in-situ measurements of bubble characteristics in bubble columns operated in the heterogeneous regime', *Chemical Engineering Science* 155, 504 – 523.

Raymond, D. R. & Zieminski, S. A. (1971), 'Mass transfer and drag coefficients of bubbles rising in dilute aqueous solutions.', *American Institute of Chemical Engineering Journal* 17(1), 57–65.

Reilly, I. G., Scott, D. S., De Bruijn, T. J. W. & MacIntyre, D. (1994), 'The role of gas phase momentum in determining gas hold-up and hydrodynamic flow regimes in bubble column operations.', *The Canadian Journal of Chemical Engineering* 72, 3–12.

Rusche, H. & Issa, R. (2015), Simulation of a reactive gas-liquid system with quadrature-based moments method., *in* 'Eleventh International Conference on Computational Fluid Dynamics in the Minerals and Process Industries', Melbourne, Victoria, Australia.

Sasaki, S., Uchida, K., Hayashi, K. & Tomiyama, A. (2017), 'Effects of column diameter and liquid height on gas holdup in air-water bubble columns.', *Experimental Thermal and Fluid Science* 82, 359–366.

Schweitzer, J. M. (2001), 'Local gas hold-up measurements in fluidized bed and slurry bubble column.', *Chemical Engineering Science* 56(3), 1103–1110.

Takahashi, M. (2005), 'ζ potential of microbubbles in aqueous solutions: Electrical properties of the gas-water interface.', *The Canadian Journal of Chemical Engineering* 109(46), 21858–21864.

Vial, C., Bendjaballah-Lalaoui, N., Poncin, S., Wild, G. & Midoux, N. (2003), 'Comparison, combination and validation of measuring techniques for local flow and turbulence analysis in bubble columns and airlift reactors.', *The Canadian Journal of Chemical Engineering* 81(3-4), 749–755.

Wellek, R. M., Agrawal, A. K. & Skelland, A. H. P. (1966), 'Shape of liquid drops moving in liquid media', *American Institute of Chemical Engineering Journal* 12(5), 854–862.

Xue, J. (2004), Bubble velocity, size and interfacial area measurements in bubble columns., PhD thesis, Sever Institute of Washington University.

Zahradník, J., Fialová, M., Kaštánek, F., Green, K. D. & Thomas, N. H. (1995), 'The effect of electrolytes on bubble coalescence and gas hold-up in bubble column reactors.', *Chemical Engineering Research and Design* 73, 341–346.

Zahradník, J., Fialová, M., Røužička, M., Drahoš, J., Kaštánek, F. & Thomas, N. H. (1997), 'Duality of the gas-liquid flow regimes in bubble column reactors', *Chemical Engineering Science* 52(21), 3811–3826.

Chapter 4

CFD simulations: hydrodynamics and mixing

4.1 Introduction

Bubble column reactors require effective mass, momentum and energy transfers between the liquid and the gaseous phases. Although bubble column reactors appear simple, their modelling is difficult. Phase velocities, gas volume fraction, bubble size, flow pattern and turbulence depend on the operating conditions and on the bubble column design and they are linked in a complex way. Moreover, in the case of heterogeneous churn-turbulent flow regime, local profiles of the properties of interest depend strongly on the radial position. Models for the simulation of bubble column reactors suitable for both homogeneous and heterogeneous regime still need to be developed.

CFD simulations are a promising tool for the study of large bubble columns in a wide range of operating conditions. A common choice is to model these systems with Reynolds-averaged Navier-Stokes (RANS) equations and by using the Eulerian-Eulerian multiphase model, describing the two phases as inter-penetrating continua, as stated by Zhang (2007), Vaidheeswaran & Lopez de Bertodano (2017). The interactions between the continuous and the disperse phases must be accurately modelled (Jakobsen et al. 2005). These interactions are dominated by different interfacial forces (McClure et al. 2013, Hlawitschka et al. 2017) and the drag force is the most important. In the case of high gas volume fractions, the distance between bubbles is small and the bubble boundary layers interact, modifying the drag force. This phenomenon can be considered by adding a swarm factor. In the literature, several drag force correlations and swarm factors have been proposed. Different swarm factors are suitable for low gas volume fractions, while few correlations have been proposed for high gas volume fractions (e.g. McClure et al. (2017b)). These correlations are often empirical or obtained through Direct Numerical Simulations. They are usually based on experiments carried out under the homogeneous regime and then they have a narrow validity range.

Drag law expressions, including swarm factor, can be studied and validated thanks to the experimental data of (Raimundo 2015) and the experiments detailed in Chapter 3 and in Gemello et al. (2018) for a wide range of superficial gas velocities, going from 0.03 m/s to 0.35 m/s and at different scales. Experimental gas hold-up, local gas volume fraction and axial liquid velocity are compared with

CFD results. The bubble size cannot be compared with the CFD simulations at this stage: classical CFD simulations consider a fixed bubble size as input parameter. The population balance model proposed in Chapter 5 will allow overcoming this limit. In the first part of this chapter, different drag laws and swarm factors are tested, with a view to obtaining a swarm factor suitable for several operating conditions.

The choice of the turbulence model is another important point for obtaining reasonable CFD results. Classical models of turbulence are based on the Boussinesq (1897) hypothesis. The choice of the turbulence model has a strong impact on the turbulent mixing, that is a key property for bubble column reactors. In the second part of this chapter, four different turbulence models, already usable in ANSYS Fluent, are tested: standard k-ε, realizable k-ε, RNG k-ε and k-ω model.

Bubble contribution to mixing is considered in this work. It affects strongly the mixing, as detailed by Alméras et al. (2016) for the homogeneous regime. With this method, shear-induced turbulence (SIT) and bubble contributions are attributable to similar diffusive properties. Alméras et al. (2015) stated that the bubbles have an influence on the dispersion of a passive scalar in the case of bubbly flows, characterizing the contribution of bubble wake interactions by adding a bubble-induced diffusivity to the scalar transport equations. Mixing due to the bubble contribution is studied in the last part of this chapter.

Turbulence due to energy transfer from gas to liquid could be included in a RANS model with different techniques, as detailed by Joshi (2001). Pfleger & Becker (2001), Yao & Morel (2004) and Rzehak & Krepper (2013) suggest adding directly the source terms in the turbulence properties transport equations, as pointed out by Fletcher et al. (2017) and McClure et al. (2017a) for predicting mixing. However, this contribution needs clarifications, in particular for bubble columns at high gas volume fractions. Sato & Sekoguchi (1975) stated that only a fraction of this contribution forms a source term for the turbulence kinetic energy. Turbulence due to energy transfer from gas to liquid is neglected in this chapter, without adding source terms in k and ε (or ω) equations.

4.2 Modelling of bubble columns

Fluid flows are defined by the continuity equation, that represents the local conservation of mass, and by the Navier-Stokes equation, that characterizes the local conservation of momentum (Bird et al. 2007):

$$\frac{\partial \rho}{\partial t} + \nabla \rho \boldsymbol{u} = 0, \tag{4.1}$$

$$\frac{\partial \left(\rho \boldsymbol{u}\right)}{\partial t} + \nabla \cdot \left(\rho \boldsymbol{u}\boldsymbol{u}\right) + \nabla p = \nabla \cdot \boldsymbol{T} + \boldsymbol{g} \tag{4.2}$$

where $\boldsymbol{T}$ is the viscous stress tensor and $\boldsymbol{g}$ is the body forces vector. For a Newtonian fluid, $\boldsymbol{T}$ is equal to:

$$\boldsymbol{T} = \mu \left[\nabla \boldsymbol{u} + \left(\nabla \boldsymbol{u}\right)^T - \frac{2}{3}\nabla \cdot \boldsymbol{u}\boldsymbol{I}\right] \tag{4.3}$$

where $\boldsymbol{I}$ is the identity matrix.

Usually, solutions can be very accurate for single-phase laminar flows and satisfying results are obtained for turbulent flows when the geometry is simple. Contrariwise multiphase flows simulations are more complex, given that interactions between phases need to be considered and then modelled.

4.2.1 Multiphase flows

Multiphase flows can generally be divided into dispersed and separated flows, as shown in Fig. 4.1 (Andersson et al. 2012).

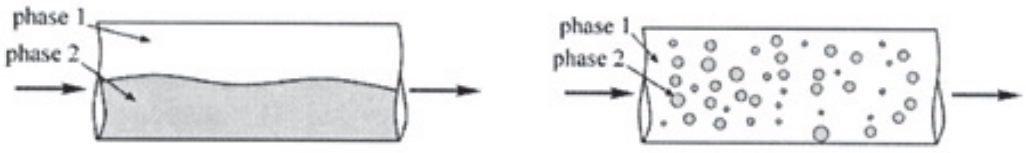

(a) *Separated flow.* (b) *Dispersed flow.*

Figure 4.1: Main classification of multiphase flow.

Bubble columns work in a dispersed flow regime: the dispersed phase is represented by the bubbles of gas and the continuous one by the liquid. If the volume fraction of the dispersed phase is high, it is difficult to obtain good results. Different approaches are possible in order to describe the behaviour of this multiphase system: Euler-Lagrange approach and Euler-Euler approach are the most used.

4.2.1.1 Euler-Lagrange approach

Euler-Lagrange approach (also called Discrete bubble model) is a model where the liquid phase is considerate continuous and the gas phase is defined as discontinuous. In this approach, the equation of motion for the continuous phase is solved using an Eulerian frame of reference, solving the time-averaged Navier-Stokes equations. The disperse phase is tracked explicitly within a Lagrangian context and the motion equation of Newton is solved for each particle individually (Suzzi et al. 2013). The dispersed phase can exchange mass, momentum and energy with the liquid. The gas phase is described by tracing several random inclusions, through the solution of an equation of motion. It is supposed that the hydrodynamic forces acting on each bubble are known. This method is limited in the number of inclusions that could be tracked, specifically only for small columns or conditions of low gas volume fraction. The assumption in this model is that the volume fraction of the secondary phase is below 10-15%. Actually, this approach cannot be applied in this work with high gas fraction.

4.2.1.2 Euler-Euler approach

In Euler-Euler approach, phases are considered as interpenetrating continua. Volume fractions for different phases are introduced in order to consider that the volume of a phase cannot be occupied at the same time by the other one. These fractions are continuous functions of time and space and their sum is equal to one. The equations, similar for each phase, are obtained by deriving the conservation equations

for each phase. The Euler-Euler approach presents three models of multiphase flow: volume of fluid (VOF), mixture model and Eulerian model.The Eulerian model is described and used in this work.

Using the Eulerian multiphase model, a single pressure is shared by all phases; momentum and continuity equations are solved instead for each phase. With the Eulerian multiphase model, the number of secondary phases is limited only by memory requirements and convergence behaviour. Any number of secondary phases can be modelled, provided that sufficient memory is available. For complex multiphase flows, it is possible that each solution is limited by convergence behaviour. The volume of phase q, V_q, is defined by:

$$V_q = \int_V \alpha_q dV \tag{4.4}$$

where:

$$\sum_{q=1}^{n} \alpha_q = 1. \tag{4.5}$$

The continuity equation for phase q is:

$$\frac{\partial \left(\alpha_q \rho_q\right)}{\partial t} + \nabla \cdot \left(\alpha_q \rho_q \boldsymbol{u}_q\right) = \sum_{p=1}^{n} \left(\dot{m}_{pq} - \dot{m}_{qp}\right) \tag{4.6}$$

where $\boldsymbol{u}_q$ is the velocity of phase q and $\dot{m}_{pq}$ characterizes the mass transfer from the phase p to the phase q.

The momentum balance for phase q is:

$$\frac{\partial \left(\alpha_q \rho_q \boldsymbol{u}_q\right)}{\partial t} + \nabla \cdot \left(\alpha_q \rho_q \boldsymbol{u}_q \boldsymbol{u}_q\right) =$$

$$= -\alpha_q \nabla p + \nabla \cdot \left(\alpha_q \boldsymbol{\tau}_q\right) + \alpha_q \rho_q \boldsymbol{g} + \sum_{p=1}^{n} \left(\dot{m}_{pq} \boldsymbol{u}_{pq} - \dot{m}_{qp} \boldsymbol{u}_{qp}\right) + \boldsymbol{F} \tag{4.7}$$

where $\boldsymbol{\tau}_q$ is stress-strain tensor for the phase q.

If phase p mass is transferred to phase q ($\dot{m}_{pq} > 0$), $\boldsymbol{u}_{pq} = u_p$; if phase q mass is transferred to phase p (i.e. $\dot{m}_{pq} < 0$), $\boldsymbol{u}_{pq} = \boldsymbol{u}_q$. If $\dot{m}_{qp} > 0$ then $\boldsymbol{u}_{qp} = \boldsymbol{u}_q$, if $\dot{m}_{qp} < 0$ then $\boldsymbol{u}_{qp} = \boldsymbol{u}_p$.

$\boldsymbol{F}$ contains the interfacial forces involved, that are detailed in section 4.2.2.

4.2.2 Interfacial forces

Dispersed gas-liquid systems are generally dominated by interfacial forces (Tabib et al. 2008) and the drag force is the most important one for bubble column reactors. In this work, several drag laws and swarm factors are tested.

The lift force is normally considered minor and it can be important for sheared flows. When velocity gradients are present in the primary fluid field, the dispersed phase is affected by a pushing force oriented perpendicular to the flow direction. It is necessary to consider this phenomenon when the flow of the continuous phase is not uniform. Including lift force in CFD simulations of bubble columns under the heterogeneous regime is still an open question. It has been found by some

authors that the lift force can be very helpful when two-dimensional simulations are performed (Joshi 2001). Lift force can be important in a wall-peaked gas volume fraction distribution linked to a boiling flow, due to the presence of shear flows, as suggested by Sugrue (2017). On the other hand, McClure et al. (2013) found lift force effect as being negligible under the heterogeneous regime for three-dimensional simulations. Finally, as the expression of the lift force coefficient at high gas fraction is still debated, and as acceptable results are obtained without including it, the lift force has not been considered in the present study. This is done also with the objective to simplify as much as possible the final CFD model obtained from the present work.

The virtual mass is generated mainly by the relative acceleration between the two phases. The virtual mass effect is due to the inertia of the liquid phase mass, which exerts a virtual force on the bubbles that accelerate relative to the liquid phase. The virtual mass is quite important when the density of the continuous phase is much bigger than the density of the dispersed phase. The virtual mass has not been considered in the present work in order to simplify the final CFD model as much as possible.

In bubble column reactors, bubbles are concentrated near the walls, not in direct contact with them: this phenomenon can be explained by adding the wall lubrication force, that acts in the direction normal to the wall. Wall lubrication force has been ignored for reasons similar to the previous forces.

The dispersion force is obtained by averaging over time the instantaneous drag. The previous hypothesis leads to two terms: the first one is the drag force and represents the mean momentum exchange between the fluids; the second term is the turbulent dispersion force, depends on the drift velocity and permits to consider the dispersion of the secondary phases caused by turbulent fluid motion transport. Secondary interfacial forces could be considered in CFD simulations but the final CFD simulations would be more complex, unstable and time-consuming.

4.2.2.1 Drag law correlations

The drag force is the most important force of interaction between the two phases. During rising motion, the bubble is accelerated by buoyancy and decelerated by pressure effects and the friction between the surface of the bubble and the surrounding fluid. In the bubble columns, the drag force is opposed to the buoyancy force during the ascensions of the bubbles if they go upwards vertically. The drag law must be studied in detail: it influences the relative velocity of the bubbles and then the gas volume fraction in the bubble column.

The drag force for the phase q can be calculated as:

$$F_{D,q} = \sum_{h=1}^{n} K_{jq}(\boldsymbol{u}_h - \boldsymbol{u}_q) \tag{4.8}$$

where the index h is for the generic phase different from q. Only two phases are present in simple bubble columns, e.g. continuous liquid and dispersed bubbles of gas. Consequently, for these systems the expression can be simplified on:

$$F_{D,q} = K_{pq}(\boldsymbol{u}_p - \boldsymbol{u}_q). \tag{4.9}$$

p is the dispersed phase and q is the continuous one.

$$K_{pq} = \frac{C_D \, Re_b \, A_i \, \mu_q}{8 \, d_p}. \tag{4.10}$$

A_i is the interfacial area between phases per unit mixture volume. The bubble Reynolds number (Re_b) is defined with respect to the relative velocity between bubble and surrounding liquid:

$$Re_b = \frac{\rho_q (\boldsymbol{u}_p - \boldsymbol{u}_q) d_p}{\mu_q}. \tag{4.11}$$

Literature reports several drag correlations for different operating conditions. It is possible to find correlations for spherical and deformed bubbles and drag laws that consider the effect of the contamination of the water.

Grace et al. (1976) and Ishii & Zuber (1979) proposed drag laws suitable for deformed bubbles. For deformed bubbles, the drag force coefficient depends on Reynolds, Eötvös and Morton numbers. Alternatively, some authors use the Froude number or the Weber number, that can be written as a function of Reynolds, Eötvös and Morton numbers.

Tomiyama (1998) proposed one of the most common drag laws:

$$C_D^{\infty} = \max \left\{ \min \left\{ \frac{24}{Re_b} \left(1 + 0.15 Re_b^{0.687}\right), \frac{72}{Re_b} \right\}, \frac{8}{3} \frac{Eo}{(4 + Eo)} \right\}, \tag{4.12}$$

where C_D^{∞} is the drag coefficient for an isolated bubble.

This drag law is suitable for both spherical and ellipsoidal bubbles, in the case of slightly contaminated air-water systems. Similar expressions are valid for other water qualities (pure and fully contaminated systems).

A more compact drag law gives similar results (Zhang et al. 2006) in the studied range:

$$C_D^{\infty} = \frac{2}{3} \sqrt{Eo}. \tag{4.13}$$

Using this drag law, the terminal bubble velocity does not depend on the bubble diameter in the diameter range from 5 to 8 mm. The drag law proposed by Tomiyama (1998) has a larger range of validity and it has the advantage that considers water contamination effects. The drag law proposed by Tomiyama (1998) is chosen for this work. More details and a comprehensive collection of drag laws for both spherical and oblate bubbles are reported in Annex B.

4.2.2.2 Swarm factor

The drag laws described above are studied for isolated bubbles and they are only suitable in the case of low gas volume fractions. This work is focused on bubble columns with high gas volume fractions: a correction term, called swarm factor h, is required:

$$h = \frac{C_D}{{C_D}^{\infty}} = \left(\frac{{u_r}^{\infty}}{u_r} \right)^2, \tag{4.14}$$

where C_D is the real drag force that acts on a bubble in the actual operating conditions.

The first swarm factors have the following form:

$$h = \frac{1}{1 - {\alpha_g}^{2n}} \tag{4.15}$$

where n is 1.39 for Bridge et al. (1964) or 1 for Wallis (1969).

Ishii & Zuber (1979) coined another swarm factor:

$$h = \frac{1}{\sqrt{\alpha_l}} = \frac{1}{\sqrt{1 - \alpha_g}}. \tag{4.16}$$

Rusche & Issa (2000) provided a factor available for oblate bubbles, $\alpha_g < 45\%$ and $27 \leq Re_b \leq 960$:

$$h = e^{3.64\,\alpha_g} + {\alpha_g}^{0.4864}. \tag{4.17}$$

Roghair et al. (2011) studied a swarm factor that can be used also in the case of high Reynolds number, for oblate bubbles with $\alpha_g < 45\%$, $150 \leq Re_b \leq 1200$, $1 \leq Eo \leq 5$ and $4 * 10^{-12} \leq Mo \leq 2 * 10^{-9}$:

$$h = \left(1 + \frac{18\,\alpha_g}{Eo}\right)(1 - \alpha_g) \tag{4.18}$$

The proposed swarm factors hinder the rise of the bubbles, increasing the effect of the drag force for high gas volume fractions. The swarm factors are higher than one at low gas volume fractions. Some of these are reported in Fig. 4.2.

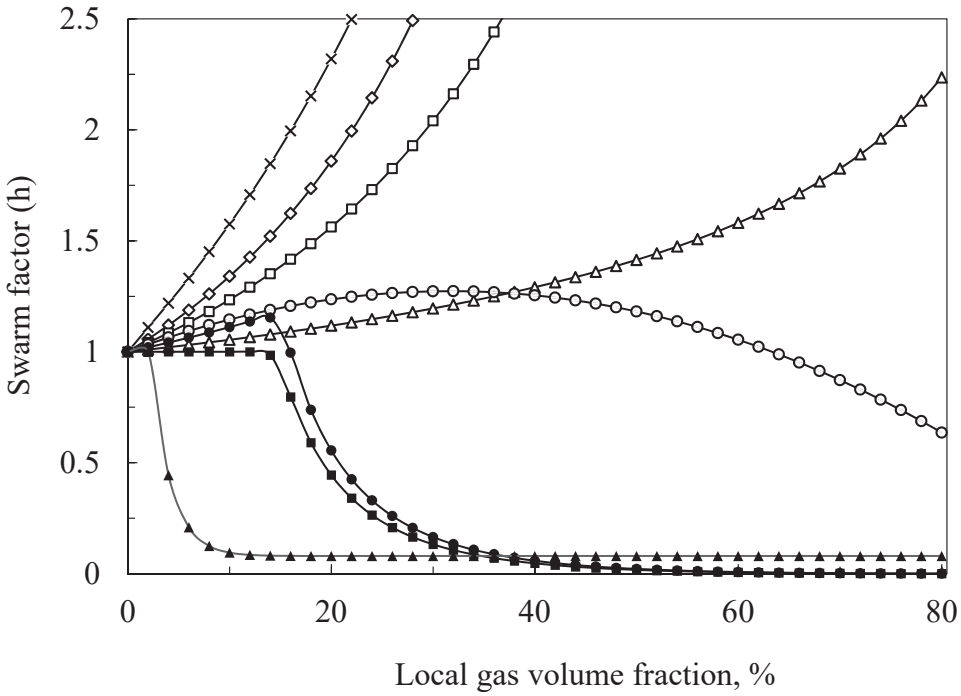

Figure 4.2: Swarm factors in function of the gas volume fraction: Bridge et al. (1964) (◇), Wallis (1969) (□), Ishii & Zuber (1979) (△), Rusche & Issa (2000) (×), Simonnet et al. (2008) (●), Roghair et al. (2011) (○), McClure et al. (2014) (■) and McClure et al. (2017b) (▲).

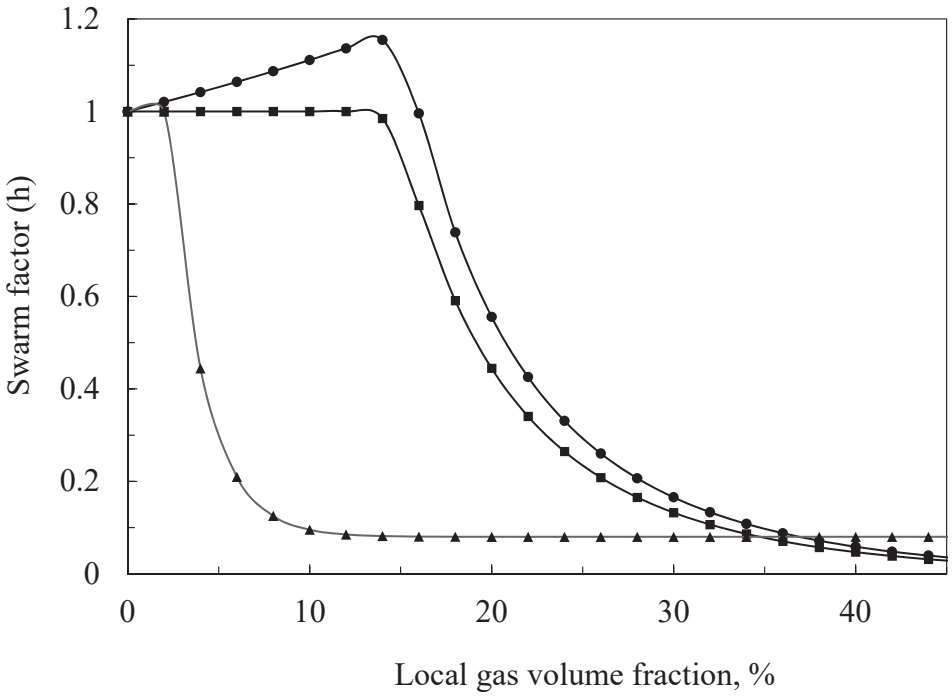

Figure 4.3: Swarm factors that decrease the effect of the drag force in function of the gas volume fraction: Simonnet et al. (2008) (●), McClure et al. (2014) (■) and McClure et al. (2017b) (▲).

Simonnet et al. (2008) propose a swarm factor that considers the existence of a critical value of gas volume fraction of 15%, above which this swarm factor decreases. This empirical expression is completely different from the previous ones. The authors state that this swarm factor has been validated for a gas volume fraction lower than 30%. This swarm factor is shown in Fig. 4.2 and in Fig. 4.3, that focuses on the swarm factors that decrease the effect of the drag force in function for high gas volume fractions.

$$h = (1-\alpha_g)\left[(1-\alpha_g)^{25} + \left(4.8\frac{\alpha_g}{1-\alpha_g}\right)^{25}\right]^{-\frac{2}{25}}. \tag{4.19}$$

McClure et al. (2014)) suggest a modified form of the swarm factor proposed by Simonnet et al. (2008):

$$h = \begin{cases} \min\left(h',\, 1.0\right) & \text{for} \quad h' > 1.0 \\ \\ 0.8h' & \text{for} \quad h' < 1.0 \end{cases} \tag{4.20}$$

where h' is the original swarm factor proposed by Simonnet et al. (2008).

McClure et al. (2017b) propose an empirical term suitable for gas volume fractions higher than 25%:

$$h = \min\left((1-\alpha_g)^n + b, 1\right), \tag{4.21}$$

where n and b are empirical constants, obtained with a least-squares fit of their data. The suggested value for n is 50, while b is linked to the sparger design.

Most of these swarm factors have been studied for air-water systems and they need to be validated for applications in other systems.

4.2.3 Modelling of turbulence

Turbulence has a main role in coalescence and break-up of bubbles and it enhances heat and mass transfer rates: turbulence consequently becomes one of the key elements in CFD simulations. Different existing turbulence models, already installed in ANSYS Fluent, are tested in this work: standard k-ε, realizable k-ε, RNG k-ε and k-ω models. The objective is to try to justify which one provides the best results and which one is the more stable, without modifying them.

Navier-Stokes equations can describe also turbulent flows: a way to simulate turbulent flows could be resolving directly this equation without turbulence models. This approach is called direct numerical simulation (DNS): due to the huge computational resources required, it cannot be used in engineering applications.

Another method could be to model only the smallest scales of turbulence, that are encountered where the flow is mainly viscous, e.g. near a wall, with a sub-grid stress model, and to resolve momentum equation only for the main flow where largest eddies are in. This approach is called large-eddy simulation (LES) and allows using coarser meshes than DNS. Intermediate-to-large turbulence is hard to model in a universal way due to anisotropy. The smallest turbulence can be easily modelled since are closer to isotropy, following the theory of Kolmogorov, that suggests that the smallest length scales are given by the Kolmogorov scale:

$$\eta = \left(\frac{\nu^3}{\varepsilon}\right)^{1/4} \tag{4.22}$$

where ν is the kinematic viscosity and ε is the turbulence dissipation rate.

The most common way to compute turbulence is averaging over time the Navier-Stokes equations by Reynolds decomposition. The concept is to split instantaneous variables into a mean time independent part and a fluctuating part. Time averaging over a reasonable time allows describing separately fluctuations and non-turbulence quantities. Applying the Reynolds decomposition to both pressure and velocity, in continuity and momentum equations, they become respectively

$$\frac{\partial\left(\alpha_q\rho_q\right)}{\partial t} + \nabla\cdot\left(\alpha_q\rho_q\langle\boldsymbol{u}_q\rangle\right) + \nabla\cdot\left(\alpha_q\rho_q\boldsymbol{u}_q'\right) = 0; \tag{4.23}$$

$$\begin{aligned}\frac{\partial\left(\alpha_q\rho_q\langle\boldsymbol{u}_q\rangle\right)}{\partial t} + \frac{\partial\left(\alpha_q\rho_q\boldsymbol{u}_q'\right)}{\partial t} + \nabla\cdot\left(\alpha_q\rho_q\left(\langle\boldsymbol{u}_q\rangle + \boldsymbol{u}_q'\right)\left(\langle\boldsymbol{u}_q\rangle + \boldsymbol{u}_q'\right)\right) + \\ \alpha_q\left(\nabla\langle p\rangle + \nabla p'\right) = \alpha_q\mu_q\left(\nabla^2\langle\boldsymbol{u}_q\rangle + \nabla^2\boldsymbol{u}_q'\right) + \alpha_q\rho_q\boldsymbol{g}_q + \boldsymbol{F}.\end{aligned} \tag{4.24}$$

where the strain-stress tensor was expressed for a Newtonian fluid.

Averaging these equations with respect to time, a new set of PDE can be obtained. This set, known as *Reynolds-averaged Navier-Stokes* (RANS), presents the following equations if the mass transfer is neglected:

$$\frac{\partial\left(\alpha_q\rho_q\right)}{\partial t} + \nabla\cdot\left(\alpha_q\rho_q\langle\boldsymbol{u}_q\rangle\right) = 0; \tag{4.25}$$

$$\begin{aligned}\frac{\partial\left(\alpha_q\rho_q\langle\boldsymbol{u}_q\rangle\right)}{\partial t} + \nabla\cdot\left(\alpha_q\rho_q\left(\langle\boldsymbol{u}_q\rangle\langle\boldsymbol{u}_q\rangle\right)\right) + \alpha_q\nabla\langle p\rangle = \\ = \alpha_q\mu_q\left(\nabla^2\langle\boldsymbol{u}_q\rangle\right) + \alpha_q\rho_q\boldsymbol{g}_q - \nabla\cdot\left(\alpha_q\rho_q\langle\boldsymbol{u}_q'\boldsymbol{u}_q'\rangle\right) + \boldsymbol{F}.\end{aligned} \tag{4.26}$$

The averaging adds a new term:

$$\boldsymbol{\tau}_q'' = \rho_q \langle \boldsymbol{u}_q' \boldsymbol{u}_q' \rangle. \tag{4.27}$$

It is an unknown symmetric second-order tensor, which has to be modelled in order to close the problem. Deriving a transport equation for the Reynolds stress tensor itself introduces a third-order tensor. Deriving an equation for this term would yield to an equation that contains fourth-order moments of the velocity components: this is noted as the closure problem. The Reynolds stress tensor (RST) is a symmetric matrix: this means that six components are unknown and six equations are needed to close the problem. The Boussinesq approximation (Andersson et al. 2012) considers RST proportional to the mean velocity gradients. The hypothesis of Boussinesq introduces the turbulent viscosity and it is the basis of several turbulence models:

$$\boldsymbol{\tau}_q'' = \rho_q \langle \boldsymbol{u}_q' \boldsymbol{u}_q' \rangle = -\frac{2}{3} \left(\rho_q k_q + \mu_{t,q} \nabla \cdot \langle \boldsymbol{u}_q \rangle \right) \boldsymbol{I} + \mu_{t,q} \left(\nabla \langle \boldsymbol{u}_q \rangle + \nabla \langle \boldsymbol{u}_q \rangle^T \right). \tag{4.28}$$

These models solve zero, one or two equations with the RANS equations. In this work, only two-equations models have been used and described.

Two-equations turbulence models are studied for a single-phase system, in order to extend them to multiphase systems three options exist (Buffo & Marchisio 2014):

- Dispersed turbulence model: the dominant process that causes the random motion of the secondary phase is the primary-phase turbulence. The turbulence is calculated only for the continuous liquid phase and extra terms are involved in primary-phase turbulence equations for considering the turbulence induced by the dispersed secondary-phase.

- Mixture turbulence model: it is applicable for separated phases, for stratified flows, and when the density ratio between phases is close to 1. In these cases, mixture properties and mixture velocities are used.

- Per-phase model: this model computes the turbulence for each phase separately. This model often provides good results, but the computational resources required are too big. For this reason, it is not often used in engineering applications.

These three models are implemented in ANSYS Fluent. For this work, only the dispersed model was used, since the density ratio between phases is very high, and so the following equations refer to this option.

4.2.3.1 Standard $k-\varepsilon$ model

The standard $k-\varepsilon$ model was proposed initially for single-phase flows by Launder & Spalding (1972). Two transport equations are added: the turbulence kinetic energy k and turbulence dissipation rate ε. This model is robust and economical: it assumes that the flow is completely turbulent. This is a direct consequence of the definition of ε, relating the large-scale quantity l to the small-scale quantity ε: when the flow is fully turbulent, the rate at which the largest eddies extract energy from the mean flow is paired with the rate at which energy goes from larger to smaller eddies (Versteeg & Malalasekera 2007).

For $k-\varepsilon$ models, the turbulent viscosity is defined as:

$$\mu_t = \rho C_{\mu t} k^2 \varepsilon^{-1}. \tag{4.29}$$

For multiphase flows, if the dispersed turbulence model is adopted, the turbulence kinetic energy equation is

$$\frac{\partial\left(\alpha_q \rho_q k_q\right)}{\partial t} + \nabla \cdot \left(\alpha_q \rho_q k_q \langle \boldsymbol{u}_q \rangle\right) = \nabla \cdot \left[\alpha_q \left(\mu_q + \frac{\mu_{t,q}}{\sigma_k}\right) \nabla k_q\right] + \\ + \alpha_q \left(G_{k,q} + G_{b,q} - \rho_q \varepsilon_q\right) + \alpha_q \rho_q S_{k,q} \tag{4.30}$$

while the turbulence dissipation rate equation is

$$\frac{\partial\left(\alpha_q \rho_q \varepsilon_q\right)}{\partial t} + \nabla \cdot \left(\alpha_q \rho_q \varepsilon_q \langle \boldsymbol{u}_q \rangle\right) = \nabla \cdot \left[\alpha_q \left(\mu_q + \frac{\mu_{t,q}}{\sigma_\varepsilon}\right) \nabla \varepsilon_q\right] + \\ + \alpha_q \frac{\varepsilon_q}{k_q} \left(C_{1\varepsilon} G_{k,q} + C_{1\varepsilon} C_{3\varepsilon} G_{b,q} - C_{2\varepsilon} \rho_q \varepsilon_q\right) + \alpha_q \rho_q S_{\varepsilon,q} \tag{4.31}$$

where $G_{k,q}$ is the generation term of the kinetic energy due to gradients of mean velocity and $G_{b,q}$ is the generation term of the kinetic energy due to buoyancy. $G_{b,q}$ is equal to zero as it is not null when a non-zero gravity field and temperature gradient are present simultaneously, while, in this case, the temperature gradient is zero and the dispersed phase density is constant; consequently $c_{3\varepsilon}$ does not need to be defined. $C_{1\varepsilon}$ and $C_{2\varepsilon}$ are constants. σ_k and σ_ε are the turbulent Prandtl numbers. $S_{k,q}$ and $S_{\varepsilon,q}$ are user-defined production terms of k and ε respectively.

$$\begin{aligned} c_{1\varepsilon} &= 1.44; \\ c_{2\varepsilon} &= 1.92; \\ c_{\mu_t} &= 0.09; \\ \sigma_k &= 1.00; \\ \sigma_\varepsilon &= 1.30. \end{aligned}$$

These values allow having a good compromise between performance and accuracy for different kind of flows and these values can be modified for a particular system.

This model is widely used due to its robustness and the ease of interpretation of terms. Best results are obtained in flows where an isotropic turbulence is presented, characterized with high Reynolds number, but some problems are present with swirling flows: flows involving curvature and regions with low Reynolds number. Literature reports several modifications of the standard model: RNG $k-\varepsilon$ and realizable$k-\varepsilon$ models are the most important variants.

4.2.3.2 RNG $k-\varepsilon$ model

The RNG model was initially developed from instantaneous Navier-Stokes equations, by using the Re-normalization group theory (Yakhot & Orszag 1986). This model allows obtaining better results with simulations in low-Re region and when the flow changes direction suddenly.

The main difference with the standard model is the presence of an extra production term in the equation of ε contained in the term $C^*_{2\varepsilon}$. A different way to

model the turbulent viscosity is applied in order to consider zones where the flow is not fully turbulent. This model is more responsive to the effects of rapid strain and streamline curvature than the standard one.

$$\frac{\partial\left(\alpha_q\rho_q k_q\right)}{\partial t}+\nabla\cdot\left(\alpha_q\rho_q k_q\langle\boldsymbol{u}_q\rangle\right)=\nabla\cdot\left[\alpha_q\left(\mu_q+\frac{\mu_{t,q}}{\sigma_k}\right)\nabla k_q\right]+$$

$$+\alpha_q\left(G_{k,q}+G_{b,q}-\rho_q\varepsilon_q\right)+\alpha_q\rho_q S_{k,q} \tag{4.32}$$

$$\frac{\partial\left(\alpha_q\rho_q\varepsilon_q\right)}{\partial t}+\nabla\cdot\left(\alpha_q\rho_q\varepsilon_q\langle\boldsymbol{u}_q\rangle\right)=\nabla\cdot\left[\alpha_q\left(\mu_q+\frac{\mu_{t,q}}{\sigma_\varepsilon}\right)\nabla\varepsilon_q\right]+$$

$$+\alpha_q\frac{\varepsilon_q}{k_q}\left(C_{1\varepsilon}G_{k,q}+C_{1\varepsilon}C_{3\varepsilon}G_{b,q}-C^*_{2\varepsilon}\rho_q\varepsilon_q\right)+\alpha_q\rho_q S_{\varepsilon,q}, \tag{4.33}$$

where

$$C^*_{2\varepsilon}=C_{2\varepsilon}+\frac{C_\mu\delta^3(1-\delta\delta_0)}{1+\beta\delta^3}, \tag{4.34}$$

$$\delta=\frac{k}{\varepsilon}S, \tag{4.35}$$

$$S=\left(2\langle\boldsymbol{S}\rangle\langle\boldsymbol{S}\rangle\right)^{1/2}, \tag{4.36}$$

where $\langle\boldsymbol{S}\rangle$ is the mean strain rate tensor and $G_{b,q}$ is null, as detailed above.

Model constants are calculated analytically by the Re-normalization group theory, obtaining

$$\begin{aligned}c_{1\varepsilon}&=1.42;\\ c_{2\varepsilon}&=1.68;\\ c_{\mu_t}&=0.0845;\\ \sigma_k&=1.00;\\ \sigma_\varepsilon&=1.393;\\ \delta_0&=4.38;\\ \beta&=0.012.\end{aligned}$$

4.2.3.3 Realizable $k-\varepsilon$ model

Realizable $k-\varepsilon$ model is used when both standard and RNG models are not realizable, i.e. Reynolds stress tensor does not satisfy some mathematical constraints, and it is consistent with the turbulent flow physics. Proposed by Shih et al. (1995), this model uses an equation for the dissipation rate based on the transport equation of the mean square vorticity fluctuation and an alternative formulation for the eddy viscosity.

The turbulence kinetic energy equation is identical to the standard $k-\varepsilon$ model, while the turbulence dissipation rate equation is

$$\frac{\partial\left(\alpha_q\rho_q\varepsilon_q\right)}{\partial t}+\nabla\cdot\left(\alpha_q\rho_q\varepsilon_q\langle\boldsymbol{u}_q\rangle\right)=\nabla\cdot\left[\alpha_q\left(\mu_q+\frac{\mu_{t,q}}{\sigma_\varepsilon}\right)\nabla\varepsilon_q\right]+$$

$$+\alpha_q\varepsilon_q\left(C_1\rho_q S+C_{1\varepsilon}C_{3\varepsilon}\frac{G_{b,q}}{k_q}-C_2\rho_q\frac{\varepsilon_q}{k_q+\sqrt{\nu_q\varepsilon_q}}\right)+\alpha_q\rho_q S_{\varepsilon,q} \tag{4.37}$$

where

$$C_1 = \max\left(0.43, \frac{\eta}{\eta+5}\right), \tag{4.38}$$

$$\eta = S\frac{k_q}{\varepsilon_q}, \tag{4.39}$$

$$S = (2\langle \boldsymbol{S}\rangle\langle \boldsymbol{S}\rangle)^{1/2}; \tag{4.40}$$

$G_{b,q}$ is null, as detailed above. Model constants are calculated to ensure good performance for canonical flows:

$$\begin{aligned} c_{1\varepsilon} &= 1.44; \\ c_2 &= 1.90; \\ \sigma_k &= 1.00; \\ \sigma_\varepsilon &= 1.20. \end{aligned}$$

This model is used for flows that present a large strain rate, i.e. flows with rotation and strong curvature. For swirling flows and flow separation, this model performs better than the standard one. The main issues are that it is less stable and the computational resources required are bigger (Cappello 2016).

4.2.3.4 $k-\omega$ model

The standard $k-\omega$ model is an empirical model based on the model of Wilcox (1998) that reports a specific dissipation ω, the frequency of the turbulence, is the quantity used for describing the length-scale of turbulence:

$$\omega_q = \frac{\varepsilon_q}{k_q}. \tag{4.41}$$

Two equations are solved:

$$\frac{\partial\left(\alpha_q\rho_q k_q\right)}{\partial t} + \nabla\cdot\left(\alpha_q\rho_q k_q\langle \boldsymbol{u}_q\rangle\right) = \nabla\cdot\left(\alpha_q\mu_{eff,k,q}\nabla k_q\right) + \alpha_q G_{k,q} + \alpha_q\rho_q S_{k,q} \tag{4.42}$$

$$\frac{\partial\left(\alpha_q\rho_q \omega_q\right)}{\partial t} + \nabla\cdot\left(\alpha_q\rho_q \omega_q\langle \boldsymbol{u}_q\rangle\right) = \nabla\cdot\left(\alpha_q\mu_{eff,\omega,q}\nabla \omega_q\right) + \alpha_q G_{\omega,q} + \alpha_q\rho_q S_{\omega,q} \tag{4.43}$$

where $G_{k,q}$ and $G_{\omega,q}$ represent respectively the generation of k and ω. $\mu_{eff,k,q}$ and $\mu_{eff,\omega,q}$ represent the effective diffusivity of turbulence kinetic energy and specific dissipation rate. $S_{k,q}$ and $S_{\omega,q}$ are user-defined source terms.

$$\mu_{eff,k,q} = \mu_q + \frac{\mu_{t,q}}{\sigma_k} \tag{4.44}$$

$$\mu_{eff,\omega,q} = \mu_q + \frac{\mu_{t,q}}{\sigma_\omega} \tag{4.45}$$

$\sigma_{k,q}$ and σ_ω are the turbulent Prandtl numbers both equal to 2. The turbulent viscosity depends on k and ω.

This model provides a better performance for low Reynolds number, adverse pressure gradients and wall-bounded boundary layer flows; wall functions are not required. A finer mesh near the wall is however necessary.

4.2.3.5 Turbulence due to energy transfer from gas to liquid

As detailed by Joshi (2001), for a single bubble that rises in liquid the pressure energy is transformed into potential energy. In a laminar flow, the gas energy is transformed into internal energy. In a turbulent flow, the gas energy is converted into turbulence in the liquid phase and finally into internal energy. The fraction of gas energy that generates turbulence depends on the operating conditions.

In a bubble column, the axial bubble velocity depends on the radial position, due to the liquid recirculation. In the central region of the column, the gas velocity is higher than the slip velocity, as the axial liquid velocity is positive. The energy released depends on the gas velocity, while the energy converted into turbulence and used for viscous dissipation depends on the slip velocity, as detailed by Joshi (2001). In the central region of the column, the energy released is higher than the dissipation. Near the wall, in contrast, the energy of the liquid phase is transferred to the gas phase.

Yao & Morel (2004) stated that the turbulence due to energy transfer from gas to liquid can be considered by adding source terms in the turbulence properties transport equations (in k and ε or ω equations). The additional turbulence due to energy transfer between the phases can be considered by adding the contribution of the drag force, that is the main interfacial force for bubble columns under the heterogeneous regime. In the case of $k-\varepsilon$ models, the source terms are:

$$S_{k,q} = K_{pq}\left(u_p - u_q\right)^2 \tag{4.46}$$

and

$$S_{\varepsilon,q} = \frac{1}{\tau_p} S_{k,q} \tag{4.47}$$

where K_{pq} has been defined in Eq. (4.10) and

$$\tau_p = \left(\frac{{d_p}^2}{\varepsilon}\right)^{1/3}. \tag{4.48}$$

Troshko & Hassan (2001) used a similar approach, but they stated that only a fraction of the energy due to the drag force is transferred to the liquid-phase turbulence. The turbulence source terms are:

$$S_{k,q} = C_{S_{k,q}} \alpha_q K_{pq}\left(u_p - u_q\right)^2 \tag{4.49}$$

and

$$S_{\varepsilon,q} = \frac{C_{S_{\varepsilon,q}}}{\tau_p'} S_{k,q} \tag{4.50}$$

where $C_{S_{k,q}}$ and $C_{S_{\varepsilon,q}}$ are user-modifiable constants. Troshko & Hassan (2001) proposed to consider these constant equal to 0.75 and 0.45 respectively.

$$\tau_p' = \frac{2 C_{VM} d_p}{3 C_D \left|u_p - u_q\right|}. \tag{4.51}$$

where C_{VM} is the virtual mass coefficient (equal to 0.5) and C_D is the drag coefficient.

A similar expression has been proposed by Simonin & Viollet (1990):

$$S_{k,q} = C_S \frac{K_{pq}}{\alpha_q \rho_q} \frac{\rho_p}{\rho_p + C_{VM}\rho_q} \left[k_{pq} - 2k_q + (\mathbf{u}_p - \mathbf{u}_q) \cdot u_{drift}\right] \tag{4.52}$$

where C_S is a constant equal to 1, k_{pq} is the covariance of the phase velocities and u_{drift} is the drift velocity. More details are presented in Simonin & Viollet (1990) and in the ANSYS Fluent Theory Guide.

The turbulence dissipation rate source term is calculated according to Elghobashi & Abou-Arab (1983):

$$S_{\varepsilon,q} = 1.2 \frac{\varepsilon_q}{k_q} S_{k,q}. \tag{4.53}$$

Sato & Sekoguchi (1975) proposed a different approach: instead of adding source terms in turbulence equations, the viscosity for the continuous phase is modified:

$$\nu_q = C_\mu \frac{k_q^2}{\varepsilon_q} + 0.6 \alpha_p d_p \left|u_p - u_q\right| \tag{4.54}$$

where C_μ is the turbulent viscosity constant.

In the case of turbulent flows, many authors stated that only a fraction of the energy due to the drag force is transformed into liquid-phase turbulence, as proposed by Troshko & Hassan (2001). Kataoka et al. (1992), Hillmer et al. (1994) and Ranade (1997) stated that the additional turbulence due to the bubble energy is compensated by the additional dissipation due to the small-scale interfacial structures. They suggested to consider $C_{S_{k,q}}$ equal to zero. Other authors used very low values for $C_{S_{k,q}}$. The model of Yao & Morel (2004) is the extreme case, where the entire gas-phase energy is converted into liquid-phase turbulence. All other models have a lower effect. Considering that this contribution is far from being well-understood under the heterogeneous flow regime, these source terms have been neglected in this chapter. This assumption has been however checked, comparing CFD results to experiments.

4.2.4 Mixing time

Mixing is a continuous process. The mixing time is defined for a predefined level of homogeneity: a deviation of 5% from the final concentration is used in this work. The normalized concentration is defined as the ratio $C(t)/C^\infty$. It does not depend on the volume used for the introduction of the scalar. A User Defined Scalar (UDS) transport equation is used to simulate the mixing of a scalar quantity. The source term of the scalar is null. The diffusion coefficient is the sum of molecular ($D_{m,q}$) and turbulent ($D_{t,q}$) diffusivities.

The turbulent diffusivity is classically linked to the turbulent viscosity through the dimensionless turbulent Schmidt number (Sc_t), that varies from 0.7 to 1 (Combest et al. 2011). An empirical approach could consider a greater global turbulent diffusion by using a lower Schmidt-turbulent number. In this work, a constant turbulent Schmidt number equal to 0.7 is used in every simulation, as suggested by Radl & Khinast (2010). Contributions of SIT and bubbles are considered. The diffusive model of Alméras et al. (2016) considers bubble contribution as a regular diffusion phenomenon, so an extra diffusivity (D_+) is added. This diffusion coefficient is anisotropic: the axial diffusivity is twice the radial diffusivity, due to the velocity

fluctuations. This model is based on the experimental analysis of the mixing of a low-diffusive scalar. The diffusive model of Alméras et al. (2016) is adopted in this work.

$$D_t = \frac{\mu_t}{\rho_l Sc_t} + D_+, \tag{4.55}$$

where μ_t is the turbulent viscosity.

Alméras et al. (2016) define the extra diffusivity due to the bubbles as:

$$D_+ = \begin{cases} D_{i,0}\alpha_g^{0.5} & \alpha_g \leq \alpha_{gc,i} \\ \\ \beta\gamma_i^2 U_R\, d & \alpha_g > \alpha_{gc,i} \end{cases} \tag{4.56}$$

where U_R is the relative velocity between gas and liquid (measured in m/s), d is the bubble diameter (in m). The constants are:

$$\begin{aligned} D_{x,0} &= 0.0029; \\ D_{z,0} &= 0.0045; \\ \alpha_{gc,x} &= 0.027; \\ \alpha_{gc,z} &= 0.041; \\ \beta &= 25; \\ \gamma_x &= 0.13; \\ \gamma_z &= 0.18. \end{aligned}$$

$\alpha_{gc,i}$ is a critical value that divides between low and high gas hold-up regimes. In the first case, the diffusivity depends on the gas volume fraction, in the other case no.

4.3 CFD simulations

For studying high gas volume fraction systems under the heterogeneous regime, the simulations ought to be transient and three-dimensional (3D), since the movement of the bubble plume is chaotic (Ekambara et al. 2005).

The Euler-Euler approach is adopted: the two phases are considered as interpenetrating continua. The Eulerian model solves momentum and continuity equations for each phase. Different two-equation turbulence models are tested.

4.3.1 Test cases and CFD setup

Three-dimensional CFD Eulerian-Eulerian simulations are carried out with ANSYS Fluent 18.0, in a wide range of operating conditions, as the superficial gas velocity ranges from 0.03 m/s to 0.35 m/s. Both homogeneous and heterogeneous flow regimes are studied (Fig. 4.4a).

Initially, a cylindrical column with a diameter of 0.4 m is tested; subsequently, other simulations with different column diameters are carried out: 0.15 m, 1 m and 3 m. Instantaneous properties are averaged over a sample time. The required time depends on the operating conditions and on the properties of interest. Every simulation is sampled over a period of 100 s as a precautionary measure. The initial transient hydrodynamics is neglected.

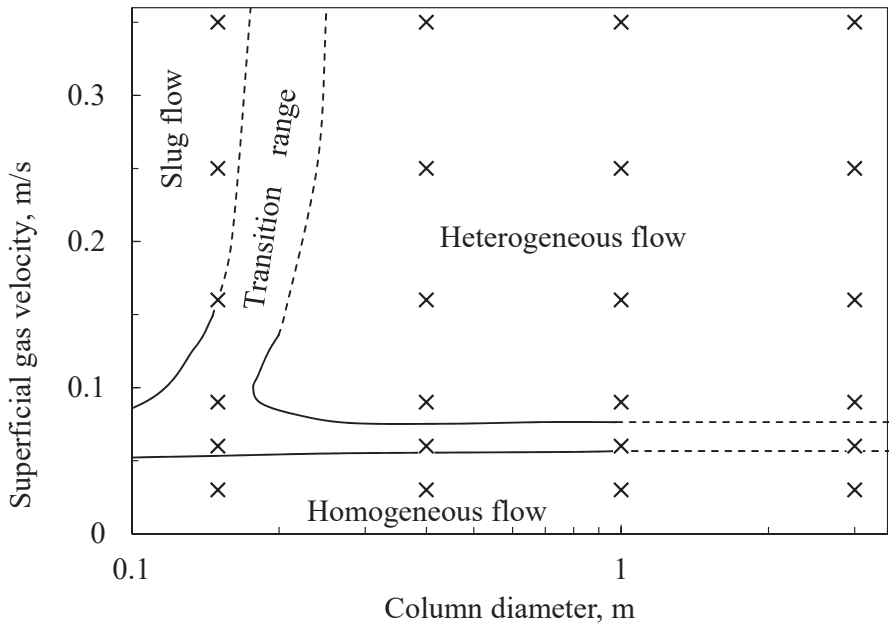

(a) *Flow regime map of Shah et al. (1982) and simulated cases (×).*

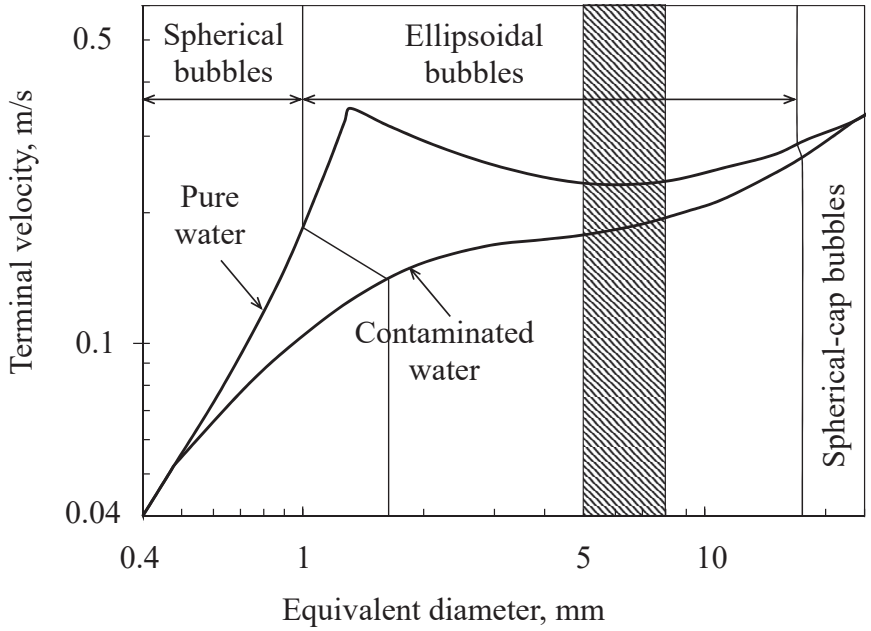

(b) *Terminal velocity diagram of Clift et al. (1978).*

Figure 4.4: Operating range of CFD simulations.

The PC-SIMPLE algorithm is used. A first-order Euler implicit temporal discretization scheme is adopted. A Green-Gauss node-based formulation is considered for the gradients calculation. The QUICK method is adopted for volume fraction and momentum. The second-order upwind method is used for the scalar. The first-order upwind is chosen for the turbulence: second-order schemes for turbulence and temporal discretization compromise severely the numerical stability. Under-relaxation factors are set equal to 0.5 for pressure, volume fraction and momentum, while they are set equal to 0.7 for turbulent equations. Maximum residual

values are imposed below 0.0001 for every equation for every simulation. Courant-Friedrichs-Lewy number (CFL) determines the first limit of the time step size: CFL ought to be lower than unity, as stated by Guédon et al. (2017). Sensitivity analysis of time discretization needs to be carried out for every operating condition and column size. The time step size is close to 0.005 s for many cases.

At this stage of the work, CFD simulations consider the bubble diameter as an input parameter. A mono-disperse approach is adopted initially: a constant bubble diameter is considered. In the previous chapter is possible to observe that the Sauter mean diameter is often between 5 mm and 9 mm. The terminal velocities are poorly affected by the bubble size in this range in the case of contaminated bubbles, has reported in Fig. 4.4b. Preliminary terminal velocity calculations based on Tomiyama (1998) and Zhang et al. (2006) drag laws are coherent with this. The averaged Sauter mean diameter is about 6.5 mm for several operating conditions. A fixed value, equal to 6.5 mm, is used in the CFD simulations of this chapter. Under the homogeneous regime, the profile is almost flat with a constant value equal to 6.5 mm. Under the heterogeneous regime, the space-averaged Sauter mean diameter is about 6.5 mm.

4.3.2 Geometry and meshes

The bubble columns studied in this work can be considered as cylinders with an initial liquid height (without gas) equal to four diameters. The total height of the column must be at least twice of the initial height of the liquid, with a view to simulating high gas volume fractions (up to 50%). The column with a diameter of 0.4 m (Fig. 4.5) has an initial height of the liquid equal to 1.6 m and a total height of 3.6 m.

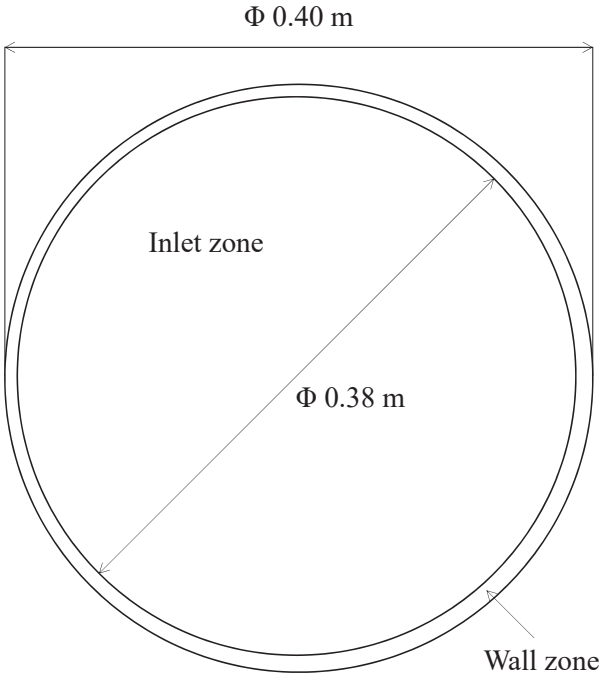

Figure 4.5: Schematic representation of the bottom of the bubble column.

As detailed in the previous chapter, experimentally the gas is injected through a sparger with 92 holes of 2 mm for the column ϕ 0.4 m. As observed in Chapter 3, using this sparger, the initial gas distribution is homogeneous: it is possible to approximate the real sparger with a homogeneous porous plate (inlet zone in Fig. 4.5). The goal of this choice is to be able to carry out industrial simulations where it is not possible to simulate the real sparger. A homogeneous sparger, where the gas enters the domain already mixed with some liquid, ensures more stable and faster CFD simulations. The best choice is to choose a fraction of gas at the gas entrance of about 50%, as stated by Li et al. (2009). In order to avoid turbulent instabilities close to the bottom, a turbulent intensity (defined as the ratio of root-mean-square of the velocity fluctuations to mean flow velocity) equal to 5% and a turbulent viscosity ratio (μ_t/μ) equal to 10 are imposed as inlet conditions. The external ring of the bottom (with a thickness of 0.01 m for the column ϕ 0.4 m) is considered as a wall (Fig. 4.5), in order to avoid convergence issues and to induce liquid recirculation. The gas outlet at the top of the column has a complete backflow of gas and it operates at atmospheric pressure. The backflow turbulent length scale and the backflow turbulent intensity are respectively equal to 0.4 m and 0.001%.

Different numerical grids are tested, starting from the column ϕ 0.4 m:

- A tetrahedral irregular mesh. It leads to completely wrong results and the column loses water (the total amount of water present in the column diminishes).
- An unstructured "cooper mesh". An unstructured quadrilateral 2D mesh is mapped at the bottom (Fig. 4.6a) and it is then extruded along the column, by using a coopering algorithm in Gambit and obtaining a hexahedral mesh. It allows obtaining acceptable results, but it requires a high computational cost.
- A structured "cooper mesh". A more regular mesh with a smaller cells number is created starting with a structured quadrilateral bottom, that is extruded by using a coopering algorithm. This mesh is reported in Fig. 4.6b.

An analysis of the sensibility of the results on the cell size is required. Different rhomboidal cooper meshes are tested, varying the cell number and size. Starting with a very fine mesh, with 500000 cells, the number of cells is diminished step by step. Until a structured rhomboidal cooper mesh with 40000 cells, the hydrodynamic results do not depend on the mesh used. Considering a mesh with less than 40000 cells, the results depend on the mesh: the accuracy required to consider the hydrodynamic phenomena is not respected, as the mesh resolution is not enough.

A structured hexahedral cooper mesh with 40000 cells (Fig. 4.6b) allows maintaining acceptable computational time and to obtain good hydrodynamic results. With this mesh, it is possible to consider the transient phenomena. Grid-independent test on the gas hold-up, by using correct drag law and swarm factor, confirms that the mesh with 40000 cells gives mesh-independent results for the column ϕ 0.4 m, as detailed in Table 4.1. This mesh gives acceptable results also for larger bubble columns, by scaling-up this mesh.

In CFD simulations, the dimensionless wall distance ($y+$) must be checked:

$$y+ = \frac{u_{fr} y}{\nu}, \tag{4.57}$$

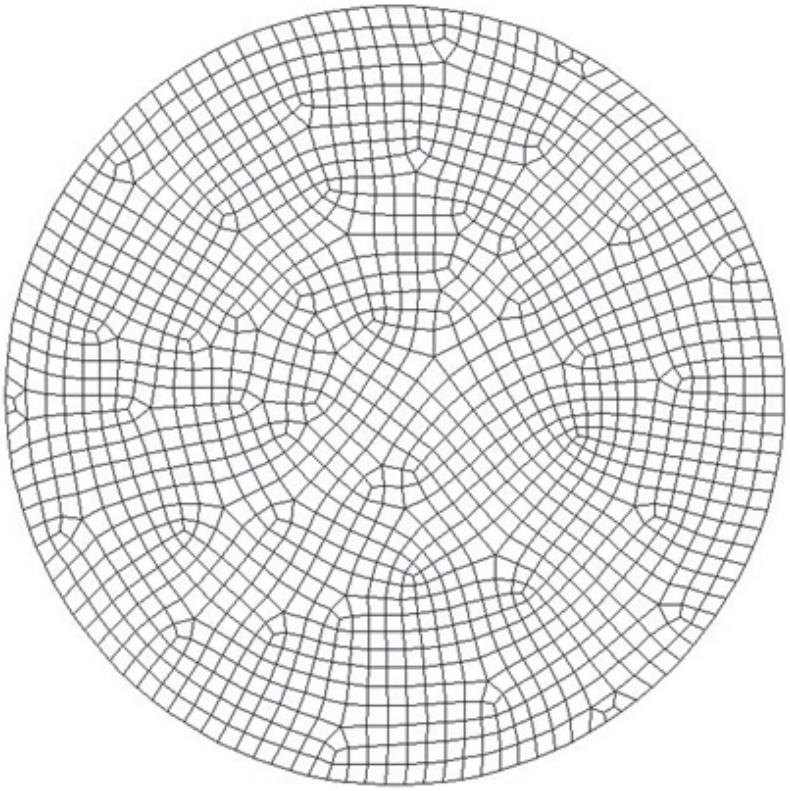

(a) *Irregular 1 cm.*

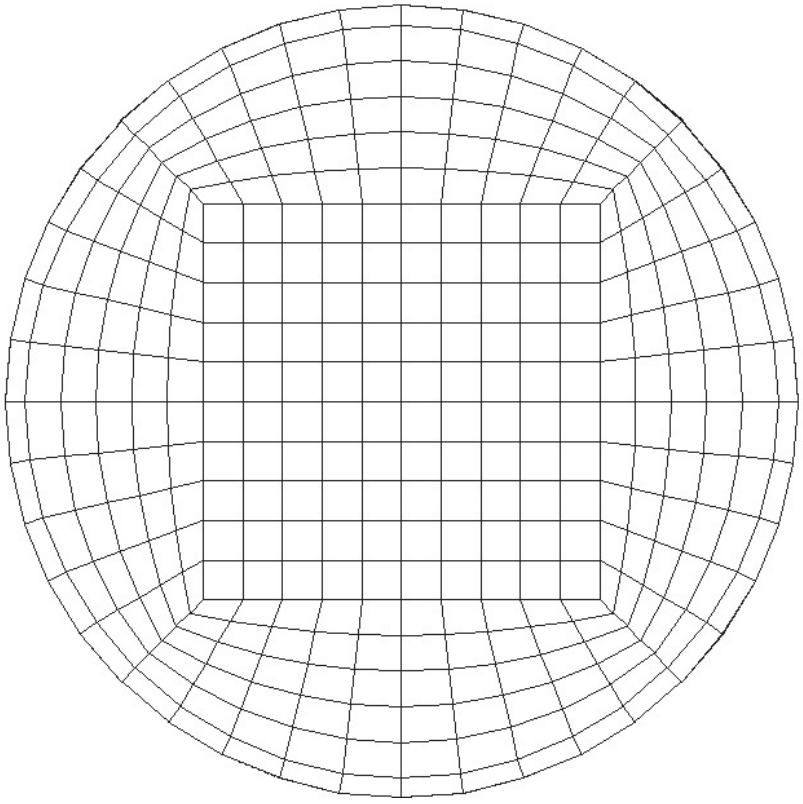

(b) *Regular 2 cm.*

Figure 4.6: Cooper meshes.

vsg, m/s	0.03	0.06	0.09	0.16	0.25	0.35
Experimental	12.8%	20.0%	20.8%	26.3%	32.2%	37.3%
500000 cells	12.5%	17.4%	19.0%	24.2%	30.1%	33.8%
150000 cells	12.4%	17.3%	19.0%	24.1%	29.8%	34.1%
40000 cells	12.6%	17.3%	18.9%	24.1%	29.6%	34.1%
10000 cells	12.1%	16.9%	22.0%	24.8%	26.8%	29.9%

Table 4.1: Grid-independent test on the gas hold-up, by using correct drag law and swarm factor, for the column ϕ 0.4 m with different structured cooper meshes.

where u_{fr} is the friction velocity at the nearest wall, y is the distance to the nearest wall and ν is the local kinematic viscosity.

It should range from 30 to 300. It affects wall shear force, pressure drop and wall lubrication force. In a large volume, $y+$ is not the most important parameter. By using the structured cooper mesh with 40,000 cells, the values of $y+$ range from 30 to 500. In this work, drag force eclipses the effects of the wall forces. Wall treatments and $y+$ can be neglected. For this reason, standard wall functions are adopted in this work.

To scale-up this bubble column, the scale-up criteria proposed by Wilkinson et al. (1992) ought to be respected, as stated by Besagni et al. (2018):

- "The diameter of the bubble column must be larger than 0.15 m".
  This criterion is satisfied for the columns ϕ 0.4 m, ϕ 1 m and ϕ 3 m. The ϕ 0.15 m column is the limit of the criterion and it could cause discrepancies.

- "The aspect ratio must be larger than 5".
  Concerning this point, the definition of the aspect ratio is important (Sasaki et al. 2016, 2017, Besagni et al. 2017). Some authors defined the aspect ratio in terms of the column height, while other authors define the aspect ratio in function of the initial liquid level. If the total height of the column is considered, the studied bubble columns have an aspect ratio that is higher than 8 and then they respect largely the criterion. If the initial liquid level is considered, the simulations are slightly below the criterion limit, as the initial liquid level is equal to 4 diameters. Under these operating conditions, Forret (2003) stated that the aspect ratio between operating liquid level (aerated height) and column diameter ought to be higher than 4. Due to the presence of high gas volume fractions in the studied systems, the operating liquid level is about 5 or 6 diameters. This criterion is respected if the actual operating liquid level is considered.

- "The holes of gas sparger larger than 1-2 mm".
  This criterion is satisfied for the three biggest columns (ϕ 0.4 m, ϕ 1 m and ϕ 3 m). These columns provide similar hydrodynamic results. The smallest column (ϕ 0.15 m) has a sparger with holes of 1 mm. This column is at the limits of the first and third criteria. For these reasons, some hydrodynamic differences could appear, compared with the other columns.

4.4 Results and discussion

4.4.1 Drag law and swarm factor

Calculations are validated by comparing CFD results with those obtained experimentally. The simulations are initially carried out on the column ϕ 0.4 m and for different superficial gas velocities with demineralised water. RNG $k-\varepsilon$ model is initially used; later other turbulence models are tested. The global gas volume fraction is the first parameter to analyse for studying the quality of drag laws and swarm factors.

The first simulations use the drag law of Schiller & Naumann (1935) for spherical bubbles (See Annex B for the complete study). At low superficial gas velocities (0.03 m/s, 0.09 m/s and 0.16 m/s) the computed global gas volume fraction is lower than the experimental one (Fig. 4.7). At higher superficial gas velocities, the

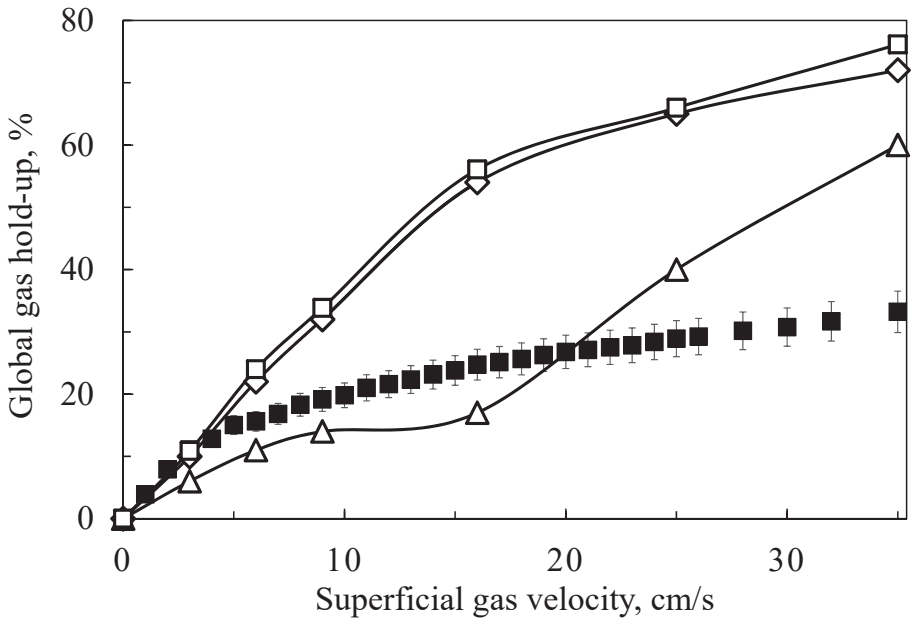

Figure 4.7: Comparison between experimental (■) and CFD gas hold-up for different superficial gas velocities in the column ϕ 0.4 m using the drag laws of Schiller & Naumann (1935) (△), Tomiyama (1998) (□) and Zhang et al. (2006) (◇) without swarm factor.

gas hold-up obtained with CFD simulations is higher than with experiments. It could mean that the drag law is too weak for low superficial gas velocities, but it is too strong for high superficial gas velocities. A drag law for oblate bubbles is then required.

The same simulations are carried out with the drag law of Tomiyama (1998), that is the most common for oblate bubbles. CFD simulations with this drag law result always in very high gas volume fractions, for any superficial gas velocity investigated, except for 0.03 m/s (Fig. 4.7). Similar results are obtained with the drag law proposed by Zhang et al. (2006) (Fig. 4.7). The inaccuracy of these models is wide, with the liquid reaching the top of the domain already for a superficial gas velocity equal to 0.16 m/s. The tendencies are however good: the global gas hold-up

is increasing with the gas velocity. It is useless to analyse the radial profile for these simulations, as the gas hold-up results are completely wrong. The drag coefficient is always too high: it is necessary to consider a swarm factor. Every simulation performed with a drag law for oblate bubbles and without swarm factors, leads to an overestimation of the gas hold-up in the case of heterogeneous regime.

The swarm factors that increase the drag force coefficient cannot be used. In the case of heterogeneous regime, the swarm factor ought to be lower than unity, in order to decrease the drag force for high gas volume fractions. The swarm factor proposed by Simonnet et al. (2008) (Equation 4.19) has this characteristic. This swarm factor is studied in this work and coupled with the drag law proposed by Tomiyama (1998). The gas hold-up predicted by implementing the swarm factor is lower than the experimental one (Fig. 4.8).

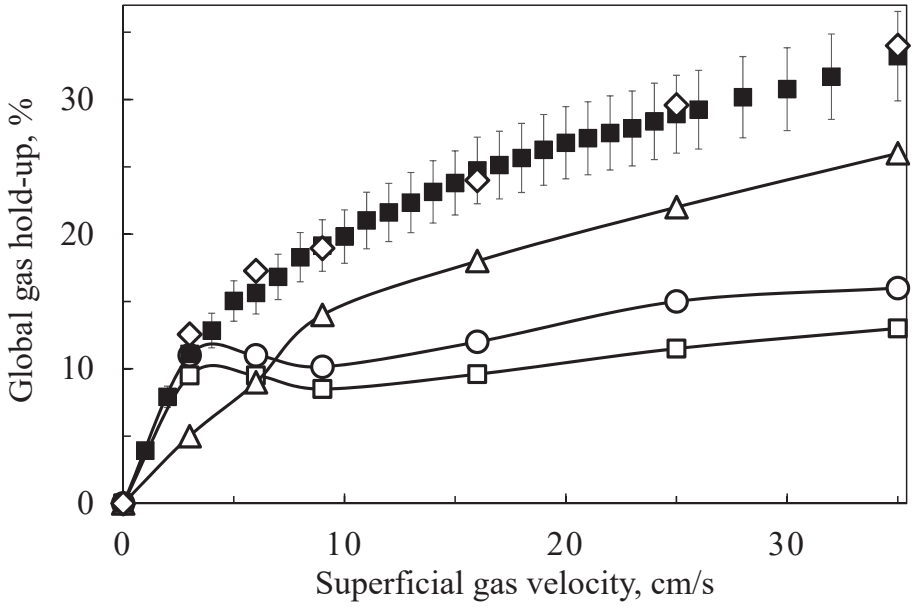

Figure 4.8: Comparison between experimental (■) and CFD gas hold-up in the column ϕ 0.4 m for different superficial gas velocities by using the drag law of Tomiyama (1998), considering the swarm factor of Simonnet et al. (2008) (○), the swarm factor of McClure et al. (2014) (□), the swarm factor of McClure et al. (2017b) (△) and the new swarm factor (◇).

The swarm factor of Simonnet et al. (2008) has a too strong effect for high gas volume fractions. If this swarm factor is used, some difficulties of convergence also appear. The instantaneous behaviour of the gas volume fraction is wrong, as shown in Fig. 4.9. Some huge accumulations of gas appear in these simulations, while these huge accumulations were not found in the experiments. In these CFD simulations, the bubbles create areas where there is only gas and areas where there is only water. This non-physical behaviour could be due to the asymptotic value of the swarm factor of Simonnet et al. (2008) in the case of very high gas volume fraction, in which this swarm factor is close to zero. Simonnet et al. (2008) validated this empirical swarm factor only for gas volume fractions lower than 30%. It is likely unsuitable for gas fractions greater than 30%. In CFD simulations, local and instantaneous gas volume fractions exceed this value, due to fluctuations. If

the local gas volume fraction is greater than 30%, the drag force decreases to almost zero and causes the unphysical formation of large accumulations of bubbles.

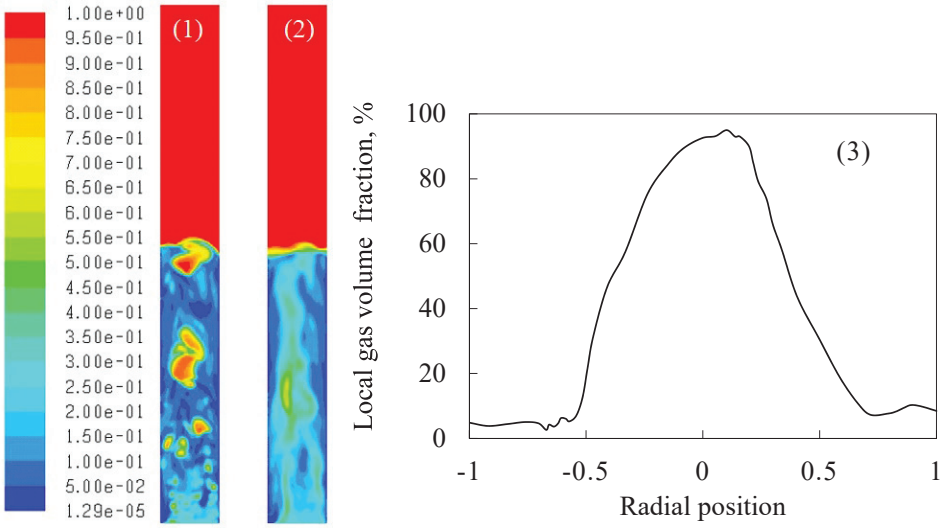

(a) Swarm factor of Simonnet et al. (2008).

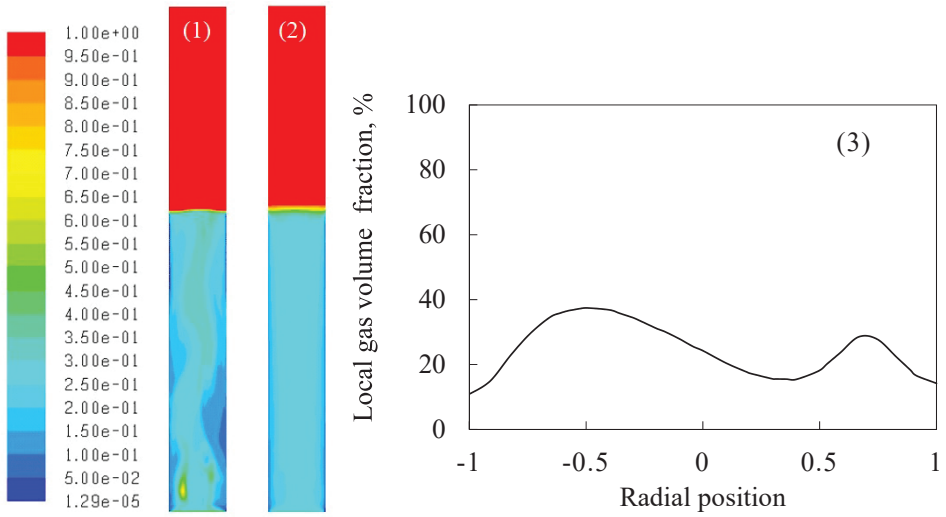

(b) New swarm factor.

Figure 4.9: Gas volume fraction for the column ϕ 0.4 m for a superficial gas velocity of 0.16 m/s: (1) instantaneous behaviour, (2) sampled behaviour and (3) instantaneous radial profile at H/D=2.5.

.

McClure et al. (2014) modified the swarm factor proposed by Simonnet et al. (2008). They used the Favre-averaged model proposed by Burns et al. (2004) for the turbulent diffusion, the drag law of Grace et al. (1976) coupled with the modified swarm factor, the k-ε model for turbulence and additional turbulence source terms due to energy transfer from gas to liquid (Pfleger & Becker 2001). Unphysical huge accumulations of bubbles are absent, thanks also to the Favre-averaged turbulent diffusion model and turbulence source terms.

McClure et al. (2017b) criticized the swarm factors of Simonnet et al. (2008) and McClure et al. (2014) for high gas volume fractions. Alternatively, McClure et al. (2017b) suggested an alternative empirical swarm factor (Equation 4.21).

Unphysical huge accumulations of bubbles are absent, but the global gas volume fraction is not well-predicted for each operating condition. McClure et al. (2017b) stated that this swarm factor predicts correctly the hydrodynamic properties only for high gas volume fractions.

The goal of this part of the work is to obtain a global swarm factor that fits well the experimental data for every operating condition. To achieve this goal, the swarm factor of Simonnet et al. (2008) is modified, adding a minimum constant value. The new swarm factor is identical to the correlation of Simonnet et al. (2008) up to 30%, but, instead of decreasing down to zero at higher gas volume fractions, it has a constant value:

$$h = \max\left\{(1-\alpha_g)\left[(1-\alpha_g)^{25} + \left(4.8\frac{\alpha_g}{1-\alpha_g}\right)^{25}\right]^{-\frac{2}{25}}, h_{min}\right\}. \tag{4.58}$$

Several minimum constant values (h_{min}) are tested. For different superficial gas velocities, the column ϕ 0.4 m gives CFD results that are in good agreement with the experiments if h_{min} is equal to 0.15 (Fig. 4.8). As shown in Fig. 4.9, huge accumulations of bubbles are absent: there are only fluctuations and preferential bubble paths, in which the air fraction is quite bigger. The instantaneous behaviour of the CFD simulations is in good agreement with the experiments.

The other bubble columns are simulated with the swarm factor reported in Eq. (4.58): ϕ 0.15 m, ϕ 1 m and ϕ 3 m. In order to keep the cell number constant, the column ϕ 0.4 m is scaled without modifying the mesh. By scaling-up, the differences are lower than 10% and consequently lower than the experimental error. The differences between experiments and CFD results are small, as shown in Fig. 4.10. A fine tuning of h_{min} would be possible between 0.12 and 0.18 to fit simulations to experiments at every scale, but it is preferable to use a fixed value (h_{min}=0.15) for scaling-up purposes. The discrepancies are slightly higher with the column ϕ 0.15 m. This column is at the limit of two Wilkinson et al. (1992) scale-up criteria, as detailed above. For these reasons, the results obtained with this column have some discrepancies. Other methods are required for scaling-down these systems.

As observed in Fig. 4.11, the radial profile of gas volume fraction is almost flat under the homogeneous regime (0.03 m/s) and it is parabolic under the heterogeneous regime (0.16 m/s). It allows recognizing the flow regime.

The axial liquid velocity strongly influences the mixing processes and it is an important parameter for bioreactors, in which shear stress and high velocities can damage the biomass, lowering the efficiency. The axial liquid velocity in the column centre obtained with CFD simulations is compared with that of experiments of Forret (2003), as shown in Fig. 4.12. These results are compared also with the correlation of Miyauchi & Shyu (1970) (Fig. 4.12). The radial profiles of axial liquid velocity are well-predicted with the new swarm factor (Fig. 4.13). By using the new swarm factor, CFD and experimental liquid velocity profiles are almost identical for every operating condition investigated in this study. The liquid velocity strongly depends on the drag law and swarm factor. As the liquid velocity profile is well-predicted, this new swarm factor, coupled with the drag law proposed by Tomiyama (1998), can be considered as correct. Consequently, this swarm factor is used in the following parts of this work.

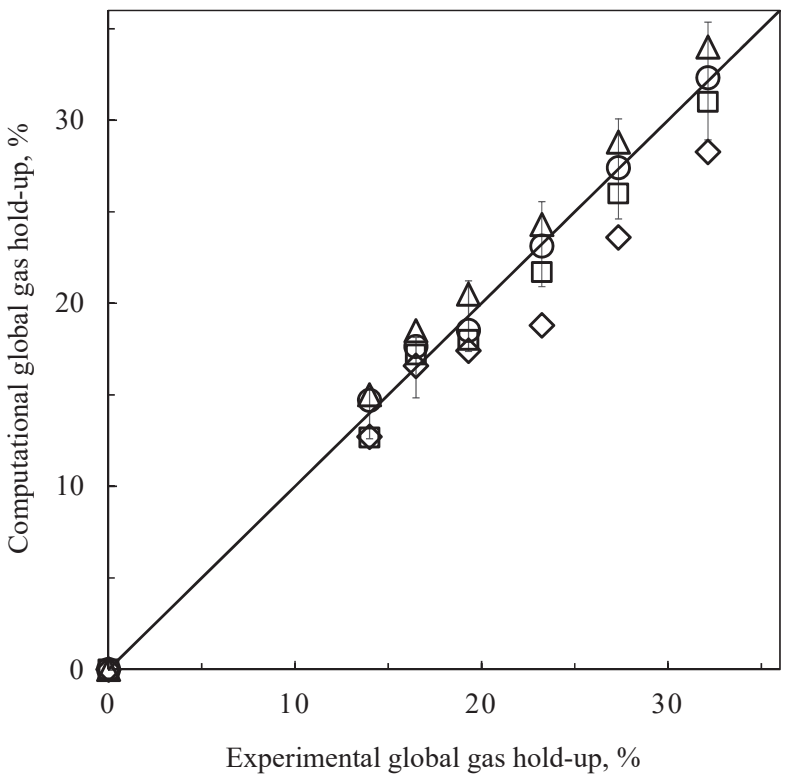

Figure 4.10: Scale-up effect on the gas hold-up using the Tomiyama (1998) drag law and the new swarm factor (h_{min}=0.15). Parity graph for the gas hold-up between experimental (Raimundo 2015) and CFD data for different columns: ϕ 0.15 m ($\diamond$), ϕ 0.4 m ($\square$), ϕ 1 m ($\bigcirc$) and ϕ 3 m ($\triangle$).

The physical meaning of the proposed swarm factor is not fully understood. Very complex interactions between bubbles and large turbulent eddies occur. Consequently, the resulting drag law, coupled with the swarm factor, can be considered as an integrated interfacial exchange term. It is considered as a drag force as it is the main force involved, but it includes probably other interfacial forces.

Standard k-ε, realizable k-ε, RNG k-ε and k-ω models are compared. The first two models give numerical errors in the case of high superficial gas velocities. The first model slightly overestimates the gas fraction in the column centre and underestimates the axial liquid velocity in the column centre in the case of heterogeneous regime, as reported in Fig. 4.14. Realizable k-ε model gives a well-predicted gas volume fraction profile and the axial liquid velocity in the column centre is underestimated, as detailed in Fig. 4.14. RNG k-ε model provides better and more stable results. With this model, gas volume fraction profile and axial liquid velocity in the column centre are well-predicted. The k-ω provides radial profiles of local gas volume fraction and axial liquid velocity very similar to those obtained with RNG k-ε model, as reported in Fig. 4.14. RNG k-ε and k-ω models seem to be the best ones due to their stability and thus they are used in the following parts of this work.

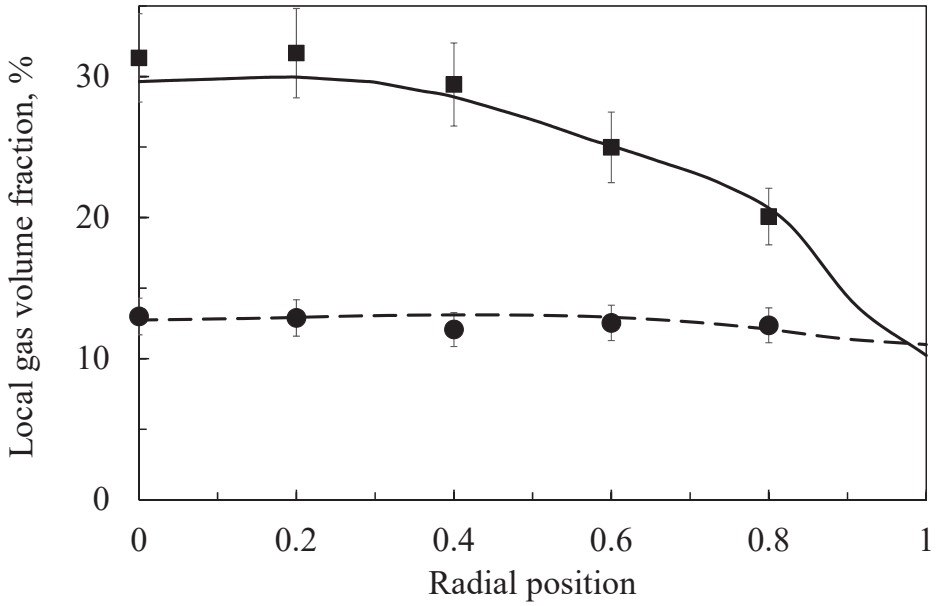

(a) ϕ *0.4 m*

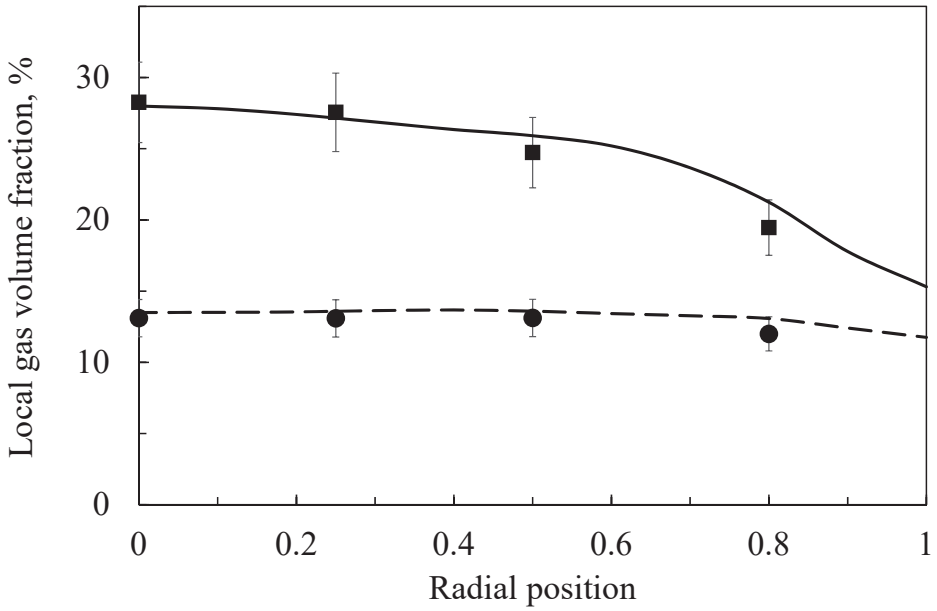

(b) ϕ *1 m*

Figure 4.11: Experimental versus CFD sampled radial profiles of the gas volume fraction at H/D=2.5 using the new swarm factor for a superficial gas velocity equal to 0.03 m/s (experimental (●) vs CFD (dashed line)) and 0.16 m/s (experimental (■) vs CFD (solid line)).

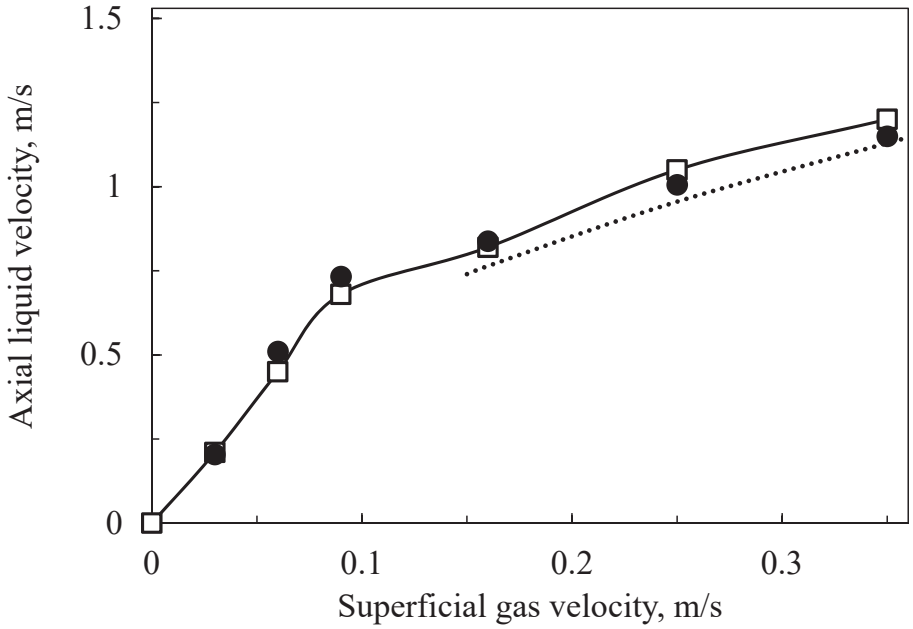

(a) ϕ *0.4 m*

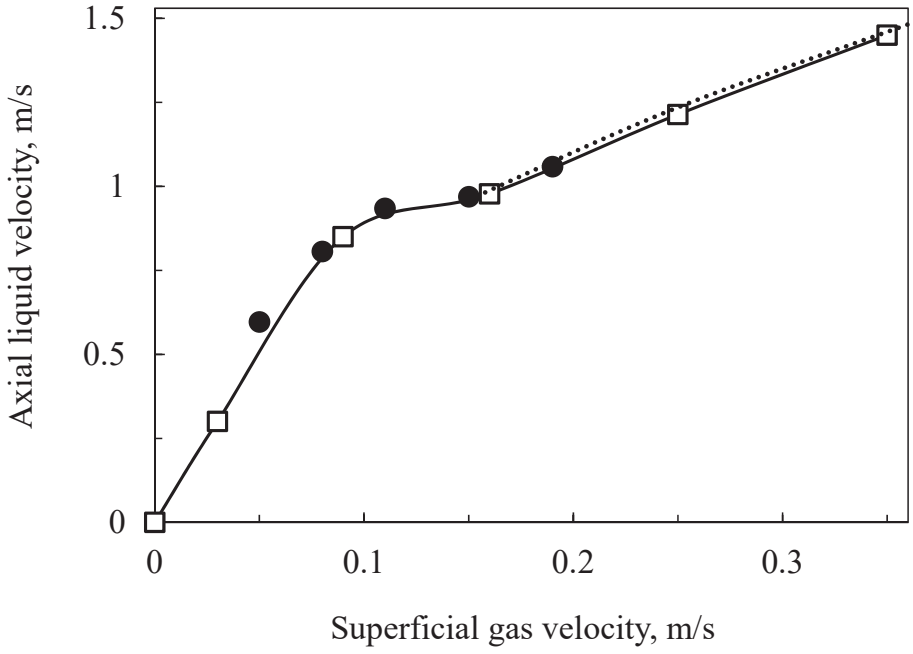

(b) ϕ *1 m*

Figure 4.12: Axial liquid velocity in the centre at H/D=3.75: experimental data of Forret (2003) (●) versus CFD data obtained using the new swarm factor (□ and solid line) versus correlation of Miyauchi & Shyu (1970) (dotted line).

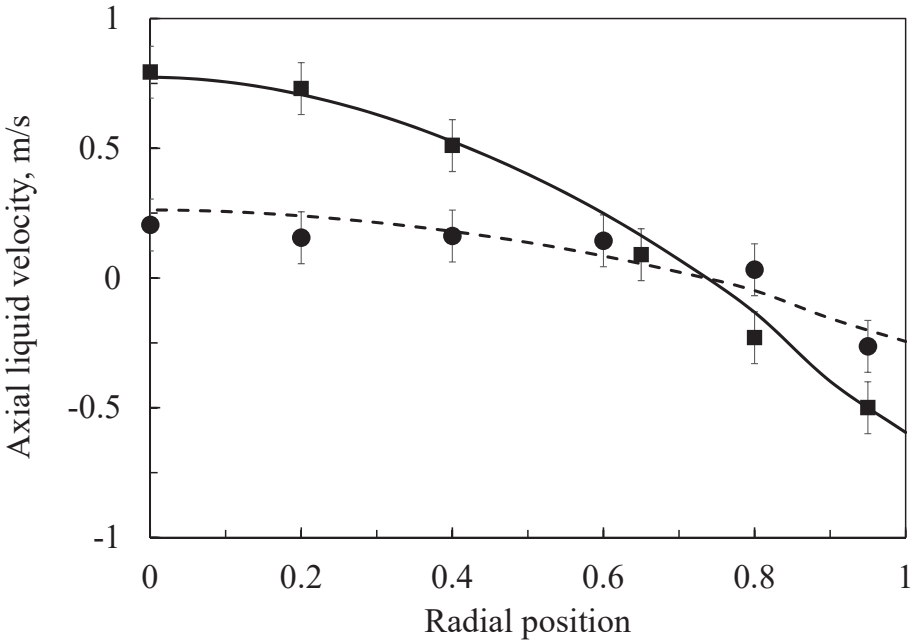

(a) ϕ *0.4 m*

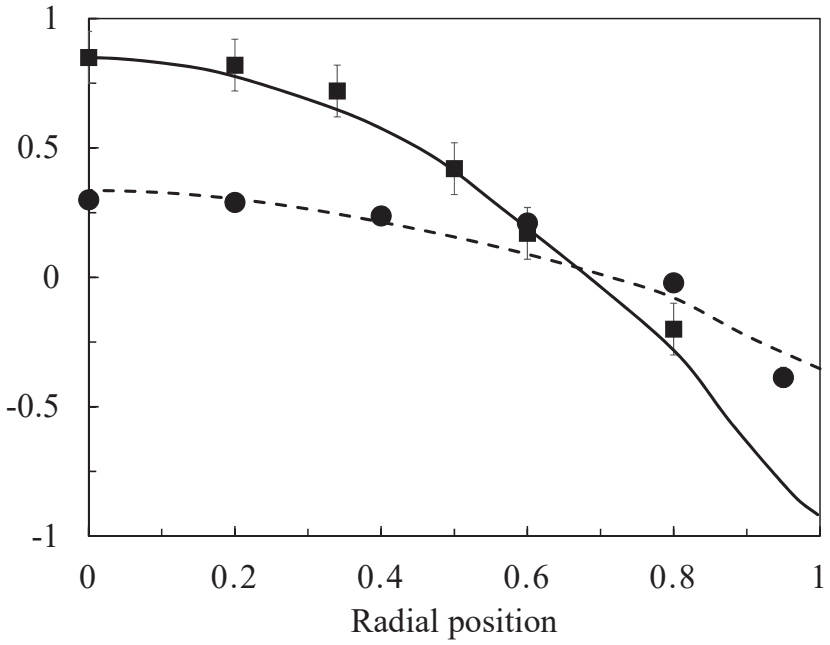

(b) ϕ *1 m*

Figure 4.13: Experimental versus CFD sampled radial profiles of the liquid velocity using the new swarm factor at H/D=3.75 for a superficial gas velocity equal to 0.03 m/s (experimental (●) vs CFD (dashed line)) and 0.16 m/s (experimental (■) vs CFD (solid line)).

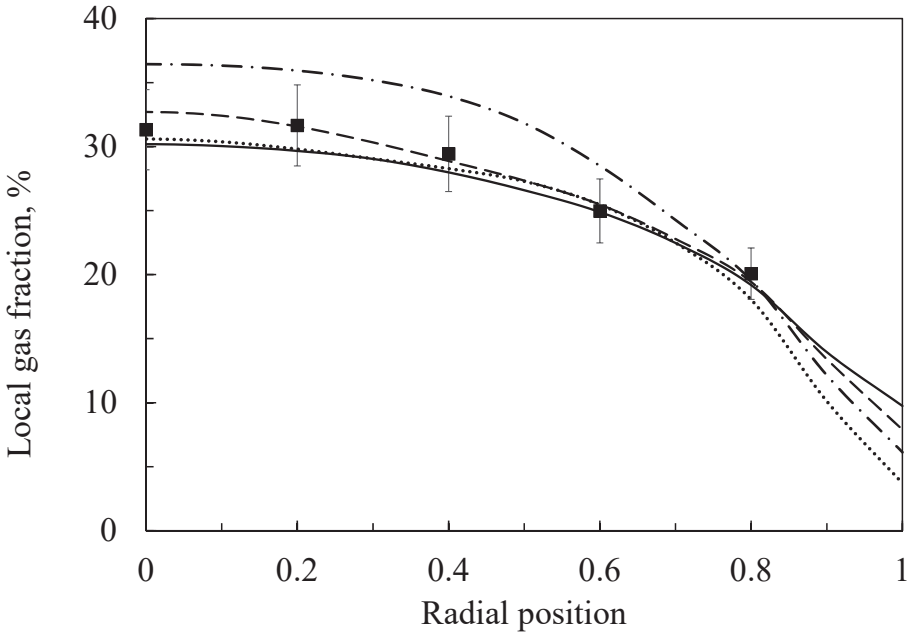

(a) Gas volume fraction at H/D=2.5.

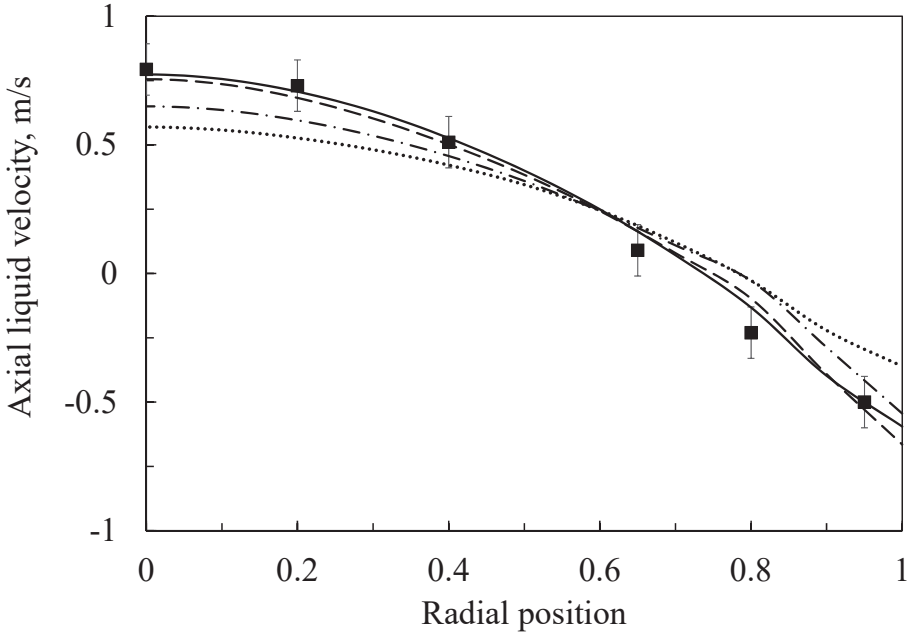

(b) Axial liquid velocity at H/D=3.75.

Figure 4.14: Turbulence models comparison of the hydrodynamic properties for the column ϕ 0.4 m and a superficial gas velocity of 0.16 m/s: standard k-ε (dash dot line), realizable k-ε (dotted line), RNG k-ε (solid line) and k-ω (dashed line).

4.4.2 Mixing time

An additional transport equation is used to simulate the mixing of a scalar quantity. The normalised concentration is used as additional transport equation. Mixing time is defined as the time necessary to reach a predefined level of homogeneity, i.e. a deviation of 5% from the final concentration. The mixing time results obtained using the RNG k-ε and the k-ω models are compared in Fig. 4.15 with the experimental data of (Forret 2003). The tracer response data are available only for the column ϕ 1 m. The diffusion coefficient is defined in three different ways for each simulation: considering only the molecular diffusivity, adding only SIT or considering SIT with bubble contribution. CFD curves are obtained by averaging the scalar concentration over the column section at the same height of the experiments. The cases simulated with only the molecular diffusivity term in the transport equation are wrong, while the other CFD cases are in good agreement with the values of the experiments. Bubble contribution does not have a great impact on the mixing time with both the turbulence models. The RNG k-ε predicts well the concentration evolution over time (Fig. 4.15). Mixing times obtained with RNG k-ε simulations under the heterogeneous regime are listed in Table 4.2.

superficial gas velocity	0.09 m/s		0.16 m/s		0.25 m/s	
Bubble contribution	yes	no	yes	no	yes	no
ϕ 0.4 m	6.70	7.70	4.70	5.50	3.40	3.60
ϕ 1 m	12.30	12.40	10.20	11.10	5.38	5.35
ϕ 3 m	36.70	37.75	31.08	31.22	23.20	23.33

Table 4.2: Mixing time (in seconds) using RNG k-ε and diffusivity model of Alméras et al. (2016) for different bubble columns.

These results confirm that bubble contribution on trasport of scalars has not great effects, except for the column ϕ 0.4 m, as shown in Fig. 4.16: a difference of about 10% appears if the superficial gas velocity is lower than 0.16 m/s. The bubble contribution should be taken into account for small-scale systems, as stated by Alméras et al. (2015). The time evolution of the scalar concentration field is represented in Fig. 4.17.

By using the model of Pfleger & Becker (2001) for considering turbulence due to energy transfer from gas to liquid, McClure et al. (2014) obtained good results for a column of 0.19 m with a square perforated sparger. McClure et al. (2014) obtained a gas volume fraction profile similar to the experimental data. In this work, the hydrodynamics is well-predicted without additional source terms in the k and ε transport equations. McClure et al. (2014) used ANSYS CFX, while the CFD simulations are realized with ANSYS Fluent in the present work. Fletcher et al. (2017) proved that, if identical closure models are used, the choice of the software does not affect the results. Different operating conditions and different geometries have been tested: it could be a partial explanation.

The proposed swarm factor allows obtaining computational results in good agreement with the experiments. Huge accumulations of bubbles are absent and the instantaneous preferential paths for bubbles (Fig. 4.9) simulate the creation of experimental instantaneous bubble macro-structure. The drag force contribution

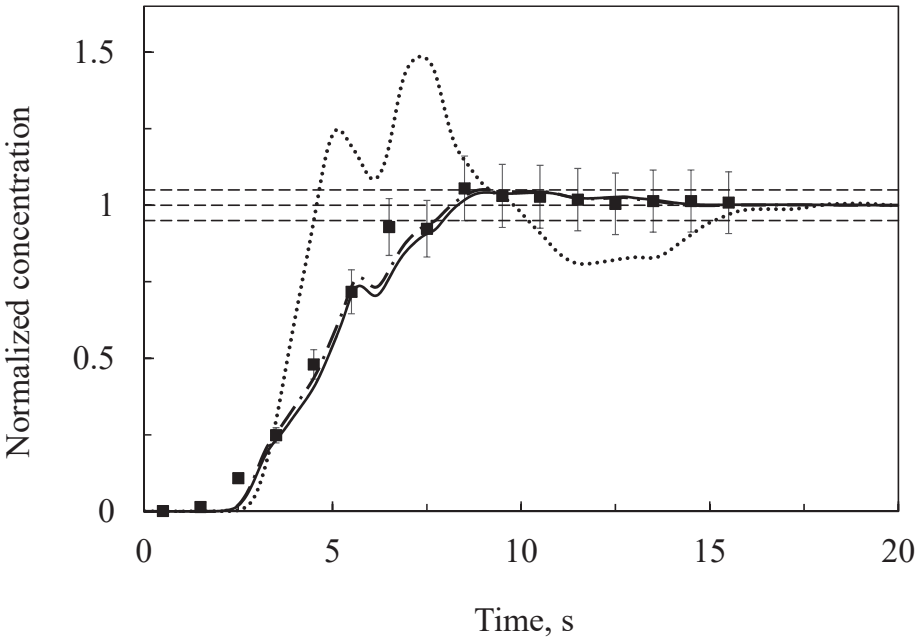

(a) RNG k-ε.

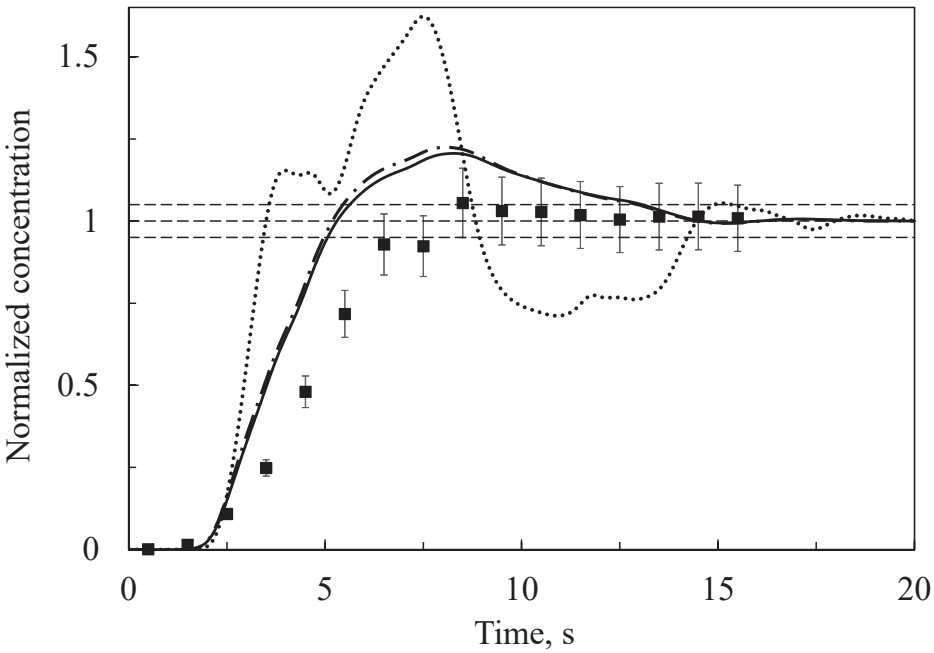

(b) k-ω.

Figure 4.15: Normalized concentration for the column ϕ 1 m and a superficial gas velocity of 0.15 m/s. Comparison of the experimental data of Forret (2003) (■) with the CFD simulations using molecular diffusivity only (dotted line), SIT (dash dot line) and SIT + bubble contribution (solid line).

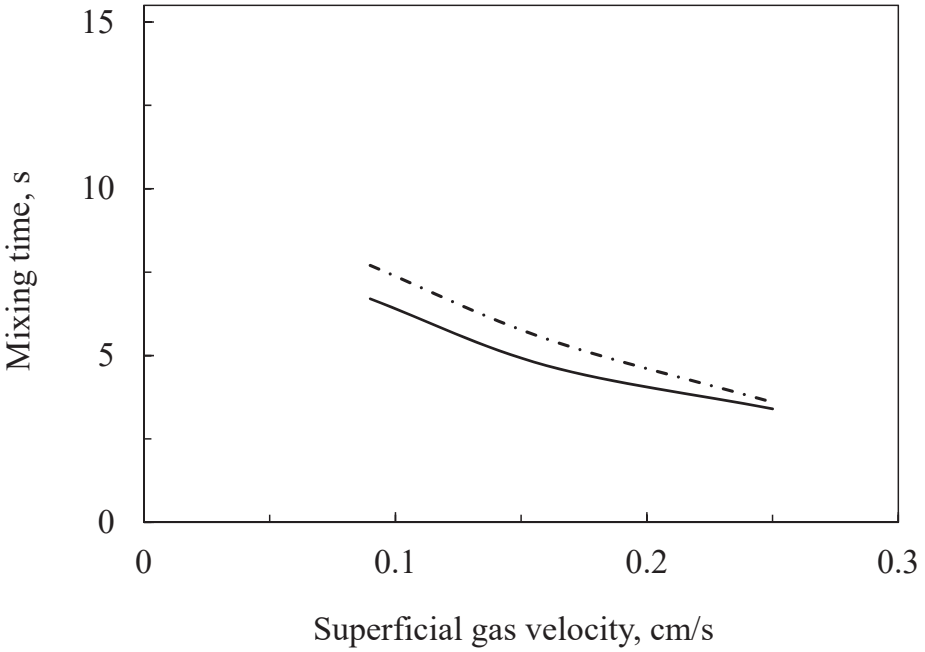

(a) ϕ *0.4 m*

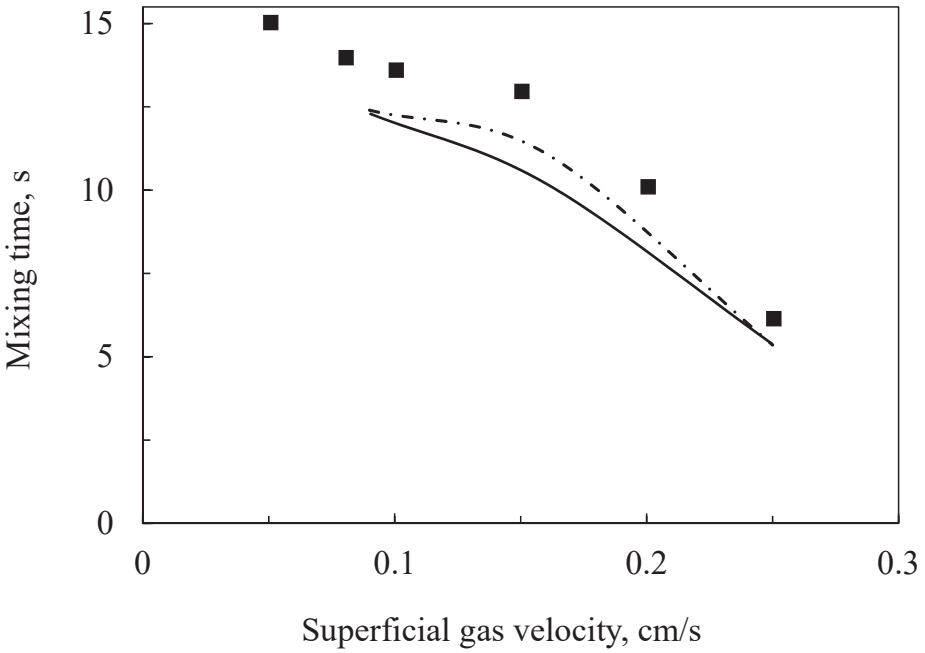

(b) ϕ *1 m*

Figure 4.16: Mixing time as a function of the superficial gas velocity, calculated by using the RNG k-ε model coupled with SIT (dash dot line) and SIT + bubble contribution (solid line). Comparison with the experimental data collected by Forret (2003) (■).

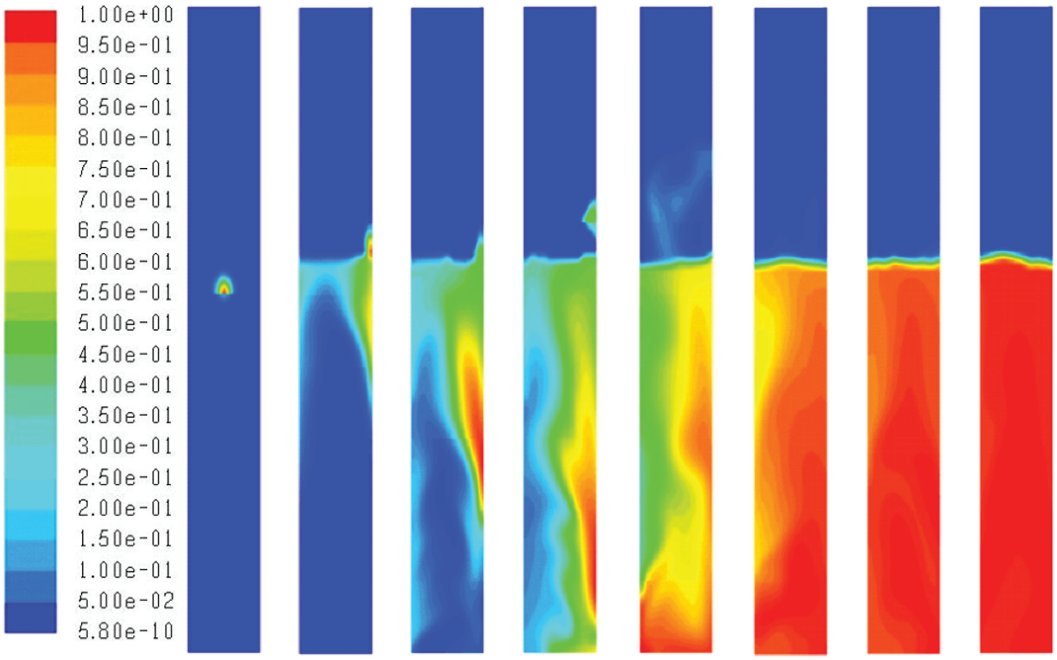

Figure 4.17: Snapshots of the scalar concentration field with RNG k-ε and Alméras et al. (2015) models for the column ϕ 0.4 m and a superficial gas velocity equal to 0.15 m/s at different times: t=0, 2, 4, 6, 8, 10, 12, 14 s from left to right.

influences the hydrodynamic behaviour and thus the mixing time. More efforts will be required to fully understand the additional turbulence due to the energy transfer from gas phase to liquid phase.

Column diameter and superficial gas velocity strongly influence the mixing time. In Fig. 4.18 and in Fig. 4.19, mixing time is presented as a function of column diameter and superficial gas velocity for both k-ω and RNG k-ε models; furthermore, the Alméras et al. (2015) turbulent diffusivity model is considered. Mixing time is low for high superficial gas velocities. Bigger columns require higher mixing time. The turbulence model choice has stronger effects when column diameter increases.

The turbulent viscosity appears directly in the diffusion coefficient and then it is an important parameter to model the scalar transport. In Fig. 4.20, the simulated viscosity is compared with several correlations. The best agreement is obtained with the correlation proposed by Kawase & Moo-Young (1989), while higher discrepancies appear with the correlations of Miyauchi & Shyu (1970) and Burns & Rice (1997). Guédon et al. (2017) arrived at the same conclusions.

Furthermore, turbulent kinematic viscosities obtained by using RNG k-ε and k-ω models, are compared in Fig. 4.20. Turbulent kinematic viscosity obtained with the k-ω is almost twice that obtained with the RNG k-ε. Mixing time computed with the RNG k-ε is lower. These aspects could appear in contradiction, but this behaviour can be explained by considering that there is the convective transport in addition to the diffusive phenomena. If only the molecular diffusion of the scalar is considered, the mixing time is longer. For the k-ω, the mixing time increase is higher, so it can be concluded that the macro recirculation is stronger for the RNG k-ε model, and it causes a quicker tracer mixing into the bubble column, even if the turbulent dispersion is lower with this turbulence model.

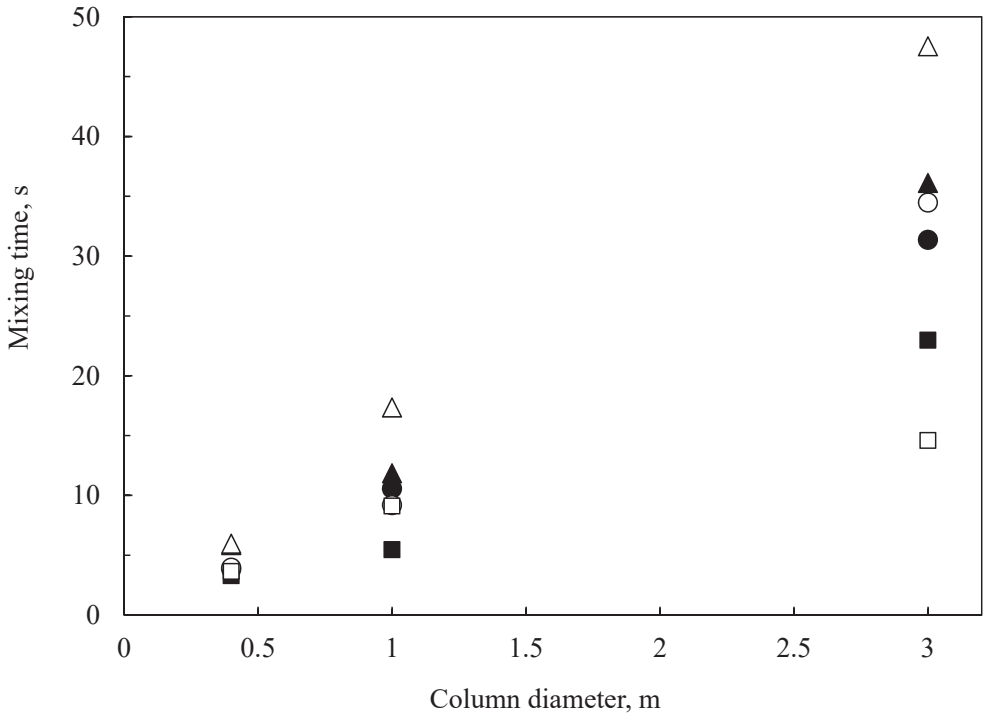

Figure 4.18: Mixing time as a function of the column diameter. Comparison between two different turbulence models: RNG k-ε (▲ 0.09 m/s, ● 0.16 m/s and ■ 0.25 m/s) and k-ω (△ 0.09 m/s, ○ 0.16 m/s m and □ 0.25 m/s).

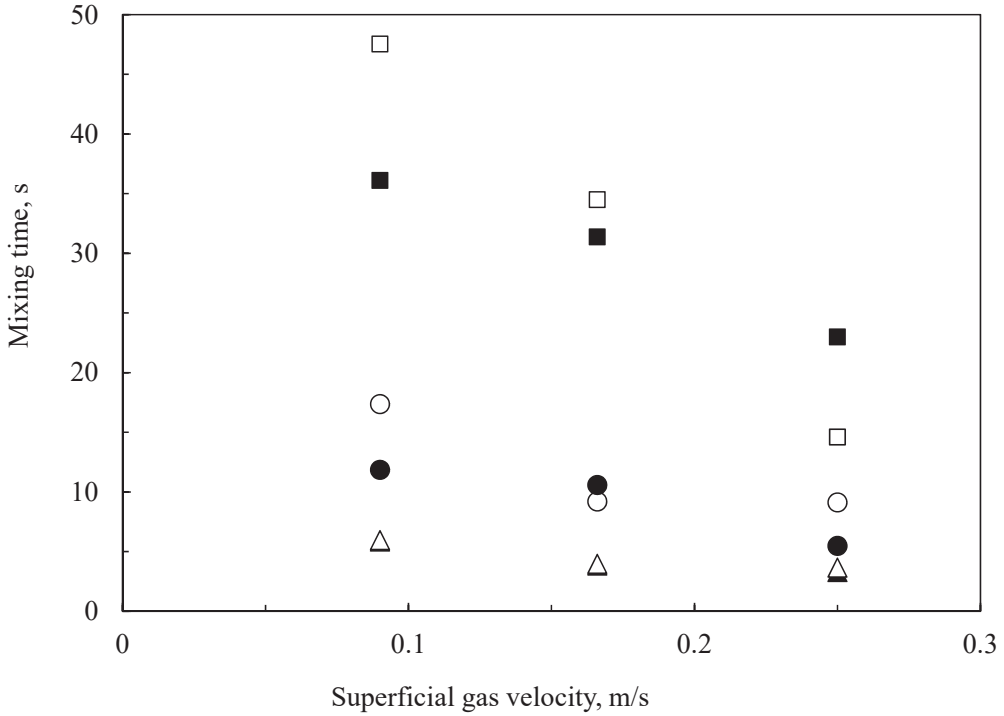

Figure 4.19: Mixing time as a function of the superficial gas velocity. Comparison between two different turbulence models: RNG k-ε (▲ ϕ 0.4 m, ● ϕ 1 m and ■ ϕ 3 m) and k-ω (△ ϕ 0.4 m, ○ ϕ 1 m and □ ϕ 3 m).

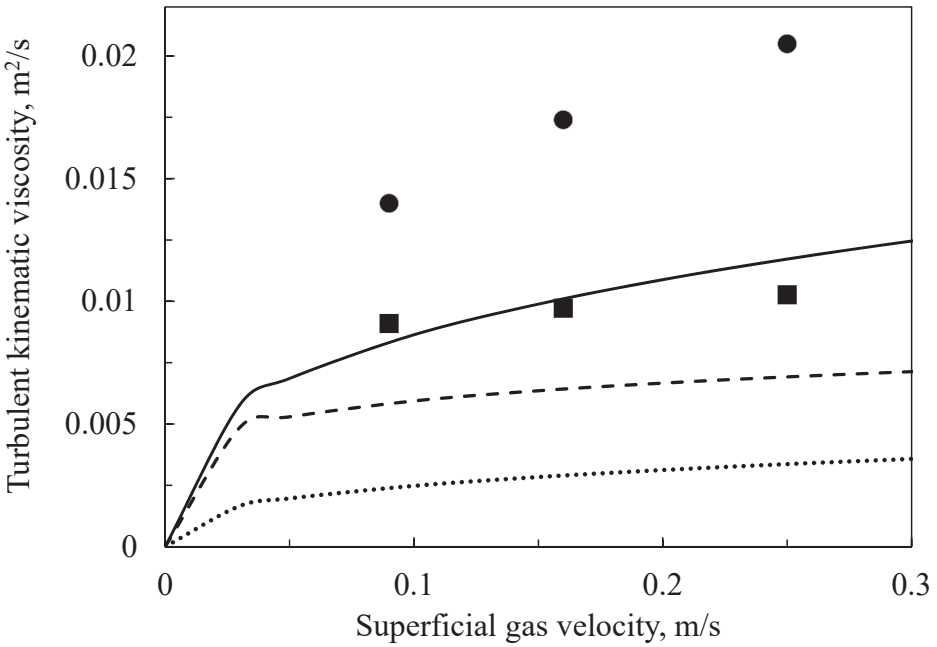

(a) ϕ *0.4 m*

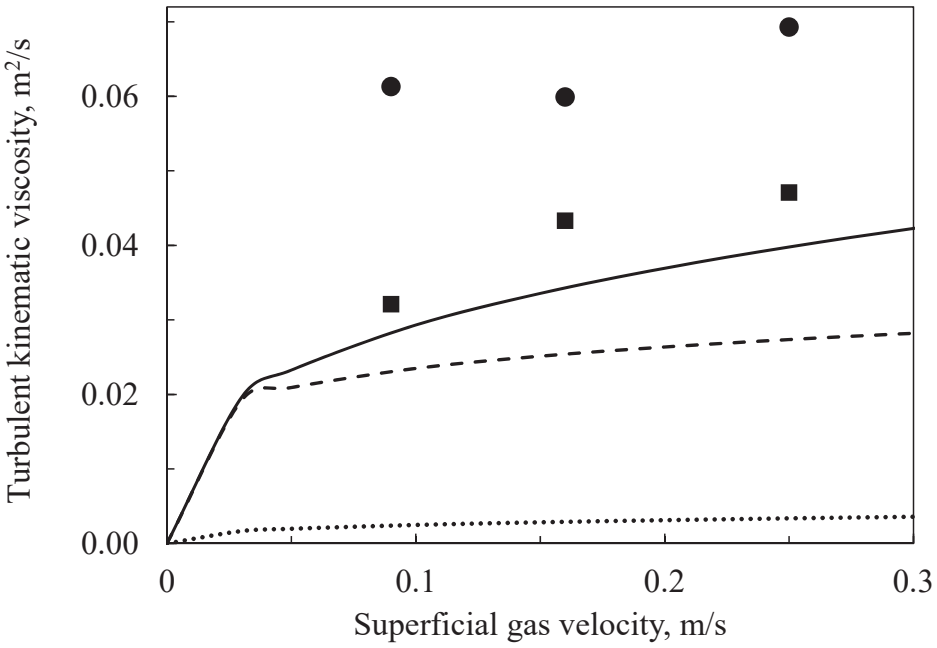

(b) ϕ *1 m*

Figure 4.20: Turbulent kinematic viscosity versus the superficial gas velocity: RNG k-ε (■) versus k-ω (●). Comparison with correlations: Burns & Rice (1997) (dotted line), Kawase & Moo-Young (1989) (solid line) and Miyauchi & Shyu (1970) (dashed line).

4.5 Conclusions and perspectives

Transient 3D simulations are required to simulate bubble columns under the heterogeneous flow regime. Gas-liquid interactions are dominated by interfacial forces. The drag force is the most important interfacial force for these systems. A drag law suitable for oblate bubbles needs to be used. The drag law proposed by Tomiyama (1998) has a wide range of validity and it has the advantage that it can consider contamination effects. For high gas volume fractions, the original drag law ought to be modified considering a swarm factor in order to decrease the drag force effect. The experimental swarm factor of Simonnet et al. (2008) has this characteristic, but its effect is too strong and the instantaneous behaviour is not well-predicted: unphysical huge accumulations of bubbles appear in the column. This swarm factor can be used for a gas volume fraction up to 30%. This value is instantaneously overcome and then the swarm factor of Simonnet et al. (2008) needs to be modified.

By adding a minimum value at the swarm factor of Simonnet et al. (2008) (Equation 4.58), the CFD results are in good agreement with the experimental data. The instantaneous behaviour is correct: unphysical huge accumulations of bubbles are absent. The CFD simulations are stable. The radial profiles of gas volume fraction and liquid velocity are well-predicted. A constant value of h_{min}=0.15 is suggested. The discrepancy between experimental data and CFD results is very small in the case of big bubble columns and then this swarm factor can be used for scaling-up purposes.

An extra diffusion coefficient due to the presence of bubbles (Alméras et al. 2015) is considered in the scalar transport equation to study the mixing time. Shear-induced turbulence is the dominant contribution in mixing processes. The RNG k-ε turbulence model predicts a mixing time that is similar to the experimental one. Mixing time is higher if only the molecular diffusion is considered to model diffusivity. Bubble contribution is often negligible for big columns. The diffusion due to the presence of bubbles has a significant effect on scalar mixing for small columns and, in these cases, the diffusive model of Alméras et al. (2015) improves the numerical results. Bubble contribution should be considered for bubble columns with a diameter up to 0.4 m.

Secondary interfacial forces, neglected in this work, near wall treatments and other boundary conditions could be considered.

Bibliography

Alméras, E., Plais, C., Euzenat, F., Risso, F., Roig, V. & Augier, F. (2016), 'Scalar mixing in bubbly flows: Experimental investigation and diffusivity modelling', *Chemical Engineering Science* 140, 114–122.

Alméras, E., Risso, F., Roig, V., Cazin, S., Plais, C. & Augier, F. (2015), 'Mixing by bubble-induced turbulence', *Journal of Fluid Mechanics* 776, 458–474.

Andersson, B., Andersson, R., Håkansson, L., Mortensen, M., Sudiyo, R., Van Wachem, B. & Hellström, L. (2012), *Computational Fluid Dynamics for Engineers*, first edn, University Press, Cambridge, UK.

Besagni, G., Di Pasquali, A., Gallazzini, L., Gottardi, E., Colombo, L. P. M. & Inzoli, F. (2017), 'The effect of aspect ratio in counter-current gas-liquid bubble columns: Experimental results and gas holdup correlations', *International Journal of Multiphase Flow* 94, 53–78.

Besagni, G., Gallazzini, L. & Inzoli, F. (2018), 'On the scale-up criteria for bubble columns', *Petroleum* .

Bird, R. B., Stewart, W. E. & Lightfoot, E. N. (2007), *Transport Phenomena*, revised second edn, John Wiley & Sons, Inc., New York, NJ.

Boussinesq, J. (1897), *Théorie de l'écoulement tourbillonnant et tumultueux des liquides dans les lits rectilignes à grande section*, Gauthier-Villars et fils.

Bridge, A. G., Lapidus, L. & Elgin, J. C. (1964), 'The mechanics of vertical gas-liquid fluidized system i: Countercurrent flow', *American Institute of Chemical Engineering Journal* 10(6), 819–826.

Buffo, A. & Marchisio, D. L. (2014), 'Modeling and simulation of turbulent polydisperse gas-liquid systems via the generalized population balance equation.', *Reviews in Chemical Engineering* 30, 73–126.

Burns, A. D., Frank, T., Hamill, I. & Shi, J. M. (2004), The favre averaged drag model for turbulent dispersion in eulerian multi-phase flows, *in* '5th International Conference on Multiphase Flow.', Yokohama, Japan.

Burns, L. F. & Rice, R. G. (1997), 'Circulation in bubble columns', *American Institute of Chemical Engineering Journal* 43(6), 1390–1402.

Cappello, V. (2016), Simulation of heterogeneous flow in large bubble column with mixing of species, Master thesis, Politecnico di Torino, Torino.

Clift, R., Grace, J. R. & Weber, M. E. (1978), *Bubbles, Drops, and Particles*, Academic Press.

Combest, D. P., Ramachandran, P. A. & Dudukovic, M. P. (2011), 'On the gradient diffusion hypothesis and passive scalar transport in turbulent flows', *Industrial & Engineering Chemistry Research* 50(15), 8817–8823.

Ekambara, K., Dhotre, M. T. & Joshi, J. B. (2005), 'CFD simulations of bubble column reactors: 1D, 2D and 3D approach', *Chemical Engineering Science* 60(23), 6733–6746.

Elghobashi, S. E. & Abou-Arab, T. W. (1983), 'A two-equation turbulence model for two-phase flows', *Physics of Fluids* 26, 931–938.

Fletcher, D. F., McClure, D. D., Kavanagh, J. M. & Barton, G. W. (2017), 'CFD simulation of industrial bubble columns: Numerical challenges and model validation successes', *Applied Mathematical Modelling* 44, 25–42.

Forret, A. (2003), Hydrodynamics scale-up of slurry bubble columns, PhD thesis, Université Claude Bernard Lyon 1-IFPEN, Lyon.

Gemello, L., Plais, C., Augier, F., Cloupet, A. & Marchisio, D. L. (2018), 'Hydrodynamics and bubble size in bubble columns: Effects of contaminants and spargers', *Chemical Engineering Science* 184, 93–102.

Grace, J., Wairegi, T. & Nguyen, T. H. (1976), 'Shapes and velocities of single drops and bubbles moving freely through immiscible liquids', *Transactions of the Institution of Chemical Engineers* 54, 167–173.

Guédon, G. R., Besagni, G. & Inzoli, F. (2017), 'Prediction of gas-liquid flow in an annular gap bubble column using a bi-dispersed eulerian model', *Chemical Engineering Science* 161, 138–150.

Hillmer, G., Weismantel, L. & Hofmann, H. (1994), 'Investigations and modelling of slurry bubble columns', *Chemical Engineering Science* 49(6), 837–843.

Hlawitschka, M., Kováts, P., Zähringer, K. & Bart, H.-J. (2017), 'Simulation and experimental validation of reactive bubble column reactors', *Chemical Engineering Science* 170, 306–319.

Ishii, M. & Zuber, N. (1979), 'Drag coefficient and relative velocity in bubbly, droplet or particulate flows', *American Institute of Chemical Engineering Journal* 25(5), 843–855.

Jakobsen, H. A., Lindborg, H. & Dorao, C. A. (2005), 'Modeling of bubble column reactors: Progress and limitations', *Industrial & Engineering Chemistry Research* 44(14), 5107–5151.

Joshi, J. B. (2001), 'Computational flow modelling and design of bubble column reactors', *Chemical Engineering Science* 56(21), 5893–5933.

Kataoka, I., Besnard, D. C. & Serizawa, A. (1992), 'Basic equation of turbulence and modelling of interfacial transfer terms in gas-liquid two-phase flow', *Chemical Engineering Communications* 118, 221–236.

Kawase, Y. & Moo-Young, M. (1989), 'Turbulence intensity in bubble columns', *The Chemical Engineering Journal* 40(1), 55–58.

Launder, B. E. & Spalding, D. B. (1972), *Lectures in Mathematical Models of Turbulence.*, Academic Press, London, U.K.

Li, G., Yang, X. & Dai, G. (2009), 'CFD simulation of effects of the configuration of gas distributors on gas-liquid flow and mixing in a bubble column', *Chemical Engineering Science* 64(24), 5104–5116.

McClure, D. D., Dolton, T. P., Barton, G. W., Fletcher, D. F. & Kavanagh, J. M. (2017a), 'Hydrodynamics and mixing in airlift contactors: Experimental work and CFD modelling', *Chemical Engineering Research and Design* 127, 154–169.

McClure, D. D., Kavanagh, J. M., Fletcher, D. F. & Barton, G. W. (2013), 'Development of a CFD model of bubble column bioreactors: Part one - A detailed experimental study', *Chemical Engineering & Technology* 36(12), 2065–2070.

McClure, D. D., Kavanagh, J. M., Fletcher, D. F. & Barton, G. W. (2017b), 'Experimental investigation into the drag volume fraction correction term for gas-liquid bubbly flows', *Chemical Engineering Science* 170, 91–97.

McClure, D. D., Norris, H., Kavanagh, J. M., Fletcher, D. F. & Barton, G. W. (2014), 'Validation of a computationally efficient computational fluid dynamics (CFD) model for industrial bubble column bioreactors', *Industrial & Engineering Chemistry Research* 53(37), 14526–14543.

Miyauchi, T. & Shyu, C.-N. (1970), 'Flow of fluid in gas bubble columns', *Kagaku Kogaku* 34(9), 958–964.

Pfleger, D. & Becker, S. (2001), 'Modeling and simulation of the dynamic flow behavior in a bubble column', *Chemical Engineering Science* 56, 1737–1747.

Radl, S. & Khinast, J. G. (2010), 'Multiphase flow and mixing in dilute bubble swarms', *American Institute of Chemical Engineering Journal* 56, 2421–2445.

Raimundo, P. M. (2015), Analysis and modelization of local hydrodynamics in bubble columns, PhD thesis, Université Grenoble Alpes.

Ranade, V. (1997), 'Modelling of turbulent flow in a bubble column reactor', *Chemical Engineering Research and Design* 75(1), 1– 23. Process and Product Development.

Roghair, I., Lau, Y. M., Deen, N. G., Slagter, H. M., Baltussen, M. W., Van Sint Annaland, M. & Kuipers, J. A. M. (2011), 'On the drag force of bubbles in bubble swarms at intermediate and high reynolds numbers', *Chemical Engineering Science* 66, 3204–3211.

Rusche, H. & Issa, R. (2000), The effect of voidage on the drag force on particles, droplets and bubbles in dispersed two-phase flow, *in* '2nd Japanese European Two-Phase Flow Meeting.', Tsukuba, Japan.

Rzehak, R. & Krepper, E. (2013), 'CFD modeling of bubble-induced turbulence', *International Journal of Multiphase Flow* 55, 138–155.

Sasaki, S., Hayashi, K. & Tomiyama, A. (2016), 'Effects of liquid height on gas holdup in air-water bubble column', *Experimental Thermal and Fluid Science* 72, 67–74.

Sasaki, S., Uchida, K., Hayashi, K. & Tomiyama, A. (2017), 'Effects of column diameter and liquid height on gas holdup in air-water bubble columns', *Experimental Thermal and Fluid Science* 82, 359–366.

Sato, Y. & Sekoguchi, K. (1975), 'Liquid velocity distribution in two-phase bubble flow', *International Journal of Multiphase Flow* 2(1), 79–95.

Schiller, L. & Naumann, N. (1935), 'A drag coefficient correlation.', *Vdi Zeitung* 77, 318.

Shah, Y. T., Kelkar, B. G., Godbole, S. P. & Deckwer, W. D. (1982), 'Design parameters estimations for bubble column reactors', *American Institute of Chemical Engineering Journal* 28(3), 353–379.

Shih, T. H., Liou, W. W., Shabbir, A. & Zhu, J. (1995), 'A new $k - \varepsilon$ eddy-viscosity model for high reynolds number turbulent flows - model development and validation.', *Computers Fluids* 24(3), 227–238.

Simonin, O. & Viollet, P. L. (1990), 'Modeling of turbulent two-phase jets loaded with discrete particles', *Phenomena in Multiphase Flows* pp. 259–269.

Simonnet, M., Gentric, C., Olmos, E. & Midoux, N. (2008), 'CFD simulation of the flow field in a bubble column reactor: Importance of the drag force formulation to describe regime transitions', *Chemical Engineering and Processing: Process Intensification* 47(9), 1726–1737.

Sugrue, R. M. (2017), A robust momentum closure approach for multiphase computational fluid dynamics applications, PhD thesis, Massachusetts Institute of Technology.

Suzzi, D., Radl, S. & Khinast, J. (2013), 'Validation of euler-euler and euler-lagrange approaches in the simulation of bubble columns.', *Chemical Engineering Transactions* 17, 585–590.

Tabib, M. V., Roy, S. A. & Joshi, J. B. (2008), 'CFD simulation of bubble column - An analysis of interphase forces and turbulence models', *Chemical Engineering Journal* 139(3), 589–614.

Tomiyama, A. (1998), 'Struggle with computational bubble dynamics', *Multiphase Science and Technology* 10(4), 369.

Troshko, A. A. & Hassan, Y. A. (2001), 'A two-equation turbulence model of turbulent bubbly flows', *International Journal of Multiphase Flow* 27(11), 1965–2000.

Vaidheeswaran, A. & Lopez de Bertodano, M. (2017), 'Stability and convergence of computational eulerian two-fluid model for a bubble plume', *Chemical Engineering Science* 160, 210–226.

Versteeg, H. & Malalasekera, W. (2007), *An introduction to computational fluid dynamics: the finite volume method.*, 2nd edn, Pearson Education Limited, Harlow, England.

Wallis, G. B. (1969), *One-dimensional two-phase flow*, 1st edn, McGraw-Hill, New York.

Wilcox, D. C. (1998), *Turbulence modeling for CFD.*, DCW Industries, Inc., La Canada, California.

Wilkinson, P. M., Spek, A. P. & Van Dierendonck, L. L. (1992), 'Design parameters estimation for scale-up of high pressure bubble column', *American Institute of Chemical Engineering Journal* 38, 544–554.

Yakhot, V. & Orszag, S. A. (1986), 'Renormalization group analysis of turbulence i basic theory.', *Journal of scientific computing* 1(1), 1–51.

Yao, W. & Morel, C. (2004), 'Volumetric interfacial area prediction in upward bubbly two-phase flow', *International Journal of Heat and Mass Transfer* 47, 307–328.

Zhang, D. (2007), Eulerian modeling of reactive gas-liquid flow in a bubble column, PhD thesis, Enschede, The Netherlands.

Zhang, D., Deen, N. G. & Kuipers, J. A. M. (2006), 'Numerical simulation of dynamic flow behavior in a bubble column: A study of closures for turbulence and interface forces', *Chemical Engineering Science* 61, 7593–7608.

Chapter 5

Population Balance Modelling of heterogeneous bubble column reactors

5.1 Introduction

Eulerian-Eulerian RANS methods allow simulating heterogeneous flows with a relatively low computational cost, as detailed in Chapter 4. These methods are often used for industrial applications. One important limitation of Eulerian-Eulerian classical CFD models is due to the assumption that every bubble has the same size and that this is an input parameter for the simulation. The use of a single bubble size hinders the prediction of local hydrodynamic properties. The polydispersity of gas bubbles is an aspect that turns out to be very important in gas-liquid multiphase flows: significant variations of bubble size are observed in bubble column reactors. Bubble polydispersity causes considerable variations in the interfacial area, affecting, in turn, the rate of exchange of mass, momentum and energy between the two phases (i.e. continuous and disperse) and between the multiphase flow and the external boundaries. A population balance model (PBM) can be coupled with CFD simulations to overcome these limits and make the CFD simulations more predictive. Classical mass, momentum and energy equations solved in multiphase flows are coupled with population balance equations (PBEs). CFD-PBM coupling allows considering the effects of bubble coalescence and breakage on the development of the interfacial area between the continuous and disperse phases.

The methods for solving the PBE could be distinguished into three groups: Classes (or sectional) Methods, Monte Carlo Methods and Moment-based Methods and only some of them are suitable for CFD implementation.

In the Classes Methods (CM) the internal coordinates, for example bubble size, is discretized. These methods, firstly developed for univariate cases (see for example the comparison performed by Vanni (2000)), are extended to multivariate cases (Kumar et al. 2008). The discretization is performed by using different techniques, as such the finite volume method proposed by Gunawan et al. (2004), the finite element method proposed by Godin et al. (1999) or the finite difference method. The MUSIG method is often used for gas-liquid flows (Frank et al. 2008). These methods could present however the following problem: they could require large computational resources, resulting in time-consuming simulations. The transport

of separated classes of bubbles, although displaying some advantages, is often time-consuming.

The second group, called Monte Carlo Method (MCM), solves stochastic differential equations that are capable of reproducing a finite number of artificial realizations of the system (Zhao et al. 2007); these methods require huge computational costs when coupled with CFD and they can be used only for simplified simulations.

The Methods of Moments solve the transport equations for some lower-order moments (Marchisio et al. 2003*a*). In other words, instead of solving the PBE, a limited number of transport equations, derived from the PBE by applying the moment transform, are solved. These methods present a closure problem that can be solved through different methods. An important class of these methods is the Quadrature-Based Moments Methods (QBMM), used in this work, where the closure problem is overcome by using an ad-hoc quadrature approximation.

In Quadrature-Based Moments Methods (QBMM), the bubble size distribution (BSD) or Number Density Function (NDF) is assumed to be the summation of some basis functions centred on the zeros of polynomials orthogonal to the BSD or NDF, or in other words, centred on the nodes of a Gaussian quadrature approximation. The quadrature approximation, calculated from the moments of the BSD or NDF, is more accurate than other methods in overcoming the closure problem even when the order of the quadrature approximation is very small (i.e. two or three). The final method, that combines the use of the moments of the BSD and the use of the quadrature approximation, can be employed for coupling with CFD simulations, as a small number of additional equations is required. For a typical problem, the evolution of the BSD can be predicted only by tracking the evolution of six moments of the BSD, corresponding to a quadrature approximation of order three. By using the CM to predict the evolution of the BSD with similar accuracy, 30 or 40 classes (and corresponding transport equations) might have to be solved, resulting in much higher computational costs (Marchisio et al. 2003*b*).

These methods are employed both for univariate and multivariate PBE, where in other words, one internal coordinate (e.g. bubble size) or multiple internal coordinates (e.g. bubble size and composition) are employed. For univariate cases, the original Quadrature Method of Moments (QMOM) (McGraw 1997) can be used. The quadrature approximation is obtained with a specific inversion algorithm.

Bubble size depends on coalescence and breakage phenomena, closely linked to operating conditions and turbulence. These phenomena are however mainly studied for low gas velocities (Falzone et al. 2018) and model small gas volume fraction. In this work, the objective is to go beyond current practice and develop a model that simulates what happens at higher superficial gas velocities. To this end, experimental data obtained by Gemello et al. (2018a) and detailed in Chapter 3 are used. Thanks to these experimental results it is possible to investigate also the effects of different initial bubble sizes and the presence of additives. The main goal of this work is to identify breakage and coalescence kernels that are capable of simulating the bubble size for both homogeneous and heterogeneous regimes. Different mechanisms are involved in bubble breakage as shown by Liao & Lucas (2009) and the main mechanism is linked to turbulent fluctuations. On the other hand, the coalescence kernel is divided between collision frequency and coalescence efficiency, as stated by Liao & Lucas (2010). Collisions are caused by several

phenomena, the turbulent fluctuations being the most important. The coalescence efficiency can be studied with three methods: film drainage model, energy model and critical approach velocity model; the first model is the most common for the homogeneous regime. Existing breakage and coalescence models were developed and validated for the homogeneous regime, where there is a lack of kernels suitable for the heterogeneous regime.

In this work, breakage and coalescence models are validated under the heterogeneous flow regime, providing a suitable and innovative set of models that can predict correctly the bubble size for a wide range of operating conditions.

Starting from the experimental results detailed in Chapter 3, the existing breakage and coalescence kernels, suitable for the homogeneous regime, are tested and extended for the heterogeneous regime. 3D transient Eulerian-Eulerian CFD simulations with ANSYS Fluent are carried out and coupled with QMOM. 0D simulations with Matlab were also performed to provide a preliminary screening of the tested coalescence and breakage models.

5.2 Population Balance Modelling

The disperse phase is constituted by discrete elements (i.e. bubbles in the case of gas-liquid systems): each element of this phase is identified by a number of coordinates, that are classified as internal and external. Two elements are identical if they have identical coordinates. External coordinates are spatial coordinates and time, while internal coordinates refer to other intrinsic properties of the elements such as volume, surface area, size, age, velocity and temperature (Marchisio & Fox 2013).

The Number-density functions (NDF) contains information about the population of bubbles, explaining how it is distributed over the properties of interest inside an infinitesimal control volume. Let us consider an infinitesimal control volume located at physical point $\mathbf{x} = (x_1, x_2, x_3)$ of measure $d\mathbf{x} = (dx_1, dx_2, dx_3)$ and at phase-space point, $\boldsymbol{\xi} = (\xi_1, \xi_2, \xi_3)$. The NDF $n_{\boldsymbol{\xi}}(t, \mathbf{x}, \boldsymbol{\xi})$ identifies the population of bubbles in the computational domain at each instant. Integrating the NDF over all possible values of the internal-coordinate vector, the total number concentration $N(t, \mathbf{x})$ is obtained, which is the total number of entities per unit volume located at time t at point $\mathbf{x}$, and it corresponds to the moment of order zero of the NDF:

$$N = m_{\boldsymbol{\xi},\mathbf{0}} = \int n_{\boldsymbol{\xi}}(\boldsymbol{\xi}) d\boldsymbol{\xi}. \tag{5.1}$$

Higher-order moments of the NDF can be defined:

$$m_{\boldsymbol{\xi},\boldsymbol{k}} = \int {\xi_1}^{k_1} ... {\xi_M}^{k_M} n_{\boldsymbol{\xi}}(\boldsymbol{\xi}) d\boldsymbol{\xi}, \tag{5.2}$$

where $\boldsymbol{k} = (k_1, k_2, ..., k_N)$. The PBE is a continuity statement expressed in terms of the NDF. The velocity of the PBE is assumed to be equal to the local velocity in the continuous phase or derivable from this. The PBE basically counts the number of elements (bubbles) belonging to a specific finite volume defined both in physical-space and phase-space. The number of elements inside this volume changes due to the movement of the bubbles in physical space, their velocities, the movement of

the bubbles in physical space, continuous processes, and because of discontinuous or discrete events, resulting in the following equation (Marchisio & Fox 2013):

$$\frac{\partial}{\partial t}\left(\int_{\Omega_x} d\mathbf{x}\int_{\Omega_\xi} d\boldsymbol{\xi}\, n_{\boldsymbol{\xi}}\right)+\int_{\Omega_\xi} d\boldsymbol{\xi}\int_{\partial\Omega_x}(n_{\boldsymbol{\xi}}\mathbf{u})\cdot \mathrm{d}\mathbf{A}_{\mathbf{x}}+$$

$$+\int_{\Omega_x} d\mathbf{x}\int_{\partial\Omega_\xi}\left(n_{\boldsymbol{\xi}}\dot{\boldsymbol{\xi}}\right)\cdot \mathrm{d}\mathbf{A}_{\boldsymbol{\xi}}=\int_{\Omega_x} d\mathbf{x}\int_{\Omega_\xi} d\boldsymbol{\xi}\, S_{\boldsymbol{\xi}}, \tag{5.3}$$

where $\mathbf{u}$ is the velocity vector of the bubbles, $\dot{\boldsymbol{\xi}}$ is the rate of change of the generic internal coordinate for the bubbles, Ω_x is the finite control volume in physical space, Ω_ξ is the finite control volume in phase space, $\partial\Omega_x$ and $\partial\Omega_\xi$ are their boundaries and $S_{\boldsymbol{\xi}}$ considers the discrete events, such as collisions between bubbles, leading to coalescence or breakage and nucleation.

If the Reynolds-Gauss theorem is applied and the equality is forced to be respected for any possible control volumes, the following equation is obtained:

$$\frac{\partial n_{\boldsymbol{\xi}}}{\partial t}+\frac{\partial}{\partial \mathbf{x}}\cdot(\mathbf{u}n_{\boldsymbol{\xi}})+\frac{\partial}{\partial \boldsymbol{\xi}}\cdot\left(\dot{\boldsymbol{\xi}}\, n_{\boldsymbol{\xi}}\right)=S_{\boldsymbol{\xi}}. \tag{5.4}$$

A generic turbulent gas-liquid flow can be considered as a dispersion of bubbles, that are characterized by their size L, composition $\boldsymbol{\phi}_b$, velocity $\mathbf{u}_b$ and possibly temperature T. The PBE is considered univariate if the population of bubbles is described by just one internal coordinate, for example bubble size or length. The PBE is called bivariate if two internal coordinates are considered, e.g. bubble size and chemical composition. Higher-dimensional PBEs are referred to as multivariate. If the bubbles are characterized by their own velocity distribution, the PBE becomes the generalized population-balance equation (GPBE) were bubble velocity is included in the PBE as an internal variable:

$$\frac{\partial n_{\boldsymbol{\xi}}}{\partial t}+\frac{\partial}{\partial \mathbf{x}}\cdot(\mathbf{u}\, n_{\boldsymbol{\xi}})+\frac{\partial}{\partial \mathbf{u}}\cdot(\dot{\mathbf{u}}\, n_{\boldsymbol{\xi}})+\frac{\partial}{\partial \boldsymbol{\xi}}\cdot\left(\dot{\boldsymbol{\xi}}\, n_{\boldsymbol{\xi}}\right)=S_{\boldsymbol{\xi}}, \tag{5.5}$$

where $\dot{\mathbf{u}}$ is the rate of change of bubble velocity, the acceleration, i.e. the forces per unit mass acting on bubbles (gravity, buoyancy, drag and other interfacial forces).

Isothermal systems are considered in this work and the bubbles have the same chemical composition. Furthermore, it is assumed that the bubble velocity is linked to the bubble size with a known algebraic relationship and therefore only bubble size remains an internal coordinate. The final PBE becomes:

$$\frac{\partial n_L}{\partial t}+\frac{\partial}{\partial \mathbf{x}}\cdot(\mathbf{u}\, n_L)+\frac{\partial}{\partial L}\left(G_L\, n_L\right)=S(L), \tag{5.6}$$

where G_L is the continuous rate of change of bubble length ($\dot{L}_L$) (due to mass transfer) and $S(L)$ considers discrete events such as coalescence and breakage (nucleation, a common phenomenon for example in fermentation processes, is not considered in this work). As mentioned the bubble velocity $\mathbf{u}$ is considered as known.

If only the size of the bubble is considered as internal coordinate, the definition in Eq. (5.2), of the moments of order k simplifies into the following expression:

$$m_{L,k}=\int_0^{+\infty} n_L(L)\, L^k\, dL. \tag{5.7}$$

With this simplified definition of the k^{th} moments, the PBE can be rewritten as:

$$\frac{\partial m_{L,k}}{\partial t} + \frac{\partial}{\partial \mathbf{x}} \cdot (\mathbf{u}_{L,k}\, m_{L,k}) = k\, G_{L,k-1} m_{L,k-1} + \bar{S}_{m_k}, \tag{5.8}$$

where $G_{L,k}$ is the average rate of change of the moment of order k:

$$G_{L,k} = \frac{\int_0^\infty G_L\, n_L(L)\, L^k\, dL}{\int_0^\infty n_L(L)\, L^k\, dL}, \tag{5.9}$$

$\mathbf{u}_{L,k}$ is the average velocity of the moment of order k:

$$\mathbf{u}_{L,k} = \frac{\int_0^\infty \mathbf{u}_L\, n_L(L)\, L^k\, dL}{\int_0^\infty n_L(L)\, L^k\, dL} \tag{5.10}$$

and the source term is written as:

$$\bar{S}_{m_k} = \int_0^\infty S_L\, L^k dL. \tag{5.11}$$

The growth term $G_{L,k}$ is neglected in this work as the mass transfer is not studied. The last term of Eq. (5.8) is the source term due to discontinuous events. This term is an unclosed term, that cannot in general be written in terms of the known moments. The term on the right side of the Eq. (5.8) strongly depends on the system that is considered. The literature reports different expressions for gas-liquid disperse bubbly systems; other correlations are available for other systems, i.e. particles, bubbles or drops in fluids (Buffo 2012). This term depends on discontinuous events, causing a discontinuous jump in phase space and can be divided in three classes (Marchisio & Fox 2013):

- zero-order processes, in which the events' rates depend only on the continuous phase, e.g. nucleation; as mentioned this is a very important process in fermentation processes, but is neglected in this work;
- first-order processes, in which each event rate depends only on the interaction of the continuous phase with an element of disperse phase, i.e. breakage;
- second-order process, in which the interactions are between two different elements of disperse phase and the continuous phase, i.e. coalescence.

Simultaneous interactions between three or more dispersed elements are very uncommon compared with the other interactions, so higher-order processes can be neglected. Moreover, a higher-order process can always be represented as a sequence of multiple second-order processes.

5.2.1 Source terms

Only breakage and coalescence are considered in this work. The source term in Eq. (5.6) can be written as the summation of the terms due to breakage and coalescence, where each phenomenon produces two terms: death and birth. The birth terms are summed up and the death terms are subtracted. Four terms are considered (Petitti et al. 2010):

- birth term due to coalescence, B^C;
- death term due to coalescence, D^C;
- birth term due to breakage, B^B;
- death term due to breakage, D^B.

Coalescence causes at the same time the formation of a new bubble and the death of two smaller bubbles that collapse together. The two terms due to coalescence can be calculated respectively as (Marchisio & Fox 2013):

$$B^C(L) = \frac{L^2}{2}\int_0^L \frac{h\left(\left(L^3+\lambda^3\right)^{1/3},\,\lambda\right)}{\left(L^3-\lambda^3\right)^{2/3}} n_L\left(\left(L^3+\lambda^3\right)^{1/3}\right) n_L(\lambda)d\lambda \tag{5.12}$$

and

$$D^C(L) = \int_0^\infty h(L,\lambda)n_L(L)n_L(\lambda)d\lambda, \tag{5.13}$$

where $h(L,\lambda)$ is the coalescence kernel (or frequency) related to two bubbles of size L and λ.

The third term is due to the formation of daughter bubbles caused by the breakage of a mother bubble:

$$B^B(L) = \int_L^\infty \beta\left(L,L'\right)\, g(L')\, n_L(L')dL', \tag{5.14}$$

where $g\left(L\right)$ is the breakage kernel (or frequency) for a bubble L and $\beta\left(L,L'\right)$ is the daughter distribution function for a daughter bubble L formed by the breakage of the mother bubble L'.

The death term due to breakage is:

$$D^B(L) = g(L)n_L(L). \tag{5.15}$$

The source term, considering a bubble of size L_1, becomes:

$$S\left(L\right) = B^C(L) - D^C(L) + B^B(L) - D^B(L). \tag{5.16}$$

Using the explicit form for all the terms and summing then up we obtain:

$$\begin{aligned} S\left(L\right) = \frac{L^2}{2}\int_0^L \frac{h\left(\left(L^3+\lambda^3\right)^{1/3},\,\lambda\right)}{\left(L^3-\lambda^3\right)^{2/3}} n_L\left(\left(L^3+\lambda^3\right)^{1/3}\right) n_L(\lambda)d\lambda + \\ - \int_0^\infty h(L,\lambda)n_L(L)n_L(\lambda)d\lambda + \\ + \int_L^\infty \beta\left(L,L'\right)\, g(L')\, n_L(L')dL' + \\ - g(L)n_L(L). \end{aligned} \tag{5.17}$$

5.2.2 Breakage kernel and daughter distribution function

Bubbles breakage in turbulent flows is determined by the hydrodynamics of the continuous liquid phase and by the interfacial interactions between the phases (Liao & Lucas 2009). This phenomenon is due to a balance between external stresses caused by the liquid phase, surface stresses of the bubble and viscous stresses. The external stresses attempt to destroy the bubbles, meanwhile the other stresses restore the shape of the bubbles. Using this balance, it is possible to predict the more stable size of the bubbles (Revankar 2001).

Breakage mechanisms can be divided into four groups (Liao & Lucas 2009):

- turbulent fluctuations and collisions;
- viscous shear forces;
- shearing-off process;
- interfacial instability.

In turbulent systems, the first group of mechanisms is the most important and breakage is mainly caused by turbulent pressure fluctuations along the surface and by collisions between bubbles and eddies. Fluctuations cause a deformation of a bubble until separating the bubble into two daughter bubbles. The main external force is the dynamic pressure difference around the bubble: breakage can be studied as a balance between dynamic pressure and surface stresses. Viscous stresses due to the gas inside the bubble are generally neglected. These become very important instead in the case of liquid droplets (Gao et al. 2016) (Li et al. 2017). The mechanisms that cause breakage due to turbulent fluctuation and collision can be classified on different criteria, that can be combined:

- turbulence kinetic energy of the bubble greater than a critical value;
- velocity fluctuation around the bubble surface greater than a critical value;
- turbulence kinetic energy of the hitting eddy greater than a critical value;
- inertial force of the hitting eddy greater than the interfacial force of the smallest daughter bubble.

Breakage due to the viscous shear forces is caused by velocity gradient around the interface and wake effect. Viscous shear forces in the continuous phase cause velocity gradients around the interface and deform the bubble, leading to breakage. Breakage can be seen as a balance between external viscous stresses and surface tension forces. Another cause of shear stress is the wake effect: if a bubble has a large part outside a wake region, the wake boundary could split. The bubble is elongated and breaks into two equal size daughters or into several smaller bubbles (Renardy et al. 2002).

Shearing-off and interfacial instability could be important if the bubble size increases: several small bubbles are sheared-off from a big one. The balance between the viscous shear force and the surface tension of the cap or slug bubbles is considered. The interfacial viscous shear forces are negligible in air-water systems as the viscosity of water is low. The shearing-off process is characterized by small

bubbles sheared-off from a big one and this phenomenon is also called erosive breakage. The shearing-off processes are due to the gas velocity profile into very large bubbles: gas molecules inside the bubble move globally at the bubble terminal velocity. Near the bubble interface, the velocity is instead equal to the liquid film (Fu & Ishii 2003).

Breakage is due to interfacial instabilities in the case of absence of liquid-phase net flow. Rayleigh-Taylor instability occurs if a density difference is present and a light liquid is accelerated into a heavy fluid. Kelvin-Helmholtz instability occurs if the density ratio is similar to one and a relative velocity exists. Turbulent fluctuations are assumed to be the dominant breakage mechanism and the other mechanisms are neglected in the case of turbulent flow.

The number and the size of the generated bubbles are necessary to describe completely breakage. This information is included in the daughter distribution function β that depends on the dimension of the parent bubble and on the local turbulence level. The number of daughter bubbles depends on the difference of density between the two phases and on the viscosity of the dispersed phase. Breakage is mainly binary if the density difference is high and the viscosity of the dispersed phase is low, as in bubble columns (Andersson et al. 2012). Only binary breakage is considered in the models; the parent bubble can break in very different daughter bubbles.

The daughter distribution functions can be divided into:

- empirical model;
- statistical model;
- phenomenological model.

The first class of daughter distribution functions requires a great number of experiments to be determined. A statistical model can be formulated in term of different distributions: delta function, normal function, beta function and uniform distribution. Phenomenological models can be classified according to the final shape: bell-shape, U-shape and M-shape. Many of these distributions are linked to a specific breakage kernel.

The first phenomenon that was studied is the breakage due to turbulent fluctuations and collisions in the case of kinetic energy of bubbles greater than a critical value. Coulaloglou & Tavlarides (1977) studied the turbulent nature of the liquid-liquid dispersion and results can be easily extended to bubbles. The breakage frequency g_i is defined as the inverse of the breakage time multiplied by the fraction of bubbles that break. The breakage time is obtained by the homogeneous isotropic turbulence theory, assuming that the bubble velocity is the same as that of the turbulent eddies. The efficiency is the fraction of bubbles that actually break: it is proportional to the fraction of drops that have a turbulence kinetic energy greater than their surface tension. Through a balance is possible to obtain the following breakage kernel:

$$g(L) = c_1 L^{-2/3} \varepsilon^{1/3} \exp\left[-\frac{c_2 \sigma}{\rho_g \varepsilon^{2/3} L^{5/3}}\right]. \tag{5.18}$$

The damping effect of bubbles on the local turbulence intensity is important for

high gas fractions and was considered by Coulaloglou & Tavlarides (1977):

$$g(L) = c_1 L^{-2/3} \frac{\varepsilon^{1/3}}{1+\alpha_g} \exp\left[-\frac{c_2 \sigma \left(1+\alpha_g\right)^2}{\rho_g \varepsilon^{2/3} L^{5/3}}\right]. \tag{5.19}$$

where α_g is the local gas volume fraction.

Prince & Blanch (1990) explained that the model of Coulaloglou & Tavlarides (1977) generally predicts a breakage frequency that appears to be lower than the experimental results for gas-liquid mixtures. The gas density in a gas-liquid system is much lower than in a liquid-liquid dispersion. In gas-liquid systems, the density of gas ρ_g could be replaced by the density of the liquid phase ρ_l (Lasheras et al. 2002). The previous expressions become respectively:

$$g(L) = c_1 L^{-2/3} \varepsilon^{1/3} \exp\left[-\frac{c_2 \sigma}{\rho_l \varepsilon^{2/3} L^{5/3}}\right] \tag{5.20}$$

and

$$g(L) = c_1 L^{-2/3} \frac{\varepsilon^{1/3}}{1+\alpha_g} \exp\left[-\frac{c_2 \sigma \left(1+\alpha_g\right)^2}{\rho_l \varepsilon^{2/3} L^{5/3}}\right]. \tag{5.21}$$

Velocity fluctuations around the bubble's surface greater than a critical value u_{cr} was initially studied by Narasimhan et al. (1979) with a stochastic model in the case of similar density and similar viscosity between the phases. The eddies arrive next to the surface of the bubble and cause differences in velocity fluctuations. The arrival of the eddies could be considered as a Poisson (rare) process. The critical velocity is calculated from the energy balance: following this theory symmetrical binary breakage is the main phenomenon, as this requires less energy than asymmetrical ones. It is inconsistent with the experimental observations of Hesketh et al. (1987), as the symmetrical binary breakage is not the main phenomenon. However, this is a controversial issue in the literature and no general theory has been developed yet.

Alopaeus et al. (2002) corrected the model, considering a dependency on turbulent dissipation rate, obtaining the following expression for drops in liquid:

$$g(L) = c_3 \varepsilon^{1/3} \operatorname{erfc}\left(\sqrt{c_4 \frac{\sigma}{\rho_l \varepsilon^{2/3} L^{5/3}} + c_5 \frac{\mu_g}{\sqrt{\rho_l \rho_g} \varepsilon^{1/3} L^{4/3}}}\right). \tag{5.22}$$

resulting however in a constant c_3 that is not dimensionless. In this model, the viscous forces are also considered in addition to the interfacial ones.

The mechanisms of bubble and droplet breakage have similarities. Laakkonen et al. (2006) modified this kernel in order to use it also for gas-liquid systems, substituting the gas viscosity with the viscosity of the continuous phase, by considering that viscous stresses that resist the breakage depend on the liquid viscosity that surrounds the bubble instead of the gas viscosity, which is low:

$$g(L) = c_3 \varepsilon^{1/3} \operatorname{erfc}\left(\sqrt{c_4 \frac{\sigma}{\rho_l \varepsilon^{2/3} L^{5/3}} + c_5 \frac{\mu_l}{\sqrt{\rho_l \rho_g} \varepsilon^{1/3} L^{4/3}}}\right), \tag{5.23}$$

where c_3, c_4 and c_5 are numerical constants. The last two constants do not depend on the studied system and they are obtained by the turbulence theory: they are

equal to $c_4 = 0.04$ and $c_5 = 0.01$. The first constant was obtained with experimental data and for very different systems (i.e. air-water systems) and it is equal to 4.0.

The daughter distribution function of Laakkonen et al. (2006) considers binary breakage, as the most common phenomenon for gas bubbles. Laakkonen et al. (2006) used a very simple daughter distribution function based on a common statistical distribution function, the β-distribution:

$$\beta\left(L,\,\lambda\right) = N_f\left(9 + \frac{33}{2}C + 9C^2 + \frac{3}{2}C^3\right)\left(\frac{L^2}{\lambda^3}\right)\left(\frac{L^3}{\lambda^3}\right)^2\left(1 - \frac{L^3}{\lambda^3}\right)^C, \tag{5.24}$$

where L is the size of the daughter bubble and λ is the size of the mother bubble. N_f is computed imposing that:

$$\int_0^\infty \beta\left(L,\,\lambda\right) dL = N_f \tag{5.25}$$

and that:

$$\int_0^\infty \beta\left(L,\,\lambda\right) L^3 dL = \lambda^3, \tag{5.26}$$

obtaining:

$$N_f = \frac{4}{3} + \frac{C}{3}. \tag{5.27}$$

The Eq. (5.24) can be rewritten as (Laakkonen et al. 2007):

$$\beta\left(L,\,\lambda\right) = \frac{1}{2}(1+C)(2+C)(3+C)(4+C)\left(\frac{L^2}{\lambda^3}\right)\left(\frac{L^3}{\lambda^3}\right)^2\left(1 - \frac{L^3}{\lambda^3}\right)^C, \tag{5.28}$$

where the constant C is assumed to be equal to 2 for binary breakage. The final form for the daughter distribution function is:

$$\beta\left(L,\,\lambda\right) = 180\left(\frac{L^2}{\lambda^3}\right)\left(\frac{L^3}{\lambda^3}\right)^2\left(1 - \frac{L^3}{\lambda^3}\right)^2. \tag{5.29}$$

Wang et al. (2003) proposed a breakage kernel due to interactions between eddies and bubbles:

$$g(L) = \int_0^{0.5} g(f_v|L) df_v, \tag{5.30}$$

where:

$$g(f_v|L) = 0.923\left(1 - \alpha_g\right)^{1/3}\int_{\lambda_{min}}^{L} P_b(f_v|L,\,\lambda)\frac{(\lambda + L)^2}{\lambda^{11/3}} d\lambda, \tag{5.31}$$

where λ_{min} is the minimum eddy size for breakage and $P_b(f_v|L,\,\lambda)$ is the breakage probability density for a bubble of size L breaking with breakage fraction f_v when hit by an eddy of size λ (Wang et al. 2004).

Prince & Blanch (1990) considered breakage due to bubble collisions with eddies equal to or smaller than the bubbles, fixing a minimum value for the eddies of $0.2L$. Only eddies having a velocity larger than the critical velocity are considered. An energy balance (considering the surface tension) provides the following kernel:

$$g(L) = \int_{0.2L}^{L} \frac{0.07\pi^4}{\lambda^4}(L+\lambda)^2\left(L^{2/3} + \lambda^{2/3}\right)^{1/2}\varepsilon^{1/3}\exp\left(-\frac{1.18\sigma}{\lambda^{2/3}\rho_l L\varepsilon^{2/3}}\right) d\lambda. \tag{5.32}$$

Prince & Blanch (1990) did not include the daughter distribution function in the model and used a uniform function.

Luo & Svendsen (1996) proposed a breakage kernel based on isotropic turbulence theory and probability, with the advantage that the daughter bubble size distribution is obtained directly from the breakage frequency:

$$g(L) = \int_0^{0.5} g(f_v|L)df_v, \tag{5.33}$$

$$\beta(f_v, L) = \frac{2g(f_v|L)}{\int_0^1 g(f_v|L)df_v}, \tag{5.34}$$

$$g(f_v|L) = 0.923\,(1-\alpha_g)\,n\left(\frac{\varepsilon}{L^2}\right)^{1/3}\int_{\xi_{min}}^1 \frac{(1+\xi)^2}{\xi^{11/3}}\exp\left(-\frac{12c_f\sigma}{\beta\rho_l\varepsilon^{2/3}L^{5/3}\xi^{11/3}}\right)d\xi, \tag{5.35}$$

where ξ is the ratio between the size of the eddies able to break the bubble and the dimension of the bubble. c_f is computed as:

$$c_f(f) = f^{2/3} + (1-f)^{2/3} - 1, \tag{5.36}$$

where f represents the volume ratio between a daughter bubble and its primitive bubble.

The ξ_{min} is related to the Kolmogorov scale $\mathcal{L}_{Kol}$:

$$\xi_{min} = \frac{11.4}{\mathcal{L}_{Kol}}\left(\frac{\mu_l^3}{\rho_l^3\varepsilon}\right)^{1/4}. \tag{5.37}$$

Lehr et al. (2002) modelled a breakage kernel following the approach of Luo & Svendsen (1996), with the difference that the kernel does not present experimental constants. The formulations of $g(L)$ and $\beta(f_v, L)$ are the same as the model of Luo & Svendsen (1996), respectively Eq. (5.33) and Eq. (5.34), whereas $g(f_v|L)$ is:

$$g(f_v|L) = \int_{L_1}^{L} 0.8413\sqrt{2}\frac{\sigma(\lambda+d)^2}{\lambda^{13/3}}\exp\left(-\frac{2\sigma}{\rho_l\varepsilon^{2/3}L_1\lambda^{2/3}}\right)d\lambda, \tag{5.38}$$

where L_1 is the smaller daughter bubble size (Wang et al. 2005*a*).

Carrica & Clausse (1993) suggested to use the following kernel in order to consider the breakage due to interfacial instability:

$$g(L) = g^*\frac{(L-L_{cr})^m}{(L-L_{cr})^m + L_{cr}^m}, \tag{5.39}$$

where L_{cr} is the critical bubble diameter, that for air-water systems is equal to $27\,mm$. g^* and m are model parameters, set to $100\,s^{-1}$ and 6.0 respectively.

No detailed studies describe this phenomenon, so it is assumed that two equal daughter bubbles are created, whereas in case of breakage due to turbulence different daughter distribution functions are available. Viscous shear forces and shearing-off process have no noticeable impact on breakage for gas-liquid systems. For this reason, these kernels are not reported in this work.

5.2.3 Coalescence kernel

Coalescence may appear more complex than breakage: not only it involves interactions of bubbles with the continuous phase but also interactions with surrounding bubbles once they collide due to the external flow and forces. Coalescence could be studied using empirical models or first-principle models. The models of the first group are simpler and they represent power law functions with parameters that are empirically adjusted, depending on disperse phase concentration, number of bubbles, size of bubbles and other physical properties, as proposed by Casamatta & Vogelpohl (1985), Konno et al. (1988), Wright & Ramkrishna (1994) and Kentish et al. (1998).

The main limitation of these empirical models is that they depend on the experimental set-up and on the geometry of the studied system. Results cannot be extended to other cases: for this reason, first-principle models are preferable and studied in this work.

Three main first-principle models are usually proposed to study the coalescence phenomenon (Liao & Lucas 2010):

- film-drainage model;
- energy model;
- critical velocity model.

The film-drainage model is the most popular. This theory is based on the idea that two bubbles, after colliding, could coalesce together or could be prevented from coalescing by the thin film of liquid that is trapped between the bubbles (Shinnar & Church 1960). When two bubbles collide, they fully define the dynamics of the balance between repulsive forces, caused by the film of liquid that separates them and the attractive forces. This dynamics in turn defines the drainage of the liquid. The phenomenon can be divided into three steps:

- approach and collision between bubbles;
- drainage of the thin film of liquid trapped between bubbles until a critical thickness;
- final merging consequent to the film ruptures.

The first step is governed by the external forces acting on the bubbles. The second step is the controlling one, as the liquid film must be drained out until a critical thickness, to obtain coalescence.

The energy model assumes that the molecular attraction forces between bubbles are weaker than the turbulent forces and assumes therefore that coalescence is controlled by the second ones. During an energetic collision, the approach velocity of two colliding bubbles overcomes a critical value and causes an immediate coalescence event. The energy model was proposed by Howarth (1964) and confirmed by the experiments of Park & Blair (1975) and Kuboi et al. (1972): they observed that a fraction of collisions causes an immediate coalescence and this fraction increases when the energy of collision grows. According to the energy model, coalescence will occur immediately when the approach velocity exceeds a critical value at the instant of collision.

The critical velocity model assumes that coalescence is favoured by gentle collisions, as observed by Doubliez (1991). Lehr et al. (2002) studied the relationship between coalescence and approach velocity, observing that a low approach velocity leads to coalescence.

For each model, the coalescence kernel can be separated into two parts: a collision frequency and a coalescence efficiency. The first term considers the number of collisions in a certain time interval. It has units of volume divided by time and its physical meaning is the following: the collision frequency multiplied by the number of bubbles per unit volume (bubble number density) represents the actual number of collisions between bubbles per unit time. The coalescence efficiency is instead a dimensionless quantity that states the fraction of collision events that actually result in coalescence events:

$$h\left(L_1, L_2\right) = h_0\left(L_1, L_2\right) \lambda\left(L_1, L_2\right), \tag{5.40}$$

where $h\left(L_1, L_2\right)$ is the coalescence kernel, $h_0\left(L_1, L_2\right)$ is the collision frequency and $\lambda\left(L_1, L_2\right)$ is the coalescence efficiency.

Bubbles collisions are caused by differences in their relative velocities. The relative motion is due to different mechanisms as summarized below:

- motion due to turbulent fluctuations in the continuous phase;
- different bubble rise velocities caused by buoyancy and other forces, e.g. drag force;
- motion due to mean-velocity gradients in the flow;
- wake-entrainment;
- capture of the bubbles in turbulent eddies.

5.2.3.1 Collision frequency

The total collision frequency is generally considered as the sum of the rates due to the previously cited mechanisms. The first is the most important at medium superficial gas velocities and the other terms are often negligible; on the contrary, at high superficial gas velocities, the wake entrainment could be important due to the formation of very large bubbles. Bubble collisions due to different bubble rise velocities cannot be ignored if the bubble rise velocity depends on the bubble size. If two bubbles are captured at the same time in one eddy, they could coalesce thanks to the flow shear rate into the eddy (Wang et al. 2006). The final coalescence frequency can, therefore, be written as a summation of five different terms:

$$h_0 = h_0^T + h_0^B + h_0^V + h_0^W + h_0^E, \tag{5.41}$$

where the overall collisions frequency is related respectively to turbulent fluctuations, buoyancy force, velocity-gradient, wake-entrainment and capture in turbulent eddies.

Collisions due to turbulent fluctuations. Bubble collisions due to turbulent eddies are calculated by analogy with the gas kinetic theory by Prince & Blanch (1990). The random movement of bubbles in a turbulent flow is considered similar to the random gas motion in the kinetic gas theory (Kennard 1938). The collision frequency due to turbulence $h_0^T(L_1, L_2)$ is calculated as the volume swept by the moving bubble in a certain time interval:

$$h_0^T(L_1, L_2) = S_{12} u_{rel}, \tag{5.42}$$

where u_{rel} is the relative approach velocity between two bubbles. S_{12} is the collision-sectional area of the colliding bubbles and can be calculated as:

$$S_{12} = \frac{\pi}{4}(L_1 + L_2)^2, \tag{5.43}$$

where L_1 and L_2 are the diameters of the colliding bubbles.

In order to obtain the relative velocity, the most common assumption is that the colliding bubbles assume the velocity of an equal-sized eddy, as considered by Coulaloglou & Tavlarides (1977), Prince & Blanch (1990) and Luo (1993). A too large eddy transports bubbles without effect on the relative movement whereas a too small eddy does not have sufficient energy to modify bubble movement. The relative velocity could therefore be calculated as (Liao & Lucas 2010):

$$u_{rel} = \sqrt{u_{t1}^2 + u_{t2}^2}, \tag{5.44}$$

where u_{t1} is the eddy velocity with size L_1 and u_{t2} is the eddy velocity with size L_2. Applying classical turbulence theories and considering the inertial subrange of isotropic turbulence, the mean turbulent velocity of an eddy is calculated as (Levich 1962):

$$u_{t1} = \sqrt{2}\varepsilon^{1/3} L_1^{1/3}. \tag{5.45}$$

The relative velocity becomes:

$$u_{rel} = \sqrt{2}\varepsilon^{1/3}\sqrt{L_1^{2/3} + L_2^{2/3}}. \tag{5.46}$$

The final expression for the collision frequency is:

$$h_0^T(L_1, L_2) = \sqrt{2}\frac{\pi}{4}(L_1 + L_2)^2 \varepsilon^{1/3}\sqrt{L_1^{2/3} + L_2^{2/3}}. \tag{5.47}$$

Prince & Blanch (1990) modified Eq. (5.47):

$$h_0^T(L_1, L_2) = C_1'(L_1 + L_2)^2 \varepsilon^{1/3}\sqrt{L_1^{2/3} + L_2^{2/3}}, \tag{5.48}$$

where C_1' is a constant that depends on the studied system and varies in the range of $0.28 - 1.11$. This equation is widely used to compute the collision frequency.

A size ratio between bubbles and eddies could be considered, while in the original model bubbles and eddies were considered equal-sized (Liao & Lucas 2010). Bubbles larger than the turbulence integral length scale $\mathcal{L}_t$ cannot be affected by

turbulence. Differences between bubble and liquid velocities are considered. Collisions lead to coalescence only if $L_1 < \mathcal{L}_t$, as stated by Colin et al. (2004):

$$u_{rel} = \begin{cases} \frac{C_t}{\sqrt{1.61}} \left(\varepsilon \frac{L_1+L_2}{2}\right)^{1/3} & L_2 < \mathcal{L}_t; \\ \frac{C_t}{\sqrt{1.61}} \left(\varepsilon L_1\right)^{1/3} & L_2 > \mathcal{L}_t. \end{cases} \tag{5.49}$$

Alternatively, to consider this effect, a parameter could be added to the Eq. (5.47) (Wang et al. 2005*b*):

$$\Pi = \exp\left[-\left(\frac{L_{bt,12}}{h_{bt,12}}\right)^6\right], \tag{5.50}$$

where $L_{bt,12}$ is the mean relative turbulent path length of bubbles and is related to the mean distance between bubbles:

$$L_{bt,12} = \sqrt{L_{bt,1}^2 + L_{bt,2}^2}, \tag{5.51}$$

where:

$$L_{bt,1} = \sqrt{2}\left(\varepsilon L_1\right)^{1/3} \left(\frac{L_1^2}{4\varepsilon}\right)^{1/3} \approx 0.89 L_1; \tag{5.52}$$

Wu et al. (1998) obtained this correction factor by assuming that average eddies and bubbles have the same order size:

$$\Pi = \left[1 - \exp\left(-C_\Pi \frac{\alpha_{\max}^{1/3} \alpha_g^{1/3}}{\alpha_{\max}^{1/3} - \alpha_g^{1/3}}\right)\right], \tag{5.53}$$

where the constant C_Π depends on the studied system and it is equal to 3 for air-water systems.

The secondmodificationisto consider the existence of bubbles that reduces the free space for bubble movement and causes an increase in the collision frequency. Another important correction is to consider the bubble presence, that reduces the free space for bubble motion and causes an increase in collision frequency. Many correlations are available to consider this effect, adding a new parameter γ (Liao & Lucas 2010):

- Wu et al. (1998)

$$\gamma = \frac{1}{\alpha_{\max}^{1/3}\left(\alpha_{\max}^{1/3} - \alpha_g^{1/3}\right)} \qquad \alpha_{\max} = 0.8; \tag{5.54}$$

- Hibiki & Ishii (2000)

$$\gamma = \frac{1}{\alpha_{\max} - \alpha_g} \qquad \alpha_{\max} = 0.52; \tag{5.55}$$

- Lehr et al. (2002)

$$\gamma = \exp\left[-\left(\frac{\alpha_{\max}^{1/3}}{\alpha_g^{1/3}} - 1\right)^2\right] \qquad \alpha_{\max} = 0.6; \tag{5.56}$$

- Wang et al. (2005*b*)

$$\gamma = \frac{\alpha_{\max}}{\alpha_{\max} - \alpha_g} \qquad \alpha_{\max} = 0.8. \tag{5.57}$$

Other correlations for γ are available in the literature.

The final equation for the collisions efficiency proposed by Wang et al. (2005*b*) is:

$$h_0\left(L_1, L_2\right) = C_2' \, \gamma \, \Pi \left(L_1 + L_2\right)^2 \varepsilon^{1/3} \sqrt{L_1^{2/3} + L_2^{2/3}}, \tag{5.58}$$

with C_2'=$\sqrt{2}\pi/4$.

Lehr et al. (2002) proposed the same general expression without Π and using γ from Eq. (5.56) instead of Eq. (5.57).

Collisions due to buoyancy. This term is non-negligible if the bubble rise velocity is strongly influenced by the size of the bubbles, as a consequence of the balance between buoyancy, gravity and drag forces. Friedlander (1977) proposed this expression:

$$h_0^B\left(L_1, L_2\right) = S_{12} |u_{r1} - u_{r2}|, \tag{5.59}$$

where u_{r1} is the rise velocity of bubble L_1, that depends on the body forces.

Velocity gradient-induced collisions. This term is normally neglected. Anyway, Friedlander (1977), for laminar shear, proposed the following expression:

$$h_0^V\left(L_1, L_2\right) = \frac{1}{6}(L_1 + L_2)^3 S_{h_R}. \tag{5.60}$$

Prince & Blanch (1990) used this formula to describe the liquid circulation due to high gas rates in bubble columns. The previous equation could be also applied to a turbulent flow, if collisions are caused by the velocity shear of the mean flow. The constant S_{h_R} could be modified.

Collisions due to wake entrainment. A large sphere-cap bubble has a big wake region, where other bubbles are accelerated, causing a collision with the former one (Bilicki & Kestin 1987). Wake-induced collisions are important for large cap bubbles into sufficiently viscous media with laminar wakes.

Kalkach-Navarro et al. (1994) derived the collision frequency due to wake-entrainment $h_0^W\left(L_1, L_2\right)$ as:

$$h_0^W\left(L_1, L_2\right) = C_2' \left(V_1 + V_2\right) \left(V_1^{1/3} + V_2^{1/3}\right)^2, \tag{5.61}$$

where C_2' is an experimental constant and V_1 and V_2 are the volumes of the two bubbles.

Considering wake interactions and bubble swarms, Colella et al. (1999) proposed an equation for bubble-bubble interactions in the column:

$$h_0^W\left(L_1, L_2\right) = u_{rel} \frac{V_1^{BOX}}{\langle l_w \rangle}, \tag{5.62}$$

where u_{rel} is the relative velocity, $\langle l_w \rangle$ is the normalized average bubbles distance (assumed equal to 1) and V_1^{BOX} is the volume that is influenced by the wake of the bubble L_1, following the theory of Nevers & Wu (1971).

Hibiki et al. (2001) calculated the wake-induced collision frequency for bubbles with uniform size as:

$$h_0^W(L_1, L_1) = C_3' C_D^{1/3} L_1^2 u_{rel}. \tag{5.63}$$

It was later extended by Wang et al. (2005*b*) and Wang et al. (2005*a*) to the multi-group case:

$$h_0^W(L_1, L_2) = C_3' C_D^{1/3} L_1^2 u_{rel}, \tag{5.64}$$

where L_1 is the diameter of the leading bubble.

Wang et al. (2005*a*) proposed also the following correlation, in order to obtain directly the coalescence kernel:

$$h_0^W(L_1, L_2) = 15.4 L_1^2\, 0.71 \sqrt{g L_1}. \tag{5.65}$$

Collisions due to capture in a turbulent-eddy. Chesters (1991) stated that collisions are dominated by viscous forces in a turbulent flow, if the bubble size is much smaller than the energy dissipating eddies, given that the bubble velocities are very similar to the liquid velocity:

$$h_0^E(L_1, L_2) = \frac{0.618}{8}(L_1 + L_2)^3 \sqrt{\frac{\varepsilon}{\nu}}. \tag{5.66}$$

A typical bubble column has eddies that vary from a minimum size depending on the Kolmogorov scale and a maximum size that depends on the operating conditions. The ratio between bubble size and turbulence length scale is very important. Usually, in bubble columns, bubbles are contained in the inertial subrange and in that case the collisions due to turbulent fluctuations are very much higher than collisions due to capture in a turbulent-eddy. In the rare case of very small bubbles, collisions due to capture in a turbulent-eddy become important.

5.2.3.2 Coalescence efficiency

Only a fraction of collisions leads to coalescence: some of the colliding bubbles separate after collision or bounce off each other. Efficiency can be divided into the three main physical models proposed: film-drainage model, energy model and critical velocity model.

Film-drainage model. The film-drainage model determines the coalescence efficiency by considering two characteristic time scales: the contact time (the time for which the bubbles stay in contact after a collision) and the drainage time (the time required by the liquid film between two particles to drain out). Coulaloglou (1975) proposed to describe the efficiency as:

$$\lambda(L_1, L_2) = \exp\left(-\frac{t_D}{t_C}\right), \tag{5.67}$$

where t_D is the drainage time and t_C is the contact time.

Different regimes of drainage can be identified according to the rigidity of the bubbles (deformable or non-deformable) and the mobility of the interfaces (immobile, partially mobile or fully mobile). Bubbles can be assumed rigid when the viscosity is very high or when their diameter is smaller than 1 mm. Chesters (1991) stated that the radial velocity in the film depends on a certain pressure variation and then on an interaction force as follows:

$$F = \frac{3\pi\mu_l L^2}{8h}\frac{\mathrm{d}h}{\mathrm{d}t}, \tag{5.68}$$

where F is the force that results again from the pressure fluctuations, the turbulent force and the repulsion forces, L is the bubbles diameter, h is the film thickness (i.e. the distance between the bubbles) and $\mathrm{d}h/\mathrm{d}t$ is the approach velocity.

Chesters (1991) derived the drainage time in case of constant compression force as

$$t_D = \frac{3\pi\mu_l}{8F}L^2 \ln\left(\frac{h_i}{h_f}\right), \tag{5.69}$$

where h_i and h_f are the thicknesses of the liquid film at the beginning and at the end of the drainage process respectively.

Jeffreys & Davies (1971) derived the drainage time for two bubbles with different diameters (L_1 and L_2) as

$$t_D = \frac{3\pi\mu_l}{F}\left(\frac{L_1 L_2}{L_1 + L_2}\right)^2 \ln\left(\frac{h_i}{h_f}\right). \tag{5.70}$$

where h_i and h_f are the thicknesses of the liquid film at the beginning and at the end of the drainage process, respectively, and F is the force that results again from the pressure fluctuations, the turbulent force and the repulsion forces.

Bubbles larger than 1 mm are considered deformable. In this case the mobility of the interface has an important effect. For immobile interfaces, the velocity profile in the film is parabolic (laminar flow) with no slip at the surface. The approximation of immobile interfaces is applicable to systems containing surfactants or if the viscosity of the dispersed phase is very high. Chesters (1991) derived the following expression for the approach velocity:

$$\frac{\mathrm{d}h}{\mathrm{d}t} = \frac{2h^3 F}{3\pi\mu_l R_a^4}, \tag{5.71}$$

with the interaction force considered proportional to the excess film pressure:

$$F \propto \pi R_a^2 \frac{4\sigma\left(L_1 L_2\right)}{L_1 L_2}, \tag{5.72}$$

where R_a is the film dimension.

And thus, integrating from h_i to h_f, the drainage time results to be:

$$t_D = \frac{3F\mu_l}{32\pi\sigma^2}\left(\frac{L_1 L_2}{L_1 + L_2}\right)^2 \left(\frac{1}{h_f^2} - \frac{1}{h_i^2}\right). \tag{5.73}$$

For partially mobile surfaces, Chesters (1991) modified the previous expression for equal-size bubbles:

$$t_D = \frac{F^{1/2}\mu_g \pi}{2\pi\sigma / L^{3/2}}\left(\frac{1}{h_f} - \frac{1}{h_i}\right). \tag{5.74}$$

Deformable bubbles with fully mobile interfaces are the most difficult to study. In the inertial-controlled limit, as for bubbles in turbulent systems, Luo (1993) proposed the following expression:

$$t_D = 0.5 \frac{u_{12} \rho_l L_1^2}{(1 + L_1/L_2)^2 \sigma}. \tag{5.75}$$

The contact time was firstly studied by Levich (1962). Chesters (1991) explained that the contact time in turbulent flows is inversely proportional to the flow strain rate for the smallest eddies and the drainage velocity model which includes the contribution of inertia and viscous forces.

For highly viscous liquids the viscous term is prevalent. The approach velocity becomes

$$\frac{\mathrm{d}h}{\mathrm{d}t} = \frac{4h\sigma}{3\mu_l L} \tag{5.76}$$

and the drainage time is equal to

$$t_D = \frac{3\mu_l \left(L_1 L_2\right)}{4\sigma \left(L_1 + L_2\right)} \ln\left(\frac{h_i}{h_f}\right). \tag{5.77}$$

If inertia is the predominant phenomenon, the drainage time becomes

$$t_D = \frac{\rho_l \left(L_1 L_2\right)^2 u_{rel}}{32\sigma \left(L_1 + L_2\right)^2} \ln\left(\frac{h_i}{h_f}\right), \tag{5.78}$$

where u_{rel} is the relative velocity of the colliding bubbles.

Luo (1993) obtained an expression for the contact time, based on a parallel film model:

$$t_C = \left(1 + \frac{L_1}{L_2}\right) \sqrt{\frac{\left(\rho_g/\rho_l + C_{VM}\right) \rho_l L_1^3}{3\left(1 + L_1^2/L_2^2\right)\left(1 + L_1^3/L_2^3\right)\sigma}}, \tag{5.79}$$

where C_{VM} is a constant with a range of 0.5 - 0.8.

Podgórska & Marchisio (2016) studied in detail these mechanisms for drops in turbulent flows, providing better expressions for these systems.

Many coalescence efficiencies are available in the literature; the most common was proposed by Coulaloglou & Tavlarides (1977), applying the film drainage model to immobile interfaces:

$$\lambda\left(L_1, L_2\right) = \exp\left[-C_1'' \frac{\mu_l \rho_l \varepsilon}{\sigma^2} \left(\frac{L_1 L_2}{L_1 + L_2}\right)^4\right]. \tag{5.80}$$

Coulaloglou & Tavlarides (1977) modified this expression, in order to consider high gas volume fraction effects:

$$\lambda\left(L_1, L_2\right) = \exp\left[-C_2'' \frac{\mu_l \rho_l \varepsilon}{\sigma^2 (1 + \alpha_g)^3} \left(\frac{L_1 L_2}{L_1 + L_2}\right)^4\right]. \tag{5.81}$$

For partially and fully mobile interfaces, Lee et al. (1987) proposed two very complex equations with many parameters. More details are reported in Liao & Lucas (2010).

Chesters (1991) studied viscous collisions and proposed:

- for immobile bubbles

$$\lambda\left(L_1, L_2\right) = \exp\left(-C_3'' \frac{9\,\mu_l L_{eq}^4 \varepsilon \rho_l}{128\sigma^2 h_f^2}\right); \tag{5.82}$$

- for partially mobile interfaces

$$\lambda\left(L_1, L_2\right) = \exp\left(-C_4'' \frac{L_{eq}^{5/2}\sqrt{3}\mu_g \mu_l^{3/4}}{2^{9/2}\sigma^{3/2}\varepsilon^{1/4}{\rho_l}^{1/4} h_f}\right); \tag{5.83}$$

- for fully mobile interfaces

$$\lambda\left(L_1, L_2\right) = \exp\left(-C_5'' \frac{3L_{eq}\sqrt{\mu_l \varepsilon \rho_l}}{4\sigma} \ln\left(\frac{h_i}{h_f}\right)\right). \tag{5.84}$$

For all cases, the equivalent length is computed as:

$$L_{eq} = \left(\frac{1}{L_1} + \frac{1}{L_2}\right)^{-1}. \tag{5.85}$$

Similar expressions were proposed by the same author (Chesters 1991) for inertial collisions.

Luo (1993) obtained an expression for the efficiency starting with the definition of the contact time shown in Eq. (5.79).

Wang et al. (2005*b*) proposed different coalescence efficiency according to the mechanism of collision involved. They refuted the validity of Eq. (5.40), modifying it as follows:

$$h_0 = h_0^T \lambda^T + h_0^W \lambda^W + h_0^B \lambda^B. \tag{5.86}$$

Wang et al. (2005*b*) considered only coalescence due to turbulent eddies, wake entrainment and different rise velocities. In order to study the coalescence due to turbulent eddies, Wang et al. (2005*b*) proposed the following equation:

$$\lambda^T\left(L_1, L_2\right) = \exp\left\{-\frac{\sqrt{0.75\left[1+\left(\frac{L_1}{L_2}\right)^2\right]\left[1+\left(\frac{L_1}{L_2}\right)^3\right]\frac{\rho_l L_1\left(u_1^2+u_2^2\right)}{\sigma}}}{\left[\frac{\rho_g}{\rho_l}+C_{VM}\right]\left[1-\frac{L_1}{L_2}\right]^3}\right\}, \tag{5.87}$$

where C_{VM} is the virtual mass coefficient.

The efficiency linked to wake entrainment is:

$$\lambda^W\left(L_1, L_2\right) = \Theta \exp\left[-0.46\rho_l^{1/2}\frac{\varepsilon^{1/3}}{\sigma^{1/2}}\left(\frac{L_1 L_2}{L_1+L_2}\right)^{5/6}\right] \tag{5.88}$$

$$\Theta = \begin{cases} \frac{(L_2 - L_c/2)^6}{(L_2 - L_c/2)^6 + (L_c/2)^6} & L_2 \geq L_c/2 \\ 0 & L_2 \leq L_c/2, \end{cases} \tag{5.89}$$

where

$$L_c = 4\sqrt{\frac{\sigma}{g\Delta\rho}}. \tag{5.90}$$

It can be coupled with the Eq. (5.65), obtaining the following kernel due to wake entrainment:

$$h^W\left(L_1, L_2\right) = h_0^W\left(L_1, L_2\right)\lambda^W\left(L_1, L_2\right) =$$

$$= 15.4\,\Theta L_1^2\,0.71\sqrt{gL_1}\exp\left[-0.46\rho_l^{1/2}\frac{\varepsilon^{1/3}}{\sigma^{1/2}}\left(\frac{L_1L_2}{L_1+L_2}\right)^{5/6}\right]. \tag{5.91}$$

Wang et al. (2005*b*) did not investigate the coalescence efficiency linked to the mechanism of different rise velocities: they set a constant value of 0.5 for the efficiency.

Energy model. Sovova (1981) developed a coalescence model for the energetic collisions of droplets, considering the ratio between kinetic collision energy and interfacial energy:

$$\lambda\left(L_1, L_2\right) = \exp\left(-C_6''\frac{E_\sigma}{E_{kinetic}}\right) = \exp\left(-C_6''\frac{\sigma\left(V_1^{2/3}+V_2^{2/3}\right)}{\frac{1}{2}\rho_g\frac{V_1V_2}{V_1+V_2}u_{rel}^2}\right). \tag{5.92}$$

A similar expression was formulated by Simon (2004):

$$\lambda\left(L_1, L_2\right) = \exp\left(-C_6''\frac{\sigma\left(V_1^{2/3}+V_2^{2/3}\right)}{\rho_g\varepsilon^{2/3}\left(V_1^{11/9}+V_2^{11/9}\right)}\right). \tag{5.93}$$

Sovova (1981) proposed a miscellaneous model, that considers both the film drainage model, both the energy model:

$$\lambda\left(L_1, L_2\right) = \lambda_1\left(L_1, L_2\right) + \lambda_2\left(L_1, L_2\right) - \lambda_1\left(L_1, L_2\right)\lambda_2\left(L_1, L_2\right), \tag{5.94}$$

where $\lambda_1\left(L_1, L_2\right)$ is calculated from the energy model and $\lambda_2\left(L_1, L_2\right)$ is calculated from the film drainage model.

Critical approach velocity model. Lehr et al. (2002) observed that above a certain relative approach velocity the bubbles bounce; if the relative approach velocity is lower than a critical value then the bubbles can collide. Starting with the observation that gentle collisions lead to more efficient coalescence, Lehr et al. (2002) proposed the following coalescence efficiency:

$$\lambda\left(L_1, L_2\right) = \min\left(\frac{u_{crit}}{u_{rel}}, 1\right), \tag{5.95}$$

here the relative velocity u_{rel} is reported in Eq. (5.46) and the critical approach velocity u_{crit} depends on the studied system and can be determined experimentally. By fitting with experiments, the u_{crit} has found to be equal to 0.08 m/s for distilled water-air systems. This critical value does not depend on the size of the bubbles in the studied range (3-8 mm). In liquid with additives the coalescence inhibition lead

to lower critical velocities. The final expression for the coalescence kernel considers also the γ correction of Eq. (5.56) resulting in (Lehr et al. 2002):

$$h\left(L_1, L_2\right) = \frac{\pi}{4}\left(L_1 + L_2\right)^2 u_{rel}\, \min\left(\frac{u_{crit}}{u_{rel}}, 1\right)\gamma \tag{5.96}$$

or alternatively in:

$$h\left(L_1, L_2\right) = \frac{\pi}{4}\left(L_1 + L_2\right)^2 \min(u_{rel}, u_{crit})\, \exp\left[-\left(\frac{\alpha_{\max}^{1/3}}{\alpha_g^{1/3}} - 1\right)^2\right]. \tag{5.97}$$

5.3 Quadrature Method of Moments (QMOM)

QBMMs constitute a particular class of very successful methods that overcome the closure problem by using quadrature approximations. A general quadrature of N nodes requires knowledge of N weights (w_i) and N nodes (L_i) with $1 \geq i \geq N$ (Marchisio & Fox 2013).

For univariate systems the internal coordinate is a scalar; for M-variate systems the internal coordinate is a vector of length M. Using QMOM, the moment equations are solved by estimating the source terms through the quadrature approximation. The quadrature approximation permits to overcome the closure problem. This approximation is determined from the available computed moments by employing moment-inversion algorithms.

This method has a degree of accuracy higher than interpolation schemes of the same order, as it makes use of a Gaussian quadrature approximation. This is done by determining the sequence of polynomials orthogonal to the unknown NDF from its moments. As the nodes of the quadrature approximation are the roots of the polynomial of order N orthogonal to the NDF, the approximation can be summarized as:

$$\int f(\xi)\, n(\xi) \mathrm{d}\xi \approx \sum_{i=1}^{N} f(\xi_i) w_i, \tag{5.98}$$

where $n(\xi)$ is the unknown NDF and ξ is here a generic internal coordinate, as for example bubble size.

This approximation is exact if $f(\xi)$ is a polynomial of order $2N-1$ or smaller (Dette & Studden 1997). An interpolation formula with N equally spaced nodes has a degree of accuracy of $N-1$; a Gaussian quadrature has a degree of accuracy of $2N-1$. For this reason, quadrature approximations are very interesting: their degree of accuracy is essentially twice that of other formulas with the same number of nodes.

A quadrature of order N is constructed by tracking the first $2N$ moments. If the number of nodes is higher, the accuracy increases, but also the computation cost increases. Moreover, numerical problems might arise when N increases. In fact, transport equations for moments of higher order are more likely to make the overall CFD simulation unstable and hinder convergence. The best compromise for bubble columns is often to use three nodes for the quadrature approximation, solving six additional moment equations for the gas phase:

$$\frac{\partial}{\partial t}\left(\rho_g m_k\right) + \nabla \cdot \left(\rho_g m_k \mathbf{u}_g\right) = \rho_g \bar{S}_{m_k}, \tag{5.99}$$

where ρ_g is the gas phase density, $\mathbf{u}_g$ is the gas phase average velocity, m_k is the moment of order k of the BSD, $\bar{S}_{m_k}$ is the normalized source term for the k^{th} moment due to coalescence and breakage.

The calculation of nodes and weights of the quadrature approximation is obtained by the moment of order k:

$$m_k = \int_o^\infty n(L)\, L^k \, \mathrm{d}L \approx \sum_{i=1}^{N=3} w_i \, L_i^k, \tag{5.100}$$

where $n(L)$ is the unknown BSD or NDF.

The moments can be normalized with respect to the local bubble volume fraction, in order to simplify the implementation:

$$m_k = \mu_k \alpha_g; \tag{5.101}$$

resulting in:

$$\frac{\partial}{\partial t}\left(\rho_g \alpha_g \mu_k\right) + \nabla \cdot \left(\rho_g \alpha_g \mu_k \mathbf{u}_g\right) = \rho_g \bar{S}_{m_k}. \tag{5.102}$$

Summarizing moments are transported into the equations and weights and nodes are used to calculate the source terms. It is necessary to use a procedure that allows determining the N quadrature nodes and weights from the $2N$ moments of the BSD. This is called inversion algorithm and will be detailed below (Marchisio & Fox 2013).

Standard procedures could be used to solve these systems but these are not very efficient. For the quadrature theory, the BSD must be non-negative and non-null in the integration interval and all its moments must exist. An orthogonal polynomial family $\{P_\alpha(L)\}$ ought to be defined in the interval of integration. The polynomials are obtained using the following recurrence formula:

$$P_{\alpha+1}(L) = (L - a_\alpha)P_\alpha(L) - b_\alpha P_{\alpha-1}(L), \tag{5.103}$$

where α varies from 0 to N and where

$$a_\alpha = \frac{\int L n(L) P_\alpha(L) P_\alpha(L) dL}{\int n(L) P_\alpha(L) P_\alpha(L) dL}, \tag{5.104}$$

$$b_\alpha = \frac{\int n(L) P_\alpha(L) P_\alpha(L) dL}{\int n(L) P_{\alpha-1}(L) P_{\alpha-1}(L) dL}. \tag{5.105}$$

The initial conditions are $P_{-1}(L) = 0$ and $P_0(L) = 1$. For the bubble size, the integration interval varies from 0 to $+\infty$.

The recursive formula generates an orthogonal polynomial family that considers the weight function (namely the BSD) in the interval of integration; it is also possible to write the coefficients a_α and b_α in terms of the moments, e.g. the following coefficients can be calculated using m_0, m_1, m_2, and m_3:

$$a_0 = \frac{m_1}{m_0}, \tag{5.106}$$

$$a_1 = \frac{m_3 m_0^2 + m_1^3 - 2 m_1 m_0}{m_2 m_0 + m_1^2 - 2 m_1^2 m_0}, \tag{5.107}$$

$$b_1 = \frac{m_2 m_0 + m_1^2 - 2m_1^2 m_0}{m_0^2}. \tag{5.108}$$

An important feature of orthogonal polynomials is that the internal coordinates are always sampled into the domain of the BSD.

Using the recursive formula of the orthogonal polynomials, it is possible to find weights and nodes by solving the following eigenvalue/eigenvector problem:

$$L \begin{bmatrix} P_0(L) \\ P_1(L) \\ P_2(L) \\ \vdots \\ P_{N-2}(L) \\ P_{N-1}(L) \end{bmatrix} = \begin{bmatrix} a_0 & 1 & & & & \\ b_1 & a_1 & 1 & & & \\ & b_2 & a_2 & 1 & & \\ & & \ddots & \ddots & \ddots & \\ & & & b_{N-2} & a_{N-2} & 1 \\ & & & & b_{N-1} & a_{N-1} \end{bmatrix} \begin{bmatrix} P_0(L) \\ P_1(L) \\ P_2(L) \\ \vdots \\ P_{N-2}(L) \\ P_{N-1}(L) \end{bmatrix} \begin{bmatrix} 0 \\ 0 \\ 0 \\ \vdots \\ 0 \\ P_N(L) \end{bmatrix}. \tag{5.109}$$

The zeros of $P_N(L)$ are the nodes of the quadrature approximation and they are the eigenvalues of the tridiagonal matrix. With a diagonal similarity transformation and preserving the eigenvalues, the matrix can be transformed into a symmetric matrix called the Jacobi matrix:

$$J = \begin{bmatrix} a_0 & \sqrt{b_1} & & & & \\ \sqrt{b_1} & a_1 & \sqrt{b_2} & & & \\ & \sqrt{b_2} & a_2 & \sqrt{b_3} & & \\ & & \ddots & \ddots & \ddots & \\ & & & \sqrt{b_{N-2}} & a_{N-2} & \sqrt{b_{N-1}} \\ & & & & \sqrt{b_{N-1}} & a_{N-1} \end{bmatrix}. \tag{5.110}$$

Calculating the eigenvalues of the Jacobi matrix is easier than calculating the eigenvalues of the initial matrix reported in Eq. (5.109) and the zeros of the polynomial $P_N(L)$. As shown by Wilf (1962), the N weights could be computed as $w_\alpha = m_0\, j_{\alpha 1}^2$, where $j_{\alpha 1}$ represent the α-th of the $j_{\alpha 1}$th eigenvector j_α of the Jacobi matrix.

The coefficients a_α and b_α of the recursive formula can be computed by means of the orthogonality condition and by using the moments. Two efficient methods for calculating the Jacobi matrix from the moments are the Product-Difference algorithm (Gordon 1981) and Wheeler algorithm (Wheeler 1974).

5.3.1 Product-difference algorithm

The product-difference (PD) algorithm, developed by Gordon (1981), is based on the theory of continued fractions of Stieltjes. The first step is to construct a matrix P with components $P_{\alpha,\beta}$ starting from the moments. It can be calculated as:

- $P_{\alpha,1} = \delta_{\alpha,1}$ for $\alpha = 1, \ldots, 2N-1$, where $\delta_{\alpha,1}$ is the Kronecker delta;
- $P_{\alpha,2} = (-1)^{\alpha-1} m_{\alpha-1}$ for $\alpha = 1, \ldots, 2N$, where $m_{\alpha-1}$ is the α-th moment;
- $P_{\alpha,\beta} = P_{\alpha,\beta-1} P_{\alpha+1,\beta-2} - P_{1,\beta-2} P_{\alpha+1,\beta-1}$ for $\alpha = 1, \ldots, 2N+2-\beta$ and $\beta = 3, \ldots, 2N+1$.

Normalized moments $m'_\alpha = m_\alpha / m_0$ could be used: in this case the final weights ought to be multiplied by m_0.

The P matrix is used to compute the coefficients of the continued fraction ζ_α, that in turn are used to calculate the coefficients a_α and b_α, imposing $\zeta_1 = 0$.

$$\zeta_\alpha = \frac{P_{1,\alpha+1}}{P_{1,\alpha} P_{1,\alpha-1}} \qquad \alpha = 2, \ldots, 2N; \tag{5.111}$$

$$a_\alpha = \zeta_{2\alpha} + \zeta_{2\alpha-1} \qquad \alpha = 1, \ldots, N; \tag{5.112}$$

$$b_\alpha = -\sqrt{\zeta_{2\alpha+1} + \zeta_{2\alpha}} \qquad \alpha = 1, \ldots, N. \tag{5.113}$$

The PD algorithm generally becomes less stable when N increases. The stability depends on the absolute values of the moments and typically problems appear when $N > 10$ (Buffo 2012). The PD algorithm fails for distributions with mean equal to zero, i.e. $m_1 = 0$, as a division by zero is performed when ζ_α are computed, but this problem is not significant when the bubble size is studied: the values of internal coordinate are strictly higher than zero (Marchisio & Fox 2013).

5.3.2 Wheeler algorithm

The Wheeler algorithm is based on a different set of basic functions $\pi_\alpha(L)$ to represent the orthogonal polynomials, instead of the powers of L (Wheeler 1974). The coefficients are obtained by the modified moments:

$$\nu_k = \int \pi_k(L) n(L)\, dL \tag{5.114}$$

where $k = 0, \ldots, 2N-1$.

Assuming that:

$$\pi_{-1}(L) = 0; \tag{5.115}$$

$$\pi_0(L) = 1; \tag{5.116}$$

$$\pi_{\alpha+1}(L) = (L - a'_\alpha)\pi_\alpha(L) - b'_\alpha \pi_{\alpha-1}(L). \tag{5.117}$$

An efficient algorithm is available in order to calculate the coefficients of the Jacobi matrix through some intermediate quantities:

$$\sigma_{\alpha,\beta} = \int n(L)\pi_\alpha(L)\pi_\beta(L) dL \tag{5.118}$$

with $\alpha, \beta \geq -1$.

The initialization is:

$$\sigma_{-1,\alpha} = 0 \qquad \alpha = 1, \ldots, 2N-2 \tag{5.119}$$

$$\sigma_{0,\alpha} = \nu_\alpha \qquad \alpha = 0, \ldots, 2N-1 \tag{5.120}$$

$$a_0 = a'_0 + \frac{\nu_1}{\nu_0} \tag{5.121}$$

$$b_0 = 0 \tag{5.122}$$

The coefficients for the Jacobi matrix are computed as:

$$\sigma_{\alpha,\beta} = \sigma_{\alpha-1,\beta+1} - (a_{k-1} - a'_{\beta})\sigma_{\alpha-1,\beta} - b_{\beta-1}\sigma_{\alpha-2,\beta} + b'_{\beta-1}\sigma_{\alpha-1,\beta-1} \quad \beta = \alpha, \ldots, 2N-\alpha-1 \tag{5.123}$$

$$a_{\alpha} = a'_{\alpha} - \frac{\sigma_{\alpha-1,\alpha}}{\sigma_{\alpha-1,\alpha-1}} + \frac{\sigma_{\alpha,\alpha+1}}{\sigma_{\alpha,\alpha}} \tag{5.124}$$

$$b_{\alpha} = \frac{\sigma_{\alpha,\alpha}}{\sigma_{\alpha-1,\alpha-1}} \tag{5.125}$$

The Wheeler algorithm is more stable than the PD algorithm, both with normalized moments $m'_{\alpha} = m_{\alpha}/m_0$ both with standard moments m_{α} (Buffo 2012); this method could be used also in the case of distributions with mean equal to zero, i.e. $m_1 = 0$. The Wheeler algorithm allows obtaining weights and abscissas for a set of realizable moments. For unrealisable moment sets, this method fails; an adaptive version proposed by Yuan & Fox (2011) of this algorithm could be used.

5.3.3 Correction algorithms

The original QMOM formulation, proposed by Marchisio et al. (2003*b*) has a significant issue: errors due to spatial and time discretization are inevitable. During the simulations, the moments could be corrupted, forming an unrealizable or inconsistent moment set. An unrealizable moment set does not correspond to any real BSD, as explained by Wright (2007). A revised QMOM version can be used in order to solve this problem; this version allows correcting corrupted moment sets, obtaining a more stable code.

A method for recovering a corrupted moment set is the Minimum Square Algorithm proposed by McGraw (1997). This iterative method is based on the idea of identifying and correcting only the moment that after adjustment maximizes the smoothness of its logarithmic function, by using a minimization procedure. The method can identify quickly the moments that ought to be corrected and the corrected values that are valid. Details are reported in Petitti et al. (2010).

Sometimes, this method is not able to correct the moment set quickly and then, after some iterations, a second correction procedure is adopted. This method has been proposed by Wright (2007) and it restores the corrupted moments with the moments calculated with the arithmetic mean of two log-normal distributions. These log-normal distributions are obtained from the first four moments, keeping fixed values for m_0 (related to the number of bubbles per unit volume) and m_3 (related to the volume fraction). Details are reported in Petitti et al. (2010).

These two algorithms have a key role in the simulations and in their stability, avoiding negative nodes and moments. These correction algorithms mainly modify the higher-order moments. The magnitude of these corrections are acceptable, thus they do not affect largely the final results, while the stability is higher. This procedure, proposed by Petitti et al. (2010), strongly influences the physical consistency of the results and solves many stability issues.

5.3.4 Source term in QMOM

It is useful to discuss a bit more in details the functional form of the source term appearing on the right-hand side of the moment transport equation, when mass

transfer is neglected and only coalescence and breakage are considered. The right-hand side term of Eq. (5.8), the source term for the k^{th} moments S_{m_k} is related to coalescence and breakage and calculated with the nodes and weight of the quadrature formula. By using three nodes, the source terms can be written as:

$$S_{m_k} = \frac{1}{2}\sum_{i=1}^{N=3} w_i \sum_{j=1}^{N=3} w_j h_{ij} \left[\left(L_i^3 + L_j^3\right)^{k/3} - L_i^k - L_j^k\right] + \sum_{i=1}^{N=3} w_i g_i \left(\bar{b}_i^k - L_i^k\right) \quad (5.126)$$

where:

- L_i and L_j are the nodes of the quadrature approximation, that can be seen as the size of the bubble "classes";
- w_i and w_j are the weights of the quadrature approximation;
- $h_{ij} = h\left(L_i,\, L_j\right)$ is the coalescence kernel generated by the interaction between bubbles of size L_i and bubbles of size L_j;
- $g_i = g\left(L_i\right)$ is the breakage kernel considering bubbles of size L_i;
- $\bar{b}_i^k$ is the k^{th} moment of the daughter distribution function of the daughter bubble L, generated by the mother bubble L_i. It is calculated as:

$$\bar{b}_i^k = \int_{L_{\min}}^{L_{\max}} \beta\left(L,\, L_i\right) L^k \,\mathrm{d}L, \quad (5.127)$$

  where the daughter bubble has $L_{\min}$ equal to zero and $L_{\max}$ equal to the mother bubble size (L_i).

The final expression for Eq. (5.126) is therefore:

$$S_{m_k} = \frac{1}{2}\sum_{i=1}^{N=3} w_i \sum_{j=1}^{N=3} w_j h_{ij} \left[\left(L_i^3 + L_j^3\right)^{k/3} - L_i^k - L_j^k\right] + \\ + \sum_{i=1}^{N=3} w_i g_i \left(\left(\int_0^{L_i} \beta\left(L,\, L_i\right) L^k \,\mathrm{d}L\right) - L_i^k\right). \quad (5.128)$$

The integral appearing in Eq. (5.128) can be solved analytically, when possible, or by using another quadrature approximation, e.g. Gauss-Legendre with 6 nodes. In this latter case the calculations require longer time and the error of the approximation often is non-negligible.

The integral of Eq. (5.127) has an analytical solution in the case of binary breakage, starting with the daughter distribution function of Laakkonen et al. (2007) (Eq. (5.29)), as observed by Petitti et al. (2010):

$$\bar{b}_i^k = \int_0^{L_i} \left(180 \left(\frac{L^2}{L_i^3}\right)\left(\frac{L^3}{L_i^3}\right)^2 \left(1 - \frac{L^3}{L_i^3}\right)^2\right) L^k \,\mathrm{d}L = \\ = \frac{3240 L_i^k}{(k+9)(k+12)(k+15)}. \quad (5.129)$$

Given this analytical solution, the daughter distribution function proposed by Laakkonen et al. (2007) is preferable in many cases.

5.4 PBM implementation

5.4.1 CFD-PBM coupling

As mentioned before, in CFD simulations with the standard Eulerian-Eulerian method, the bubbles are assumed to be monodispersed, i.e. with the same size. A population balance model (PBM) can be coupled with CFD simulations in order to overcome this limitation. In this work the Quadrature Method of Moments (QMOM) with three nodes is employed, as the recommended option for univariate PBM. With this method, six additional gas-phase transport equations are solved:

$$\frac{\partial}{\partial t}\left(\rho_g \alpha_g \mu_k\right) + \nabla \cdot \left(\rho_g \alpha_g \mu_k \mathbf{u}_g\right) = \rho_g S_{m_k} \tag{5.130}$$

where μ_k is the moment of order k normalized with respect to the local bubble volume fraction and S_{m_k} is the source term calculated with the quadrature formula and reported in Eq. (5.126). To overcome stability issues, the correction algorithms suggested by Petitti et al. (2010) are used.

The QMOM method can be implemented following this methodology:

- write a User Defined Function (UDF) that implements the QMOM method and compile it;
- add 6 User Defined Scalars (UDS) for the gas dispersed phase, for which six equations are solved;
- add memories (User Defined Memories - UDM) in order to check the different parameters and values obtained by the QMOM;
- hook in macros/subroutines defined in UDF and for the source terms for the scalars, where the source terms are calculated in the UDF. The Sauter mean diameter is the bubble size considered in CFD simulations;
- set the boundary conditions for scalars of the moments. The bubbles are initialized with a log-normal distribution centred on a mean value and with a fixed variance, according to the work of Petitti et al. (2010);
- initialize the User Defined Scalars in the entire volume at the boundary values through patch operation, in order to minimize the initial death time.

Different strategies can be used to couple QMOM with the Eulerian-Eulerian solver in ANSYS Fluent. The three groups of bubbles can be considered as:

- a single phase moving with the same velocity, that is calculated by computing the interfacial forces with the Sauter mean diameter d_{32} (Buffo et al. 2013);
- a single phase moving with a size-dependent velocity; generally, a quadratic dependence of bubble velocity versus bubble size is assumed (Marchisio & Fox 2013);
- three different phases, with their properties (Mazzei et al. 2012).

The first choice is the cheapest in terms of computational time, whereas the last one is the most expensive. This choice is really important and influences results and computational cost. The main difference between the first and the second option is due to the effect of the velocity on the drag force. The version of QMOM that considers the same velocity for each bubble is extremely robust and allows obtaining the bubble size and with a solving for the PBM with an increase of the computational time, in comparison with the standard time with an increase in the time for Eulerian-Eulerian simulations of just 30%.

5.4.2 Zero-dimensional simulations

Three-dimensional transient CFD simulations provide very accurate results. However for studying new breakage and coalescence kernels is necessary to carry out many simulations for different operating conditions: several weeks are necessary to obtain a correct kernel. To overcome this problem and to obtain preliminary results, a zero-dimensional (0D) model can be used. An ideally mixed system is assumed, even if the local flow conditions affect the population dynamics (De Bona et al. 2016). In 0D models, spatial homogeneity and perfect mixing of the disperse and continuous phases is assumed (Buffo et al. 2016).

The zero-dimensional lumped model considers the volume-average value of the turbulent dissipation rate; it is implemented in MATLAB and it is computationally very cheap (Buffo et al. 2016): in some seconds it is possible to carry out several simulations. This model permits to study the evolution of the moments of the BSD; the hydrodynamic properties and the parameters are introduced as input. The turbulent dissipation rate and the other properties of interest show a spatial dependence: under certain operating conditions this effect can be neglected and the system evolution can be written in terms of volume-averaged properties.

The original population equation reads as follows:

$$\frac{\partial n(t,\mathbf{x},L)}{\partial t} + \frac{\partial}{\partial \mathbf{x}} \cdot (\mathbf{u}_g n(t,\mathbf{x},L)) = S(t,\mathbf{x},L) \tag{5.131}$$

and it can be volume-averaged. If the BSD is volume-averaged, according to the following definition:

$$\bar{n}(t,L) = \frac{1}{V}\int_V n(t,\mathbf{x},L)d\mathbf{x} \tag{5.132}$$

and the PBE is volume-average the next equation is obtained:

$$\frac{\partial \bar{n}(t,L)}{\partial t} = \frac{1}{V}\int_V S(t,\mathbf{x},L)d\mathbf{x} = \bar{S}(t,L). \tag{5.133}$$

In case of lumped models and for systems where only breakage and coalescence are considered Eq. (5.133) becomes:

$$\begin{aligned}\frac{\partial \bar{n}(t,L)}{\partial t} = \frac{1}{2}\int_0^L h\left(\bar{\varepsilon}, \left(L^3+\lambda^3\right)^{1/3}, \lambda\right)\bar{n}\left(\left(L^3+\lambda^3\right)^{1/3}, t\right)\bar{n}(\lambda,t)d\lambda + \\ -\bar{n}(L,t)\int_0^\infty h(\bar{\varepsilon},L,\lambda)\bar{n}(\lambda,t)d\lambda + \\ + \int_L^\infty \beta(L',L)\, g(\bar{\varepsilon},L')\, n(L',t)dL' - g(\bar{\varepsilon},L)\bar{n}(L,t),\end{aligned} \tag{5.134}$$

and applying the moment transformation, it becomes:

$$\frac{d\bar{m}_k}{dt} = \bar{S}_{m_k}, \tag{5.135}$$

where $\bar{S}_{m_k}$ is the source term. For the lumped 0D model, the source is evaluated with the kernels calculated with the volume-averaged turbulent dissipation rate:

$$\bar{\varepsilon} = \frac{\sum_i \varepsilon_i V_i}{V} \tag{5.136}$$

where ε_i is the turbulent dissipation rate in the i^{th} cell of the CFD simulation and V_i is the volume of this cell. The volume-averaged turbulent dissipation rate is computed by CFD 3D simulations in the same operating conditions. The source term expression is equal to Eq. (5.126), but the coalescence (h_{ij}) and breakage (g_i) kernels are calculated considering the volume-averaged properties, e.g. $\bar{\varepsilon}$.

Some corrections could be applied in order to obtain more accurate results. The volume-averaged turbulent dissipation rate could be computed by the CFD simulations with an average that considers the turbulent dissipation rate seen by the bubbles (Favre-like average seen by the bubbles) instead of a turbulent dissipation rate seen by the continuous phase, as detailed in Annex C:

$$\bar{\varepsilon}' = \frac{\sum_i \varepsilon_i \alpha_{g_i}}{\sum_i \alpha_{g_i}} \tag{5.137}$$

where α_{g_i} is the gas fraction.

Also the spatial distribution of the turbulent dissipation rate could be considered, in a homogeneous 0D model. Calculating the source term, spatial integrals appear in breakage and coalescence kernels. The assumption of volume-averaged turbulent dissipation rate of the lumped 0D model is not always suitable, as the dependency of the kernel on the turbulent dissipation rate is not linear. Buffo et al. (2016) specified that the homogeneous 0D model provides better results than the lumped 0D model. it is in fact more complex and it is more computationally expensive. It should be used only if the lumped 0D model provides inaccurate results compared with the 3D CFD simulations for same operating conditions.

5.5 Test case description and setup

5.5.1 Experimental test cases

As detailed in Chapter 3 experiments were conducted in a 0.4 m diameter cylindrical bubble column for a range of superficial gas velocities between 0.03 m/s and 0.35 m/s. It allows studying both the homogeneous and the heterogeneous flow regimes. Different hydrodynamic properties were measured: gas hold-up, local gas fraction, liquid velocity and bubbles Sauter mean diameter. The gas is injected through a perforated sparger at the bottom of the column. The sparger has 92 holes of 2 mm of diameter (Fig. 3.4b), ensuring a homogeneous distribution of the gas. Subsequently, another perforated sparger is used (7 holes of 9 mm) (Fig. 3.4c): this allows generating big bubbles and this data is used to decouple breakage and coalescence phenomena.

Experiments with different qualities of water (i.e. demineralised water, tap water and demineralised water with small percentages of ethanol) allow considering the effect of additives in the coalescence kernel. They strongly modify hydrodynamics and bubble size, as reported by McClure et al. (2013, 2014, 2015). Gemello et al. (2018a) stated that the presence of additives affects the mobility of the gas-liquid interface, that influences the coalescence efficiency, while but it has little effect on breakage. Additives at low concentrations did not modify significantly the surface tension. This result suggests that coalescence is affected by the modification of physical properties, but relevant descriptors are still not identified.

The turbulence model choice is investigated in this work. The turbulent dissipation rate is an important parameter for breakage and coalescence kernels. It has never been measured directly in heterogeneous bubbly flows, due to the lack of a reliable measurement method. Forret (2003) studied the turbulent viscosity in bubble columns in a wide range of operating conditions. A correlation for the calculation of the turbulent viscosity in the column centre was proposed:

$$\nu_t = 0.036\, D^{1.6} u_{sg}^{0.11}. \tag{5.138}$$

where D is the column diameter (in m) and u_{sg} is the superficial gas velocity (in m/s).

Furthermore, Forret (2003) studied its radial profile: it is flat until the normalized radial position of 0.8 and after it decreases quickly to zero at the wall. The turbulence kinetic energy is experimentally calculated by using a Pavlov tube at 400 Hz for a superficial gas velocity of 0.16 m/s. By calculating the turbulent viscosity, with the Forret (2003) correlation and profile, and by measuring the turbulence kinetic energy, the turbulence dissipation rate can be approximated, as detailed below (Eq. (5.143)).

5.5.2 CFD simulations setup

Simulations are performed using the commercial CFD code ANSYS Fluent 18.0. Simulations are carried out using a Eulerian-Eulerian multiphase method, as detailed Chapter 4. Classical CFD simulations presented in Chapter 4 are coupled with the PBM, using the same geometry, mesh and setup. In this work, the Quadrature Method of Moments (QMOM) with three nodes is employed. To avoid inconsistent moment sets, the QMOM version suggested by Petitti et al. (2010) is used. For the PBM, six equations are added in Fluent (User Defined Scalars - UDS). Initially, the simulations are carried out by approximating the 92-holes sparger with a homogeneous porous plate. In the CFD simulations, the gas enters the column already mixed with the liquid with a constant gas volume fraction. The bubbles, that enter the system, have an initial log-normal distribution centred on a mean value and with a fixed variance, according to the work of Petitti et al. (2010). Initially, the inlet bubble size is imposed equal to 7.7 mm. Standard wall function is used. The drag law of (Tomiyama 1998) is adopted, with the swarm factor proposed in the previous chapter.

Turbulence property influence the coalescence and breakage kernels. The main turbulence properties of interest are the turbulent viscosity, the turbulence kinetic energy and the turbulence dissipation rate. The turbulence dissipation rate plays a direct role in the coalescence and breakage kernels. Initially, the simulations are

carried out by using the RNG k-ε model. In order to avoid convergence problems at the interface, the Kato & Launder (1993) modification is applied in the k equation and the turbulence dissipation rate is computed only where the gas volume fraction is lower than 70%. Other turbulence models are also tested, comparing the turbulence properties with experimental data and existing correlations. In this work, several turbulence models are studied beside RNG k-ε such as standard k-ε and k-ω. Subsequently, turbulence due to energy transfer from gas-phase to liquid-phase is considered by adding a source term in the turbulence equations or by modifying the liquid-phase visocsity (detailed in Section 4.2.3.5); it is coupled with the RNG k-ε model and tested.

5.6 Results and discussion

Initially, simulations are carried out with the typical kernels developed for the homogeneous regime:

- only collisions due to turbulent eddies are considered. The coalescence kernel of Prince & Blanch (1990) is used;
- the coalescence efficiency is computed using the film drainage model, with the expression proposed by Coulaloglou & Tavlarides (1977);
- it is assumed that breakage is due to turbulence; these simulations use the breakage kernel of Coulaloglou & Tavlarides (1977);
- the daughter distribution function of Laakkonen et al. (2007) is considered.

This set of kernels will be referred to as "homogeneous" kernels in the remainder of this work.

The first property for screening the quality of the kernel predictions is the Sauter mean diameter. If this does not result in good agreement with experiments, the kernels are certainly wrong. Experimental data suggest that the Sauter mean diameter increases or remains constant when the superficial gas velocity is increased. The homogeneous kernels provide a wrong behaviour: the Sauter mean diameter decreases when the superficial gas velocity increases, as shown in Fig. 5.1. The Sauter mean diameter is acceptably predicted only under the homogeneous regime with these kernels althought it is underestimated.

The radial profile of Sauter mean diameter is wrong under the heterogeneous regime, as the experimental profiles have a parabolic shape, whereas the CFD profiles with homogeneous kernels are almost flat, as shown in Fig. 5.2. Results confirm that the homogeneous breakage and coalescence kernels ought to be modified in the case of the heterogeneous regime.

5.6.1 0D simulations

Many simulations need to be carried out in order to develop a kernel suitable for bubble columns working under the heterogeneous regime: each kernel has to be applied on simulations with different superficial gas velocities and column diameters. The realization of thousands of 3D CFD simulations is computationally too heavy, even when using a super-computer with simultaneous parallel simulations.

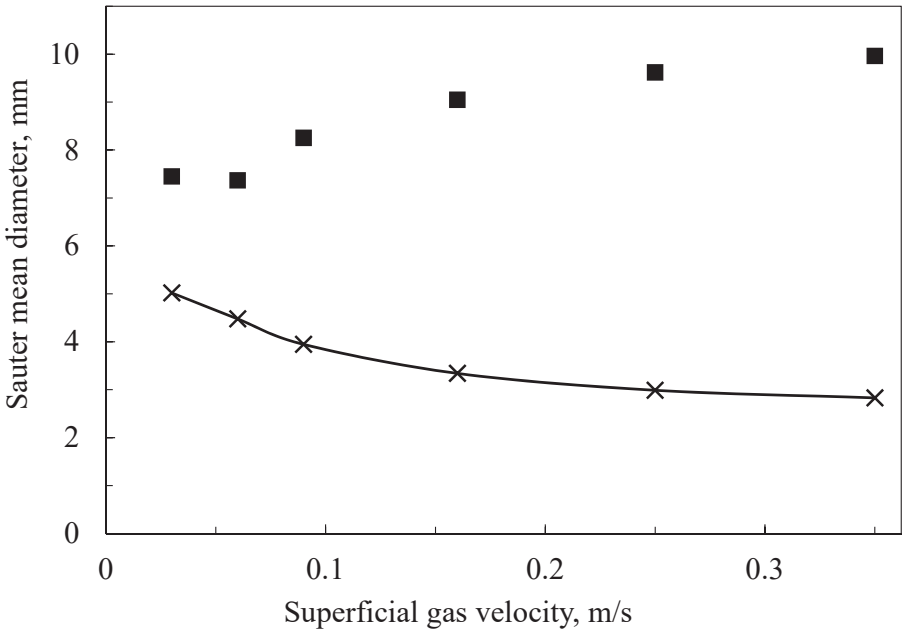

Figure 5.1: Volume-average Sauter mean diameter at different superficial gas velocities at H/D=2.5. Experimental data (■) versus CFD results obtained with homogeneous kernels (red line and ×).

To screen the proposed kernels, 0D simulations with MATLAB are carried out, by using a lumped model, as explained in Section 5.4.2.

The spatial and time average of the hydrodynamics and turbulence properties is used in this work. For calculating the time-average of the properties of interest, the Favre-like average seen by the bubbles or the liquid may be used instead of the Reynolds average. The effect of this choice is quite small and often negligible: the radial profiles obtained with the Favre-like average are similar to those obtained with the Reynolds average for every property, as detailed in Annex C.

0D results are then validated and refined with 3D CFD results. Within a few minutes, it is possible to obtain the evolution of the Sauter mean diameter for each column and superficial gas velocity. The simulation time is computed as the residence time for a plug flow reactor:

$$t = 4\frac{D_C[m]}{v_{sg}[m/s]}\frac{\alpha_g}{1-\alpha_g} \tag{5.139}$$

A constant residence time is not physically correct, but it allows understandingof the residence time effect. The differences between using the residence time of a plug flow reactor or a constant sufficiently-long residence time are low. After a few seconds, an equilibrium between breakage and coalescence is reached.

The obtained results lead to the conclusion that the homogeneous kernels are not suitable in the heterogeneous regime. They predict a decrease in Sauter mean diameter if the superficial gas velocity is increased, as shown in Fig. 5.3.

The breakage kernel of Coulaloglou & Tavlarides (1977) (see Eq. (5.18)) cannot therefore be used: coupled with every coalescence kernel, the bubble size is almost zero in the case of the heterogeneous regime (Fig. 5.3). The damping modification of the breakage kernel of Coulaloglou & Tavlarides (1977) (see Eq. (5.19)) has

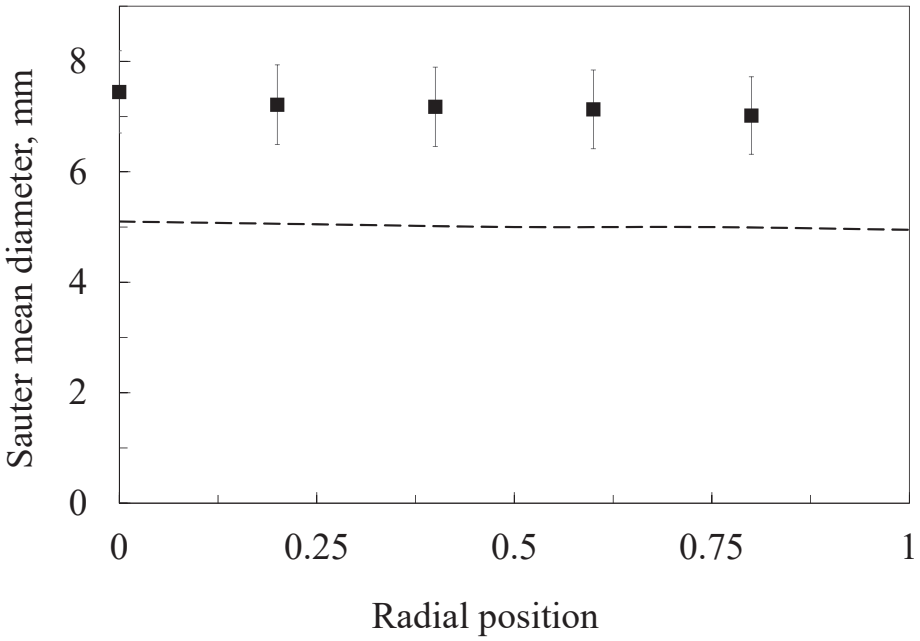

(a) 0.03 m/s.

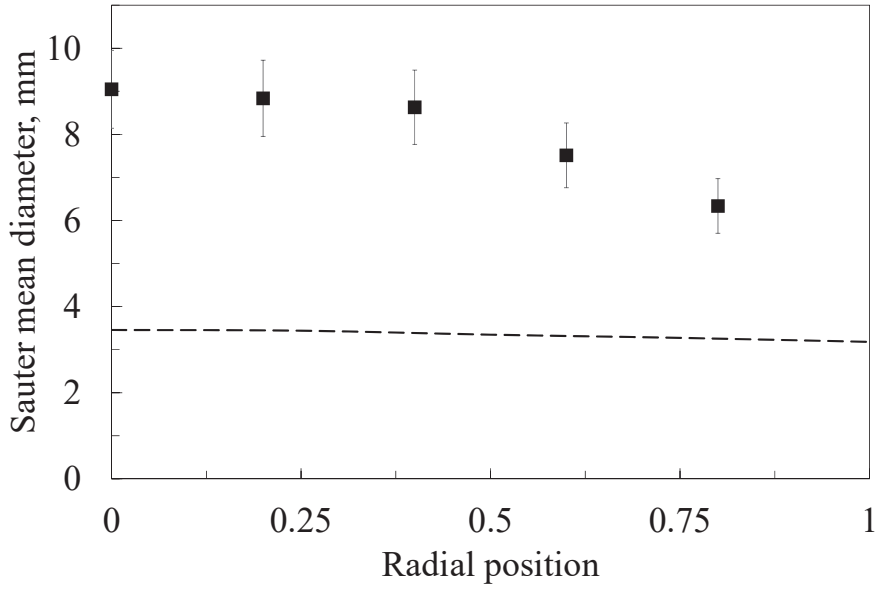

(b) 0.16 m/s.

Figure 5.2: Sauter mean diameter profile in the case of homogeneous (0.03 m/s) and heterogeneous (0.16 m/s) flow regimes at H/D=2.5. Experimental data (■) versus CFD results obtained with homogeneous kernels (dashed line).

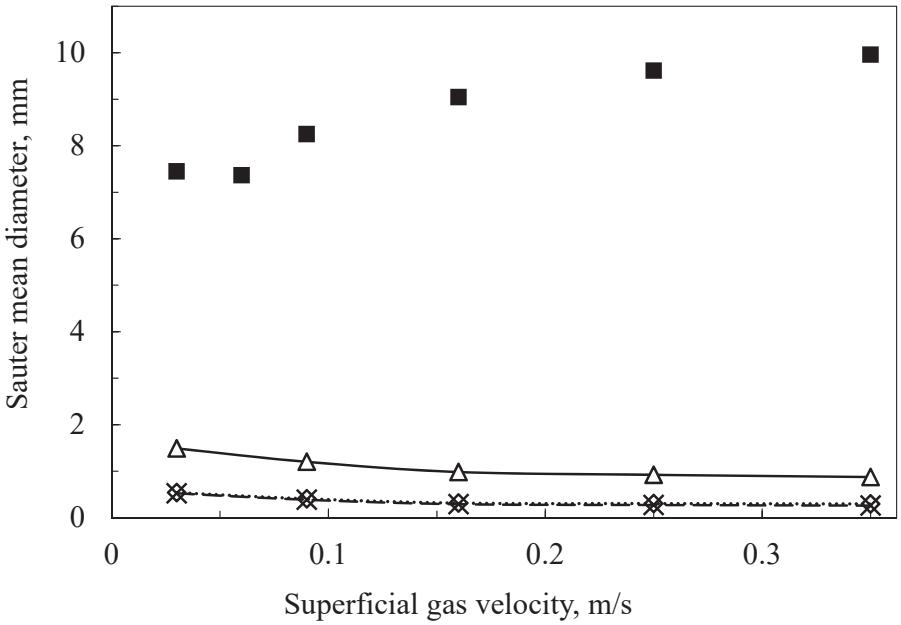

Figure 5.3: Averaged Sauter mean diameter at different superficial velocities with 0D simulations: experimental data (■) versus 0D simulations with the breakage kernels of Coulaloglou & Tavlarides (1977) (dashed line and ◇), Coulaloglou & Tavlarides (1977) with damping effect (dotted line and ×) and Laakkonen et al. (2007) (solid line and △) coupled with the homogeneous coalescence kernels.

very little effect. The bubble size obtained with the breakage kernel of Laakkonen et al. (2007) is slightly better, but still not acceptable if coupled with homogeneous coalescence kernels.

In 0D simulations the coalescence and breakage kernels can be studied separately in order to understand the source of mismatch with the observed experimental data. Closer observation of the simulation data reveal that the problem is the coalescence kernel that predict zero coalescence resulting in a decrease of the Sauter mean diameter when the superficial gas velocity increases. These results confirm that the coalescence kernel ought to be modified. The efficiency of Coulaloglou & Tavlarides (1977) is not suitable for the heterogeneous regime, in fact the turbulent dissipation rate is too high and the coalescence efficiency is almost zero for high ε. Every coalescence efficiency obtained with the film drainage model is not suitable: the Sauter mean diameter decreases if the superficial gas velocity grows (Fig. 5.4). Therefore another model, more properly describing the phenomena involved during bubble coalescence under the heterogeneous regime, must be used.

The critical approach velocity model proposed by Lehr et al. (2002) is then tested. This coalescence kernel provides a correct behaviour for the Sauter mean diameter: it increases with the superficial gas velocity, but the values are incorrect, as shown in Fig. 5.5. This kernel looks interesting, but the constants have to be modified and more accurate kernel constants can be obtained with 3D CFD simulations.

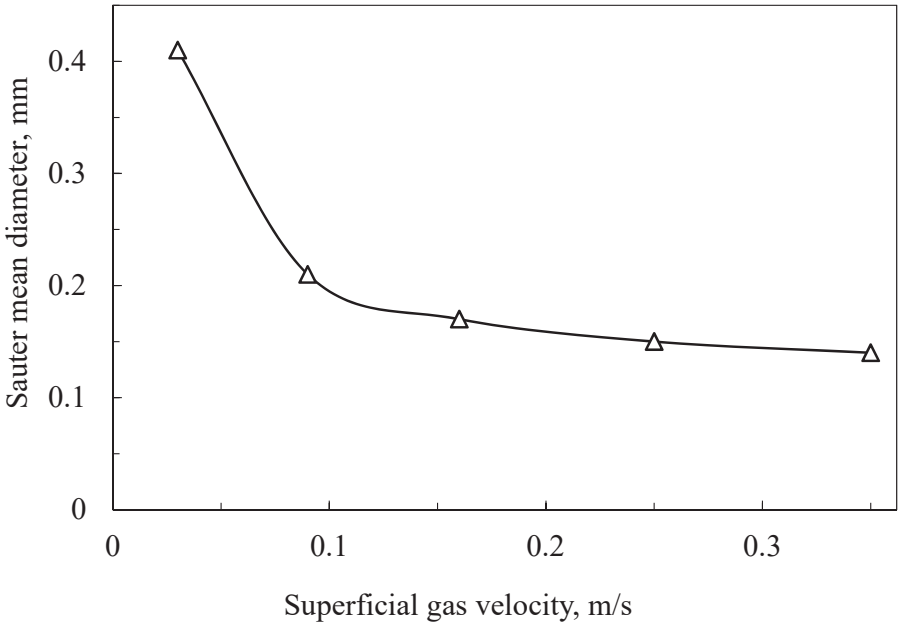

Figure 5.4: Averaged Sauter mean diameter at different superficial velocities obtained with 0D simulations without breakage (only coalescence obtained with the film drainage model), starting with an initial bubble size equal to 0.1 mm (solid line and △).

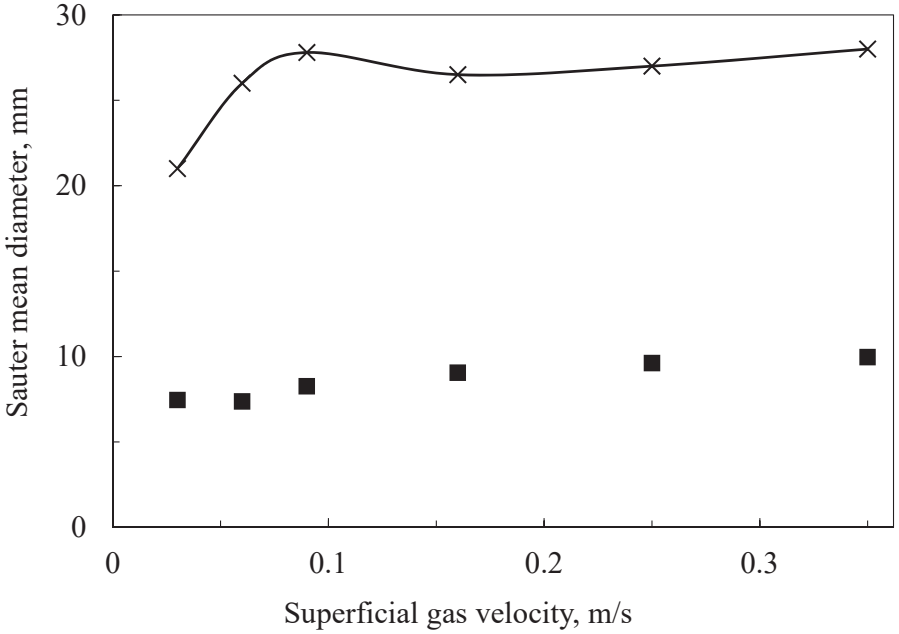

Figure 5.5: Averaged Sauter mean diameter at different superficial velocities with 0D simulations: experimental data (■) versus 0D simulations with the collision frequency of Lehr et al. (2002), the coalescence efficiency of Lehr et al. (2002) and the breakage kernel of Laakkonen et al. (2007) (solid line and ×).

5.6.2 Kernel parameter identification with 3D CFD simulations

Several combinations of breakage and coalescence kernels are studied. Different models for the breakage kernel, collision frequency and coalescence efficiency are tested, while the daughter distribution function of Laakkonen et al. (2007) is used, because of its analytical solution. 0D simulation results allow excluding the coalescence efficiency kernels based on the film drainage model. Nevertheless, some simulations by using the film drainage model are carried out in order to validate the 0D simulations.

As detailed at the beginning of Chapter 5.6, "homogeneous" kernels cannot be used in the case of bubble columns under the heterogeneous regime. Breakage and coalescence phenomena can be studied separately to understand the causes of discrepancy. The coalescence kernel predicts a Sauter mean diameter decrease when the superficial gas velocity increases, as shown in Fig. 5.6. As reported above

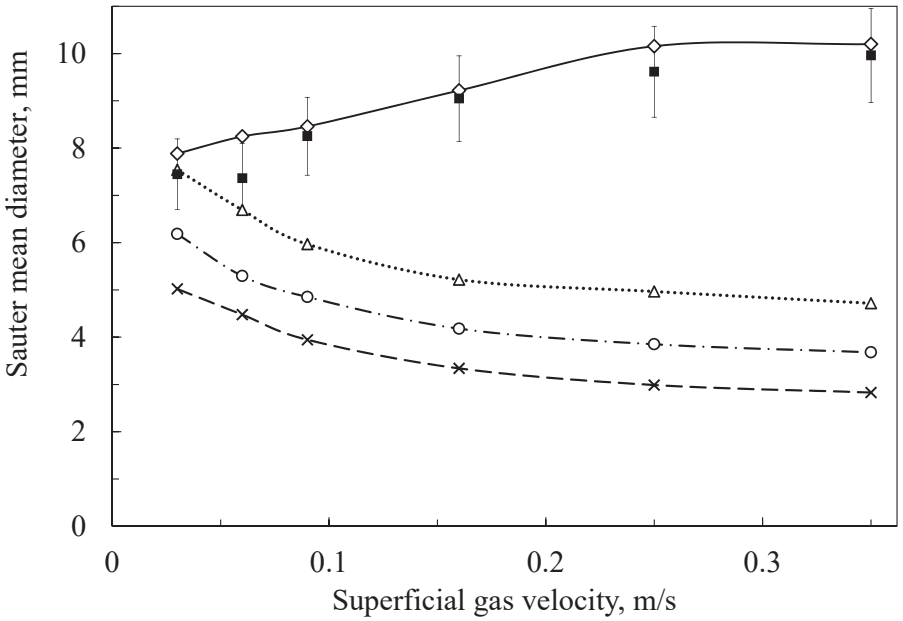

Figure 5.6: Sauter mean diameter at different superficial gas velocities: experimental data (■) versus CFD results obtained with homogeneous kernels (dashed line and ×), with film drainage velocity model and Laakkonen et al. (2006) breakage (dash-dot line and ○), with film drainage model without breakage (dotted line and △) and with the critical approach velocity model and the Laakkonen et al. (2006) breakage kernel (solid line and ◇).

in 0D simulations, coalescence efficiency of Coulaloglou & Tavlarides (1977) cannot be used in the case of heterogeneous regime. The turbulent dissipation rate is too high and the coalescence efficiency decreases too much for high turbulent dissipation rates. The kernels of coalescence efficiency based on the film drainage model are not suitable, as the Sauter mean diameter decreases when the superficial gas velocity increases (Fig. 5.6). These results confirm that the film drainage model does not well describe the heterogeneous flow regime, in accordance with 0D simulations. The Sauter mean diameter profiles should be parabolic, whereas the CFD profiles

with homogeneous kernels are completely flat for every operating condition, as shown in Fig. 5.7. In order to further validate these results, some corrections for high gas volume fractions are proposed. The breakage kernel of Coulaloglou & Tavlarides (1977) with damping effect (Eq. (5.19)), coalescence efficiency of Wang et al. (2005*b*) (Eq. (5.58)) and Coulaloglou & Tavlarides (1977) for high gas fraction (Eq. (5.81)) have been tested. These corrections are not enough to obtain acceptable results if they are used with a film drainage model coalescence efficiency.

The breakage kernel of Coulaloglou & Tavlarides (1977) with damping effect, reported in Eq. (5.19), cannot be used: the Sauter mean diameter is too low for both the homogeneous and heterogeneous regimes. By using the breakage kernel proposed by Laakkonen et al. (2007), the results are in a better agreement with experiments. As detailed above, the breakage kernel of Laakkonen et al. (2007) could provide realistic results if coupled with a correct coalescence kernel.

The critical approach velocity model of Lehr et al. (2002) is then tested. The critical approach velocity model results in a correct trend for the Sauter mean diameter, that increases with the superficial gas velocity, although the numerical absolute values are not exact. This kernel seems interesting but it is necessary to modify the constants.

The objective is to obtain a model with a wider range of validity, suitable under different operating conditions, with a focus on the heterogeneous regime. Under the heterogeneous regime, the best results seem to be obtained by coupling the collision frequency of Wang et al. (2005*b*), the coalescence efficiency of Lehr et al. (2002), the breakage kernel of Laakkonen et al. (2006) and the daughter distribution function of Laakkonen et al. (2007).

The critical approach velocity is equal to 0.08 m/s for pure water. The critical approach velocity has a lower value for tap water (contaminated water). With the collision frequency of Wang et al. (2005*b*), the bubble size increases with the superficial gas velocity but its values are higher than in the experiments. As suggested by Buffo (2012), the constant $\sqrt{2}\pi/4$ should be replaced with an empirical constant that can be fitted with CFD simulations. This set of kernels provides a space-averaged Sauter mean diameter that slightly increases with the superficial gas velocity and its values are similar to experimental data if a constant equal to 0.16 is used, as demonstrated in Fig. 5.6.

The Sauter mean diameter profiles obtained with this model are compared with the experimental data in Fig. 5.7 for different operating conditions. The radial profiles of Sauter mean diameter are well-predicted. CFD and experimental profiles are in a good agreement. The Sauter mean diameter profile is parabolic in case of heterogeneous regime. These profiles are quite correct for every superficial gas velocity. The main discrepancies appear next to the wall. The profile is almost flat for a superficial gas velocity equal to 0.03 m/s, that corresponds to the homogeneous regime. These preliminary results are in accordance with the experiments and they must be validated by analysing the effects of turbulence, initial conditions and scale-up.

The film drainage model cannot be used in the case of heterogeneous regime, as the turbulence dissipation rate is too high. It causes a contact time than is too low compared with the film drainage time and thus the efficiency is almost zero. The critical approach velocity model does not consider contact and drainage time, but the relative velocity between two colliding bubbles and then the efficiency is

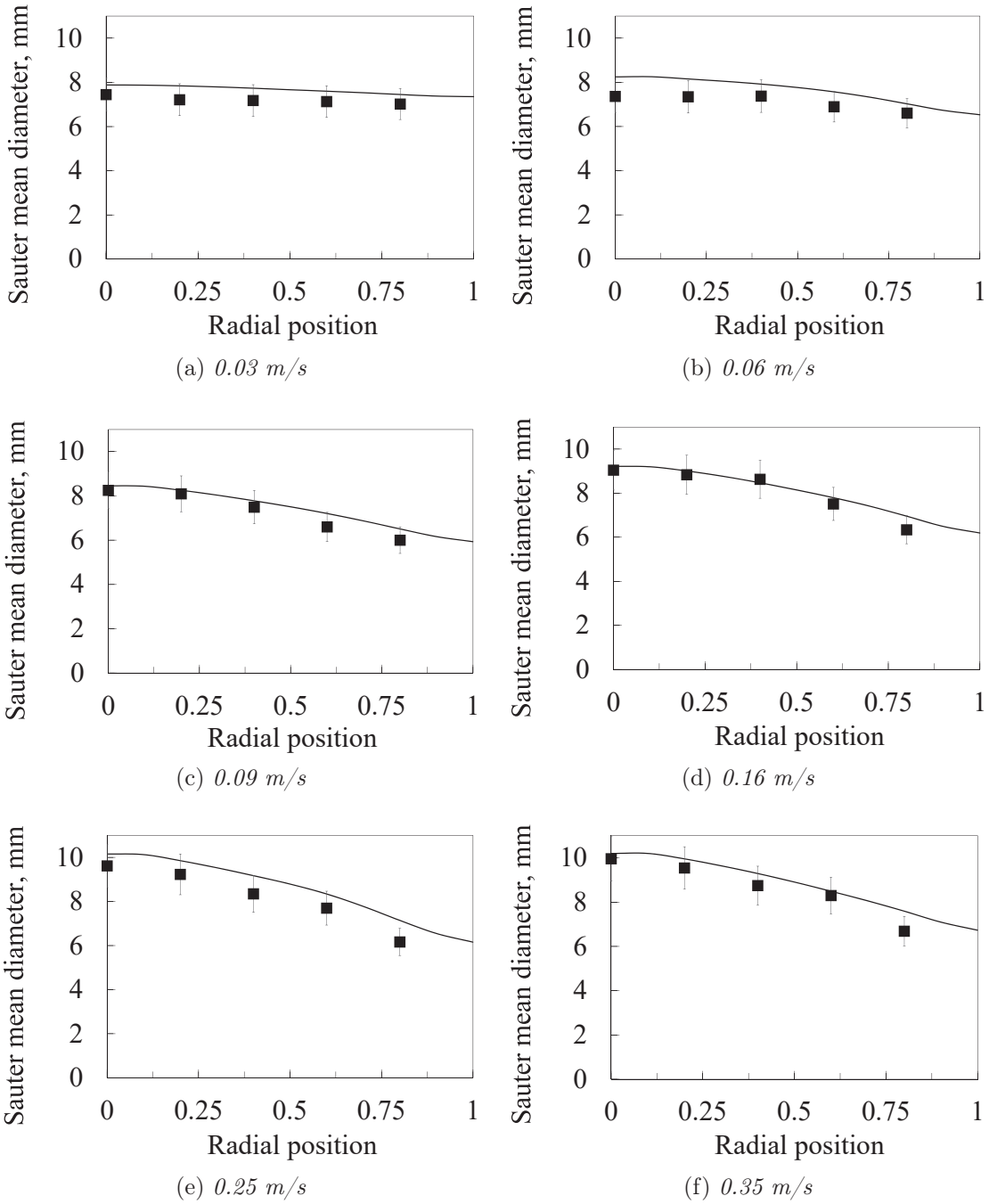

(a) *0.03 m/s* (b) *0.06 m/s*

(c) *0.09 m/s* (d) *0.16 m/s*

(e) *0.25 m/s* (f) *0.35 m/s*

Figure 5.7: Sauter mean diameter profile at different superficial gas velocities at H/D=2.5. Experimental data (■) versus CFD results obtained with critical approach velocity model and Laakkonen et al. (2006) breakage.

not zero in the case of heterogeneous regime. If two bubbles approach at a velocity lower than the critical one, they coalesce also under the heterogeneous regime. The critical approach velocity model is used in the following part of this work.

5.6.3 CFD-PBM simulations validation

5.6.3.1 Hydrodynamics validation

The hydrodynamics was well-predicted using a fixed bubble size, as detailed in Chapter 4. CFD-PBM coupling allows to understand if the swarm factor proposed in the previous chapter can be used also for poly-disperse systems. The drag law can be modified in order to consider the effect of bubble size distribution as follows:

$$F_D \approx \frac{3}{4}\frac{\alpha_g \rho_l}{\rho_g}|u_{rel}|u_{rel}\frac{\int L^2\, C_D\,(L)\; n\, dL}{\int L^3\, n\, dL}$$
$$\approx \frac{3}{4}\frac{\alpha_g \rho_l}{\rho_g}|u_{rel}|u_{rel}\frac{\sum_{i=1}^{3} w_i L_i^2\, C_D\,(L)}{\sum_{i=1}^{3} w_i L_i^3}. \tag{5.140}$$

With the operating conditions investigated in this work, the minimum value used in Eq. (4.58) ought to be increased (h_{min}=0.3). The presence of small and big bubbles increases the risk of huge accumulation of bubbles. The value of h_{min} here proposed can be used both with a fixed bubble size (without PBM) and with a PBM. For the biggest columns, i.e. ϕ 1 m and ϕ 3 m, the classical value of h_{min}=0.15 can be used and then this value can be considered as suitable for industrial purposes. Since with the column ϕ 0.4 m, with h_{min}=0.15 and in presence of a PBM, big accumulations of bubbles occur for high gas volume fractions, a value of 0.30 is used in this chapter. The choice of this value influences only the CFD hydrodynamics for very high superficial gas velocities, i.e. equal to 0.25 m/s and 0.35 m/s, while the effect is lower in the other cases.

CFD-PBM simulations using the default drag force and the drag force presented in Eq. (5.140) are compared in the case of the heterogeneous regime. The effect of the modification of the drag force is low, as observed in Fig. 5.8. It can be due to the fact that the terminal velocity is almost constant in this size range (Gemello et al. (2018b)). This drag force correction is robust and the computational time is not affected. This effect could be important under presence of a class of bubbles smaller than 2 mm or bigger than 10 mm. The CFD-PBM global hydrodynamics is correct, as observed by Gemello et al. (2018b) without PBM: gas gold-up, local gas fraction (Fig. 5.8a) and liquid velocity (Fig. 5.8b) are similar to the experimental results. The swarm factor proposed by Gemello et al. (2018b) and detailed in Chapter 4 can be considered as valid for poly-disperse systems.

5.6.4 Turbulence model effects

The turbulence properties (i.e. turbulent viscosity, turbulence kinetic energy and turbulence dissipation rate) influence the coalescence and breakage kernels. In particular, the turbulence dissipation rate plays a direct role in the coalescence and breakage kernels. The simulations presented before are carried out by using the RNG k-ε model. Other turbulence models ought to be tested, comparing the turbulence properties with experimental data and existing correlations. In

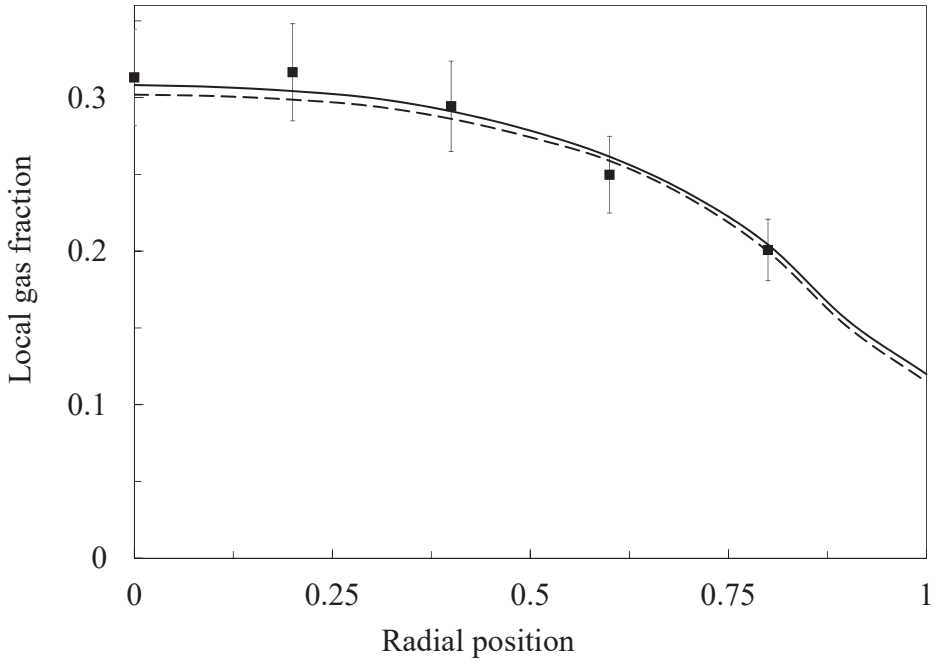

(a) Gas volume fraction at H/D=2.5.

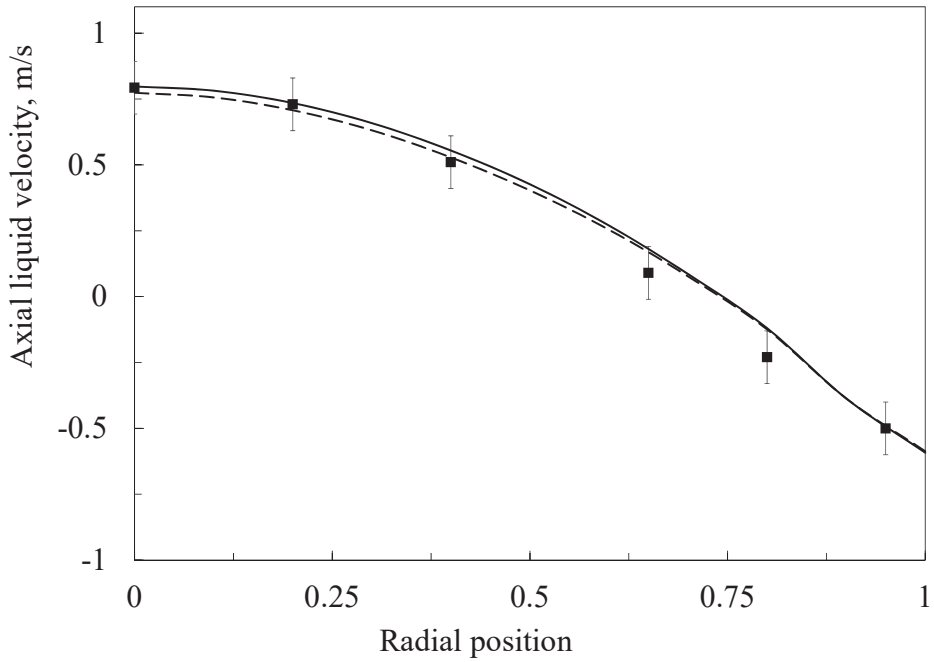

(b) Axial liquid velocity at H/D=3.75.

Figure 5.8: Effect of PBM on the hydrodynamics for a superficial gas velocity of 0.16 m/s. Experimental data (■) versus CFD results using a fixed bubble size equal to 8 mm (without PBM) (dashed line) and considering PBM and corrected drag force (Eq. (5.140)) (solid line).

this work several turbulence models are studied: RNG k-ε, standard k-ε and k-ω. Contributions of the turbulence due to energy phase transfer, following the models proposed by Yao & Morel (2004), Troshko & Hassan (2001), Simonin & Viollet (1990) and Sato & Sekoguchi (1975) (detailed in Section 4.2.3.5), are coupled with

the RNG k-ε model and tested.

Forret (2003) studied the turbulent viscosity in bubble columns in a wide range of operating conditions. She proposed a correlation for the calculation of the turbulent viscosity in the column centre:

$$\nu_t = 0.036 D^{1.6} v_{sg}^{0.11}. \tag{5.141}$$

Furthermore, Forret (2003) studied its radial profile. The radial profile should be flat until a normalized radial position of 0.8 and then decrease quickly to zero at the wall (see Fig. 5.9).

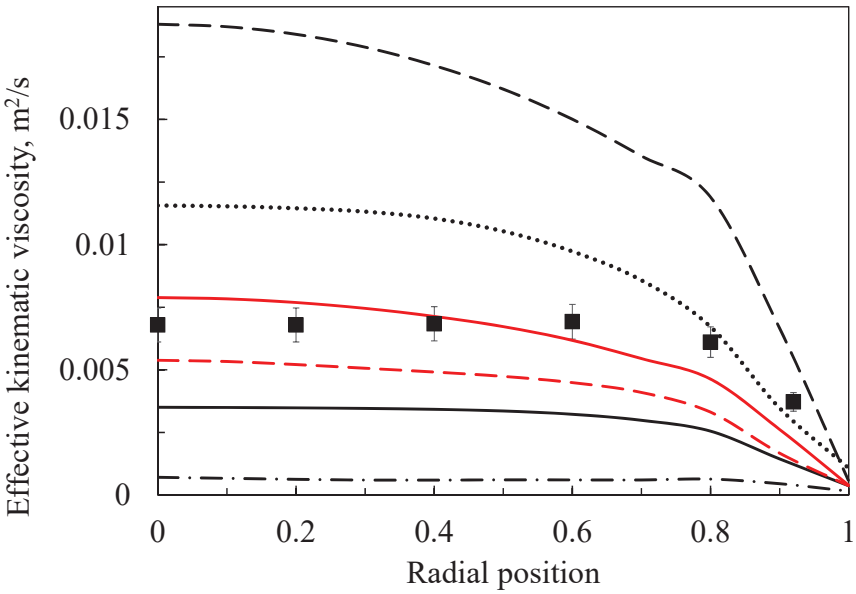

Figure 5.9: Kinematic turbulent viscosity for the column ϕ 0.4 m with a superficial gas velocity equal to 0.16 m/s at H/D=2.5. Data obtained by Forret (2003) (■) versus CFD results with different turbulence models: RNG k-ε (black solid line), standard k-ε (black dashed line), realizable k-ε (black dotted line), standard k-ω (red solid line) and SST k-ω (red dashed line).

The standard k-ω model provides turbulent viscosity value closer to the correlation, but a wrong radial profile in the case of heterogeneous regime. The RNG k-ε model underestimates the turbulent viscosity, while the realizable k-ε model overestimates it. The standard k-ε model strongly overestimates it. These results are compared in Fig. 5.9.

In Chapter 4, different kinematic turbulent viscosity have been tested and compred with CFD results, as shown in Fig. 4.20. The best agreement was obtained with the correlation of Kawase & Moo-Young (1989), while higher discrepancies appear with the correlations of Miyauchi & Shyu (1970) and Burns & Rice (1997). By using the the correlation of Kawase & Moo-Young (1989), the RNG k-ε model seems to provide the best results. The choice of the kinematic turbulent viscosity correlation influences the comparison between the turbulence models.

The turbulence kinetic energy can be calculated using the fluctuating liquid velocity components:

$$k = \frac{1}{2}\left(\overline{(u')^2} + \overline{(v')^2} + \overline{(w')^2}\right). \tag{5.142}$$

The turbulence kinetic energy is experimentally calculated by using a Pavlov tube at 400 Hz for a superficial gas velocity of 0.16 m/s, as reported in Fig. 5.10.

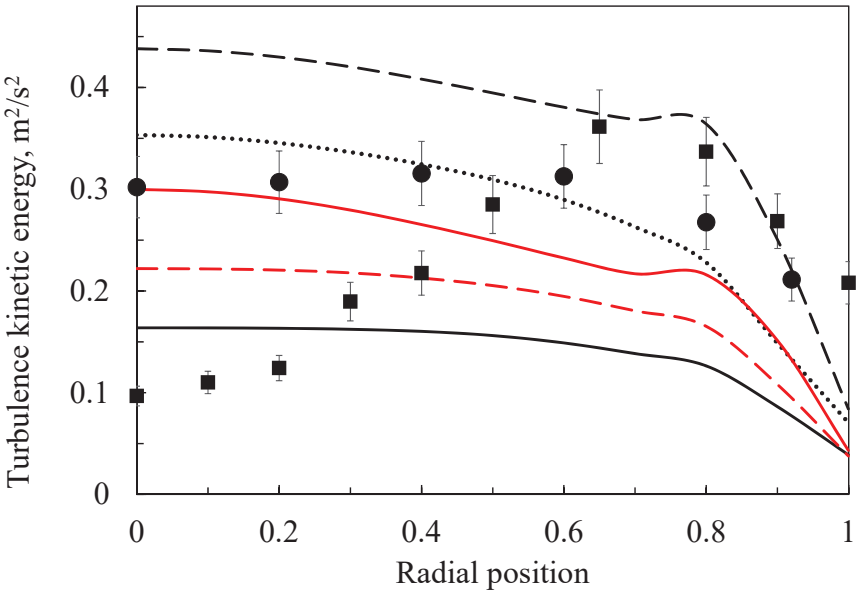

Figure 5.10: Turbulence kinetic energy for the column ϕ 0.4 m with a superficial gas velocity equal to 0.16 m/s at H/D=2.5. Experimental data obtained by Forret (2003) (■) and in this work (●) versus CFD results with different turbulence models: RNG k-ε (black solid line), Standard k-ε (black dashed line), Realizable k-ε (black dotted line), Standard k-ω (red solid line) and SST k-ω (red dashed line).

The experimental data are compared with CFD results in Fig. 5.10. The realizable k-ε and standard k-ω models provide the most similar turbulence kinetic energy. The RNG k-ε and standard k-ε models provide quite acceptable results.

In order to consider the contribution of the turbulence due to energy transfer from gas-phase to liquid-phase, different models have been compared, coupled with the RNG k-ε model. They are detailed in Section 4.2.3.5. The results are reported in Fig. 5.11. The strongest effect has been considered by Yao & Morel (2004), that assumed that the entire gas-phase energy due to the drag force passes in the liquid-phase turbulence, by adding turbulence source terms. By using the model of Yao & Morel (2004), the calculated turbulence kinetic energy is the lowest one and the furthest from the experimental data collected in this work. The models of Troshko & Hassan (2001) and Simonin & Viollet (1990) considers that only a fraction of the energy due to the drag force passes in the liquid-phase turbulence.With these two models, the turbulence kinetic energy is similar to that calculated without the effect of the turbulence due to energy transfer. The model of Sato & Sekoguchi (1975), that modifies the liquid-phase viscosity, strongly increases the turbulence kinetic energy.

By calculating the turbulent viscosity with the Forret (2003) correlation and profile and by measuring the turbulence kinetic energy, as detailed above, the turbulence dissipation rate can be approximated:

$$\varepsilon = C_\mu \frac{k^2}{\nu_t}, \tag{5.143}$$

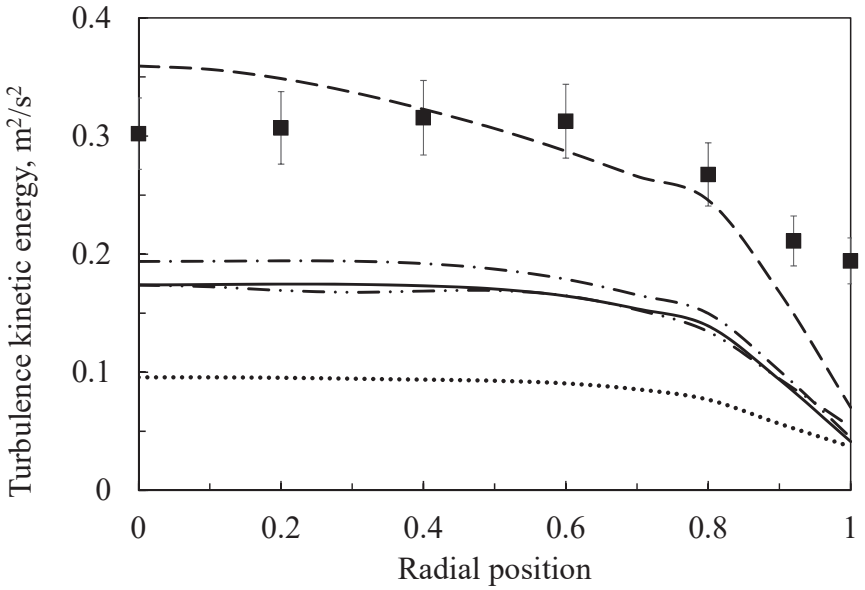

Figure 5.11: Turbulence kinetic energy for the column ϕ 0.4 m with a superficial gas velocity equal to 0.16 m/s at H/D=2.5. Experimental data obtained in this work (●) versus CFD results with RNG k-ε model (solid line) coupled with different models for considering the turbulence due to energy transfer from gas-phase to liquid-phase: Yao & Morel (2004) (dotted line), Troshko & Hassan (2001) (dash-dot-dot line), Simonin & Viollet (1990) (dash-dot line) and Sato & Sekoguchi (1975) (dashed line).

where C_μ is a numerical constant approximately equal to 0.09 in many cases and equal to 0.085 in ANSYS Fluent.

Every turbulence model underestimates the turbulence dissipation rate. The standard k-ε and standard k-ω models slightly underestimate the turbulence dissipation rate, while the discrepancies are higher with the other models. All the other models have turbulence dissipation rate values smaller than the experimental one of about 20-40%. These results are reported in Fig 5.12.

Power consumption per unit of mass should equal to the loss of potential energy per unit of mass, i.e. the turbulence dissipation rate considering an energy balance. The power consumption per unit of volume (P/V) can be calculated with the following formula (Roels & Heijnen 1980, Menzel et al. 1990):

$$P/V = \frac{1}{H}\, p\, u_{sg} \ln\left(1 + \rho_l \frac{g\, H\, (1-\bar{\alpha}_g)}{p}\right), \tag{5.144}$$

where H is the operating liquid height, p is the external pressure, u_{sg} is the superficial gas velocity, ρ_l is the density of the liquid phase, g is the gravity acceleration and $\bar{\alpha}_g$ is the global gas volume fraction.

Considering a superficial gas velocity equal to 0.16 m/s, with a global gas volume fraction equal to 0.24, the turbulence dissipation rate should be equal to 1.08 m^2/s^3, slightly bigger than the values presented in Fig. 5.12.

The contribution of the turbulence due to energy transfer from gas-phase to liquid-phase on the turbulence dissipation rate is presented in Fig 5.13. Every model tested in this work has a positive effect on the turbulence dissipation rate:

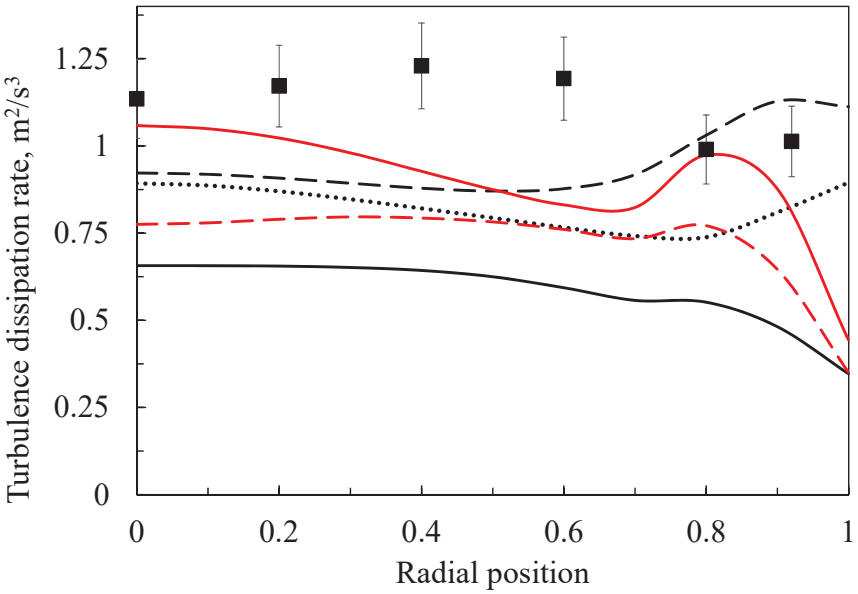

Figure 5.12: Turbulence dissipation rate for the column ϕ 0.4 m with a superficial gas velocity equal to 0.16 m/s at H/D=2.5. Data obtained with Eq. (5.143) (■) versus CFD results with different turbulence models: RNG k-ε (black solid line), Standard k-ε (black dashed line), Realizable k-ε (black dotted line), Standard k-ω (red solid line) and SST k-ω (red dashed line).

it is higher than the one calculated without considering the turbulence due to the energy transfer. The results are more similar to the data calculated with Eq. (5.143).

The turbulence properties comparison strongly depends on the turbulent viscosity correlation choice. The standard k-ω model seems to be the best choice if the the turbulent viscosity is calculated with the Forret (2003) correlation, while the RNG k-ε model seems to be the best one if the turbulent viscosity correlation proposed by Kawase & Moo-Young (1989) is adopted. The contribution of the turbulence due to energy transfer from gas-phase to liquid-phase has a positive effect on the turbulence dissipation rate, while the effect on the turbulence kinetic energy strongly depends on the model that is adopted.

The objective of this part of the work is not to compare the turbulent properties or to suggest a better turbulence model, but understand the effect that turbulent properties have on coalescence and breakage. The effect of the turbulence model choice on the Sauter mean diameter is quite low, as shown in Fig. 5.14. Every turbulence models provides similar results. The standard k-ε presents some differences next to the wall, with a more pronounced profile. The effect of the turbulence due to energy transfer from gas-phase to liquid-phase on the Sauter mean diameter is low (Fig. 5.15).

It is possible to conclude that the coalescence and breakage kernels studied in this work are suitable for many turbulence models and the best results are obtained with the RNG k-ε, realizable k-ε and standard k-ω and SST k-ω models. This set of kernel can be used also if the turbulence due to energy transfer from gas to liquid is considered. One possible explanation is that using the critical approach velocity model, the effect of the turbulence dissipation rate on the coalesce

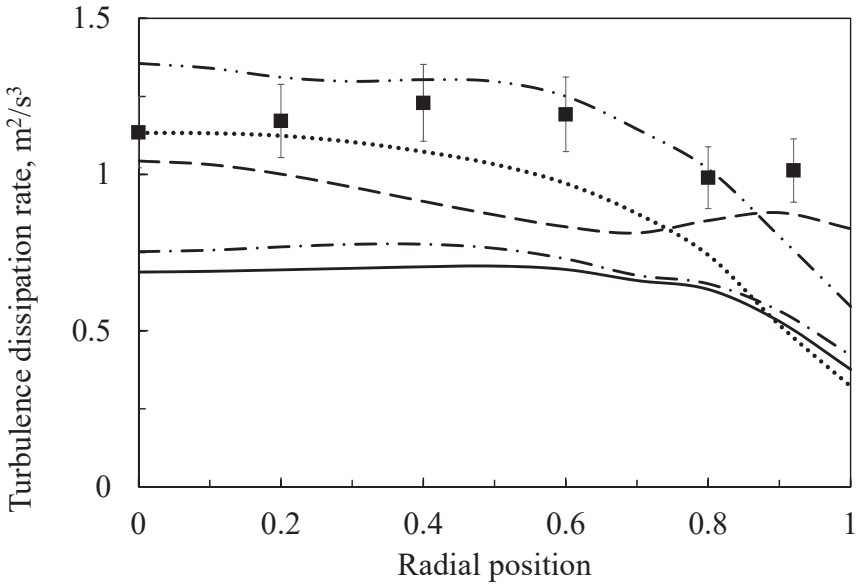

Figure 5.13: Turbulence dissipation rate for the column ϕ 0.4 m with a superficial gas velocity equal to 0.16 m/s at H/D=2.5. Data obtained with Eq. (5.143) (■) versus CFD results with RNG k-ε model (solid line) coupled with different models for considering the turbulence due to energy transfer from gas-phase to liquid-phase: Yao & Morel (2004) (dotted line), Troshko & Hassan (2001) (dash-dot-dot line), Simonin & Viollet (1990) (dash-dot line) and Sato & Sekoguchi (1975) (dashed line).

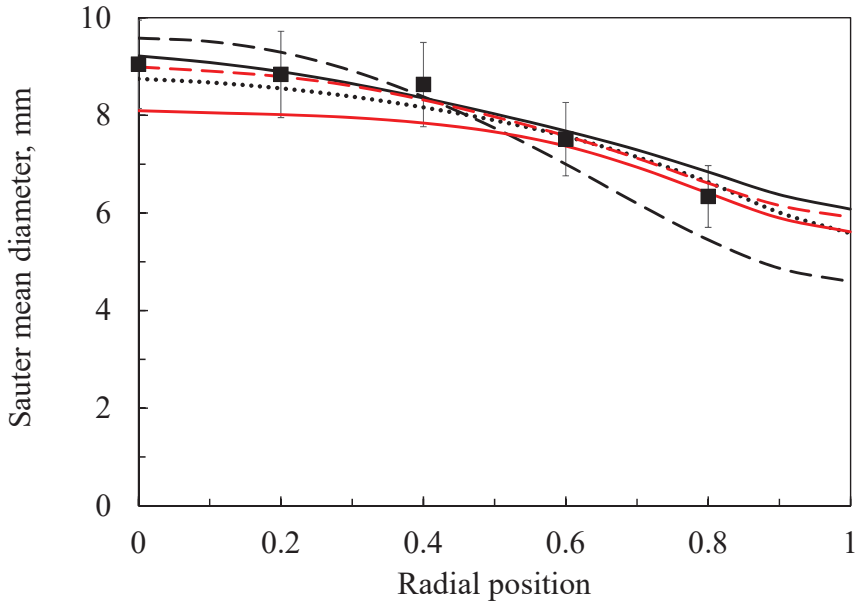

Figure 5.14: Sauter mean diameter for the column ϕ 0.4 m with a superficial gas velocity equal to 0.16 m/s at H/D=2.5. Experimental data obtained by Gemello et al. (2018a) (■) versus CFD results with different turbulence models: RNG k-ε (black solid line), Standard k-ε (black dashed line), Realizable k-ε (black dotted line), Standard k-ω (red solid line) and SST k-ω (red dashed line).

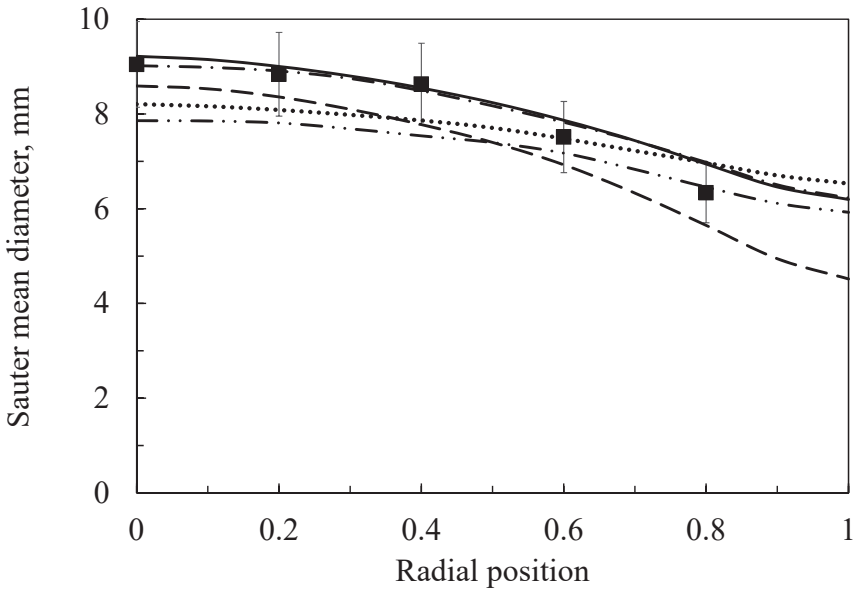

Figure 5.15: Sauter mean diameter for the column ϕ 0.4 m with a superficial gas velocity equal to 0.16 m/s at H/D=2.5. Experimental data obtained by Gemello et al. (2018a) (■) versus CFD results with RNG k-ε model (solid line) coupled with different models for considering the turbulence due to energy transfer from gas-phase to liquid-phase: Yao & Morel (2004) (dotted line), Troshko & Hassan (2001) (dash-dot-dot line), Simonin & Viollet (1990) (dash-dot line) and Sato & Sekoguchi (1975) (dashed line).

kernel is almost null under the operating conditions of the heterogeneous regime. When the relative velocity is higher than the critical one, the relative velocity appears in the numerator of the collision frequency and in the denominator of the coalescence efficiency. By multiplying them, the relative velocity, that depends on the turbulence dissipation rate, disappears under these operating conditions.

The simulations carried out with the RNG k-ε are the most stable and therefore this method has been adopted. The constants of this work, i.e. the minimum value of the swarm factor and the constant for the coalescence frequency of Wang et al. (2005*b*), have been fitted considering the RNG k-ε model without the turbulence due to energy transfer from gas to liquid. Similar constants would be obtained if the best fittings are carried out with other turbulence methods.

5.6.5 Water contamination effects on bubble size

As seen in Chapter 3, additives and contaminants lower the Sauter mean diameter. Only an empirical modification of the kernel is proposed here, as there is a lack of physical descriptors that could explain more quantitatively the coalescence behaviour. In accordance with Lehr & Mewes (1999) water contamination effects can be considered by lowering the critical approach velocity value.

In this work, several critical approach velocity values are tested, using the 0D model. A linear correlation between the critical approach velocity value and the volume-average Sauter mean diameter is shown in Fig. 5.16. The critical approach velocity model is valid for contaminated systems, as shown in Fig. 5.17.

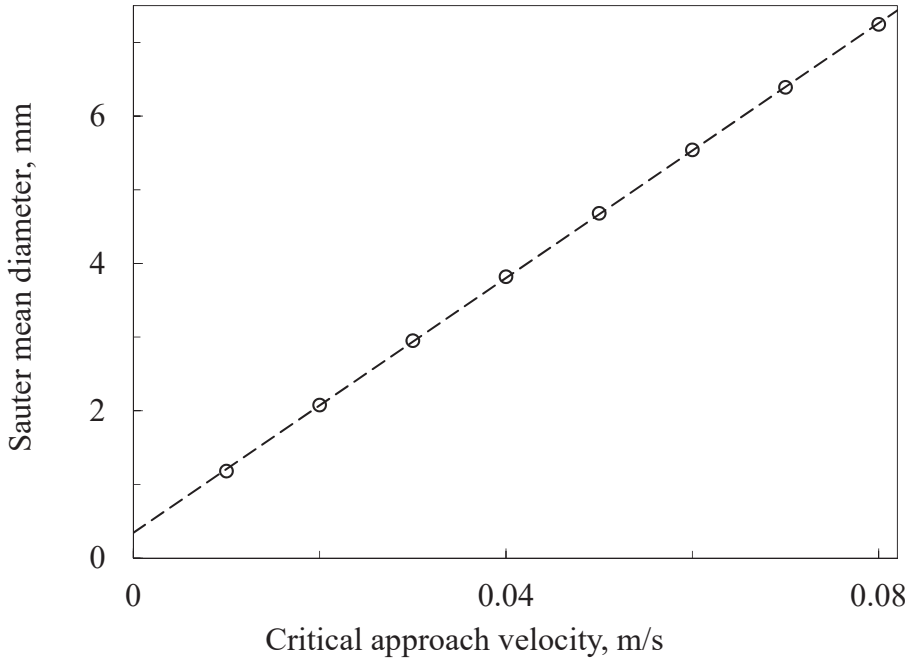

Figure 5.16: Effect of the critical approach velocity value on the Sauter mean diameter with a superficial gas velocity equal to 0.16 m/s.

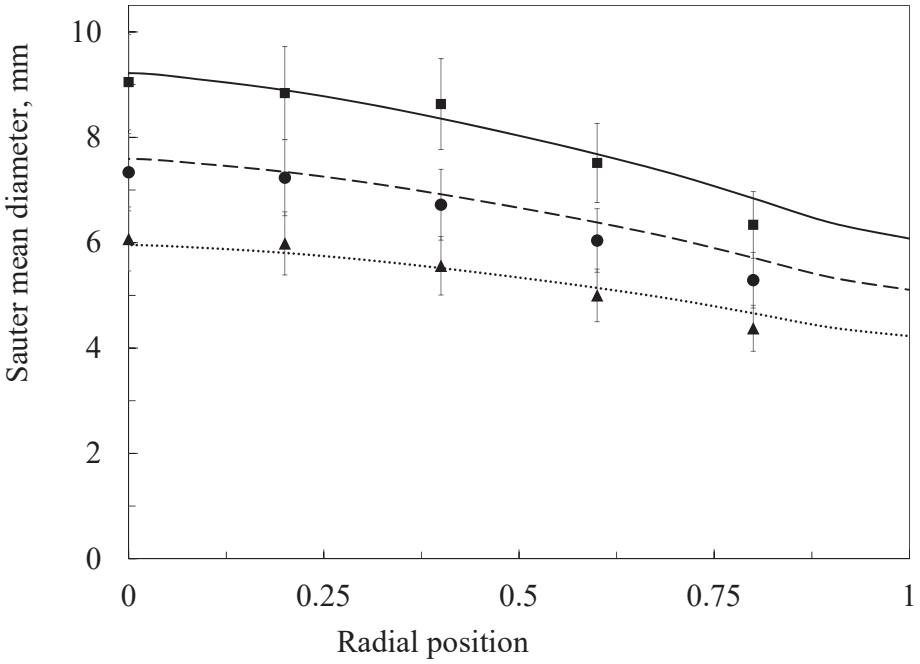

Figure 5.17: Ethanol effect on the Sauter mean diameter with a superficial gas velocity equal to 0.16 m/s. Experimental data obtained by Gemello et al. (2018a) with demineralised water (■), ethanol 0.01% (●) and ethanol 0.05% (▲) versus CFD results with different critical approach velocities: 0.08 m/s (demineralised water) (solid line), 0.065 m/s (ethanol 0.01%) (dashed line) and 0.05 m/s (ethanol 0.05%) (dotted line).

By knowing the space-averaged Sauter mean diameter, it is possible to obtain the critical approach velocity model and this value can be used to study the Sauter

mean diameter at different radial and axial positions with CFD-PBM simulations. The volume-average Sauter mean diameter is affected by the concentration and by the nature of the additive. The critical approach velocity values are obtained from the experimental profile and using the values reported in Fig. 5.16. For the 0.05% ethanol solution, a critical approach velocity equal to 0.05 m/s can be adopted, while for the 0.01% ethanol solution and for tap water, a critical approach velocity equal to 0.065 m/s can be used. The values obtained in this work can be used in different bubble columns. More experiments and liquid properties data would be useful to find a correlation that links these properties to the bubble size and obtain a fully predictive tool, as partially suggested by Lehr & Mewes (1999).

5.6.5.1 Inlet bubble size effects on the final bubble size

The inlet BSD is important and can influence the bubble size in the entire bubble column. In particular, it is important to remember to divide the values of the moments imposed as inlet boundary conditions by the inlet gas volume fraction. If not the system may perceive a fake bubble concentration, much lower than the real one. Bubble breakage is due to the surrounding liquid and then is not largely affected by this error. On the contrary, coalescence depends both on the surrounding liquid and on the interactions between the bubbles; therefore, an incorrect bubble density leads to an incorrect coalescence kernel.

As shown in Fig. 5.18 and in Fig. 5.19, the CFD-PBM model can manage small variations of inlet bubble size inside the experimental range.

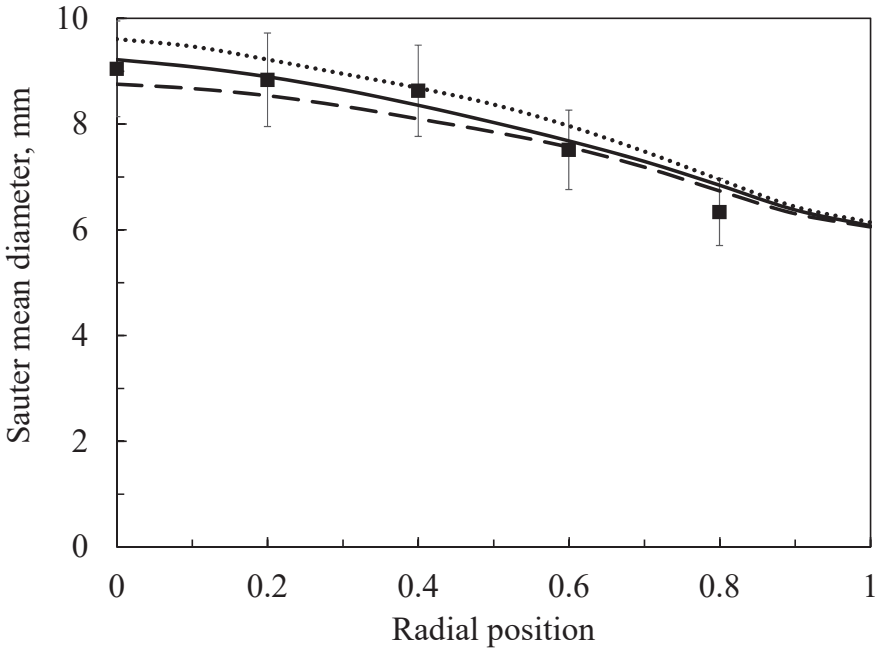

Figure 5.18: Effect of the inlet bubble size on the radial profile at H/D=2.5 with a superficial gas velocity equal to 0.16 m/s. Experimental data obtained by Gemello et al. (2018a) with the 92-holes sparger (■) versus CFD results with a homogeneous sparger and different inlet bubble sizes: 6.5 mm (dashed line), 7.7 mm (solid line) and 10 mm (dotted line).

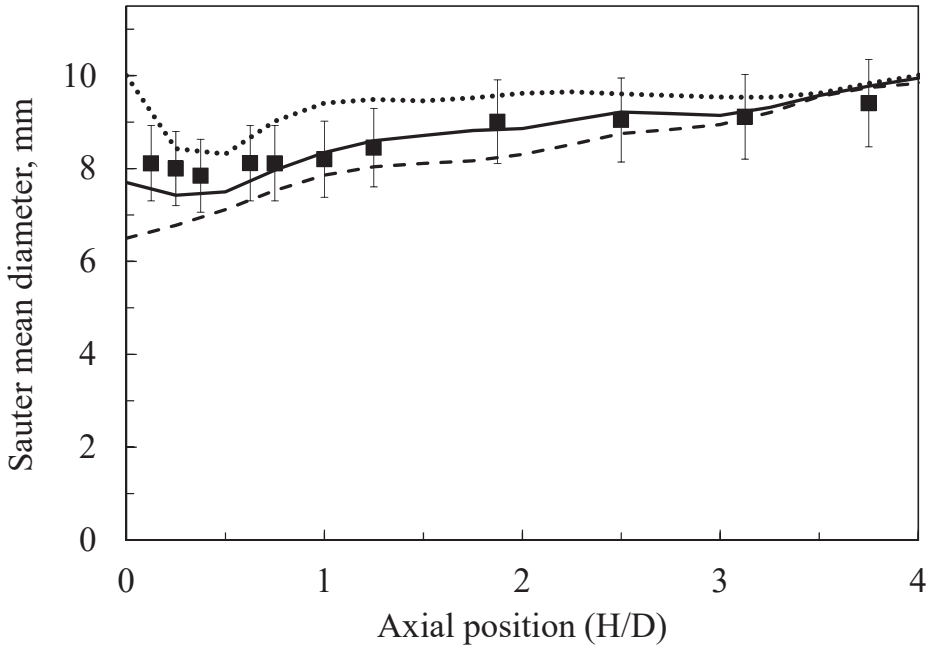

Figure 5.19: Effect of the inlet bubble size on the axial profile at the centre of the column with a superficial gas velocity equal to 0.16 m/s. Experimental data obtained by Gemello et al. (2018a) with the 92-holes sparger (■) versus CFD results with a homogeneous sparger and different inlet bubble sizes: 6.5 mm (dashed line), 7.7 mm (solid line) and 10 mm (dotted line).

By using an initial bubble size slightly lower than the previous one, equal to 6.5 mm, the bubble size is almost the same above a height of 1 m. By using an initial bubble size equal to 10 mm, the bubble size is slightly higher, but it is still acceptable. Small variations of initial bubble size are not very important, as the system reaches an equilibrium between coalescence and breakage.

5.6.5.2 Sparger effects on the bubble size

Gemello et al. (2018a) realized experiments with two different spargers. Firstly, a perforated sparger with several small holes (2 mm) is used. It generates bubbles with a Sauter mean diameter between 5 mm and 10 mm. The profile close to the bottom is almost flat, as detailed in Chapter 3. A sparger with 7 holes of 9 mm is then used, in order to modify the inlet bubble size. It causes the formation of big bubbles close to the bottom of the column, above the holes. The sparger choice radically influences the bubble dimension in the lowest part of the column. A perforated sparger with big holes causes the formation of big bubbles in the lowest part of the column, above the holes. The breakage of the bubbles is the predominant phenomenon if big bubbles are present. The bubble size decreases quickly along the axial position and the bubbles are almost not affected by the sparger after some centimetres. They reach quickly the equilibrium bubble dimension.

The previous simulations were realized by considering the high number of holes of the first sparger (92 holes) as a homogeneous porous plate. In CFD-PBM simulations, the gas enters the column already mixed with the liquid. A constant inlet gas volume fraction is assumed. The initial Sauter mean diameter is fixed equal

to 7.7 mm with a narrow log-normal bubble size distribution. These approximations are valid to simulate the sparger with 92 holes. Similar results are obtained by using an initial homogeneous bubble size slightly smaller (6.5 mm) or bigger (10 mm), as detailed above.

If the sparger with 7 holes is approximated with a homogeneous porous plate with a high inlet Sauter mean diameter (e.g. 15 mm), the results are wrong and the bubbles are bigger than the real ones for every column position, as observed in Fig. 5.20. The Sauter mean diameter is not able to reach the final equilibrium size obtained in the experiments. The CFD-PBM model cannot manage a homogeneous inlet bubble size that is much bigger than the real one. It confirms that the inlet boundary conditions are important in these systems.

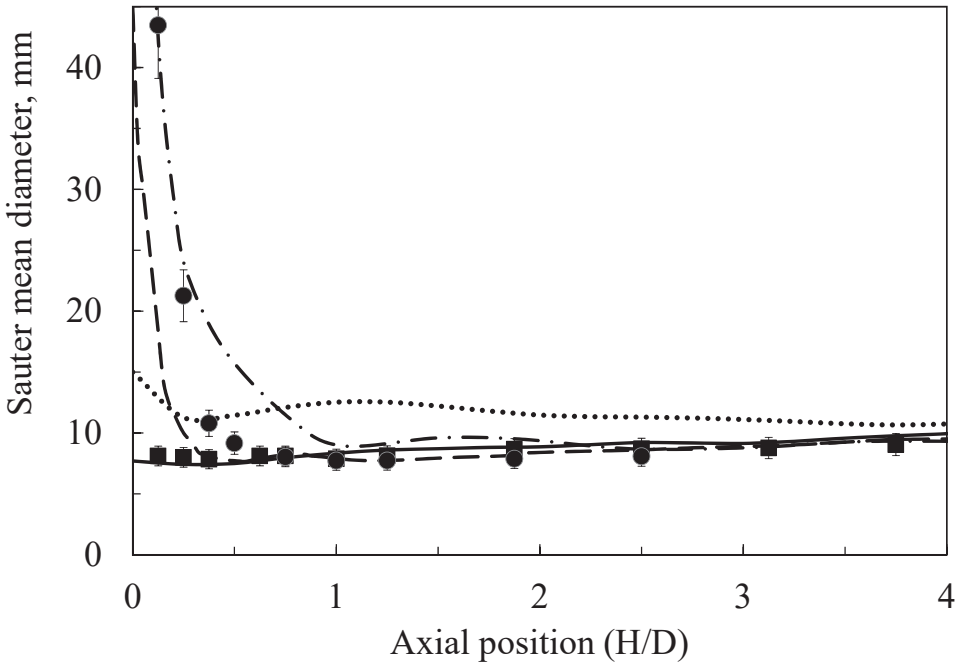

Figure 5.20: Effect of the sparger on the axial profile at the centre of the column of the Sauter mean diameter with a superficial gas velocity equal to 0.16 m/s. Experimental data obtained by Gemello et al. (2018a) with the 92-holes sparger (■) and the 7-holes sparger (●) versus CFD results with different spargers: homogeneous sparger with initial Sauter mean diameter equal to 7.7 mm (solid line) and 15 mm (dotted line) and non-homogeneous sparger with maximum initial Sauter mean diameter equal to 45 mm (Fig. 5.21) (dashed line) and 90 mm (dash-dot line).

New boundary conditions at the inlet (bottom) ought to be used. Spargers with few big holes need to be modelled with non-homogeneous and more realistic boundary conditions. The new sparger is created by using bubble size and gas fraction measured close to the bottom with the 7-holes sparger. These properties were measured at H=10 cm (H/D=0.25). Inlet bubble size and gas fraction depend on radial and azimuthal positions, with maximum values in correspondence of the real holes of the 7-holes sparger. The used inlet bubble size is reported in Fig. 5.21. The inlet gas fraction is imposed equal to 100% in correspondence of the 7 holes and equal to 0 in the other parts of the bottom. The inlet gas velocity magnitude

is calculated in order to obtain a correct superficial gas velocity (iterative method), and it depends on the imposed inlet gas fraction and on the used interpolation method.

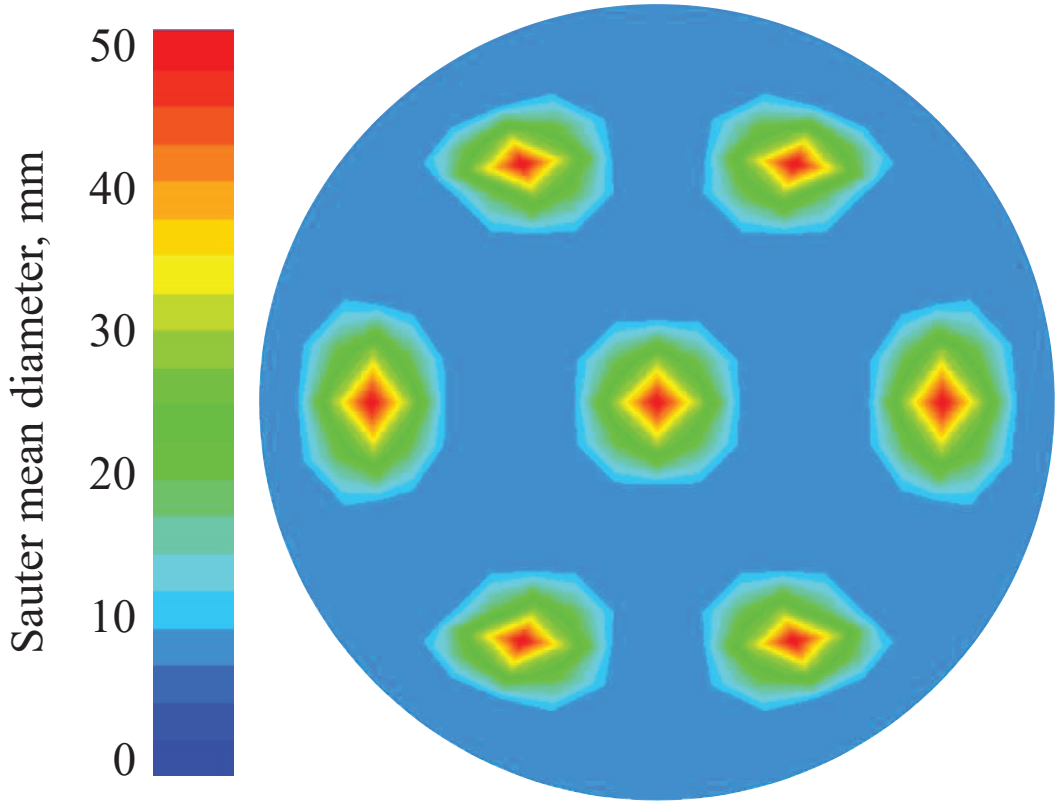

Figure 5.21: Inlet Sauter mean diameter with the 7-holes sparger.

The effect of the 7-holes sparger is important close to the bottom, in CFD-PBM simulations (Fig. 5.20). With this sparger, big bubbles appear close to the bottom. These big bubbles disappear quickly and the sparger effect is almost null above 1 m. The behaviour is in good agreement with the experimental data. In CFD-PBM simulations, the equilibrium size is reached a little slower, but the agreement is still good. An important aspect is that, in the CFD simulations, the turbulence dissipation rate is low next to the sparger. It might be used to study more in detail the turbulence models, with a focus on the turbulence properties in the lowest part of the column. A study on the effects of the inlet turbulence properties would be useful to further validate the kernels proposed in this work.

Considering these results, the effects of breakage and coalescence can be partially decoupled. Close to the bottom, the breakage is the main phenomenon and the coalescence is negligible. In this region, where the breakage is the principal phenomenon, the bubble size behaviour is quite correct, as the Sauter mean diameter decreases quickly, in good agreement with the experimental data. If both the breakage kernel and the final equilibrium bubble size are correct, the coalescence model can be considered as correct. Breakage and coalescence kernels are valid over a wide range of conditions.

5.6.6 Scale-up effects

Raimundo (2015) collected experimental data with tap water by using bubble columns at different scales: the column diameters were equal to 0.15 m, 0.4 m, 1 m and 3 m. The Sauter mean diameter does not change too much when the column diameter changes. It may be assumed that the behaviour is the same with demineralised water.

The initial rhomboidal cooper mesh with 40,000 cells, obtained and used with the column ϕ 0.4 m, is scaled up, in order to analyse the scale-up effect on the Sauter mean diameter in the CFD-PBM simulations. Grid-independent tests are required and they confirm that this mesh can be used for scale-up purposes, as reported in Chapter 4.

In the CFD-PBM simulations, the Sauter mean diameter is approximately the same also if the column diameter changes (Fig. 5.22). CFD-PBM results are quite in accordance with the experimental data of Raimundo (2015). Similar results are obtained by using RNG k-ε and k-ω turbulence models, as shown in Fig. 5.22. It means that the breakage and coalescence kernels proposed above can be used for the scale-up of these systems, with different turbulence models.

The final goal of this work is the industrial scale-up of bubble columns under the heterogeneous flow regime. Industrially, the Sauter mean diameter is not known *a priori* and it is often difficult to obtain it. The four bubble columns are simulated using different homogeneous inlet bubble sizes. The inlet Sauter mean diameter has an important effect with the smallest bubble columns. As presented in Fig. 5.23, the inlet bubble size partially influences the Sauter mean diameter at H/D=2.5 for the column ϕ 0.4 m, while its influence is almost zero for the columns ϕ 1 m and ϕ 3 m. The time needed for one bubble to reach H/D=2.5 is longer in the biggest columns than in the smallest ones. It allows reaching the equilibrium bubble size with a wider range of inlet Sauter mean diameters. The Sauter mean diameter obtained with the CFD simulations are compared with the experimental data presented in Chapter 3, that was obtained with demineralised water in the column ϕ 0.4 m (Fig. 5.23). New experiments by using bubble columns at different scales should be carried out in order to improve these models. Fortunately, industrial bubble columns are usually large and it means that the lack of knowledge about the bubble size close to the bottom does not strongly influence the final Sauter mean diameter.

5.7 Conclusions and perspectives

CFD simulations are frequently used for the study of bubble columns under industrial operating conditions and bubble size plays a key role in the hydrodynamics and transport phenomena for these systems. CFD simulations are coupled with a population balance model (PBM) in order to consider coalescence and breakage phenomena.

Coalescence and breakage phenomena are caused by different mechanisms and the most important are linked to turbulent fluctuations in the continuous phase. Breakage causes the formation of daughter bubbles and it is then necessary to define both the breakage frequency (breakage kernel) and the daughter distribution function. Coalescence rate is instead quantified by a kernel in turn divided into two parts: a collision frequency and a coalescence efficiency. The collision frequency

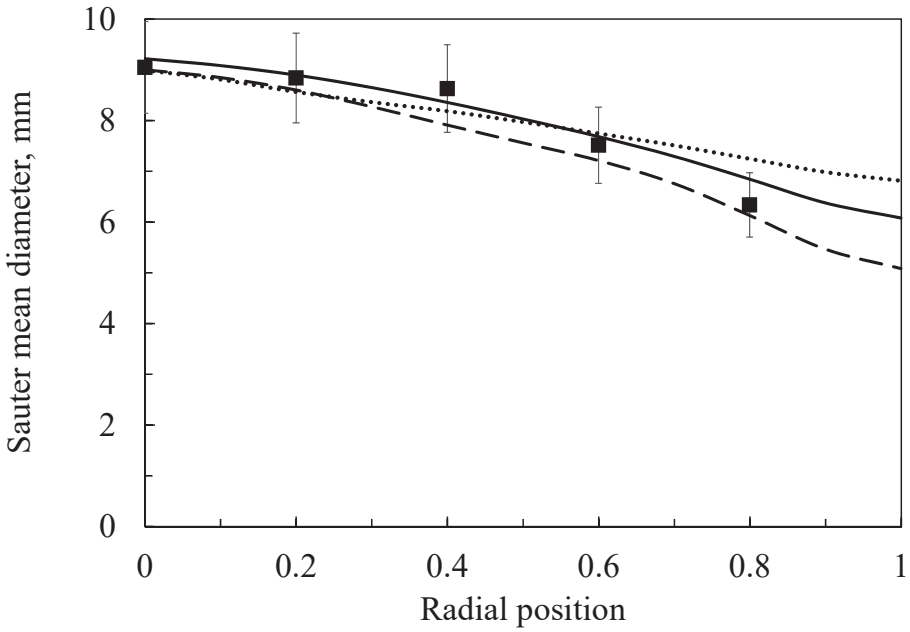

(a) RNG k-ε model.

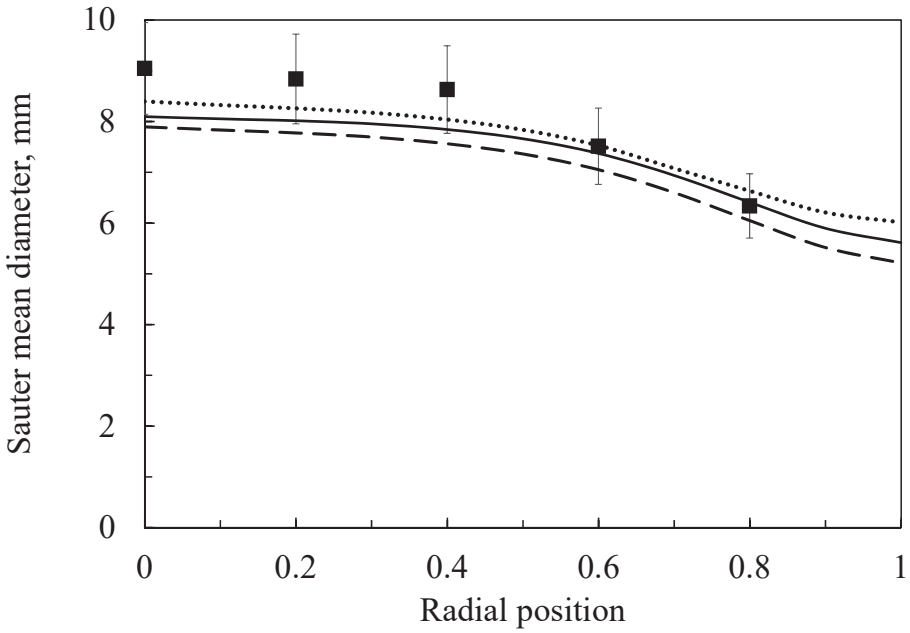

(b) Standard k-ω model.

Figure 5.22: Scale-up effect with a superficial gas velocity equal to 0.16 m/s and different turbulence models on the radial profile of Sauter mean diameter at H/D=2.5. Experimental data obtained by Gemello et al. (2018a) on the column ϕ 0.4 m (■) versus CFD results with different bubble column: ϕ 0.4 m (solid lines), ϕ 1 m (dashed lines) and ϕ 3 m (dotted lines).

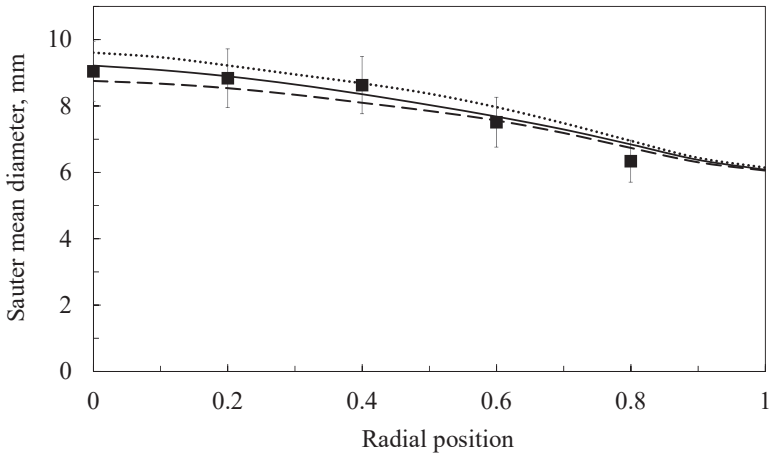

(a) ϕ *0.4 m*

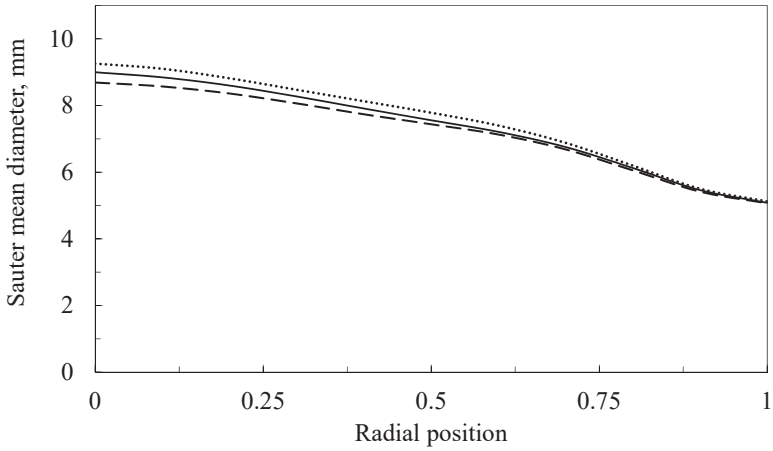

(b) ϕ *1 m*

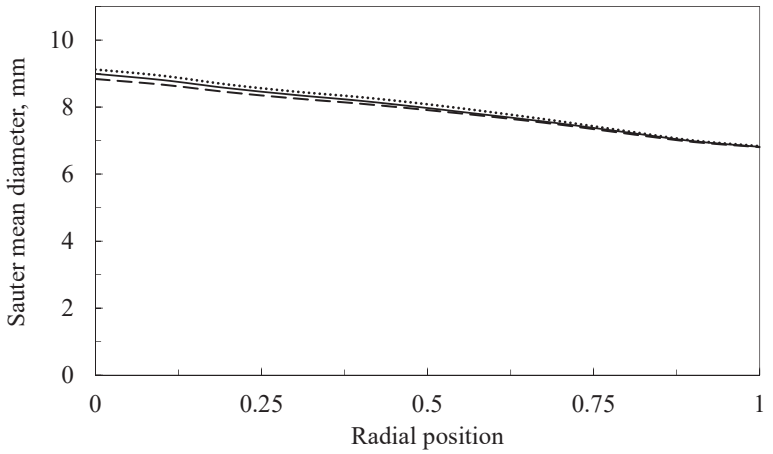

(c) ϕ *3 m*

Figure 5.23: Effect of inlet bubble size (homogeneous sparger) for different bubble columns with a superficial gas velocity equal to 0.16 m/s on the radial profile of Sauter mean diameter at H/D=2.5. Experimental data obtained by Gemello et al. (2018a) on the column ϕ 0.4 m (■) versus CFD results with different inlet bubble sizes: 6.5 mm (dashed lines), 7.7 mm (solid lines) and 10 mm (dotted lines).

defines the number of collisions while the coalescence efficiency is the fraction of colliding bubbles that actually coalesce. The latter one can be studied by using different methods: film drainage model, energy model and critical approach velocity model. The film drainage model is the most used for the homogeneous regime. The work of this chapter suggests that the critical approach velocity model is the best one for the heterogeneous regime. The best breakage kernels and the collision frequency need to be coupled with the critical approach velocity model. The mean bubble Sauter mean diameter predicted by the model in good agreement with the experiments for both the homogeneous and the heterogeneous flow regimes if the kernels are correctly fitted. Its radial profile has a parabolic shape under the heterogeneous regime, while it is almost flat under the homogeneous regime.

The best set of breakage and coalescence kernels in the case of heterogeneous regime seems to be the breakage kernel proposed by Laakkonen et al. (2006), the daughter distribution function proposed by Laakkonen et al. (2007), the modified collision frequency proposed by Wang et al. (2005*b*) and the critical approach velocity model for coalescence efficiency proposed by Lehr et al. (2002). These equations are reported here:

- Breakage kernel - Laakkonen et al. (2006)

$$g(L) = c_3 \varepsilon^{1/3} \operatorname{erfc}\left(\sqrt{c_4 \frac{\sigma}{\rho_l \varepsilon^{2/3} L^{5/3}} + c_5 \frac{\mu_l}{\sqrt{\rho_l \rho_g} \varepsilon^{1/3} L^{4/3}}}\right),$$

  with $c_3 = 4.0$, $c_4 = 0.04$ and $c_5 = 0.01$.

- Daughter distribution function - Laakkonen et al. (2007)

$$\bar{b}_i^k = \frac{3240 L_i^k}{(k+9)(k+12)(k+15).}$$

- Collision frequency - Wang et al. (2005*b*)

$$h_0\left(L_1, L_2\right) = C_2' \gamma \Pi \left(L_1 + L_2\right)^2 \varepsilon^{1/3} \sqrt{L_1^{2/3} + L_2^{2/3}},$$

  where $C_2' = 0.16$, while Π and γ are two correction factors:

  - Wu et al. (1998), $\Pi = \left[1 - \exp\left(-C_\Pi \frac{\alpha_{\max}^{1/3} \alpha_g^{1/3}}{\alpha_{\max}^{1/3} - \alpha_g^{1/3}}\right)\right]$, with $C_\Pi = 3$;
  - Wang et al. (2005*b*), $\gamma = \frac{\alpha_{\max}}{\alpha_{\max} - \alpha_g}$, with $\alpha_{\max} = 0.8$.

- Coalescence efficiency - Lehr et al. (2002)

$$\lambda\left(L_1, L_2\right) = \min\left(\frac{u_{crit}}{u_{rel}}, 1\right),$$

  with u_{crit}=0.08 m/s for demineralised water, lower for contaminated systems.

Coalescence and breakage kernels are generally affected by turbulence properties. Many turbulence models are tested: their effect on the bubble size seems fairly small. The coalescence and breakage kernels proposed in this chapter can be used with many turbulence models involved in Eulerian-Eulerian simulations. The contribution of the turbulence due to the energy transfer from the gas-phase to the liquid-phase is still an open question and it affects the turbulence properties. Its effects on the bubble size is low, if the set of coalescence and breakage kernels proposed in work is used. This set of kernels is suitable for several turbulence models and even if the turbulence due to the energy transfer is considered.

The previous set of kernels has been obtained, under the heterogeneous regime, with demineralised water using a homogeneous gas sparger. It is also valid for less-coalescent liquids, i.e. contaminated water and ethanol solutions. Contaminants and additives effects can be considered with an adjusted value of the critical approach velocity. CFD-PBM simulations well predict hydrodynamics and bubble size for these systems. More experiments with additives and experimental data on the liquid properties are required to obtain a fully predictive tool, that considers the additive effects *a priori*. The link between liquid physical properties and coalescence needs to be clarified.

The CFD-PBM simulations with this set of kernels are not very sensitive to the inlet bubble size. The results are in agreement with the experiments obtained by using the sparger with many small holes. On the other hand, these simulations cannot consider an inlet bubble size much larger than the experimental one. The inlet boundary conditions are important. It is necessary to model the sparger with few big holes with non-homogeneous and realistic inlet boundary conditions. In this work, the sparger with few big holes is modelled using the experimental gas fraction and bubble size measured in the lowest part of the column. It allows the correct prediction of hydrodynamics and bubble size for this sparger.

The proposed set of kernels seems to be suitable also for the industrial scale-up of bubble columns under the heterogeneous regime, but more studies and experimental data are required.

Bibliography

Alopaeus, V., Koskinen, J., Keskinen, K. I. & Majander, J. (2002), 'Simulation of the population balances for liquid-liquid systems in a nonideal stirred tank. part 2 - parameter fitting and the use of the multiblock model for dense dispersions', *Chemical Engineering Science* 57(10), 1815–1825.

Andersson, B., Andersson, R., Håkansson, L., Mortensen, M., Sudiyo, R., Van Wachem, B. & Hellström, L. (2012), *Computational Fluid Dynamics for Engineers*, first edn, University Press, Cambridge, UK.

Bilicki, Z. & Kestin, J. (1987), 'Transition criteria for two-phase flow patterns in vertical upward flow.', *International Journal of Multiphase Flow* 13, 283–298.

Buffo, A. (2012), Multivariate population balance for turbulent gas-liquid flows., PhD thesis, Politecnico di Torino, Torino, Italy.

Buffo, A., De Bona, J., Vanni, M. & Marchisio, D. L. (2016), 'Simplified volume-averaged models for liquid-liquid dispersions: Correct derivation and comparison with other approaches.', *Chemical Engineering Science* 153, 382–393.

Buffo, A., Vanni, M., Marchisio, D. L. & Fox, R. O. (2013), 'Multivariate Quadrature-Based Moments Methods for turbulent polydisperse gas-liquid systems', *International Journal of Multiphase Flow* 50, 41–57.

Burns, L. F. & Rice, R. G. (1997), 'Circulation in bubble columns', *American Institute of Chemical Engineering Journal* 43(6), 1390–1402.

Carrica, P. M. & Clausse, A. A. (1993), *A Mathematical Description of the Critical Heat Flux as Nonlinear Dynamic Instability*, G. Gouesbet and A. Berlemont. Instabilities in Multiphase Flow, Plenum Press, New York.

Casamatta, G. & Vogelpohl, A. (1985), 'Modeling of fluid dynamics and mass transfer in extraction columns', *German Chemical Engineering* 8, 96–103.

Chesters, A. K. (1991), 'The modeling of coalescence processes in fluid-liquid dispersions: A review of current understanding', *Chemical Engineering Research and Design: transactions of the Institution of Chemical Engineers: Part A* 69, 259–270.

Colella, D., Vinci, D., Bagatin, R., Masi, M. & Abu Bakr, E. (1999), 'A study on coalescence and breakage mechanisms in three different bubble columns', *Chemical Engineering Science* 54(21), 4767–4777.

Colin, C., Riou, X. & Fabre, J. (2004), Turbulence and shear-induced coalescence in gas-liquid pipe flows, *in* 'ICMF 2004 - 5th International Conference on Multiphase Flow', Yokohama, Japan.

Coulaloglou, C. A. (1975), Dispersed phase interactions in an agitated flow vessel, PhD thesis, Illinois Institute of Technology, Chicago, Illinois.

Coulaloglou, C. A. & Tavlarides, L. L. (1977), 'Description of interaction processes in agitated liquid-liquid dispersions', *Chemical Engineering Science* 32, 1289–1297.

De Bona, J., Buffo, A., Vanni, M. & Marchisio, D. L. (2016), 'Limitations of simple mass transfer models in polydisperse liquid-liquid dispersions.', *Chemical Engineering Journal* 296, 112–121.

Dette, H. & Studden, W. J. (1997), *The Theory of Canonical Moments with Applications in Statistics, Probability, and Analysis.*, John Wiley and Sons., New York.

Doubliez, L. (1991), 'The drainage and rupture of a non-foaming liquid film formed upon bubble impact with a free surface', *International Journal of Multiphase Flow* 17, 783–803.

Falzone, S., Buffo, A., Vanni, M. & Marchisio, D. L. (2018), 'Simulation of turbulent coalescence and breakage of bubbles and droplets in the presence of surfactants, salts, and contaminants', *Advances in Chemical Engineering* 52, 125–188.

Forret, A. (2003), Hydrodynamics scale-up of slurry bubble columns., PhD thesis, Université Claude Bernard Lyon 1 - IFPEN, Lyon, France.

Frank, T., Zwart, P. J., Krepper, E., Prasser, H. M. & Lucas, D. (2008), 'Validation of cfd models for mono- and polydisperse airâĂŞwater two-phase flows in pipes', *Nuclear Engineering and Design* 238(3), 647–659.

Friedlander, S. K. (1977), *Smoke, Dust and Haze*, Wiley, New York.

Fu, X. Y. & Ishii, M. (2003), 'Two-group interfacial area transport in vertical air-water flow: I. mechanistic model', *Nuclear Engineering and Design* 219(2), 14 –168.

Gao, Z., Li, D., Buffo, A., Podgórska, W. & Marchisio, D. L. (2016), 'Simulation of droplet breakage in turbulent liquid-liquid dispersions with CFD-PBM: Comparison of breakage kernels', *Chemical Engineering Science* 142, 277–288.

Gemello, L., Cappello, V., Augier, F., Marchisio, D. L. & Plais, C. (2018b), 'CFD-based scale-up of hydrodynamics and mixing in bubble columns', *Chemical Engineering Research and Design* 136, 846–858.

Gemello, L., Plais, C., Augier, F., Cloupet, A. & Marchisio, D. L. (2018a), 'Hydrodynamics and bubble size in bubble columns: Effects of contaminants and spargers', *Chemical Engineering Science* 184, 93–102.

Godin, F. B., Cooper, G., D. & Rey, A. D. (1999), 'Numerical methods for a population-balance model of a periodic fermentation process.', *American Institute of Chemical Engineering Journal* 45, 1359–1364.

Gordon, R. G. (1981), 'Error bounds in equilibrium statistical mechanics', *Journal of Mathematical Physics* 9, 655–663.

Gunawan, R., Fusman, I. & Braatz, R. D. (2004), 'High resolution algorithms for multidimensional population balance equations.', *American Institute of Chemical Engineering Journal* 50, 2738–2749.

Hesketh, R. P., Russell, T. W. F. & Etchells, A. W. (1987), 'Bubble size in horizontal pipelines.', *American Institute of Chemical Engineering Journal* 33, 663–667.

Hibiki, T. & Ishii, M. (2000), 'One-group interfacial area transport of bubbly flows in vertical round tubes', *International Journal of Heat and Mass Transfer* 43, 2711–2726.

Hibiki, T., Takasama, T. & Ishii, M. (2001), 'Interfacial area transport of bubbly flow in a small diameter pipe', *Journal of Nuclear Science and Technology* 38, 614–620.

Howarth, W. J. (1964), 'Coalescence of drops in a turbulent flow field', *Chemical Engineering Science* 19, 33–38.

Jeffreys, G. V. & Davies, G. A. (1971), *Coalescence of Liquid Droplets and Liquid Dispersion: Recent Advances in Liquid-Liquid Extraction*, 1 st edn, Pergamon Press, Oxford, UK.

Kalkach-Navarro, S., Lahey Jr., R. T. & Drew, D. A. (1994), 'Analysis of the bubbly/slug flow regime transition', *Nuclear Engineering and Design* 151(1), 15–39.

Kato, M. & Launder, B. E. (1993), The modeling of turbulent flow around stationary and vibrating square cylinders, *in* '9th Symposium on Turbulent Shear Flows', Kyoto, Japan.

Kawase, Y. & Moo-Young, M. (1989), 'Turbulence intensity in bubble columns', *The Chemical Engineering Journal* 40(1), 55–58.

Kennard, E. H. (1938), *Kinetic Theory of Gases*, McGraw-Hill, New York.

Kentish, S. E., Stevens, G. W. & Pratt, H. R. C. (1998), 'Estimation of coalescence and breakage rate constants within a kühni column', *Industrial & Engineering Chemistry Research* 37(3), 1099–1106.

Konno, M., Muto, T. & Saito, S. (1988), 'Coalescence of dispersed drops in an agitated tank', *Journal of Chemical Engineering of Japan* 21, 335–338.

Kuboi, R., Komasawa, I. & Otake, T. (1972), 'Collision and coalescence of dispersed drops in turbulent liquid flow', *Journal of Chemical Engineering of Japan* 5, 423–424.

Kumar, J., Peglow, M., Warnecke, G. & Heinrich, S. (2008), 'The cell average technique for solving multi-dimensional aggregation population balance equations', *Computers & Chemical Engineering* 32, 1810–1830.

Laakkonen, M., Alopaeus, V. & Aittamaa, J. (2006), 'Validation of bubble breakage, coalescence and mass transfer models for gas-liquid dispersion in agitated vessel', *Chemical Engineering Science* 61, 218–228.

Laakkonen, M., Moilanen, P., Alopaeus, V. & Aittamaa, J. (2007), 'Modelling local bubble size distributions in agitated vessels', *Chemical Engineering Science* 62, 721–740.

Lasheras, J. C., Eastwood, C., Martínez-Bazán, C. & Montañés, J. L. (2002), 'A review of statistical models for the break-up of an immiscible fluid immersed into a fully developed turbulent flow', *International Journal of Multiphase Flow* 28, 247–278.

Lee, C. H., Erickson, L. E. & Glasgow, L. A. (1987), 'Bubble break-up and coalescence in turbulent gas-liquid dispersions', *Chemical Engineering Communications* 59, 65–84.

Lehr, F. & Mewes, D. (1999), 'A transport equation for the interfacial area density applied to bubble columns', *Chemical Engineering Science* 56, 1159–1166.

Lehr, F., Millies, M. & Mewes, D. (2002), 'Bubble-size distributions and flow fields in bubble columns', *American Institute of Chemical Engineering Journal* 48(11), 2426–2443.

Levich, V. G. (1962), *Physicochemical Hydrodynamics*, Prentice Hall, Englewood Cliffs, NJ.

Li, D., Gao, Z., Buffo, A., Podgórska, W. & Marchisio, D. L. (2017), 'Droplet breakage and coalescence in liquid-liquid dispersions: Comparison of different kernels with EQMOM and QMOM', *American Institute of Chemical Engineering Journal* 63(6), 2293–2311.

Liao, Y. & Lucas, D. (2009), 'A literature review of theoretical models for drop and bubble breakup in turbulent dispersions', *Chemical Engineering Science* 64, 3389–3406.

Liao, Y. & Lucas, D. (2010), 'A literature review on mechanisms and models for the coalescence process of fluid particles', *Chemical Engineering Science* 65, 2851–2864.

Luo, H. (1993), Coalescence, breakup and liquid circulation in bubble column reactors, PhD thesis, The Norwegian Institute of Technology, Trondheim, Norway.

Luo, H. & Svendsen, H. F. (1996), 'Modeling and simulation of binary approach by energy conservation analysis', *Chemical Engineering Communications* 145, 145–153.

Marchisio, D. L. & Fox, R. O. (2013), *Computational Models for Polydisperse Particulate and Multiphase Systems*, Cambridge Series in Chemical Engineering, Cambridge University Press, Cambridge, UK.

Marchisio, D. L., Vigil, R. D. & Fox, R. O. (2003*a*), 'Implementation of the quadrature method of moments in CFD codes for aggregation-breakage problems', *Chemical Engineering Science* 58, 3337–3351.

Marchisio, D. L., Vigil, R. D. & Fox, R. O. (2003*b*), 'Quadrature method of moments for aggregation-breakage processes', *Journal of Colloid and Interface Science* 258, 322–334.

Mazzei, L., Marchisio, D. L. & Lettieri, P. (2012), 'New quadrature-based moment method for the mixing of inert polydisperse fluidized powders in commercial cfd codes.', *American Institute of Chemical Engineering Journal* 58(10), 3054–3069.

McClure, D. D., Deligny, J., Kavanagh, J. M., Fletcher, D. F. & Barton, G. W. (2014), 'Impact of surfactant chemistry on bubble column systems', *Chemical Engineering & Technology* 37(4), 652–658.

McClure, D. D., Kavanagh, J. M., Fletcher, D. F. & Barton, G. W. (2013), 'Development of a CFD model of bubble column bioreactors: Part one - a detailed experimental study', *Chemical Engineering & Technology* 36(12), 2065–2070.

McClure, D. D., Norris, H., Kavanagh, J. M., Fletcher, D. F. & Barton, G. W. (2015), 'Towards a CFD model of bubble columns containing significant surfactant levels', *Chemical Engineering Science* 127, 189–201.

McGraw, R. (1997), 'Description of aerosol dynamics by the quadrature method of moments.', *Aerosol Science and Technology* 27, 255–265.

Menzel, T., In der Weide, T., Staudacher, O., Wein, O. & Onken, U. (1990), 'Reynolds stress model for bubble column reactor', *Industrial & Engineering Chemistry Research* 29(6), 988–994.

Miyauchi, T. & Shyu, C.-N. (1970), 'Flow of fluid in gas bubble columns', *Kagaku Kogaku* 34(9), 958–964.

Narasimhan, G., Ramakrishna, D. & Gupta, J. P. (1979), 'A model for transitional breakage probability of droplets in agitated lean liquid-liquid dispersions', *Chemical Engineering Science* 34, 257–265.

Nevers, N. & Wu, J. L. (1971), 'Bubble coalescence in viscous fluids.', *American Institute of Chemical Engineering Journal* 17, 182–186.

Park, J. Y. & Blair, L. M. (1975), 'The effect of coalescence on drop size distribution in an agitated liquid-liquid dispersion', *Chemical Engineering Science* 30, 1057–1064.

Petitti, M., Nasuti, A., Marchisio, D. L., Vanni, M., Baldi, G., Mancini, N. & Podenzani, F. (2010), 'Bubble size distribution modeling in stirred gas-liquid reactors with QMOM augmented by a new correction algorithm.', *American Institute of Chemical Engineering Journal* 56, 36–53.

Podgórska, W. & Marchisio, D. L. (2016), 'Modeling of turbulent drop coalescence in the presence of electrostatic forces', *Chemical Engineering Research and Design* 108, 30–41.

Prince, M. J. & Blanch, H. W. (1990), 'Bubble coalescence and break-up in air-sparged bubble columns', *American Institute of Chemical Engineering Journal* 36, 1485–1499.

Raimundo, P. M. (2015), Analysis and modelization of local hydrodynamics in bubble columns, PhD thesis, Université Grenoble Alpes.

Renardy, Y., Cristini, V. & Li, J. (2002), 'Drop fragment distributions under shear with inertia', *International Journal of Multiphase Flow* 28, 1125–1147.

Revankar, S. T. (2001), Coalescence and breakup of fluid particles in multi-phase flow, *in* 'ICMF 2001 - 4th International Conference on Multiphase Flow', NewOrleans, Louisiana, USA.

Roels, J. A. & Heijnen, J. J. (1980), 'Power dissipation and heat production in bubble columns: Approach based on nonequilibrium thermodynamics', *Biotechnology and Bioengineering* 22(11), 2399–2404.

Sato, Y. & Sekoguchi, K. (1975), 'Liquid velocity distribution in two-phase bubble flow', *International Journal of Multiphase Flow* 2(1), 79–95.

Shinnar, R. & Church, J. M. (1960), 'Predicting particle size in agitated dispersions', *Industrial and Engineering Chemistry* 52, 253–256.

Simon, M. (2004), Koaleszenz von Tropfen und Tropfenschwärmen, PhD thesis, Teschinschen Universtität Kaiserslautern, Kaiserslautern, Germany.

Simonin, O. & Viollet, P. L. (1990), 'Modeling of turbulent two-phase jets loaded with discrete particles', *Phenomena in Multiphase Flows* pp. 259–269.

Sovova, H. (1981), 'Breakage and coalescence of drops in a batch stirred vessel - ii comparison of model and experiments', *Chemical Engineering Science* 36, 1567–1573.

Tomiyama, A. (1998), 'Struggle with computational bubble dynamics.', *Multiphase Science and Technology* 10(4), 369.

Troshko, A. A. & Hassan, Y. A. (2001), 'A two-equation turbulence model of turbulent bubbly flows', *International Journal of Multiphase Flow* 27(11), 1965–2000.

Vanni, M. (2000), 'Approximate population balance equation for aggregation-breakage processes', *International Journal of Multiphase Flow* 221, 143–160.

Wang, T. F., Wang, J. F. & Jin, Y. (2003), 'A novel theoretical breakup kernel function for bubbles/droplets in a turbulent flow', *Chemical Engineering Science* 58(20), 4629–4637.

Wang, T. F., Wang, J. F. & Jin, Y. (2004), 'An efficient numerical algorithm for "a novel theoretical breakup kernel function of bubble/droplet in a turbulent flow"', *Chemical Engineering Science* 59, 2593–2595.

Wang, T. F., Wang, J. F. & Jin, Y. (2005*a*), 'Population balance model for gas-liquid flows: Influence of bubble coalescence and breakup models', *Industrial & Engineering Chemistry Research* 44(11), 7540–7549.

Wang, T. F., Wang, J. F. & Jin, Y. (2005*b*), 'Theoretical prediction of flow regime transition in bubble columns by the population balance model', *Chemical Engineering Science* 60, 6199–6209.

Wang, T., Wang, J. & Jin, Y. (2006), 'A CFD-PBM coupled model for gas-liquid flows', *American Institute of Chemical Engineering Journal* 52, 125–140.

Wheeler, J. C. (1974), 'Modified moments and gaussian quadratures.', *Rocky Mountain Journal of Mathematics* 4, 287–296.

Wilf, H. (1962), *Mathematics for the Physical Sciences.*, John Wiley and Sons., New York.

Wright, D. L. (2007), 'Numerical advection of moments of the particle size distribution in eulerian models.', *Journal of Aerosol Science* 38, 352–369.

Wright, H. & Ramkrishna, D. (1994), 'Factors affecting coalescence frequency of droplets in a stirred liquid-liquid dispersion', *American Institute of Chemical Engineering Journal* 40, 767–776.

Wu, Q., Kim, S. & Ishii, M. (1998), 'One-group interfacial area transport in vertical bubbly flow', *International Journal of Heat and Mass Transfer* 41, 1103–1112.

Yao, W. & Morel, C. (2004), 'Volumetric interfacial area prediction in upward bubbly two-phase flow', *International Journal of Heat and Mass Transfer* 47, 307–328.

Yuan, C. & Fox, R. O. (2011), 'Conditional quadrature method of moments for kinetic equations.', *Journal of Computational Physics* 230, 8216–8246.

Zhao, H., Maisels, A., Matsoukas, T. & Zheng, C. (2007), 'Analysis of four Monte-Carlo methods for the solution of population balances in dispersed systems', *Powder Technology* 173, 38–50.

Chapter 6

Concluding remarks and future works

The objective of this work is to correctly predict the bubble size distributions in bubble columns and to study breakage and coalescence under industrial operating conditions, focusing the attention on the heterogeneous flow regime.

To study these phenomena, new experimental data is required. Under the heterogeneous regime, the liquid recirculation is strong and the radial profiles of gas volume fraction, liquid velocity and mean bubble size have a strong concavity. The presence of contaminants and additives in the continuous phase, namely water, (demineralized water, tap water and demineralised water with small quantities of ethanol) has a strong effect on bubble size and coalescence. Bubbles in demineralised water are significantly bigger than in tap water. The addition of small quantities of ethanol into demineralised water greatly decreases the bubble size, delays regime transition and increases the gas volume fraction under the heterogeneous flow regime. The presence of ethanol modifies the surface bubble mobility and decreases bubble coalescence. The relevant physical properties, that cause these differences, still need to be identified. Surface tension is one of them, but its variation is not the only explanation for these differences and more studies are required to understand the factors that prevent coalescence. The relationship between the physical properties of liquids and coalescence kernels needs to be clarified. More experiments with additives and experimental data on the relevant liquid properties can be useful to consider them in the coalescence and breakage kernels and to obtain a fully predictive tool.

The sparger choice strongly influences the bubble size and the hydrodynamics close to the bottom. With a sparger perforated with big holes, there is an accumulation of big bubbles in the lowest part of the column, in which bubble breakage is the main phenomenon. The effects of ethanol and sparger were combined to decouple coalescence and breakage phenomena. The presence of additives almost does not influence breakage, while its effect is important on bubble coalescence, as the surface mobility changes. For these reasons, in this thesis several experiments have been carried out, that allow to study correctly Sauter mean diameter and hydrodynamic properties in a wide range of operating conditions under the heterogeneous regime, in presence of contaminants and additives and by using different perforated spargers.

The study of bubble size distributions (BSD) could be interesting, but the cross-correlation technique used in the present work is not able to measure the BSD, as it calculates only the Sauter mean diameter. An interesting experimental perspective could be to couple a classical optical probe method for BSD, that currently is not suitable for the heterogeneous regime, with a cross-correlation technique for Sauter mean diameter, in order to rescale the BSD under the heterogeneous regime.

The experimental results are used to carry out 3D URANS (Unsteady Reynolds-averaged Navier-Stokes equations) CFD (Computational Fluid Dynamics) simulations and the main results of this validation can be summarized as follows:

- Bubble column reactors under the heterogeneous flow regime are dominated by interfacial forces and the drag force is the most important. Hydrodynamic profiles have a strong link with interfacial forces and turbulence. A drag law suitable for oblate bubbles, such as Tomiyama (1998), needs to be used. This should be modified by considering a swarm factor, to incorporate the swarm effect. It must decrease the drag force for high gas volume fractions. For very high gas volume fractions, the swarm factor of Simonnet et al. (2008) causes convergence issues and an incorrect instantaneous behaviour, with bubbles that create unphysical huge accumulations of bubbles. By modifying the swarm factor of Simonnet et al. (2008), CFD hydrodynamics is in agreement with experimental data. A minimum value is added to the swarm factor of Simonnet et al. (2008). The radial profiles of gas volume fraction and phases velocity are well predicted. The scale-up effects on hydrodynamics are investigated and it is possible to state that this swarm factor can be assumed suitable for industrial scale-up purposes. These results allow predicting correctly the hydrodynamics of bubble columns under the heterogeneous regime, in the case of fixed bubble size.

- Turbulence has strong effects on these systems. Different turbulence models are tested. An extra diffusion coefficient due to bubbles, as presented by Alméras et al. (2015) is considered, in order to simulate the dispersion of a scalar. The RNG k-ε turbulence model predicts turbulence properties and scalar mixing reasonably, with good agreement with experimental data. The extra diffusion coefficient due to bubbles cannot be neglected for the smallest column, as it has a significant effect on scalar mixing (about 15%), while it is negligible in other cases. The main contribution is due to the Shear Induced Turbulence (SIT).

- CFD simulations coupled with a Population Balance Model (PBM) to predict the bubble size distribution show that bubble size influences the hydrodynamics and the BSD is required to estimate the interfacial area and the local heat and mass transfer rate. Numerous mechanisms are involved in bubble coalescence and breakage. The existing models of breakage (Liao & Lucas 2009) and coalescence (Liao & Lucas 2010), developed for the homogeneous regime, are tested under the heterogeneous regime. The coalescence kernel can be divided in collision frequency and coalescence efficiency. Breakage and collision frequency mechanisms are linked to turbulent fluctuations. The coalescence efficiency can be studied through the film drainage model under the homogeneous regime, while it is not suitable for the heterogeneous regime. The

best model under the heterogeneous regime seems to be the critical approach velocity model. The breakage model of Laakkonen et al. (2006), the collision frequency model of Wang et al. (2005) with a modified constant and the critical approach velocity model for coalescence efficiency of Lehr et al. (2002) are demonstrated in this work to be suitable for the heterogeneous regime. The Sauter mean diameter of the bubbles predicted with this set of models is in agreement with experimental data for both the homogeneous and the heterogeneous regimes. The radial profile of the Sauter mean diameter is parabolic under the heterogeneous regime and almost flat under the homogeneous regime, in agreement with experiments. Hydrodynamics is still well predicted.

- Turbulence properties influence the coalescence and breakage kernels and, in particular, the turbulence dissipation rate plays a direct role. Testing different turbulence models, it is possible to conclude that the set of kernels proposed in this work can be used with different classical turbulence models involved in Eulerian-Eulerian simulations.

- The proposed set of kernels allows carrying out simulations that are able to handle small changes in inlet bubble size. The CFD-PBM results are in agreement with experimental data obtained with the sparger formed by several small holes (homogeneous gas distribution). These simulations cannot handle a homogeneous inlet bubble size much higher than the experimental data. The sparger with a few big holes needs to be modelled with non-homogeneous and more realistic inlet boundary conditions. In this work, Experimental gas fraction and bubble size measured close to the bottom are used to model this sparger. Hydrodynamics and bubble size are well predicted by using realistic inlet boundary conditions.

- The set of kernels proposed in this work can be used for scale-up purposes, but more experiments and CFD studies are necessary on this topic. Experimental data with demineralized water, with or without alcohol addition at larger scale can be useful to validate these CFD-PBM models for industrial scale-up. CFD simulations with different geometries and meshes of industrial-scale bubble columns should be carried out.

Some limits have not yet been overcome and different perspectives and future works are possible:

- The swarm factor proposed in this work is able to correctly predict the hydrodynamics, but it has the limit to be empirical. The original swarm factor of Simonnet et al. (2008) was obtained thanks to experimental data and the correction proposed in this work is obtained thanks to a CFD fitting. A theoretical model might provide suitable results for different gas-liquid systems. Moreover, the study of secondary interfacial forces, that are not considered in this work, could be an interesting perspective.

- More studies on the cntribution of the turbulence due to energy transfer from gas-phase to liquid-phase could be an important perspective. A comparison between the effects of these models and the effects of the extra diffusivity model of Alméras et al. (2015) should be carried out.

- The critical approach velocity model of Lehr et al. (2002) has the advantage that it can be successfully applied to less coalescent systems (alcohol solutions). The effect of the additives can be considered with an adjusted critical approach velocity. But the relevant physical properties that cause coalescence diminution still need to be identified. Surface tension variation is too small to justify the bubble size differences. The critical approach velocity model should be based on a more solid theoretical foundation. As detailed above, other experiments with additives and measurements of the liquid properties are required.

- Moreover, a theoretical basis and DNS simulations could be used to obtain a fully predictive set of kernels.

The ultimate goal would be to obtain completely *a-priori* industrial CFD-PBM simulations, without the need for experiments.

Bibliography

Alméras, E., Risso, F., Roig, V., Cazin, S., Plais, C. & Augier, F. (2015), 'Mixing by bubble-induced turbulence', *Journal of Fluid Mechanics* 776, 458–474.

Laakkonen, M., Alopaeus, V. & Aittamaa, J. (2006), 'Validation of bubble breakage, coalescence and mass transfer models for gas-liquid dispersion in agitated vessel', *Chemical Engineering Science* 61, 218–228.

Lehr, F., Millies, M. & Mewes, D. (2002), 'Bubble-size distributions and flow fields in bubble columns', *American Institute of Chemical Engineering Journal* 48(11), 2426–2443.

Liao, Y. & Lucas, D. (2009), 'A literature review of theoretical models for drop and bubble breakup in turbulent dispersions.', *Chemical Engineering Science* 64, 3389–3406.

Liao, Y. & Lucas, D. (2010), 'A literature review on mechanisms and models for the coalescence process of fluid particles.', *Chemical Engineering Science* 65, 2851–2864.

Simonnet, M., Gentric, C., Olmos, E. & Midoux, N. (2008), 'CFD simulation of the flow field in a bubble column reactor: Importance of the drag force formulation to describe regime transitions', *Chemical Engineering and Processing: Process Intensification* 47(9), 1726–1737.

Tomiyama, A. (1998), 'Struggle with computational bubble dynamics.', *Multiphase Science and Technology* 10(4), 369.

Wang, T. F., Wang, J. F. & Jin, Y. (2005), 'Theoretical prediction of flow regime transition in bubble columns by the population balance model', *Chemical Engineering Science* 60, 6199–6209.

Appendix A

Experimental data

Superficial gas velocity, m/s	Global gas volume fraction, %			
	DMW	Tap water	Ethanol 0.01%	Ethanol 0.05%
0.01	3.50	3.50	3.15	3.50
0.02	7.69	6.96	6.72	8.22
0.03	10.78	10.93	10.98	12.49
0.04	12.73	13.34	13.54	16.69
0.05	14.83	15.23	15.37	19.63
0.06	15.50	16.72	17.13	21.79
0.07	16.61	18.94	18.94	23.26
0.08	18.10	20.15	20.15	25.27
0.09	18.93	20.17	21.41	26.65
0.10	19.75	20.25	22.37	27.97
0.11	20.94	21.44	23.49	29.25
0.12	21.52	22.02	23.86	30.34
0.13	22.29	22.79	25.11	31.39
0.14	23.00	23.72	26.32	32.26
0.15	23.70	25.31	27.10	32.98
0.16	24.60	26.02	27.44	33.54
0.17	25.00	26.37	28.26	34.64
0.18	25.55	26.55	29.44	35.17
0.20	26.74	27.74	29.77	36.35
0.22	27.41	27.91	31.15	38.22
0.24	28.39	28.39	31.76	39.64
0.25	28.86	28.86	32.64	40.17
0.26	29.18	29.68	33.22	40.67
0.28	30.11	30.61	33.80	41.46
0.30	30.72	31.72	34.92	42.23
0.32	31.46	32.46	36.00	42.89
0.35	33.18	34.18	37.08	45.12

Table A.1: Global hold-up for demineralised water (DMW), tap water, ethanol 0.01% and ethanol 0.05% for the column ϕ 0.4 m.

Radial position	Local gas volume fraction, %					
	0.03 m/s	0.06 m/s	0.09 m/s	0.16 m/s	0.25 m/s	0.35 m/s
0.00	12.99	21.07	25.01	31.32	38.36	46.09
0.20	12.89	21.16	24.51	31.65	39.42	45.23
0.40	12.07	20.88	22.16	29.43	36.21	41.39
0.60	12.54	20.80	19.08	24.98	29.76	36.29
0.80	12.37	18.62	16.99	20.07	24.04	29.42

Table A.2: Local gas volume fraction at H/D=2.5 with demineralised water.

Radial position	Local gas volume fraction, %					
	0.03 m/s	0.06 m/s	0.09 m/s	0.16 m/s	0.25 m/s	0.35 m/s
0.00	12.6	21.5	23.4	30.7	37.7	43.0
0.20	13.0	20.5	22.8	30.0	34.1	43.4
0.40	12.2	20.0	22.4	27.7	34.1	42.0
0.60	12.3	20.5	20.5	25.6	30.4	36.2
0.80	12.2	19.0	15.8	20.8	23.7	26.6

Table A.3: Local gas volume fraction at H/D=2.5 with tap water.

Radial position	Local gas volume fraction, %					
	0.03 m/s	0.06 m/s	0.09 m/s	0.16 m/s	0.25 m/s	0.35 m/s
0.00	12.95	22.75	26.90	34.06	40.50	48.00
0.20	12.70	22.38	26.66	34.05	41.50	46.60
0.40	12.26	22.46	24.64	31.48	38.20	43.50
0.60	12.30	22.44	21.54	27.06	32.00	38.00
0.80	12.23	20.58	18.80	22.19	26.00	31.00

Table A.4: Local gas volume fraction at H/D=2.5 with ethanol 0.01%.

Radial position	Local gas volume fraction, %					
	0.03 m/s	0.06 m/s	0.09 m/s	0.16 m/s	0.25 m/s	0.35 m/s
0.00	12.88	26.12	29.73	37.43	43.65	51.23
0.20	12.33	24.81	29.89	36.14	44.60	48.68
0.40	12.65	25.62	28.37	33.65	39.15	46.54
0.60	11.82	25.71	25.23	29.57	33.05	40.10
0.80	11.95	24.50	21.50	23.31	28.15	33.40

Table A.5: Local gas volume fraction at H/D=2.5 with ethanol 0.05%.

Axial position	Local gas volume fraction, %		
	DMW	Tap water	Ethanol 0.05%
0.125			10.35
0.25	9.1	9.2	9.53
0.375	9.01	9.1	9.06
0.5	9.71	9.8	10.21
0.625	10.27		
0.75	10.83	10.5	10.83
1	10.83	11	11.33
1.25	11.65348	11.5	12.04
1.875	12.27	12.15	12.77
2.5	12.6	12.7	12.88
3.125	12.6	12.75	13.04
3.75	13	13.02	13.12

Table A.6: Local gas volume fraction at the column centre at different axial positions with a superficial gas velocity equal to 3 cm/s (homogeneous regime) with demineralised water (DMW), tap water and ethanol 0.05%.

Axial position	Local gas volume fraction, %		
	DMW	Tap water	Ethanol 0.05%
0.125	29.21	30.3	30.68
0.25	28.7	29.52	30.67
0.375	28.175	28.87	31.24
0.5	27.63	28.765	31.61
0.625	27.63	28.01	
0.75	27.64	28.31	32.2
1	27.63	28.4	31.95
1.25	28.385	28.735	32.65
1.875	28.735	30.455	34.16
2.5	30.7	31.335	37.43
3.125	31.44		37.75
3.75	32.3	34.015	39.34

Table A.7: Local gas volume fraction at the column centre at different axial positions with a superficial gas velocity equal to 16 cm/s (heterogeneous regime) with demineralised water (DMW), tap water and ethanol 0.05%.

Radial position	Axial liquid velocity, m/s			
	0.03 m/s	0.06 m/s	0.09 m/s	0.16 m/s
0.00	0.20	0.51	0.81	0.88
0.20	0.15	0.49	0.67	0.66
0.40	0.18	0.38	0.41	0.50
0.60	0.14	0.28	0.24	0.23
0.75	0.12	-0.02	-0.10	-0.12
0.80	-0.06	-0.28	-0.28	-0.27
0.90	-0.18	-0.43	-0.46	-0.44
0.95	-0.35	-0.56	-0.59	-0.66

Table A.8: Axial liquid velocity at H/D=2.5 with demineralised water.

Radial position	Axial liquid velocity, m/s		
	DMW	Tap water	Ethanol 0.05%
0.00	0.87	1.00	1.06
0.20	0.75	0.87	0.93
0.40	0.55	0.58	0.60
0.60	0.25	0.28	0.29
0.75	-0.13		
0.80	-0.28	-0.35	-0.46
0.90	-0.48		
0.95	-0.73	-0.49	-0.59

Table A.9: Axial liquid velocity at H/D=2.5 with a superficial gas velocity equal to 16 cm/s (heterogeneous regime) with demineralised water (DMW), tap water and ethanol 0.05%.

Radial position	Sauter mean diameter, mm					
	0.03 m/s	0.06 m/s	0.09 m/s	0.16 m/s	0.25 m/s	0.35 m/s
0.00	7.45	7.36	8.25	9.05	9.62	9.96
0.20	7.22	7.35	8.10	8.84	9.23	9.55
0.40	7.18	7.38	7.49	8.63	8.35	8.75
0.60	7.13	6.90	6.60	7.51	7.70	8.30
0.80	7.02	6.60	6.00	6.34	6.17	6.69

Table A.10: Sauter mean diameter at H/D=2.5 with demineralised water.

Radial position	Sauter mean diameter, mm				
	0.03 m/s	0.09 m/s	0.16 m/s	0.25 m/s	0.35 m/s
0.00	5.68	6.74	7.11	7.41	7.62
0.20	5.58	6.24	6.97	7.53	8.07
0.40	6.38	5.87	6.83	7.22	7.49
0.60	5.56	5.54	5.67	6.17	6.06
0.80	5.33	4.35	4.07	4.76	5.14

Table A.11: Sauter mean diameter at H/D=2.5 with tap water.

Radial position	Sauter mean diameter, mm					
	0.03 m/s	0.06 m/s	0.09 m/s	0.16 m/s	0.25 m/s	0.35 m/s
0.00	6.61	6.80	7.07	7.34	8.01	8.41
0.20	6.52	6.78	7.00	7.23	7.99	7.79
0.40	6.61	6.60	6.49	6.72	7.02	7.82
0.60	6.59	6.21	5.78	6.04	6.53	7.01
0.80	6.40	6.10	5.25	5.29	5.52	5.38

Table A.12: Sauter mean diameter at H/D=2.5 with ethanol 0.01%.

Radial position	Sauter mean diameter, mm					
	0.03 m/s	0.06 m/s	0.09 m/s	0.16 m/s	0.25 m/s	0.35 m/s
0.00	5.83	5.85	5.88	6.07	6.66	6.92
0.20	5.98	5.85	5.83	5.99	6.78	6.76
0.40	6.01	5.71	5.33	5.56	5.68	6.40
0.60	6.08	5.87	4.94	5.00	4.94	5.72
0.80	5.83	5.82	4.46	4.38	4.47	3.99

Table A.13: Sauter mean diameter at H/D=2.5 with ethanol 0.05%.

Axial position	Sauter mean diameter, mm	
	DMW	Ethanol 0.05%
0.125	8.80	8.05
0.25	8.75	
0.375	8.67	8.91
0.50	7.29	8.17
0.625	7.52	
0.75	7.62	6.93
1.00	6.98	6.95
1.25	7.26	7.52
1.875	6.99	6.84
2.50	7.30	6.79
3.125	7.20	6.76
3.75	6.85	7.04

Table A.14: Sauter mean diameter at the column centre at different axial positions with a superficial gas velocity equal to 3 cm/s (homogeneous regime) with demineralised water (DMW) and ethanol 0.05%.

Axial position	Sauter mean diameter, mm	
	DMW	Ethanol 0.05%
0.125	8.11	6.89
0.25	8.00	6.87
0.375	7.84	6.50
0.50		6.48
0.625	8.11	6.40
0.75	8.11	6.35
1.00	7.89	6.40
1.25	8.13	6.07
1.875	8.66	6.38
2.50	8.70	6.07
3.125	8.77	6.38
3.75	9.05	6.70
4.375	9.37	
5.00	9.81	

Table A.15: Sauter mean diameter at the column centre at different axial positions with a superficial gas velocity equal to 16 cm/s (heterogeneous regime) with demineralised water (DMW) and ethanol 0.05%.

Axial position	Local gas volume fraction, %			
	92-holes sparger		7-holes sparger	
	DMW	Ethanol 0.05%	DMW	Ethanol 0.05%
0.125		1.80	10.35	3.82
0.25	9.10	4.15	9.53	4.76
0.375	9.01	4.58	9.06	4.51
0.50	9.71	5.06	10.21	5.71
0.625	10.27			
0.75	10.83	6.55	10.83	6.28
1.00	10.83	6.88	11.33	7.49
1.25	11.65	7.72	12.04	8.36
1.875	12.27	8.43	12.77	9.49
2.50	12.60	8.99	12.88	10.03
3.125	12.60	10.21	13.04	11.23
3.75	13	11.03	13.12	12.14

Table A.16: Local gas volume fraction at the column centre at different axial positions with a superficial gas velocity equal to 3 cm/s (homogeneous regime) with demineralised water (DMW) and ethanol 0.05%: 92-holes sparger versus 7-holes sparger.

Axial position	Local gas volume fraction, %			
	92-holes sparger		7-holes sparger	
	DMW	Ethanol 0.05%	DMW	Ethanol 0.05%
0.125	29.21	39.58	30.68	48.55
0.25	28.7	39.95	30.67	44.48
0.375	28.175	29.14	31.24	32.84
0.50	27.63	26.11	31.61	29.5
0.625	27.63			
0.75	27.64	26.01	32.2	29.16
1.00	27.63		31.95	29.07
1.25	28.39	25.68	32.65	29.37
1.875	28.74	27.8	34.16	30.62
2.50	30.7	30.08	37.43	35.87
3.125	31.44	31.84	37.75	36.36
3.75	32.3	32.48	39.34	38.9

Table A.17: Local gas volume fraction at the column centre at different axial positions with a superficial gas velocity equal to 16 cm/s (heterogeneous regime) with demineralised water (DMW) and ethanol 0.05%: 92-holes sparger versus 7-holes sparger.

Axial position	Local gas volume fraction, %			
	92-holes sparger		7-holes sparger	
	DMW	Ethanol 0.05%	DMW	Ethanol 0.05%
0.125		42.61	38.58	51.93
0.250	35.10		36.89	
0.375	34.62	41.32	36.94	43.75
0.50	34.62	37.16	38.02	40.40
0.625	33.67		38.03	
0.75	33.72	34.44	39.16	38.23
1.00	34.81	33.76	40.32	37.53
1.25	35.15	33.54	43.00	38.35
1.875	35.67	35.57	43.65	40.12
2.50	37.70	37.91	45.37	42.71
3.125	38.38	39.08	48.12	45.44
3.75	40.30	41.72		47.19

Table A.18: Local gas volume fraction at the column centre at different axial positions with a superficial gas velocity equal to 25 cm/s (heterogeneous regime) with demineralised water (DMW) and ethanol 0.05%: 92-holes sparger versus 7-holes sparger.

Radial position	Local gas volume fraction, %			
	92-holes sparger		7-holes sparger	
	H/D=2.50	H/D=0.25	H/D=2.50	H/D=0.25
0.00	12.99	9.01	9.20	9.01
0.20	12.89	7.77	9.25	7.77
0.40	12.07	8.50	9.42	8.50
0.60	12.54	7.21	8.60	7.21
0.80	12.37	7.74	7.27	7.74

Table A.19: Local gas volume fraction with a superficial gas velocity equal to 3 cm/s (homogeneous regime) with demineralised water at two different heights (H/D=2.5 versus H/D=0.25): 92-holes sparger versus 7-holes sparger.

Radial position	Local gas volume fraction, %			
	92-holes sparger		7-holes sparger	
	H/D=2.50	H/D=0.25	H/D=2.50	H/D=0.25
0.00	31.32	29.50	31.00	29.50
0.20	31.65	29.13	31.33	29.13
0.40	29.43	28.16	31.34	28.16
0.60	24.98	27.80	27.11	27.80
0.80	20.07	28.19	22.58	28.19

Table A.20: Local gas volume fraction with a superficial gas velocity equal to 16 cm/s (heterogeneous regime) with demineralised water at two different heights (H/D=2.5 versus H/D=0.25): 92-holes sparger versus 7-holes sparger.

Axial position	Sauter mean diameter, mm			
	92-holes sparger		7-holes sparger	
	DMW	Ethanol 0.05%	DMW	Ethanol 0.05%
0.125	8.80		8.05	14.72
0.250	8.75	10.77		10.61
0.375	8.67	7.92	8.91	7.44
0.500	7.29	7.50	8.17	8.27
0.625	7.52	7.60		
0.750	7.62	7.30	6.93	7.77
1.000	6.98	7.60	6.95	7.30
1.250	7.26	7.03	7.52	7.31
1.875	6.99	7.53	6.84	7.36
2.500	7.30	7.25	6.79	6.63
3.125	7.20	7.00	6.76	6.90
3.750	6.85	7.10	7.04	6.46

Table A.21: Sauter mean diameter at the column centre at different axial positions with a superficial gas velocity equal to 3 cm/s (homogeneous regime) with demineralised water (DMW) and ethanol 0.05%: 92-holes sparger versus 7-holes sparger.

Axial position	Sauter mean diameter, mm			
	92-holes sparger		7-holes sparger	
	DMW	Ethanol 0.05%	DMW	Ethanol 0.05%
0.125	8.11	43.47	6.89	41.31
0.25	8.00	21.26	6.87	20.78
0.375	7.84	10.80	6.50	10.90
0.50		9.17	6.48	8.21
0.625	8.11		6.40	
0.75	8.11	8.04	6.35	7.07
1.00	7.89	7.72	6.40	6.22
1.25	8.13	7.73	6.07	6.08
1.875	8.66	7.88	6.38	5.89
2.50	8.70	8.09	6.07	6.38
3.125	8.77	8.25	6.38	
3.75	9.05	8.63	6.70	

Table A.22: Sauter mean diameter at the column centre at different axial positions with a superficial gas velocity equal to 16 cm/s (heterogeneous regime) with demineralised water and ethanol 0.05%: 92-holes sparger versus 7-holes sparger.

Axial position	Sauter mean diameter, mm			
	92-holes sparger		7-holes sparger	
	DMW	Ethanol 0.05%	DMW	Ethanol 0.05%
0.125	8.97	24.11	6.77	22.97
0.25	8.86	26.88	6.54	24.11
0.375	8.70	12.46	6.38	11.15
0.50	8.84	9.33	6.43	8.33
0.625	8.97			
0.75	8.97	7.99	6.33	6.77
1.00	8.74	7.63	6.48	6.45
1.25	8.98	7.89	6.65	6.07
1.875	9.21	8.35	6.92	6.28
2.50	9.56	8.58	6.66	6.63
3.125	9.62	8.59	7.24	6.88
3.75	9.58	8.97	7.23	6.89

Table A.23: Sauter mean diameter at the column centre at different axial positions with a superficial gas velocity equal to 25 cm/s (heterogeneous regime) with demineralised water and ethanol 0.05%: 92-holes sparger versus 7-holes sparger.

Radial position	Sauter mean diameter, mm			
	92-holes sparger		7-holes sparger	
	H/D=2.50	H/D=0.25	H/D=2.50	H/D=0.25
0.00	7.25	8.30	6.81	8.30
0.20	6.80	8.12	6.96	8.12
0.40	7.18	7.74	6.79	7.74
0.60	7.13	7.05	6.40	7.05
0.80	7.02	7.37	6.23	7.37

Table A.24: Sauter mean diameter with a superficial gas velocity equal to 3 cm/s (homogeneous regime) with demineralised water at two different heights (H/D=2.5 versus H/D=0.25): 92-holes sparger versus 7-holes sparger.

Radial position	Sauter mean diameter, mm			
	92-holes sparger		7-holes sparger	
	H/D=2.50	H/D=0.25	H/D=2.50	H/D=0.25
0.00	9.05	8.00	8.40	8.00
0.20	8.84	8.05	8.20	8.05
0.40	8.63	8.01	7.84	8.01
0.60	7.51	7.90	7.07	7.90
0.80	6.34	7.48	6.60	7.48

Table A.25: Sauter mean diameter with a superficial gas velocity equal to 16 cm/s (heterogeneous regime) with demineralised water at two different heights (H/D=2.5 versus H/D=0.25): 92-holes sparger versus 7-holes sparger.

Appendix B

Drag laws

B.1 Drag laws for spherical bubbles

The first drag law was formulated by Stokes (1851), for $Re_b << 1$ and spherical totally contaminated bubbles:

$$C_D = \frac{24}{Re_b}. \tag{B.1}$$

Schiller & Naumann (1935) corrected this relation to extend the field until $Re_b \leq 800$, and it is the most utilized for bubble columns in homogeneous regime:

$$C_D = \frac{24}{Re_b}\left(1 + 0.15\, Re_b^{0.687}\right). \tag{B.2}$$

A constant value for $Re_b > 1000$ is considered in order to use this correlation in a larger field:

$$C_D = \begin{cases} \frac{24}{Re_b}\left(1 + 0.15\, Re_b^{0.687}\right) & Re_b \leq 1000; \\ 0.44 & Re_b \geq 1000. \end{cases} \tag{B.3}$$

Subsequently, different correlations have been developed; in general the coefficient depends on the Reynolds number.

Other important drag laws were proposed by Zhang & Vanderheyden (2002):

$$C_D = 0.44 + \frac{24}{Re_b} + \frac{1}{1 + \sqrt{Re_b}} \tag{B.4}$$

and by Fdhila & Duineveld (1996):

$$C_D = \frac{24}{Re_b}\left(1 + 0.9135\, Re_b^{0.6305}\right). \tag{B.5}$$

B.2 Drag laws model for oblate bubbles

For a deformed bubble, the drag coefficient depends on the Reynolds, the Eötvös and the Morton number:

$$C_D = f(Re_b,\, Eo,\, Mo). \tag{B.6}$$

In certain cases, some authors use the Weber number or the Frounde number. Both these numbers can be written in function of the Reynolds, Eötvös and Morton

number. It is necessary to take three independent dimensionless numbers.

$$We = \frac{\rho_q \, u_r^2 \, d_{eq}}{\sigma} = Re_b^2 \left(\frac{Mo}{Eo} \right)^{1/2}; \tag{B.7}$$

$$Fr = \sqrt{\frac{\rho_q \, v_r^2}{\Delta\rho \, g \, d_{eq}}} = \sqrt{\frac{We}{Eo}} \tag{B.8}$$

where u_r is the relative velocity between the two phases.

For different operating conditions, Fan et al. (1999) found an empirical correlation to obtain directly the relative velocity. It can give a first idea for several systems, with spherical and ellipsoidal bubbles:

$$u_r = \left(\frac{\sigma g}{\rho_q} \right)^{1/4} \left[\left(\frac{Mo^{-1/4}}{K_b} \left(\frac{\Delta\rho}{\rho_q} \right)^{5/4} d'^2 \right)^{-n} + \left(\frac{2\,c}{d'} + \frac{\Delta\rho d'}{2\,\rho_q} \right)^{-n/2} \right]^{-1/n} \tag{B.9}$$

with:

$$d' = d_b \sqrt{\frac{\rho_l \, g}{\sigma}};$$
$$K_b = \max\left(K_{b0} \, Mo^{-0.038}, \, 12 \right);$$
$K_{b0} = 10.2$ for organic and 14.7 for aqueous solution;
$n = 1.6$ for clean and 0.8 for contaminated systems;
$c = 1.2$ for pure liquid and 1.4 for multi-composition liquid.

Maxworthy et al. (1996) proposed to use for deformed bubbles:

$$C_D = \begin{cases} \min\left\{ \dfrac{4}{3} \dfrac{Eo}{We_c}, \, \dfrac{8}{3} Eo^{2/3} \right\} & \text{for} \quad Eo \leq 7.12 \\ \dfrac{8}{3} \dfrac{4\,Eo}{(9.5 + Eo)} & \text{for} \quad Eo \geq 7.12 \end{cases} \tag{B.10}$$

where:

$$We_c = \max(0.517 ln(Mo) + 7.624, \, 2.326) \tag{B.11}$$

Tomiyama (1998) suggested to use for deformed bubbles:

$$C_D = \frac{8}{3} \frac{Eo}{(4 + Eo)}. \tag{B.12}$$

This expression for $Eo > 40$ tends to a constant value of 8/3, as calculated by Davies & Taylor (1950) for a regime of spherical cap.

In case of spherical bubbles Tomiyama (1998) used the drag law of Levich (1962), available for $Re >> 1$:

$$C_D = \frac{48}{Re_b}. \tag{B.13}$$

Tomiyama (1998) obtained a correlation usable for every regime:

$$C_D = \max\left\{ \min\left\{ \frac{24}{Re_b} \left(1 + 0.15 \, Re_b^{0.687} \right), \, \frac{48}{Re_b} \right\}, \, \frac{8}{3} \frac{Eo}{(4 + Eo)} \right\}. \tag{B.14}$$

Dijkhuizen et al. (2010) proposed a correlation suitable for spherical and deformed bubbles:

$$C_D = \sqrt{{C_D}^2\left(Re_b\right) + {C_D}^2\left(Eo\right)}; \tag{B.15}$$

$$C_D\left(Re_b\right) = \frac{16}{Re_b}\left(1 + \frac{Re_b}{8 + 0.5\left(Re + 3.315\,{Re_b}^{0.5}\right)}\right); \tag{B.16}$$

$$C_D\left(Eo\right) = \frac{4\,Eo}{\left(9.5 + Eo\right)}. \tag{B.17}$$

Zhang et al. (2006) suggested a shorter correlation that gives results very similar to the others:

$$C_D = \frac{2}{3}\sqrt{Eo}. \tag{B.18}$$

In case of boiling regime, the most used correlation was proposed by Ishii & Zuber (1979), considering the effect of the gas fraction inside:

$$C_D = \frac{8}{3}(1 - \alpha_g)^2. \tag{B.19}$$

Tomiyama et al. (2002) coined also another correlation:

$$C_D = \frac{8}{3}\frac{Eo}{E^{2/3}\left(1 - E^2\right)^{-1}Eo + 16\,E^{4/3}}F^{-2} \tag{B.20}$$

where:

$$F = \frac{\sin^{-1}\left(\sqrt{1 - E^2}\right) - E\left(\sqrt{1 - E^2}\right)}{\left(1 - E^2\right)} \tag{B.21}$$

and E is the shape factor that is:

$$E = \frac{1}{1 + 0.163\,Eo^{0.757}}. \tag{B.22}$$

Hosokawa & Tomiyama (2009) calculated E starting by the E_0, the shape factor in an infinite medium.

$$E_0 = \begin{cases} 1 & Ta \geq 1; \\ \left\{0.81 + 0.206\,\tanh\left[\left(0.8 - \log_{10} Ta\right)2\right]\right\}^3 & 39.8 \geq Ta; \\ 0 & 39.8 \geq Ta. \end{cases} \tag{B.23}$$

Using the Tadaki number:

$$Ta = Re_b\,Mo^{0.23}. \tag{B.24}$$

Starting by E_0, it is possible to obtain E:

$$E = E_0\,\max\left\{1 - 0.35\frac{y}{D}, 0.65\right\} \tag{B.25}$$

where y is the distance by the wall and D the diameter of the column.

Bibliography

Davies, R. M. & Taylor, G. (1950), 'The mechanics of large bubbles rising through extended liquids and through liquids in tubes.', *Proceedings A - The Royal Society* 200, 1062.

Dijkhuizen, W., Roghair, I., Annaland, M. & Kuipers, J. (2010), 'DNS of gas bubbles behaviour using an improved 3D front tracking model-drag force on isolated bubbles and comparison with experiments.', *Chemical Engineering Science* 65(4), 1415–1426.

Fan, L., Yang, G., Lee, D. & Luo, X. (1999), 'Some aspects of high-pressure phenomena of bubbles in liquids and liquid-solid suspensions.', *Chemical Engineering Science* 54, 4681–4709.

Fdhila, R. & Duineveld, P. (1996), 'The effect of surfactant on the rise of spherical bubble at high reynolds and peclet number.', *Physics of Fluid* 8(2), 310–321.

Hosokawa, S. & Tomiyama, A. (2009), 'Multi-fluid simulation of turbulent bubbly in pipe flows.', *International Journal of Multiphase flow* 28, 1497–1519.

Ishii, M. & Zuber, N. (1979), 'Drag coefficient and relative velocity in bubbly, droplet or particulate flows', *American Institute of Chemical Engineering Journal* 25(5), 843–855.

Levich, V. G. (1962), *Physicochemical Hydrodynamics*, Prentice Hall, Englewood Cliffs, NJ.

Maxworthy, T., Gnann, C., Kürten, M. & Durst, F. (1996), 'Experiments on the rise of air bubbles in clean viscous liquids.', *Journal of Fluid Mechanics* 321, 421–441.

Schiller, L. & Naumann, N. (1935), 'A drag coefficient correlation.', *Vdi Zeitung* 77, 318.

Stokes, G. G. (1851), 'On the effect of the internal friction of fluids on the motion of pendulums.', *Cambridge Philos. Trans.* 9, 8–106.

Tomiyama, A. (1998), 'Struggle with computational bubble dynamics.', *Multiphase Science and Technology* 10(4), 369.

Tomiyama, A., Celata, G., Hokosawa, S. & Yoshida, S. (2002), 'Terminal velocity of single bubbles in surface tension force dominant regime.', *International Journal of Multiphase flow* 28, 1497–1519.

Zhang, D., Deen, N. G. & Kuipers, J. A. M. (2006), 'Numerical simulation of dynamic flow behavior in a bubble column: A study of closures for turbulence and interface forces', *Chemical Engineering Science* 61, 7593–7608.

Zhang, D. & Vanderheyden, W. (2002), 'The effects of mesoscale structures on the disperse two-phase flows and their closures for dilute suspensions.', *International Journal of Multiphase Flow* 28, 805–822.

Appendix C

Favre-like average

C.1 Favre-like average definition

The Favre-like or phase average, in two-fluid models, allows to make a time average of the property of a phase by taking into account the instantaneous local volume fraction of this phase (Favre 1965, O'Brien 2012). The Favre mean can replace the Reynolds mean in multiphase flows (Burns et al. 2004).

A generic variable Θ, can be divided into a mean part $\widetilde{\Theta}$ and a fluctuating part Θ'' if a phase-fraction weighted average is used (O'Brien 2014):

$$\Theta = \widetilde{\Theta} + \Theta'', \tag{C.1}$$

$$\widetilde{\Theta} = \frac{\int \alpha_i(t)\Theta(t)dt}{\int \alpha_i(t)dt}, \tag{C.2}$$

that is equal to:

$$\widetilde{\Theta} = \frac{\overline{\alpha_i \Theta}}{\overline{\alpha_i}}, \tag{C.3}$$

where α_i is the instantaneous local gas volume fraction of the phase i.

In this work different properties are calculated with both Reynolds and Favre-like average: axial velocities of the two phases, Sauter mean diameter and turbulence properties.

The gas volume fraction (and consequently the liquid volume fraction) is the same by using Reynolds and Favre-like averages.

The axial gas velocity with the Favre-like average seen by the bubbles ($\widetilde{u}_g$) is calculated as follows:

$$\widetilde{u}_g = \frac{\overline{\alpha_g u_g}}{\overline{\alpha_g}}, \tag{C.4}$$

where u_g is the instantaneous axial gas velocity and α_g is the instantaneous gas volume fraction.

Consequently, by using the Reynolds average, the axial gas velocity can be divided into a mean part $\overline{\alpha}_g$ and a fluctuating part u'_g, as follows (O'Brien 2014):

$$\alpha_g = \overline{\alpha}_g + \alpha'_g, \tag{C.5}$$

while, by using the Favre-like average, the axial gas velocity can be divided into a mean part $\overline{\alpha}_g$ and a fluctuating part u'_g (O'Brien 2014):

$$\alpha_g = \widetilde{\alpha}_g + \alpha''_g. \tag{C.6}$$

Concerning the axial liquid velocity, the Favre-like average seen by the liquid phase should be considered ($\widetilde{u}_l$):

$$\widetilde{u}_l = \frac{\overline{\alpha_l u_l}}{\overline{\alpha_l}}, \tag{C.7}$$

where u_l is the instantaneous axial liquid velocity and α_l is the instantaneous liquid volume fraction, that is the complementary of the instantaneous gas volume fraction.

The Sauter mean diameter with the Favre-like average seen by the bubbles ($\widetilde{d}_{32,g}$) is defined as:

$$\widetilde{d}_{32,g} = \frac{\overline{\alpha_g d_{32}}}{\overline{\alpha_g}}, \tag{C.8}$$

where d_{32} is the instantaneous Sauter mean diameter.

The turbulence properties refer to the liquid, but they can affect bubble coalescence and breakage phenomena. For this reason, the Favre-like averages seen by both the bubbles and the liquid are calculated. Concerning the turbulence kinetic energy, the Favre-like averages seen by the bubbles $\widetilde{k}_g$ and the liquid $\widetilde{k}_l$ are calculated respectively as:

$$\widetilde{k}_g = \frac{\overline{\alpha_g k}}{\overline{\alpha_g}} \tag{C.9}$$

and

$$\widetilde{k}_l = \frac{\overline{\alpha_l k}}{\overline{\alpha_l}}, \tag{C.10}$$

where k is the instantaneous turbulence kinetic energy.

The Favre-like averages of the turbulence dissipation rate seen by the bubbles $\widetilde{\varepsilon}_g$ and liquid $\widetilde{\varepsilon}_l$

$$\widetilde{\varepsilon}_g = \frac{\overline{\alpha_g \varepsilon}}{\overline{\alpha_g}} \tag{C.11}$$

and

$$\widetilde{\varepsilon}_l = \frac{\overline{\alpha_l \varepsilon}}{\overline{\alpha_l}}, \tag{C.12}$$

where ε is the instantaneous turbulence dissipation rate.

C.2 Favre-like average effects

The effect of the Favre-like average on the properties listed above is studied in this work by comparing the Reynolds averages with the Favre-like averages. In this part of the work, the radial profiles, obtained with the column ϕ 0.4 m and a superficial gas velocity equal to 0.16 m/s (heterogeneous regime) at H/D=2.5, are compared.

The effect of the Favre-like average on the axial liquid velocities is quite small (Fig. C.1). The Favre-like average seen by the liquid is slightly smaller than the Reynold average for every radial position, except at the wall, where the means are identical.

The effect on the axial gas velocity could be considered. Expect at the wall, the use of the Favre-like average, instead of the Reynolds average, causes an increase of this property, as shown in Fig. C.2.

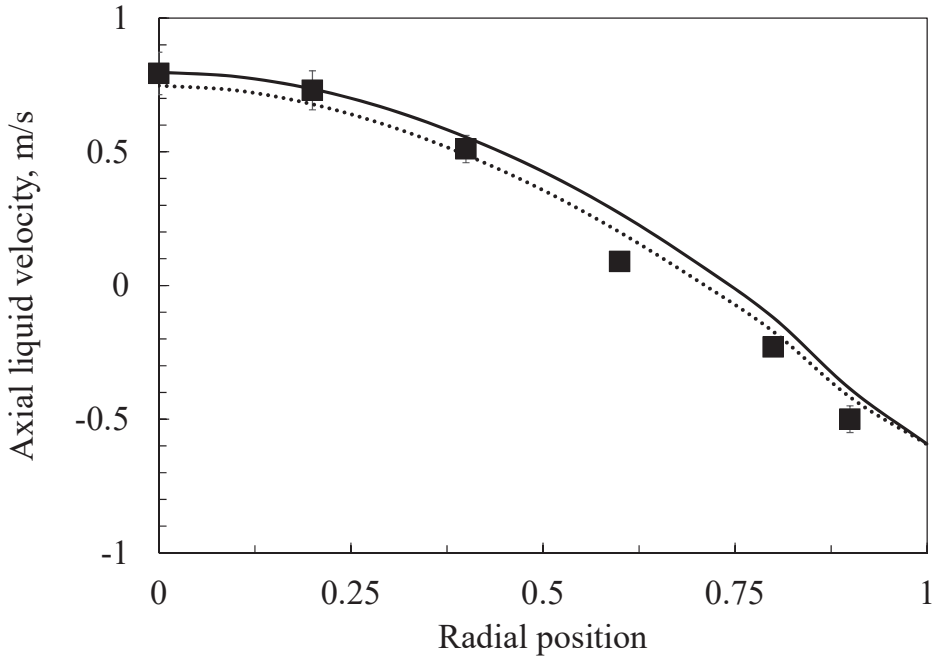

Figure C.1: Radial profile of the axial liquid velocity for a superficial gas velocity of 0.16 m/s at H/D=2.5. Experimental data (■) versus CFD results obtained by considering the Reynolds average (solid line) and the Favre-like average seen by the liquid (dotted line).

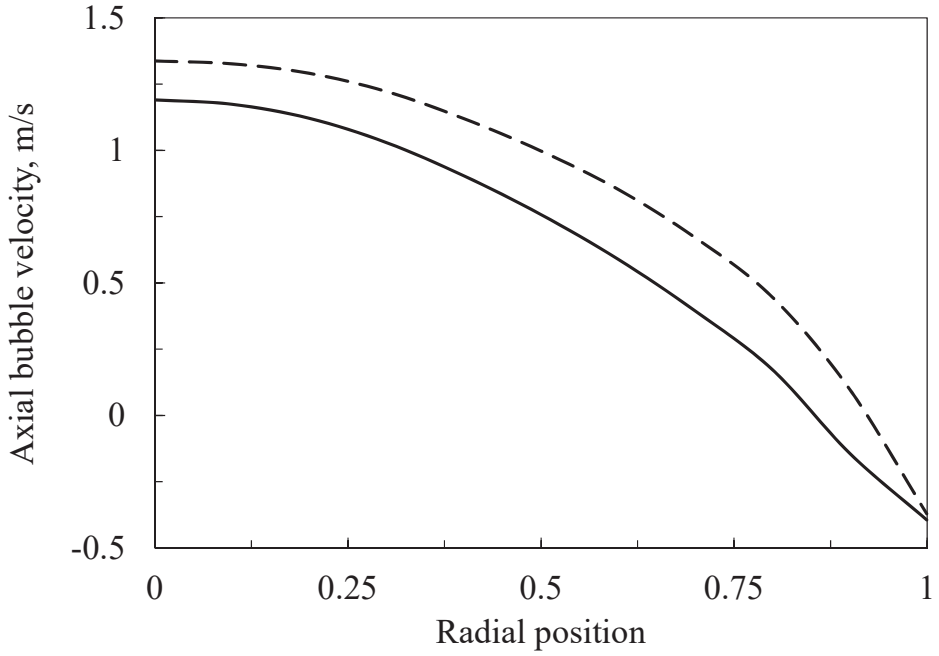

Figure C.2: Radial profile of the axial gas velocity for a superficial gas velocity of 0.16 m/s at H/D=2.5. Experimental data (■) versus CFD results obtained by considering the Reynolds average (solid line) and the Favre-like average seen by the bubbles (dashed line).

The Sauter mean diameter, if calculated with the Favre-like average seen by the bubbles, has an increase lower than 10% . The radial profile shape is the same and the discrepancies are lower close to wall. The radial profiles of the Sauter mean diameter are reported in Fig. C.3.

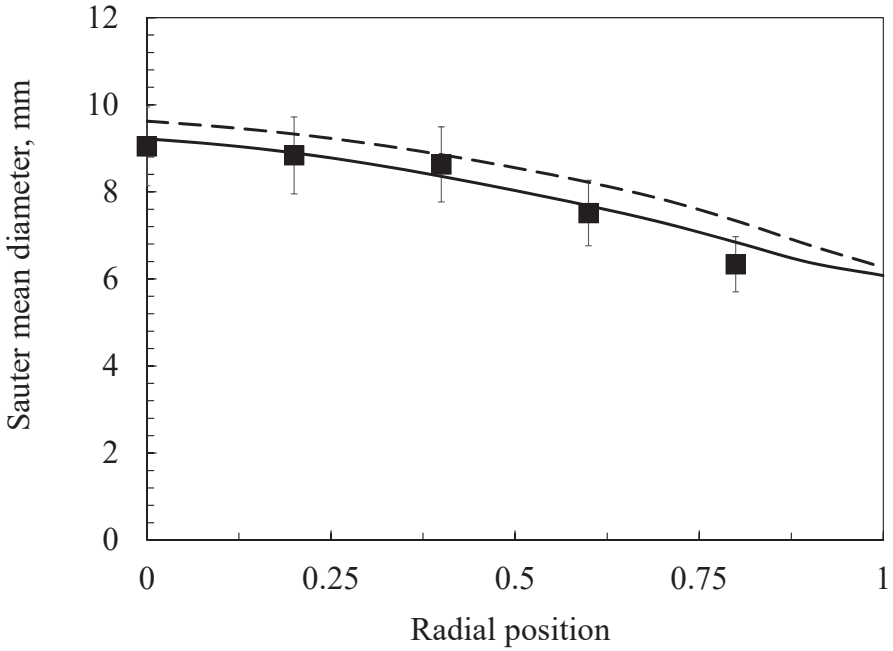

Figure C.3: Radial profile of the Sauter mean diameter for a superficial gas velocity of 0.16 m/s at H/D=2.5. Experimental data (■) versus CFD results obtained by considering the Reynolds average (solid line) and the Favre-like average seen by the bubbles (dashed line).

The effects of the Favre-like averages on the turbulence properties are almost negligible, as shown in Fig. C.4 and C.5 for turbulence kinetic energy and turbulence dissipation rate respectively. The radial profile calculated with Favre-like average seen by the bubbles is slightly higher than the classical one, while those calculated with the Favre-like average seen by the liquid is slightly lower.

For every property, the radial profile is slightly influenced by the Favre-like average and its effect is often negligible. The Favre-like average seen by the bubbles slightly increases every property, while the Favre-like average seen by the liquid has the opposite effect.

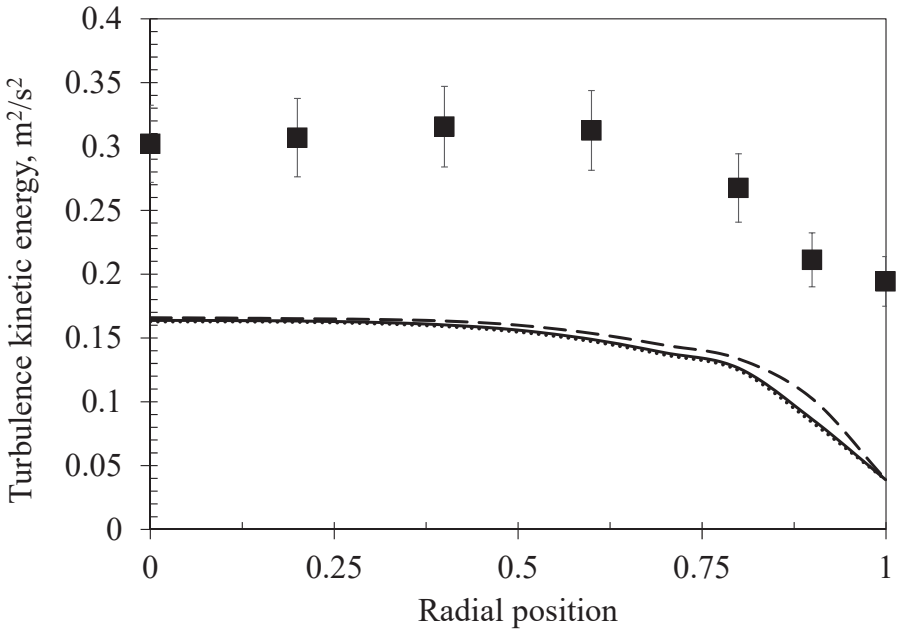

Figure C.4: Radial profile of the turbulence kinetic energy for a superficial gas velocity of 0.16 m/s at H/D=2.5. Experimental data (■) versus CFD results obtained by considering the Reynolds average (solid line) and the Favre-like average seen by the bubbles (dashed line) and the liquid (dotted line).

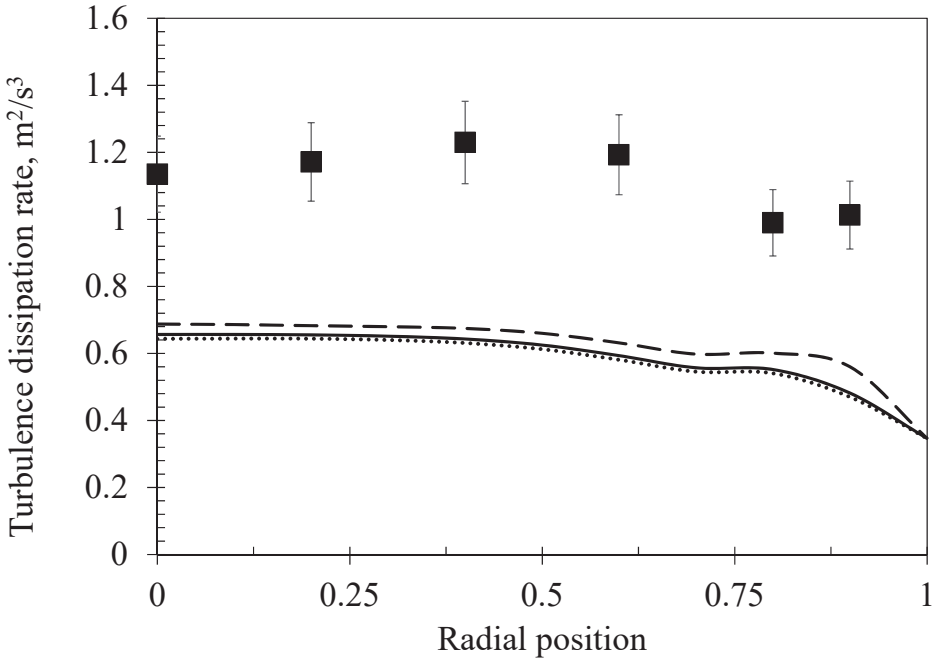

Figure C.5: Radial profile of the turbulence dissipation rate for a superficial gas velocity of 0.16 m/s at H/D=2.5. Experimental data (■) versus CFD results obtained by considering the Reynolds average (solid line) and the Favre-like average seen by the bubbles (dashed line) and the liquid (dotted line).

Bibliography

Burns, A. D. B., Frank, T., Hamill, I. & Shi, J. M. (2004), The Favre averaged drag model for turbulent dispersion in eulerian multi-phase flows., *in* '5th International Conference on Multiphase Flow, ICMF-2004', Yokohama, Japan.

Favre, A. (1965), 'Equations des gaz turbulents compressibles. i. Formes générales.', *Journal de Mécanique* 4, 361–390.

O'Brien, T. (2012), A Favre-averaged turbulence model for gas-particle flows., *in* '2012 AIChE Annual Meeting', Pittsburgh, Pennsylvania, USA.

O'Brien, T. (2014), A multiphase turbulence theory for gas-solids flows using Favre-averaging., *in* '2014 NETL Workshop on Multiphase Flow Science', Morgantown, West Virginia, USA.